TUM School of Engineering and Design

Einfluss der Oberflächentopographie auf ausgewählte Materialeigenschaften von *B. subtilis* Biofilmen

Dissertation von

Elif Nur Hayta

Technische Universität München

TECHNISCHE UNIVERSITÄT MÜNCHEN

TUM School of Engineering and Design

Einfluss der Oberflächentopographie auf ausgewählte Materialeigenschaften von *B. subtilis* Biofilmen

Elif Nur Hayta

Vollständiger Abdruck der von der TUM School of Engineering and Design der Technischen Universität München zur Erlangung des akademischen Grades

einer

Doktorin der Ingenieurwissenschaften (Dr.-Ing)

genehmigten Dissertation.

Vorsitz:	Prof. Dr. Alisa Machner
Prüfer der Dissertation:	1. Prof. Dr. Oliver Lieleg
	2. Prof. Dr. Benedikt Sabass

Die Dissertation wurde am 27.12.2021 bei der Technischen Universität München eingereicht und durch die TUM School of Engineering and Design am 24.03.2022 angenommen.

Summary

Biofilm is a sessile form of bacterial communities. Here, the surrounding polymer matrix provides protection and robustness to the bacteria which makes biofilms hard to remove. Although this can be harmful when biofilms contaminate industrial and medical equipments, we can also benefit from this robustness of biofilms: As a combination of living, functional microbial communities and robust, resilient, sticky and viscoelastic materials, biofilms have found many applications in various fields including agriculture, environmental biotechnology, medicine, bioprocess engineering, electricity generation or construction. To further improve the material properties and functionality of biofilms in these applications, the biofilm matrix can be manipulated. For this purpose, several components such as macromolecules, metal ions, minerals, nanoparticles, enzymes and other bacteria can be added to the biofilm matrix. In this dissertation, a broad range of applications of natural and modified biofilms and interesting strategies to modify the biofilm matrix are presented.

In many of these applications biofilms are exposed to water; thus, their wetting behavior plays a crucial role. The interaction of biofilm with water-soluble components and with shear forces created by liquid flow is determined by the wettability of biofilms. For instance, the resistance of biofilms against solubilized toxic substances (i. e. antibiotics) and erosion is directly related to its wettability. The wetting behavior of a surface depends on its chemistry and roughness, and for biofilms, both are related to the matrix composition. For instance, the biofilms generated by *B. subtilis* NCIB 3610 and B-1 differ in matrix composition, and thus in their wetting behavior. Although both biofilms are superhydrophobic with extremely high contact angle values, NCIB 3610 biofilms exhibit high adhesion towards water (i. e. rose-like superhydrophobicity) while B-1 biofilms strongly repel water (i. e. lotus-like superhydrophobicity). Due to this difference in the mode of superhydrophobicity, B-1 biofilms are more resistant to erosion through shear forces than NCIB 3610 biofilms. In this study, the main component of highly water repellant B-1 biofilms is artificially added to the NCIB 3610 biofilm matrix during growth to improve the erosion resistance of these biofilms. Indeed, by the enrichment with PGA, the erosion resistance of NCIB 3610 biofilms increases to an intermediate level between unmodified NCIB 3610 and B-1 biofilms. Interestingly, contact angle hysteresis of PGA-enriched NCIB 3610 biofilms exhibits a similar trend and placed at a degree

between unmodified NCIB 3610 and B-1 biofilms, while the static contact angle does not change for enriched NCIB 3610 biofilms. As the contact angle hysteresis is a measure of water adhesion of a surface, these results indicate a change in the mode of superhydrophobicity. Considering that this cannot be achieved by a chemical modification, the surface topography of biofilms is examined in detail. It is revealed that reduced cavity structures on the surface change the wettability of enriched NCIB 3610 biofilms. Surprisingly, the viscoelastic and microscopic penetration properties of the biofilms are not affected by the artificial incorporation of PGA. Moreover, similar results can be obtained by addition of other polymers with different charges and molecular sizes such as alginate and PEG. This shows that a wide range of polymers can be employed for the same purpose.

Another option to modify biofilms can be cocultivation of different bacteria. This is a mechanism used by microorganisms in nature to benefit from each other. Most natural biofilms such as oral biofilms and the gut flora are multi-species communities. Also, these microbial consortia can be generated artificially in laboratories to investigate the interactions between microorganisms in these multispecies biofilms or to combine desired properties from different microorganisms. However, it is not fully understood yet how the material properties of such multispecies biofilms are determined. To obtain a better understanding of the material properties of co-cultivated biofilms, in this thesis, the surface topography and wetting behavior of binary mixtures of *B. subtilis* NCIB 3610, *natto* and B-1 strains are investigated. For all binary mixtures tested here, the morphology of the co-cultured (daughter) colonies resembles that of one of the parent strains. This macro-morphologically dominating strain is also found to be abundant in terms of numbers. However, owing to the presence of the other parent in small numbers, the surface roughness and wetting behavior of these daughter colonies are slightly but significantly different from those of the dominating parent. The presence of the 'other' strain can be detected only by a micro-topographical quantitative analysis of the biofilm; it is not observable by macro-morphological investigations alone. This highlights the ability, and even necessity, of a micro-topographical analysis of the biofilm surface by profilometry to characterize a multi-species biofilm.

Due to the ability of quantitative topographical analyses to detect the contributions of strains to co-cultured biofilms, 3D-imaging can also be used to classify the biofilms. In the last part of this thesis, biofilms of three *B. subtilis* strains (NCIB 3610, B-1 and

natto) are classified according to their surface topography. For this purpose, four machine learning algorithms (*k*-nearest neighbors, Gaussian naïve bayes, logistic regression and random forest) are trained with the topographical data containing 21 surface parameters obtained from biofilms of these strains generated on MSgg Medium. All algorithms can successfully classify these biofilm colonies according to their wetting behavior with very high accuracies. Indeed, with this approach, also the biofilms cultivated on LB medium and other biological samples such as plant leaves with different wetting behaviors (i. e. hydrophilic, rose-like and lotus-like superhydrophobic) are successfully classified regarding their topography and wetting properties as well. Furthermore, to examine the most effective surface features determining the wetting behavior, a feature elimination is performed. Here, four parameters (S_{dr}, S_{dq}, V_{vv} and S_{pc}) -among 21- are shown to be the ones which have the strongest impact on distinguishing surfaces with different wetting behaviors.

Overall, this thesis reveals the high relevance of the surface topography on certain material properties of *B. subtilis* biofilms. To benefit from biofilms in various applications, it is crucial to understand the material properties of these functional living materials. The findings presented here may help to develop novel strategies to produce more robust biofilms for biotechnological applications and provide an insight into the relation between the surface topography and the wetting behavior of complex surfaces.

Zusammenfassung

Biofilme sind eine oberflächengebundene Art von bakteriellen Gemeinschaften. Die Polymermatrix, die die Bakterien umgibt, bietet Schutz und Widerstandsfähigkeit. Dadurch sind Biofilme schwer zu entfernen. Zwar können Biofilme schweren Schaden anrichten, wenn sie industrielle oder medizinische Geräte kontaminieren, man kann aber von dieser Robustheit der Biofilme auch profitieren. Als sowohl funktionelle, lebendige, mikrobielle Gemeinschaften wie auch robuste, klebrige, beständige und viskoelastische Materialien finden Biofilme Anwendung in vielen Bereichen wie z. B. der Landwirtschaft, der industriellen und Umwelt-Biotechnologie, der Medizin, der Stromerzeugung sowie dem Bauwesen. Um die Materialeigenschaften und die Funktionalität der Biofilme für diese Anwendungen zu verbessern, kann die Biofilmmatrix gezielt manipuliert werden. Dafür kann die Biofilmmatrix mit Nanopartikeln, Makromolekülen, Mineralen, Metallionen, Enzymen oder anderen Bakterien angereichert werden. In dieser Doktorarbeit wird ein breites Spektrum von Anwendungen von natürlichen und modifizierten bakteriellen Biofilmen und interessante Strategien zur Modifikation von Biofilmmatrix dargestellt.

Da die Biofilme bei diesen Anwendungen häufig Wasser ausgesetzt werden, spielt ihr Benetzungsverhalten eine zentrale Rolle. Viele Eigenschaften von Biofilmen wie ihre Erosionsbeständigkeit oder ihre Antibiotikaresistenz werden durch die Art ihrer Wechselwirkung mit Wasser bestimmt. Die Benetzbarkeit einer Oberfläche hängt sowohl von ihrer Chemie als auch ihrer Rauigkeit ab, und beides wird durch die Matrixzusammensetzung der Biofilme beeinflusst. Zum Beispiel unterscheiden sich die *B. subtilis* NCIB 3610 und B-1 Biofilme in der Matrixzusammensetzung und damit auch im Benetzungsverhalten. Beide Biofilme sind zwar superhydrophob und zeigen sehr hohe Kontaktwinkel, aber NCIB 3610 Biofilme weisen eine starke Adhäsion gegenüber Wasser (d.h. Rosen-ähnliche Superhydrophobie) auf, während B-1 Biofilme Wassertropfen abperlen lassen (d.h. Lotus-ähnliche Superhydrophobie). Wegen dieses Unterschieds in der Art der Superhydrophobie sind B-1-Biofilme resistenter gegen Erosion als NCIB 3610-Biofilme. In dieser Doktorarbeit wurde nun der Hauptbestandteil der stark wasserabweisenden B-1-Biofilme der NCIB 3610-Biofilmmatrix während des Wachstums künstlich hinzugefügt, um die Erosionsbeständigkeit dieses Biofilms zu verbessern. Durch die Anreicherung mit PGA steigt die Erosionsbeständigkeit von NCIB 3610 Biofilmen auf einen mittleren

Zustand, der zwischen dem von nicht-modifizierten NCIB 3610 und B-1 Biofilmen liegt. In ähnlicher Weise liegt auch die Kontaktwinkelhysterese der mit PGA angereicherten NCIB 3610-Biofilme auf einem Zwischen-Niveau, während sich der statische Kontaktwinkel der PGA-angereicherten NCIB 3610-Biofilme nicht ändert. Dies bedeutet eine Veränderung in der Art der Superhydrophobie, weil die Kontaktwinkelhysterese als ein Maß für die Wasseradhäsion einer Oberfläche gilt. Da dies durch eine chemische Modifikation nicht erreicht werden kann, wird als nächstes die Oberflächentopographie der Biofilme ausführlich untersucht. Dadurch wird gezeigt, dass verringerte Vertiefungen auf der Oberfläche für die veränderte Benetzbarkeit der angereicherten NCIB 3610 Biofilme verantwortlich sind. Dagegen werden die viskoelastischen und mikroskopischen Penetrationseigenschaften der Biofilme durch die Anreicherung mit PGA nicht beeinflusst. Außerdem können ähnliche Ergebnisse auch durch Zugabe anderer Polymere mit unterschiedlichen Nettoladungen und Molekülgrößen wie Alginat und PEG erzielt werden. Dies zeigt, dass ein breites Spektrum von Polymeren für den gleichen Zweck verwendet werden kann.

Eine andere Möglichkeit für die Modifikation von Biofilmen ist die Ko-Kultivierung von verschiedenen Bakterien. Das ist eine natürliche, mikrobielle Strategie, die von Mikroorganismen in Natur genutzt wird, um voneinander zu profitieren. Die meisten natürlichen Biofilme, wie z. B. orale Biofilme und die Darmflora, sind Multi-Spezies-Gemeinschaften. Diese mikrobiellen Konsortien können auch im Labor künstlich erzeugt werden, um die Wechselwirkungen zwischen den Mikroorganismen in diesen Multi-Spezies-Biofilmen zu untersuchen oder um erwünschte Eigenschaften verschiedener Mikroorganismen zu kombinieren. Es ist jedoch nur wenig verstanden, wie die Materialeigenschaften solcher Multi-Spezies-Biofilme bestimmt werden. Um ein besseres Verständnis der Materialeigenschaften von ko-kultivierten Biofilmen zu bekommen, werden in dieser Doktorarbeit die Oberflächentopographie und das Benetzungsverhalten von binären Mischungen von *B. subtilis* NCIB 3610, *natto* und B-1 Stämmen untersucht. Bei allen hier getesteten binären Mischungen ähnelt die Morphologie der ko-kultivierten (Tochter-)Kolonien einem der Elternstamm-Biofilme. Dieser makromorphologisch dominierende Stamm ist auch zahlenmäßig mehrheitlich vorhanden. Aufgrund des Vorhandenseins des anderen Elternstammes in geringer Zahl unterscheiden sich die Oberflächenrauigkeit und das Benetzungsverhalten dieser Tochterkolonien jedoch geringfügig, aber signifikant von der des dominierenden Elternstammes. Das Vorhandensein des "anderen" Stammes kann aber nur durch

eine mikrotopographische, quantitative Analyse des Biofilms erkannt werden, durch makromorphologische Untersuchungen ist dies nicht möglich. Dies hebt den Vorteil und sogar die Notwendigkeit einer mikrotopographischen Analyse der Biofilmoberflächen durch Profilometrie zur Untersuchung eines Multi-Spezies-Biofilms hervor.

Aufgrund der Fähigkeit einer quantitativen topographischen Analyse, die Beiträge einzelner Stämme zu ko-kultivierten Biofilmen zu erkennen, kann eine 3D-Bildgebung auch zur Klassifizierung der Biofilme verwendet werden. Im letzten Teil dieser Arbeit wurden daher Biofilme von drei *B. subtilis* Stämmen (NCIB 3610, B-1 und *natto*) bezüglich ihrer Oberflächentopographie klassifiziert. Dafür wurden zunächst 21 Oberflächenparameter von auf MSgg Medium gewachsenen Biofilmen bestimmt. Danach wurden vier Algorithmen des maschinellen Lernens (*k*-Nearest Neighbors, Gaussian Naïve Bayes, Logistische Regression und Random Forest) mit diesen topographischen Daten konfrontiert. Alle Algorithmen können diese Biofilmkolonien tatsächlich erfolgreich (d.h. mit sehr hoher Genauigkeit) in Bezug auf ihr Benetzungsverhalten klassifizieren. Außerdem können auf LB-Medium kultivierte Biofilme und andere biologische Proben wie Pflanzenblätter mit unterschiedlichem Benetzungsverhalten (d. h. hydrophil, Rosen-ähnlich und Lotus-ähnlich superhydrophob) ebenfalls mit diesem Ansatz erfolgreich klassifiziert werden, indem ähnliche topographische Daten verwendet werden. Um die wichtigsten Oberflächenmerkmale für das Benetzungsverhalten zu finden, wird eine Dimensionsreduktion durchgeführt. Dadurch wird gezeigt, dass nur vier ($\boldsymbol{S}_{\mathbf{dr}}$, $\boldsymbol{S}_{\mathbf{dq}}$, $\boldsymbol{V}_{\mathbf{vv}}$ und $\boldsymbol{S}_{\mathbf{pc}}$) von 21 Parametern zur Unterscheidung der Oberflächen mit unterschiedlichem Benetzungsverhalten unstreitig sind.

Insgesamt zeigt diese Doktorarbeit die hohe Relevanz der Oberflächentopographie für bestimmte Materialeigenschaften von *B. subtilis* Biofilmen auf. Um von Biofilmen bei verschiedenen Anwendungen zu profitieren, ist ein gutes Verständnis der Materialeigenschaften dieser funktionellen, lebendigen Materialien zentral. Die hier vorgestellten Erkenntnisse können dazu beitragen, neue Strategien zur Herstellung robusterer Biofilme für biotechnologische Anwendungen zu entwickeln und einen detaillierten Einblick in die Beziehung zwischen der Oberflächentopographie und dem Benetzungsverhalten komplexer Oberflächen zu erhalten.

Inhaltsverzeichnis

1 Einleitung

Im Laufe der Jahrtausende passten sich Bakterien immer weiter an, um sich vor Umwelteinflüssen zu schützen. Eine der zu diesem Zweck entwickelten Strategien ist die Bildung von Oberflächen-haftenden Gemeinschaften, bei denen die Bakterien sich in eine selbst abgesonderte, polymere Matrix einbetten. Die Geschichte dieser sogenannten *„Biofilme“* beginnt mit der Anheftung eines einzelnen Bakteriums an eine biotische oder abiotische Oberfläche (d.h., einer unmittelbaren Anlagerung). Danach vermehren sich die Bakterien und bilden Mikrokolonien. Hier beginnt die Herstellung von extrazellulären, polymeren Substanzen (EPS) wie z.B. Proteinen und Polysacchariden (d.h., eine unumkehrbare Anlagerung). Die weitere Entwicklung dieser Mikrokolonien führt zur Reifung des Biofilms. Im Verlauf dieses Reifungs-prozesses bilden sich Kanäle innerhalb des Biofilms, die es Wasser und Nährstoffen ermöglichen, die inneren Schichten des Biofilms zu erreichen. Bei einem reifen Biofilm sind die Bakterien von der EPS-Matrix vollständig umgeben, und es bildet sich eine uneinheitliche Struktur aus Zellhaufen, Kanälen und abgesonderter EPS. Mit weiterer Reifung des Biofilms wird die Diffusion von Nährstoffen und Gasen aber eingeschränkt, und bakterielle Abfallstoffe sammeln sich im Biofilm an. Das erzeugt Bereiche innerhalb des Biofilms mit vielen toten Bakterien, was dann zur Abtrennung mancher Biofilmteile führt. Nach dieser Ausbreitung bilden die abgetrennten Biofilmteile neue Biofilme an einer anderen Oberfläche aus. Durch diesen Lebensstil (Abbildung 1.1) unterscheiden sich die Biofilmbakterien von planktonischen Zellen in vielen Aspekten [1].

Hier ist der Haupt-Verantwortliche für diesen Unterschied vor allem die Polymermatrix, die die Bakterien umgibt. In den meisten Biofilmen machen die Mikroorganismen nur ca. 10 % der Trockenmasse aus, während der Rest aus der polymeren Matrix besteht, die Polysaccharide, Proteine, Nukleinsäure, extrazelluläre DNA und Lipide enthalten kann. Deswegen spielen diese EPS eine wichtige Rolle für viele Biofilmmerkmale. Zuallererst sind die EPS verantwortlich für die Haftung der Bakterien an eine Oberfläche (Adhäsion) und zueinander (Kohäsion). Sobald die Bakterien an der Oberfläche gebunden sind, wird die 3D-Archtitektur der Biofilme von der EPS bestimmt. Die Polymere binden auch Wasser und schützen die Bakterien so in trockenen Umgebungen. Auch bieten sie Schutz vor Umgebungsbelastungen wie toxischen Stoffen (z.B. Antibiotika) oder pH-Veränderungen, erlauben aber das

Aufnehmen von vorteilhaften Stoffen (wie z. B Nährstoffen, organischen Molekülen oder anorganische Ionen) in die innere Schicht des Biofilms [1]. Mithilfe dieser schwamm-artigen Struktur finden Biofilme auch Anwendung bei der Entgiftung von Fluiden [2,3], der Herstellung von Mineralen [4,5], oder der Immobilisierung von Enzymen oder anderer katalytischer Einheiten [6–8]. Sie können auch Spender und Akzeptoren für Elektronen sein und ermöglichen Redoxreaktionen innerhalb des Biofilms. Zusätzlich fördert der horizontale Transfer von genetischem Material (DNA) die Mutationen der Bakterien. Darüber hinaus können manche Matrix-Substanzen von den Bakterien des Biofilms als Nährstoffe genutzt werden [1].

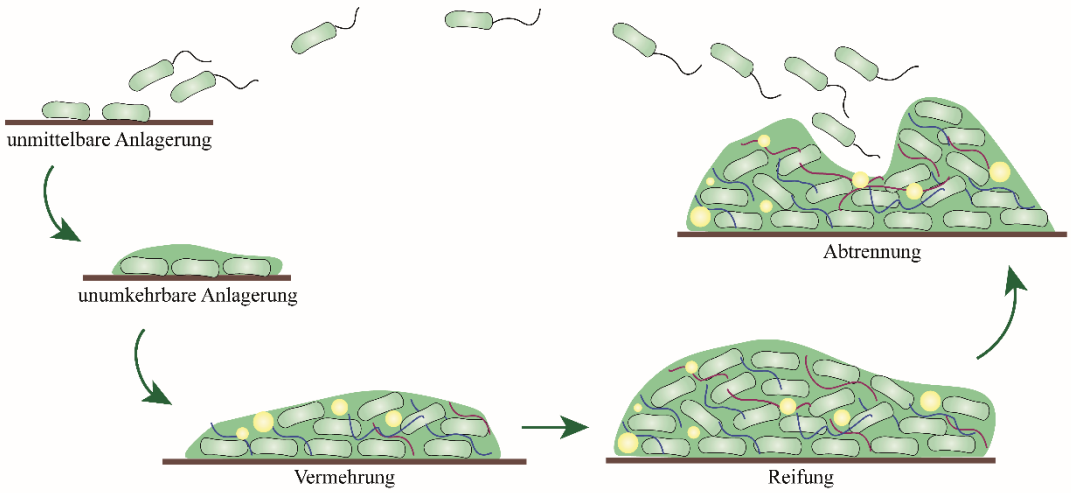

Abbildung 1.1. Stufen der Biofilmbildung. Einzelnen Bakterien haften an einer Oberfläche. Dann vermehren sie sich und sondern EPS ab bis sie einen reifen Zustand erreichen. Mit weiterer Reifung des Biofilms finden Abtrennungen einzelner Biofilm-Bereiche statt. Die freigegebenen Bakterien bilden dann neue Biofilme auf anderen Oberflächen. Die schematische Darstellung wird von Bakar *et al.* wiedergegeben [9].

Mit alle diesen Fähigkeiten erzeugt die EPS viele robuste Eigenschaften in den Biofilmen (Abbildung 1.2). Biofilme sind schleimige, viskoelastische und selbst-heilende, lebendige Materialien. Mit ihrem hohen Wassergehalt und wegen des hohen Anteils an Polymeren verhalten sich die Biofilme wie Polymer-Gele. Daher dominiert der elastische Anteil des viskoelastischen Verhaltens den viskosen Anteil, vor allem bei niedrigen Deformationsfrequenzen. Im Gegensatz dazu fließen Biofilme unter hohen Scherkräften (d.h. ihr viskoser Anteil dominiert dann das Materialverhalten), aber dennoch bleiben sie an der Oberfläche angehaftet. Mit ihren besonderen viskoelastischen Eigenschaften können Biofilme ihren elastischen Zustand wiedererhalten wenn die Scherkräfte wegfallen; daher sind sie schwer von

Oberflächen zu entfernen [10]. Außerdem erlauben die EPS die lokale Bewegung, die Proliferation und die Kommunikation von Bakterien. Somit können Biofilme als lebendige Materialien schnell auf Umgebungsänderungen reagieren und sich an das Umfeld anpassen. Das Durchlassen den vorteilhaften Stoffen und die Blockierung der Diffusion von toxischen Stoffen tragen zur Aufrechterhaltung der Lebensfähigkeit von Biofilmbakterien bei. Zusammen mit den viskoelastischen Eigenschaften macht außerdem das Phänomen der Superhydrophobie manche Biofilme erosionsbeständig und resistent gegen toxische Chemikalien [1].

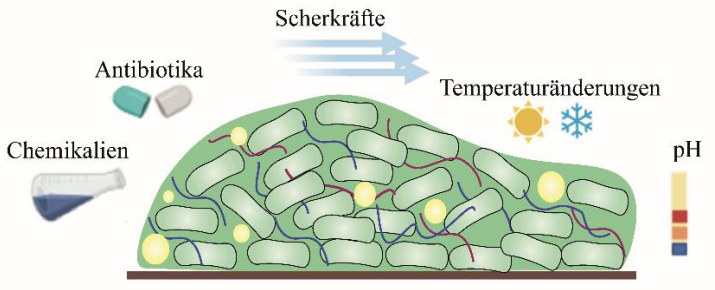

Abbildung 1.2. EPS verleiht Biofilme Beständigkeit gegen extreme Umgebungsbedingungen. Sie schützen die Bakterien vor toxischen Substanzen, Umgebungsänderungen oder Scherkräften.

Als robuste, klebrige und schleimige Hydrogele verursachen Biofilme schwere Schäden in industriellen und medizinischen Einrichtungen, z.B. Korrosion von metallischen Pipelines, Kontaminationen in der Lebensmittelverarbeitung oder Besiedelung von Kathetern. Deshalb ist die Bekämpfung von Biofilmen in den letzten Jahrzehnten ein Schwerpunkt der Biofilmforschung geworden [11–13]. Allerdings müssen die oben erwähnten, starken Eigenschaften der bakteriellen Biofilme nicht immer ein Fluch sein. Diese Stabilität und Funktionalität der Biofilme können der Menschheit in zahlreichen Bereichen auch dienen. Zum Beispiel können die EPS, die Bakterien vor schwierigen Bedingungen schützen, auch Pflanzen vor anderen pathogenen Mikroorganismen schützen und das Pflanzenwachstum fördern [14]. Um bestimmte Merkmale der Biofilme zu verstärken und um zusätzliche Funktionen hinzufügen, kann die EPS der Biofilme auch mit Nanopartikeln, Makromolekülen, Mineralen, Metallionen, Enzymen oder anderen Bakterien angereichert werden. In Kapitel 4.1 werden Anwendungen von natürlichen und modifizierten bakteriellen Biofilmen in verschiedenen Bereichen wie der Landwirtschaft, der industriellen und Umwelt-Biotechnologie, der Medizin und dem Bauwesen sowie der Elektrotechnik dargestellt. Hier dienen Biofilme als robuste und funktionelle, lebendige Materialien.

Wie oben erwähnt spielen die physikalischen Eigenschaften eine zentrale Rolle für ihr biologisches Verhalten und die Anwendung bakterieller Materialien. Ein wichtiges Beispiel ist auch das Benetzungsverhalten: Es bestimmt die Wechselwirkung der Materialoberfläche mit wässrigen Lösungen und den durch Fluid-Strömung erzeugten Scherkräften. So ist beispielsweise die Beständigkeit von Biofilme gegen toxische wasserlösliche Stoffe (z.B. Antibiotika) und gegen Erosion durch Scherkräfte abhängig von ihrem Benetzungsverhalten [15]. Die Benetzbarkeit einer Oberfläche wird durch ihre chemische Struktur und Rauigkeit bestimmt [16]. Bei bakteriellen Biofilme hängen beide dieser Merkmale von der Zusammensetzung der Biofilmmatrix ab [17,18]. Zum Beispiel ist ein hydrophobes Oberflächenprotein, *BslA*, verantwortlich für die Hydrophobie der Biofilmkolonien von *Bacillus subtilis* [19–21]. Mutanten, die unfähig sind, dieses Protein abzusondern, weisen Biofilme mit hydrophilem Benetzungsverhalten auf. Dieses Oberflächen-Hydrophobin beschichtet den ganzen Biofilm überall, dort, wo die Bakterien eine Grenzfläche erzeugt: Luft-Biofilm, Agar-Biofilm oder Flüssigkeit-Pellicle [22]. Dadurch bestimmt dieses oberflächenaktive, hydrophobe Protein sowohl die chemischen als auch physikalischen Eigenschaften der Biofilmoberfläche [21]. Nach Kesel et al. beeinflusst *BslA* nicht nur die Benetzbarkeit der *B. subtilis* NCIB 3610 Biofilme, sondern es nimmt auch Einfluss auf die Steifigkeit und die Größe des Biofilms (zusammen mit anderen Matrixkomponenten wie den Amyloid-Faserbildende Protein *TasA* und den Exopolysacchariden, siehe Kapitel 2.1 für Einzelheiten) [18].

Da die Rauigkeit (neben der chemischen Struktur) das Benetzungsverhalten einer Oberfläche stark beeinflusst, reicht die Information über Vorhandensein von *BslA* allein jedoch nicht aus, um die Benetzung eines Biofilms zu verstehen. Zum Beispiel unterscheiden sich die Benetzungsverhalten der Biofilme von NCIB 3610 und B-1 Stämmen, obwohl die Biofilmkolonien dieser Stämme beide *BslA* aufweisen: Während NCIB 3610 Biofilmkolonien Rosen-ähnliche Superhydrophobie aufweisen, sind die Oberflächen von B-1 Biofilmen Lotus-ähnlich superhydrophob [23]. Obwohl beide dieser Biofilme superhydrophob (Kontaktwinkelwerte sind höher als 135°) sind, zeigen nur NCIB 3610 Biofilme eine starke Adhäsion gegenüber Wasser, während die Wassertropfen von der Oberfläche von B-1 Biofilme abrollen (siehe Kapitel 3. 2). Hier kommt die Rauigkeit der Oberflächen ins Spiel. Der Unterschied in der Matrixzusammensetzung von diesen bakteriellen Biofilmen führt zu unterschiedlichen strukturellen Oberflächenmerkmalen. Durch eine Genexpressions-

analyse zeigten Kesel *et al.* außerdem, dass beide, von NCIB 3610 und B-1 gebildete Biofilme Exopolysaccharide, *TasA* und *BslA* enthalten; B-1 Biofilme bestehen aber hauptsächlich aus Polyglutaminsäure (PGA), welche sich nicht in NCIB 3610 Biofilmen findet [17]. Die Anwesenheit der PGA beeinflusst die Steifigkeit und die Rauigkeit der B-1 Biofilme: Sie weisen im Vergleich zu NCIB 3610 Biofilmen ein geringeres Speichermodul und eine höhere Oberflächenrauigkeit auf.

Zusammenfassend werden also die Steifigkeit, das Benetzungsverhalten und die Oberflächenrauigkeit der bakteriellen Biofilme durch die jeweilige Matrixzusammensetzung bestimmt. Weiterhin bedingen diese Eigenschaften der Biofilme ihre Erosionsbeständigkeit, die ein wichtiges Merkmal von Biofilmen ist. In einer früheren Arbeit zeigten Kretschmer *et al.* den Einfluss jedes Matrixbestandteils auf diese Erosionsbeständigkeit der NCIB 3610 Biofilme: Die Exopolysaccharide und das *BslA* Protein spielen hierbei die größte Rolle [24]. In ähnlicher Weise wurde auch die Erosion von B-1 Biofilmen untersucht [25]. Beide Arbeiten zeigten, dass die Elastizität der Biofilme durch die Anreicherung der EPS-Matrix mit bestimmten Metallionen erhöht wird und damit die Erosionsbeständigkeit verbessert wird. Da die EPS von NCIB 3610 und B-1 Biofilme variieren, ist zu erwarten, dass sie sich unterschiedlich gegen Erosion durch Scherkräfte verhalten. In Kapitel 4.2 wird die Erosionsbeständigkeit dieser Biofilme erforscht. Weiterhin wird der Hauptbestandteil der B-1 Biofilme (d.h. PGA) sowie ausgewählte andere Polymere mit verschiedenen Nettoladungen und Molekulargewichten zu den NCIB 3610 Biofilme hinzugefügt und es wird untersucht, wie die NCIB 3610 Biofilme dadurch beeinflusst werden.

Bislang wurde hier dargestellt, wie einige Komponenten der EPS-Matrix bestimmte Biofilmeigenschaften beeinflussen und wie erwünschte Eigenschaften von Biofilmen durch Beimengung verschiedener Zusatzstoffe verbessert werden können. Allerdings muss diese Beimengung nicht immer künstlich geschehen sein: Bakterien tun dies auch in der Natur, indem sie sich mit anderen Mikroorganismen zusammenschließen und Multi-Spezies Gemeinschaften bilden. Auf diese Weise kann ein Bakterium von einer Eigenschaft des anderen profitieren, und es können so die Anpassungsfähigkeit, Adhäsion, Kohäsion, Belastbarkeit oder Virulenz der bakteriellen Gemeinschaften verbessert werden [26,27]. Nach Sadiq *et al.* ist die Ko-Kultivierung von verschiedenen Darmbakterien sogar für die Bildung von Biofilmen in der Darmflora nötig [28].

Die meisten natürlichen Biofilme enthalten eine Vielfalt von Mikroorganismen. Trotzdem sind die Multi-Spezies-Biofilme nicht gut verstanden. Die Interspezies-Interaktionen innerhalb von ko-kultivierten Biofilme wurden bereits aus einer mikrobiologischen Sicht eingehend untersucht (Abbildung 1.3). Verschiedene Aspekte der Multispezies-Biofilmbildung wie die räumliche Organisation der Kolonien, das Quorum Sensing (d.h mikrobielle Kommunikation) und Evolution innerhalb der Kolonien und die Bekämpfung von Pathogenen oder schädlichen, konkurrierenden Bakterien wurden erforscht [27,29,30]. Polymikrobielle Gemeinschaften sind komplexe Konsortien, die von vielen Faktoren wie die unmittelbare Anheftung, Adhäsion, mikrobielle Bewegungsfreiheit, Art der Nährstoffquellen, Wachstumsrate der beitragenden Bakterien, Quorum-Sensing, Bakteriocin-Herstellung sowie EPS-Produktionsrate beeinflusst werden [31]. Jayathilake et al. stellten dar, dass EPS-erzeugende Bakterien langfristig einen Vorteil gegenüber anderen Bakterien haben [31]. Die Zusammensetzung der EPS hängt aber nicht nur von den zum Biofilm beitragenden Bakterien, der Verfügbarkeit der Nährstoffe und den Umgebungs-bedingungen ab; die Synthese und räumliche Organisation der EPS variiert auch zwischen Mono- und Multi-Spezies Biofilmen [14].

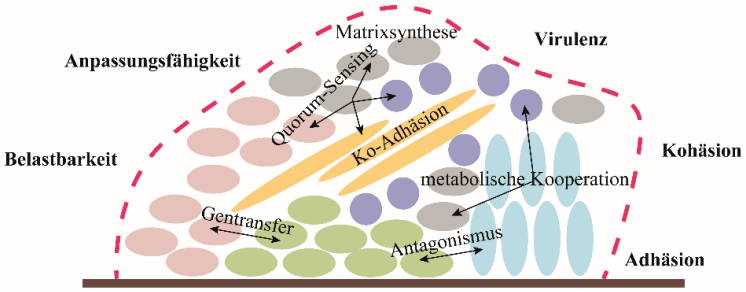

Abbildung 1.3. Eine schematische Darstellung der Wechselwirkungen innerhalb eines Multi-Spezies-Biofilms und mögliche Auswirkungen. Zuerst haften die primären Bakterien an eine Oberfläche, dann andere Bakterien an diese Primärbakterien (Ko-Adhäsion). Während des Reifungsprozesses treten eine Vielzahle von synergistischen und/oder antagonistischen Wechselwirkungen auf: Die Bakterien konkurrieren miteinander oder sie können metabolisch zusammenarbeiten, um Nährstoffe abzubauen oder um Nahrungsketten zu entwickeln. Die schematische Darstellung wird von Marsh *et al.* wiedergegeben [32].

Da die EPS die Materialeigenschaften der Biofilme stark beeinflussen, ist es zu erwarten, dass die physikalischen Eigenschaften der Multi-Spezies-Biofilme von der Ko-Kultivierung stark geprägt werden. Dennoch wurde bislang nicht viel über die Materialeigenschaften solcher Multi-Spezies-Biofilme geforscht. Es ist z. B. derzeit nicht klar, was das Benetzungsverhalten oder die Oberflächenrauigkeit einer ko-

kultivierten Biofilmkolonie bestimmt. Diese Eigenschaften von binären Mischungen von *B. subtilis* NCIB 3610, *natto* und B-1 Stämmen werden in Kapitel 4.3 eingehend untersucht. Durch eine quantitative, metrologische Analyse der Oberflächentopographie können so nicht nur die mengenmäßig dominierenden Bakterien, sondern auch die für die Materialeigenschaften prägenden Stämme der ko-kultivierten Biofilmkolonien erkannt werden.

Die quantitative Analyse der Oberflächentopographie ist eine häufig eingesetzte Methode in der Materialerforschung. Wie oben erwähnt beeinflusst die Topographie der Oberfläche wichtige Materialeigenschaften. Biokompatibilität [33], Adhäsion [34], Beständigkeit [35,36], Reibung [37] sowie Benetzungsverhalten sind Beispiele. Die detaillierte Beziehung zwischen Benetzungsverhalten und Oberflächenrauigkeit einer Materialoberfläche ist derzeit ein spannendes Thema der Materialwissenschaft [38–40]. Besonders wichtig ist die Rauigkeit einer Oberfläche für die Ausprägung superhydrophober Eigenschaften. Die Superhydrophobie wird typischerweise mit extrem hohe Kontaktwinkelwerten und unterschiedliche Adhäsionsverhalten des Wassers beschrieben [41]. Die oben erklärten Modi von Superhydrophobie, d. h. Rosen-ähnlich und Lotus-ähnlich, sind die häufigen Beispiele der verschiedenen Wasseradhäsion der superhydrophoben Oberflächen. Die Höhe, der Achsabstand sowie andere geometrische Merkmale von Oberflächenstrukturen wie z. B. die Konvexität, Konkavität oder Rundheit sind wichtige Faktoren, die den Modus der Superhydrophobie bestimmen. Zudem erfordert eine Oberfläche eine Rauheit im Mikro- und Nanobereich, um die extremen Formen der Superhydrophobie (d. h. Rosen-ähnlich oder Lotus ähnlich) zu erreichen [42,43]. Zum Beispiel weisen mit einem Wachs bedeckte, raue Blätteroberflächen infolge der Lufteinschlüsse ein Lotus-ähnliches superhydrophobes Benetzungsverhalten auf.

Die Natur ist voll von Beispielen der Superhydrophobie: Pflanzenblätter, Flügel der Insekten, der Zikaden oder der Schmetterlingen, Füße der Geckos, Augen der Mücke, sowie bakterielle Biofilme können superhydrophob sein [44]. Nach Werb *et al.* zeigen NCIB 3610 Biofilme hydrophiles, Rosen-ähnlich oder Lotus-ähnlich superhydrophobes Benetzungsverhalten je nach verwendetem Nährstoffmedium [45]. Die Autoren dieser Studie zeigten, dass die Matrixzusammensetzung der Biofilme sich durch die Nährstoffverfügbarkeit verändert. Dadurch variiert auch die Rauigkeit der auf unterschiedlichen Nährstoffmedien gezüchteten Biofilme. Darüber hinaus kann das Benetzungsverhalten eines reifen Biofilms auch durch Behandlung mit

verschiedenen Lösungen verändert werden, die die Oberflächentopographie der Biofilme beeinflussen [35]. Durch Aufbringen von konzentrierten Ethanol-, Salz- oder Zucker-Lösungen auf eine Biofilmoberfläche sinkt die Rauigkeit der Biofilme bedingt durch osmotische Dehydrationseffekte der Oberflächenstrukturen. Dadurch werden superhydrophobe Biofilme teilweise sogar hydrophil, und sie verlieren ihre Beständigkeit gegen Erosion und Antibiotikabehandlung.

Diese wichtige Beziehung zwischen der Oberflächentopographie und dem Benetzungsverhalten spielt daher eine zentrale Rolle für das Schicksal der Biofilme, weil die Benetzbarkeit eines Biofilms viele andere Eigenschaften beeinflusst. Um den Einfluss bestimmter Topographiemerkmale auf die Benetzbarkeit von Materialien zu verstehen, werden typischerweise künstliche, regelmäßig strukturierte Oberfläche untersucht [43]. Allerdings ist es für komplexe, unregelmäßige Oberflächen nicht so einfach, deren Oberflächenmerkmale und ihr Benetzungsverhalten zu korrelieren. Bisher werden erwünschte Eigenschaften von Materialoberflächen durch zeitaufwändige Versuch-und-Irrtum-Ansätze erzielt. Hierzu kann aber nur die Rauigkeit-Benetzung-Beziehung von komplexen Oberflächen durch neu entwickelte maschinelle Lernmethode schneller analysiert werden, sondern es kann so auch die Optimierung eines Materialentwicklungsprozess erleichtert werden. In Kapitel 4.4. werden die Biofilme von *B. subtilis natto*, NCIB 3610, und B-1 Stämmen und verschiedene Pflanzenblätter mit hydrophilem, Rosen-ähnlich und Lotus-ähnlich superhydrophobem Benetzungsverhalten durch vier maschinelle Lernalgorithmen in Bezug auf ihre Benetzungsverhalten klassifiziert, indem die Algorithmen mit mikrotopographischen Daten dieser Oberflächen konfrontiert werden. Außerdem werden die wichtigsten topographischen Parameter für die Unterscheidung zwischen hydrophilen, Rosen-ähnlich, und Lotus-ähnlich superhydrophoben Oberflächen identifiziert.

2 Materialien

2.1 Bakterienstämme

In dieser Arbeit wurden drei verschiedene Stämme von *B. subtilis* Bakterien verwendet, die sich in der Matrixzusammensetzung unterscheiden. *B. subtilis* ist ein weitgehend erforschter Angehöriger der Gattung *Bacillus*. Es handelt sich um aerobe, Endosporen-bildende, stabförmige, Gram-positive Bodenbakterien. Sie können eine Vielzahl von organischen Stoffen oxidieren. Ihre Fähigkeit auf unkomplizierten Medien zu wachsen, ermöglicht die Verwendung von *B. subtilis* als Modellorganismus für Gram-positive Bakterien allgemein, sowie der Erforschung der Endosporen- oder Biofilmbildung im Speziellen.

Einer der in dieser Arbeit verwendeten Stämme ist NCIB 3610, dessen Matrix das Amyloid-Faserbildende Protein *TasA* [46,47], das Oberflächenschichtshydrophobin *BslA* [22,48] und die Exopolysaccharide [49] beinhaltet; letzteres wird vom *epsA-O* Operon exprimiert. Wenn NCIB 3610 Bakterien auf LB Agarplatten inkubiert werden, beeinflussen die Exopolysaccharide und das *BslA* Protein die Dimensionen des Biofilms [18], z.B. den Bereich, den die Biofilme abdecken. Zusammen mit *TasA* bestimmt BslA die Höhe der Biofilmkolonien, aber mit gegensätzlichen Effekten: Während *TasA* die Biofilmhöhe reduziert, erhöht *BslA* sie. Zusätzlich hängt die Rauigkeit der Biofilmoberfläche von *BslA* ab [18].

Die Biofilme der anderen zwei Stämme, *natto* und B-1, bestehen zwar hauptsächlich aus Poly-γ-Glutaminsäure (Polyglutamat), aber der B-1 Stamm exprimiert zusätzlich das hydrophobe Protein *BslA* [17]. Dieses Protein ermöglicht das superhydrophobe Benetzungsverhalten der B-1 Biofilme, während die *natto* Biofilme unter den gleichen Bedingungen hydrophil bleiben. Tabelle 2.1 zeigt das Benetzungsverhalten von NCIB 3610, *natto* und B-1 Biofilmen, die auf den LB (Luria/Miller) und MSgg (Minimal Salz Glycerin Glutamat) Nährmedien bei den Temperaturen von 30 °C und 37 °C mit niedriger (~25%) Feuchtigkeit angezüchtet wurden.

Tabelle 2.1: Benetzungsverhalten von *B. subtilis* NCIB 3610, B-1 und *natto* Biofilme angezüchtet auf verschiedenen Nährmedien laut [50]

T [°C]	Medium	***B. subtilis* NCIB 3610**	***B. subtilis* B-1**	***B. subtilis natto***
37	LB	hydrophil	Lotus-ähnlich superhydrophob	hydrophil
	MSgg	Rosen-ähnlich superhydrophob	Lotus-ähnlich superhydrophob	hydrophil
30	LB	hydrophil	Lotus-ähnlich superhydrophob	hydrophob
	MSgg	Rosen-ähnlich superhydrophob	Lotus-ähnlich superhydrophob	hydrophob

2.2 Nährmedien

Um die Übernachtkulturen der Bakterien herzustellen, wurden ein extern bezogenes LB (Luria/Miller) Medium (Carl-Roth, Karlsruhe, Deutschland) mit einer Konzentration von 25 g/L (2,5%) benutzt, das 5 g/L Hefeextrakt, 10 g/L Trypton und 10 g/L Natriumchloride (NaCl) enthält. Die bakteriellen Biofilme wurden auf 1,5% Agar angezüchtet, der entweder mit LB oder MSgg (Minimal Salz Glycerin Glutamat) Medien versetzt war.

LB ist ein komplexes und nährstoffreiches Medium. Im Gegensatz dazu bietet ein chemisch gut definiertes MSgg Medium nur die minimalen Nährstoffe für das Bakterienwachstum. Laut Gallegos-Monterrosa *et al.*, [8] beeinflussen die Nährstoffe die Biofilmeigenschaften, z.B. die Matrixzusammensetzung oder die Komplexität der Biofilmstruktur [51]. Aus diesem Grund wurden die Biofilme in dieser Arbeit auf zwei verschiedenen Medien (LB und MSgg) gebildet, um so Biofilme mit unterschiedlichen Eigenschaften zu erhalten (siehe Tabelle 2.1).

Medium E wurde für die Herstellung von Polyglutamat durch den B-1 Stamm verwendet. Natrium-L-Glutamat in der Lösung ermöglicht hier nicht nur Bakterienwachstum, sondern auch die Herstellung des Polyglutamats [52].

2.3 Polymere

2.3.1 Poly-γ-Glutaminsäure

Poly-γ-Glutaminsäure (Polyglutamat, PGA) ist ein natürliches polyanionisches Polymer, das von verschiedenen Gram-positiv Bakterien sowie ausgewählten Archaeen und Eukaryoten synthetisiert wird. Es besteht aus den durch γ-Verbindungen verknüpften D- und/oder L-Glutamat Enantiomeren (Abbildung 2.1) [52,53]. PGA kann entweder an den Zellen haften oder in der Biofilmmatrix freigesetzt sein, und der jeweilige Zustand bestimmt seine Aufgabe. Wenn es an *Bacillus anthracis* und *Staphylococcus epidermidis* Bakterien haftet, schützt es diese Bakterien vor Phagozytose durch Makrophagen und wirkt somit als Virulenzfaktor. Freigesetztes PGA dagegen verstärkt den Widerstand der Bakterien gegen widrige Umgebungsbedingungen [53].

Die Polymergröße hängt entweder von den synthetisierenden Organismen oder von den Isolationsmethoden ab. Die Größe der von *B. subtilis* hergestellten PGA-Moleküle variiert zwischen 160 kDa und 1500 kDa [53]. Für das von *B. subtilis* B-1 synthetisierte PGA beträgt die Größe 1000 kDa [54]. Auch in dieser Doktorarbeit wird das vom B-1 Stamm hergestellte und dann gereinigte PGA verwendet. Die Herstellungs- und Isolationsmethode des PGAs wird in Anhang A.2 ausführlich beschrieben.

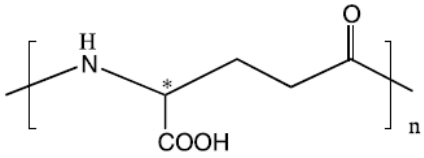

Abbildung 2.1. Die chemische Struktur von Poly- γ-Glutaminsäure. PGA Polymere bestehen aus durch Amidbindungen verbundene D- und/oder L-Glutaminsäureeinheiten [52].

Da PGA hydrophil, biokompatibel, wasserlöslich, essbar, biologisch abbaubar und schadstofffrei ist, kann es in verschiedenen Bereichen wie Medizin, Lebensmittel- oder Kunststoffe-Industrie als Verdickungsmittel, Gefrierschutzmittel, Feuchthaltemittel, Wirkstoffträger, Schwermetallabsorptionsmittel, Gelbildner oder biologischer Klebstoff verwendet werden [52]. In dieser Doktorarbeit wurde PGA künstlich als Beispiel für ein polyanionisches Polymer der Matrix von NCIB 3610 Biofilm hinzugefügt, um die Kolonieeigenschaften zu verändern.

2.3.2 Alginsäure

Alginsäure (Alginat) ist ein von Algen oder Bakterien hergestelltes natürliches Polysaccharid. Sie ist der hauptsächliche Matrixbestandteil der Biofilme von *Azetobacter vinelandii* und der Biofilme zahlreicher Arten der Gattung *Pseudomonas* [55,56]. Dieses polyanionische, hydrophile Polymer bestimmt viele Materialeigenschaften der bakteriellen Biofilme wie die Biofilmsteifigkeit, die Biofilm- und Zelladhäsion, als auch die Biofilmschichtdicke [57].

Die chemische Struktur des Alginats ist etwas heterogen: es besteht aus linearen Mischungen von 1-4 verbundenen α-L-Guluronat (G)-, ß-D-Mannuronat (M)- oder abwechselnden GM-Blöcken (Abbildung 2.2) [55,56]. Die Zusammensetzung und das Verhältnis der G- und M-Reste des Alginats hängen von dessen Quelle ab. Die Steifigkeit, die Stabilität und die Funktionalität der Alginat-Polymere werden durch dieses Verhältnis bestimmt. Zum Beispiel bestimmen das M/G-Verhältnis, die Länge der G-Blöcke und das Molekulargewicht der Alginat Polymere die Fähigkeit der Hydrogelbildung, weil nur G-Blöcke in der Lage sind, sich mit zweiwertigen Kationen in Chelatkomplexen zu vernetzen [56,58].

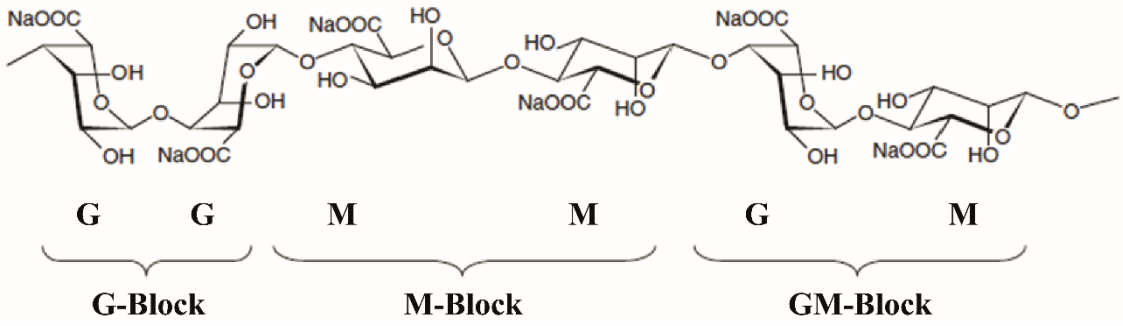

Abbildung 2.2. Chemische Struktur des Alginats. Alginat Polymere bestehen aus G-, M- und GM-Blöcken [55].

Zurzeit werden bereits mehr als 200 verschiedene Derivate des Alginats in der Literatur beschrieben. Diese unterschiedlichen Vernetzungsmethoden zusammen mit dieser Vielfältigkeit der Alginat-Struktur ergeben einstellbare Materialeigenschaften und ermöglichen somit auch die Anwendung des Alginats im Biomedizinbereich [56]. Neben seinen anderen Eigenschaften wird dieses gelbildende Polymer auch aufgrund seiner Biokompatibilität in der Wundheilung, der Gewebezüchtung und der Wirkstoffabgabe angewendet. Außerdem wird es als Modell für die Untersuchung des

bakteriellen Wachstums innerhalb einer Polymermatrix genutzt [59]. In dieser Arbeit wurde zusätzlich das extern bezogene, von Braunalgen synthetisierte Natrium-Alginat in die Matrix des NCIB 3610 Biofilms gegeben, um die Veränderung der Kolonieeigenschaften zu untersuchen.

2.3.3 Polyethylenglykol

Polyethylenglykol (PEG) ist ein synthetisches Polymer, das aus sich wiederholenden Ethylen Glykol-Einheiten besteht (Abbildung 2.3). Es kann entweder durch anionische Polymerisierung oder Ringöffnungspolymerisation von Ethylenoxid gebildet werden [60]. Ferner können PEG Polymere mit chemisch aktiven funktionellen Einheiten verbunden werden. Diese reaktiven Derivate des PEGs können weiter mit Proteinen oder pharmazeutischen Wirkstoffen konjugiert werden [61]. Diese sogenannte PEGylierung ist eine häufig verwendete Methode, um die Biokompatibilität und die Stabilität der Stoffe im Blutkreislauf zu verbessern [60–62]
.

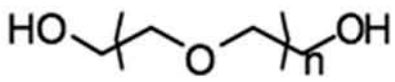

Abbildung 2.3. Chemische Struktur von Polyethylenglykol. PEG wird durch Polymerisierung von Ethylenoxid gebildet [60].

PEG ist ein hydrophiles, bei allen pH-Werten neutrales und biologisch inertes Polymer. Außerdem ist es gut löslich in Wasser und in verschiedenen organischen Lösungsmitteln. Diese vorteilhaften Eigenschaften sowie die strukturelle Flexibilität von PEG ermöglichen dessen Verwendung als Gefrierschutzmittel, Gleitmittel, Lebensmittelzusatzstoff oder Bewuchsschutzstoff sowie dessen Einsatz in der Gewebezüchtung, zur Wirkstoffabgabe sowie in Lebensmittel- oder Kosmetikprodukten [60–62].

Die Größe der gebildeten Polymeren variiert zwischen 200-8,000,000 g/mol [60] und bestimmt Polymereigenschaften wie Lösbarkeit, Schmelztemperatur und anderer Wärmeverhalten [60,63]. In dieser Arbeit wurden zwei PEG Moleküle mit verschiedenen Molekülgrößen (600 und 10000 g/mol) benutzt, um den Einfluss der Größe der zugefügten Polymere auf die Biofilmeigenschaften zu testen.

2.4 Antibiotika

In dieser Arbeit wurden zwei Antibiotika, Tetracyclin und Kanamycin, verwendet, um die Permeabilität der Biofilme zu testen. Da die Barrierewirkung der Biofilmmatrix gegenüber solchen Antibiotika bekannt ist, ist für Biofilmbakterien im Vergleich zu planktonischen Bakterien eine höhere Antibiotikakonzentration nötig [64]. Aus diesem Grund wurde in dieser Arbeit eine ca. 150-mal höhere Konzentration als die minimale Hemmkonzentration dieser Antibiotika für planktonischen *B. subtilis* Bakterien verwendet [65,66].

2.4.1 Tetracyclin

Tetracyclin ist ein Breitbandantibiotikum, das gegen Gram-positive und Gram-negative Bakterien wirksam ist. Es gibt zwei Sorten von Tetracyclin: die atypische ist bakterizid und die typische ist bakteriostatisch. Während die atypische Sorte (z.B. Chelocardin, 6-Thiatetracylin und Anhydrotetracyclin) die bakterielle Zellmembran aufbricht, verhindert die typische Sorte (Tetracyclin, Chlortetracyclin, Doxycyclin und Minocyclin) die Bindung der Aminoacyl-tRNA an die A-Stelle des mRNA-Ribosom-Komplexes. Dadurch kann keine neue Aminosäure zum verlängernden Polypeptid binden und folglich werden die Proteinsynthese und das Bakterienwachstum inhibiert [67,68].

2.4.2 Kanamycin

Kanamycin gehört zu den Breitband-Aminoglykosid-Antibiotika. Aminoglykoside weisen eine hohe Affinität für prokaryotische rRNA auf. Die Bindung von Kanamycin an die 30S Untereinheit des Ribosoms ruft eine Fehlablesung der mRNA hervor, die die Herstellung von funktionsunfähigen oder sogar toxischen Proteinen verursacht [69,70]. Darüber hinaus verhindert dieses Antibiotikum die Translokation der peptidyl-tRNA während der Proteinsynthese [69–71].

3 Methoden und theoretischer Hintergrund

3.1 Optische Untersuchungen

3.1.1 3D-Laser-Rastermikroskopie

Eine häufig verwendete Methode für die Oberflächenanalyse ist die Laser-Rastermikroskopie. Die detaillierten Strukturen einer Probe im Nanobereich können durch diese Laseroptik abgebildet werden. Dafür werden Bilder mit einer großen Tiefenschärfe über den gesamten Messbereich (durch *xy*-Raster) erfasst. Eine Lochblende vor dem Detektor blockiert gestreutes Licht und verbessert so die Bildqualität. Die höchste Werte der gemessenen Lichtintensität erhält man, wenn die Probenoberfläche im Fokus des Strahlengangs liegt: dann ist die Lichtreflexion maximal. Durch die Zusammenstellung dieser Punkte maximaler Reflexion (*z*-Achsenposition) an jeder *x*- und *y*-Achsenpositionen wird ein 3D-Bild der Probenoberfläche erfasst (Abbildung 3.1) [72].

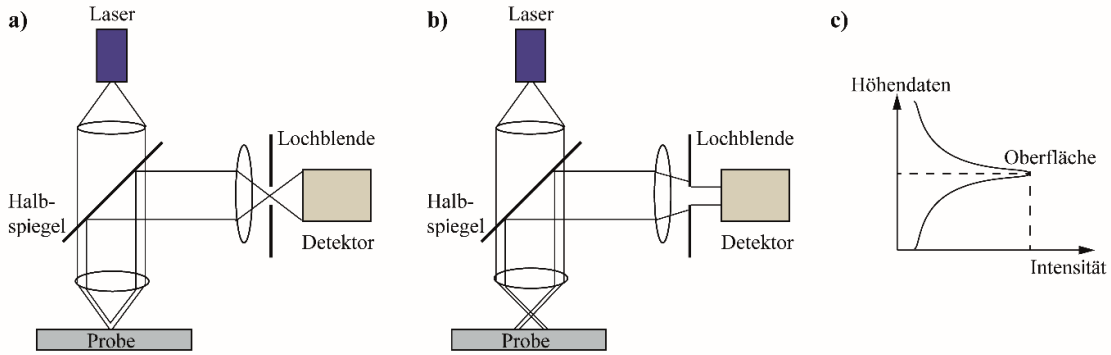

Abbildung 3.1. Laseroptik. Der Durchgang des ganzen Lichts ist möglich, wenn das Bild scharf ist (**a:** scharfes Bild**, b:** unscharfes Bild). Durch eine Kombination der *z*-Achsenpositionen von jedem Pixel wird ein 3D-Bild der Probe erzeugt, die der höchsten Intensität entsprechen (**c**).

Diese optische Methode bringt große Vorteile: Geringere Unschärfe der Bilder bei erhöhter Auflösung, gute Kontrasteffekte mit einfachem Equipment, quantitative Darstellung des Probenreliefs, verbessertes Signal-Rausch-Verhältnis, elektronische Einstellung der Vergrößerung, *xy*-Raster über weite Bereiche und Verwendung von weniger komplexen Objektiven sind dadurch möglich. Diese Methode kann mit Weißlicht oder Laserlicht verwendet werden. Laserlichtquellen erzeugen monochrome

Lichtstrahlen mit einem hohen Maß von Polarisation, und somit Kohärenz. Die Laserlichtquellen, die hohe-Intensität erzeugen, sind daher sehr geeignet für diese Art von Mikroskopie. Aufgrund dieser Vorteile ist die Laser-Rastermikroskopie bei Oberflächenuntersuchungen weit verbreitet [73].

Das in dieser Doktorarbeit verwendete Gerät (VK-X1000, Keyence) ist mit einer Laser- und einer weißen LED-Lichtquelle ausgestattet und kann drei Arten von Bilddaten erzeugen: ein Laserintensitätsbild, ein Bild mit Höhendaten und ein „Farb"bild. Das letzte wird durch weißes LED-Licht erhalten. Für die Messung wird das Laserlicht erst auf eine Position der *z*-Achse fokussiert. Danach wird der Bildbereich im Sichtfeld abgetastet, indem es (bei hoher Auflösung) in 1204x768 Pixel unterteilt wird. Der Detektor erfasst das reflektierte Licht an jedem Pixel. Anschließend verschiebt sich der Fokus der Objektivlinse entlang der *z*-Achse und die Intensitätsmessung wird an allen Nachbarpunkten auf die gleiche Weise wiederholt. Durch Bestimmung der *z*-Achsenposition mit der höchsten Intensität erhält man die Höhendaten. Diese Höhendaten werden kombiniert, um ein 3-D Bild der Oberflächen zu erzeugen. Laserintensitätsbilder können auch durch Kombination der Intensitätswerte erstellt werden [72].

Dieses Gerät kann einen Messbereich von 7 mm in der Höhe und 675x506 µm in der Breite mit 20x Objektivvergrößerung (480x Gesamtvergrößerung) abtasten. Hierbei können 3D-Bilder der Oberflächen mit einer Auflösung von 0,5 nm in *z*-Richtung bzw. 120 nm in *xy*-Richtung erzeugt werden. Danach werden die Höhendaten dieser Bilder von einer Software (MultiFileAnalyzer, Keyence) ausgewertet, um die Rauheitsparameter nach der Norm ISO 25178-2:2012 zu bestimmen. Mithilfe dieser 24 Rauheitsparameter können die Oberflächen dann beurteilt werden. Diese Parameter werden in 5 Kategorien eingeteilt: Höhen-, Hybrid-, Funktions-, und Funktions-Volumenparameter sowie räumliche Parameter (siehe Tabelle 3.1 und Anhang A.4) [74].

Die Höhenparameter werden aus Höhenänderungen berechnet, während die räumlichen Parameter in Beziehung zur Ebenen-Richtung gesetzt werden. Die Hybridparameter werden sowohl aus Höhenänderungen als auch der Ebenen-Richtung bestimmt. Die Funktions- und Funktionsvolumenparameter werden mithilfe einer Materialanteilkurve (Abbot-Firestone-Kurve) berechnet [74].

Tabelle 3.1. Rauheitsparameter nach ISO 25178-2:2012

Höhenparameter	
S_q	Mittlere quadratische Höhe
S_a	Mittlere arithmetische Höhe
S_z	Maximale Höhe
S_p	Maximale Spitzenhöhe
S_v	Maximale Taltiefe
S_{sk}	Schiefe
S_{ku}	Steilheit
Hybridparameter	
S_{dr}	Entwickeltes Übergangsflächenverhältnis
S_{dq}	Mittlerer quadratischer Gradient
S_{pd}	Spitzendichte
S_{pc}	Arithmetischer Mittelwert der Spitzenkrümmung
Funktionsparameter	
S_k	Kernhöhe
S_{pk}	Reduzierte Spitzenhöhe
S_{vk}	Reduzierte Talhöhe
S_{mr1}	Oberer Materialanteil
S_{mr2}	Unterer Materialanteil
S_{xp}	Extremwert der Spitzenhöhe
Funktions-Volumenparameter	
V_{vv}	Talleervolumen
V_{vc}	Kernleervolumen
V_{mp}	Spitzenmaterialvolumen
V_{mc}	Kernmaterialvolumen
Räumliche Parameter	
S_{al}	Autokorrelationslänge
S_{tr}	Textur-Seitenverhältnis
S_{td}	Texturrichtung

Ein häufig verwendeter Parameter für Oberflächencharakterisierung ist die mittlere quadratische Höhe (S_q): Sie entspricht der Standardabweichung der Höhenkoordinaten [74].

$$S_q = \sqrt{\frac{1}{A}\iint_A z^2(x,y)\,dx\,dy} \qquad \text{(Gleichung 1)}$$

Dennoch kann S_q (ähnlich wie die mittlere arithmetische Höhe, S_a) nicht die Spitzen, Täler und die Abstände der verschiedenen Texturmerkmale unterscheiden. Zwei Oberflächen mit denselben S_q-Werten können tatsächlich völlig unterschiedlich aussehen [75]. Für eine detaillierte Untersuchung einer Oberfläche werden deshalb mehrere Parameter benötigt.

Zum Beispiel gibt es noch die Maximale Höhe (S_z), welche der Summe aus der maximalen Spitzenhöhe (S_p) und der maximalen Taltiefe (S_v) entspricht:

$$S_z = S_p + S_v \qquad \text{(Gleichung 2)}$$

wobei $S_p = \max_A z(x,y)$ und $S_z = \min_A z(x,y)$ sind.

Die Spitzenhöhe ist relevant für den Kontakt der Oberfläche mit einer Flüssigkeit oder einer anderen Oberfläche zusammen, und die Taltiefe beeinflusst die Flüssigkeitsretentionskapazität der Oberfläche. Allerdings beschreiben S_p und S_v nur die Höhe von einzelnen Punkten einer Oberfläche; daher sollten auch andere Parameter verwendet werden, um die Spitzen- und Tälerstrukturen einer Probe genau zu bestimmen [74].

So gelten das Talleervolumen (V_{vv}) und das Kernleervolumen (V_{vc}) als Maße für die Flüssigkeitsretentionskapazität von Oberflächen: Oberflächen mit hohen Werten von V_{vv} und V_{vc} halten mehr Flüssigkeiten, wenn sie benetzt werden. Um die V_{vv} - und V_{vc} -Werte einer Oberfläche zu berechnen, wird die Abbot-Firestone-Kurve verwendet. q % des Leervolumens des flächenhaften Materialanteils (standardmäßig verwendet man q=80) entspricht dem Talleervolumen (V_{vv}). In ähnlicher Weise gibt das Kernleervolumen (V_{vc}) die Differenz des Leervolumens zwischen p % und q % des flächenhaften Materialanteils (standardmäßig p=10 und q=80) an [74].

Die Unterscheidung von Oberflächen mit identischer (Spitzen)höhe erfordert die Verwendung anderer (Spitzen)parameter wie z. B. die mittleren quadratischen Gradienten (S_{dq}):

$$S_{dq} = \sqrt{\frac{1}{A}\iint_A \left[\left(\frac{\partial z(x,y)}{\partial x}\right)^2 + \left(\frac{\partial z(x,y)}{\partial y}\right)^2\right] dx\, dy} \qquad \text{(Gleichung 3)}$$

Aus relativ großen, langwelligen Komponenten bestehende Oberflächen weisen kleine S_{dq}-Werte auf, während der S_{dq}-Wert einer aus kurzwelligen Komponenten-bestehenden Oberfläche größere Werte annimmt. S_{dq} gilt als ein Maß für sowohl die Amplitude als auch den Abstand der Oberflächenmerkmale. Ein anderer Parameter ist der arithmetische Mittelwert der Spitzenkrümmung (S_{pc}), der verwendet wird, um

die Spitzenstruktur einer Oberfläche zu beschreiben. Ein kleiner Wert zeigt an, dass die Spitzen abgerundete Formen haben. Im Gegensatz dazu bedeutet ein größerer S_{pc}-Wert nadelartige Strukturen. Der S_{pc} wird wie folgt berechnet:

$$S_{pc} = -\frac{1}{2n}\sum_{k=1}^{n}\left(\frac{\partial^2 z(x,y)}{\partial x^2} + \frac{\partial^2 z(x,y)}{\partial y^2}\right) \qquad \text{(Gleichung 4)}$$

Da die in dieser Arbeit verwendete Software die Verschmelzung der Spitzen von Mikrohügelbereichen mit den angrenzenden Bereichen nicht unterstützt, entspricht dieser Parameter (S_{pc}) nicht der ISO 25178-2: 2012 [74].

Schließlich ist das entwickelte Übergangsflächenverhältnis (S_{dr}) ein Parameter, der häufig für die Beschreibung der gesamten Rauheit von Oberflächen verwendet wird. S_{dr} beschreibt das Verhältnis der Fläche zum Definitionsbereich und wird wie folgt berechnet:

$$S_{dr} = \frac{1}{A}\left[\iint_A \left(\sqrt{\left[1 + \left(\frac{\partial z(x,y)}{\partial x}\right)^2 + \left(\frac{\partial z(x,y)}{\partial y}\right)^2\right]} - 1\right) dx\, dy\right] \qquad \text{(Gleichung 5)}$$

S_{dr} ist ein hybrider Parameter. Das heißt, dass S_{dr} von sowohl der Höhe als auch der Wellenlänge (d.h. dem Abstand bestimmter Strukturmerkmale) der Oberfläche abhängt. Sein Wert erhöht sich mit einer ansteigenden Höhenamplitude und einer sinkenden Wellenlänge [74]. Da S_{dr} mit dem Rauigkeitsfaktor (R_f) zusammenhängt, ist er weit verbreitet, um die Benetzung, die Adhäsion und die Beschädigung von Oberflächen zu untersuchen [75]. In dieser Doktorarbeit wurde S_{dr} als ein zentraler Parameter für die Bestimmung der Oberflächenrauigkeit verwendet. Mithilfe der anderen Rauheitsparameter wurden dann Unterschiede zwischen den Biofilmoberflächen bestimmt.

3.1.2 Raster-Elektronenmikroskopie

Die Elektronenmikroskopie nutzt für die Bildherstellung Elektronen anstatt sichtbares Lichts. Während die Wellenlänge des sichtbaren Lichts zwischen 500 nm und 1000 nm variiert, berechnet sie sich beispielweise zu 0,0043 nm für ein Elektron mit einer Beschleunigungsspannung von 80 kV. Da das Auflösungsvermögen sich

nach der Abbe'schen Gleichung mit kleinerer Wellenlänge erhöht, ermöglicht die Elektronmikroskopie bessere Auflösungen und Vergrößerungen als Lichtmikroskopie.

Es gibt zwei Haupttechniken der Elektronmikroskopie: Die Transmissionselektronenmikroskopie (TEM) und die Rasterelektronenmikroskopie (REM). Während die Elektronen bei der TEM die Probe durchstrahlen, wird bei der REM der Elektronstrahl auf einen Punkt der Probenoberfläche fokussiert und die Probe zeilenweise abgerastert. Deswegen ist die REM geeignet, die Oberflächentopographie zu untersuchen.

In einem Rasterelektronenmikroskop werden die aus einer Kathode emittierten Elektronen mit einer Beschleunigungsspannung von zwischen 200 V und 50 kV in Richtung der Probe beschleunigt. Elektromagnetische Felder werden verwendet, um den Elektronenstrahl zu lenken: Er wird durch eine Kondensorlinse gebündelt und durch eine Objektlinse auf die Probenoberfläche fokussiert. Mithilfe einer Ablenkspule führt man den Elektronenstrahl über die Probe hin und her und rastert die Oberfläche zeilenweise ab. Die auf die Probe ankommenden Elektronen wechselwirken mit den Atomkernen und Hüllenelektronen der Probenatome. Wenn sie von der Probe elastisch gestreut werden, ergeben diese Rückstreuelektronen (RE) die Kontrastdaten der Bilder. Außerdem können entweder RE oder Strahlelektronen mit den Hüllenelektronen der Probe so wechselwirken, dass Sekundärelektronen (SE) mit geringer Energie (3-5 eV) freigegeben werden. Hierbei können aber nur die in Oberflächennahen Schichten erzeugten SE die Probe verlassen. Anschließend werden die SE und RE von verschiedenen Detektoren detektiert und somit ein Topographiebild erstellt. In dieser Doktorarbeit wurden REM-Bilder der bakteriellen Biofilme für eine qualitative Untersuchung der Oberflächentopographie bei hohen Vergrößerungen aufgenommen, die sonst mit Lichtmikroskopie nicht erreichbar sind [76].

3.1.3 Fluoreszenzmikroskopie

Die Elektronen von manchen Molekülen werden durch Licht bestimmter Wellenlänge angeregt und dann aus dem Grundzustand in einen angeregten Zustand gehoben. Weil sie vor der Rückkehr in den Grundzustand durch Vibration einen Teil ihrer Energie verlieren, senden sie dabei Licht mit längerer Wellenlänge aus. Diese Moleküle werden „Fluorophor (Fluorochrom)" genannt, und die Nutzung der Fluoreszenz ist in der Bildgebung weit verbreitet.

Fluoreszenzmikroskopie ist eine Art der Lichtmikroskopie. Bei der Fluoreszenzmikroskopie muss Anregungs- und Emissionslicht effizient trennbar sein. Dazu werden zwei Filter eingesetzt: Der Anregungsfilter lässt nur Licht bestimmter Wellenlänge mit hoher Intensität durch. Das vom Fluorophor emittierte Licht – sogenanntes Fluoreszenzlicht- wird wieder vom Objektiv aufgefangen und passiert den dichroitischen Spiegel, der nur für Licht mit längerer Wellenlänge durchlässig ist. Dann engt der Emissionsfilter das passierte Licht in seiner Bandbreite ein, damit möglichst nur Fluoreszenz-Licht für die Bildgebung erhält [76].

In dieser Doktorarbeit wurde die Fluoreszenzmikroskopie zur Bestimmung der Anwesenheit von Fluoreszenzmarkierten Bakterien und zur quantitativen Bestimmung des Anteils von lebendigen und toten Bakterien verwendet.

3.2 Benetzungsverhalten und Kontaktwinkelmessungen

Der Zusammenhalt einer Flüssigkeit wird durch attraktive Kohäsionskräfte erzielt. Im stabilen Zustand wirken diese Kräfte gleichmäßig in alle Raumrichtungen mit den benachbarten Molekülen der Flüssigkeit. Natürlich haben die Moleküle an einer Oberfläche aber weniger Bindungen mit Nachbarmolekülen als die im Volumen einer Flüssigkeit. Infolgedessen haben die Moleküle an der Oberfläche überschüssige Energie. Diese Energie wird Oberflächenenergie oder Oberflächenspannung (γ) genannt und als Energie pro Fläche [J/m^2] oder als Kraft pro Länge [N/m] angegeben. Zusätzlich entspricht die Oberflächenspannung der Energiezufuhr, die für die Entstehung einer Oberfläche, d. h. das Aufbrechen der Bindungen zwischen benachbarten Molekülen, erforderlich ist [77].

Wenn ein Flüssigkeitstropfen auf eine feste, ebene Oberfläche aufgebracht wird, wirken drei Grenzflächenenergien: die zwischen den Festkörper-Flüssigkeit (γ_{SL}), Flüssigkeit-Luft (γ_{LA}) und Festkörper-Luft (γ_{SA})-Grenzflächen gebildet werden (siehe Abbildung 3.2). In einem Gleichgewichtszustand bildet dieser Tropfen einen charakteristischen Winkel (θ_0) entlang der sogenannten Dreiphasenkontaktlinie:

$$\gamma_{SA} - (\gamma_{SL} + \gamma_{LA} \cos \theta_0) = 0 \qquad \text{(Gleichung 6)}$$

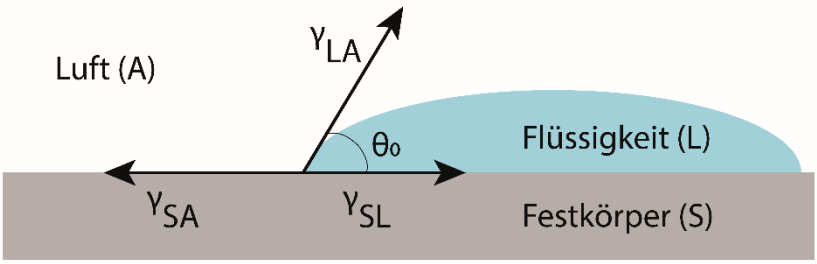

Abbildung 3.2. Dreiphasenkontaktlinie. Drei Grenzflächenenergien zwischen Festkörper-Flüssigkeit (γ_{SL}), Flüssigkeit-Luft (γ_{LA}) und Festkörper-Luft (γ_{SA})-Grenzflächen wirken auf die Flüssigkeit, die auf einen Festkörper aufgebracht wird.

Aus dieser Beziehung kann der sogenannte statische Kontaktwinkel (θ_0) für den Fall perfekter (d.h. topographisch ebener und chemisch homogener) Oberflächen nach der Young'schen Gleichung berechnet werden [78]:

$$\cos\theta_0 = \frac{\gamma_{SA} - \gamma_{SL}}{\gamma_{LA}} \qquad \text{(Gleichung 7)}$$

Der statische Kontaktwinkel nimmt Werte zwischen 0° und 180° an; er gilt als Maß der Benetzbarkeit einer Oberfläche: Wenn die Oberfläche gut mit Wasser benetzbar ist, wird sie „hydrophil" genannt und der Kontaktwinkel ist dann kleiner als 90°. Im Gegensatz dazu beschreibt ein Kontaktwinkel größer als 90° „hydrophobe" Oberflächen, die nicht gut mit Wasser benetzbar sind.

3.2.1 Wenzel- und Cassie-Zustände der Benetzung

Die oben angegebene Young'sche Gleichung gilt für perfekte Oberflächen, allerdings sind die meisten natürlichen oder synthetischen Oberflächen nicht perfekt. Die Rauigkeit und die chemische Struktur einer Oberfläche beeinflussen das Benetzungsverhalten der Substanzen. Für eine chemisch homogene Oberfläche mit einer Rauigkeit R_f wird der Kontaktwinkel (θ) nach der Wenzel-Gleichung berechnet; hier beschreibt R_f das Verhältnis der gesamten Fläche des Festkörpers zu seiner ebenen projizierten Fläche [79] :

$$\cos\theta = R_f \cdot \cos\theta_0 \qquad \text{(Gleichung 8)}$$

wobei $R_f = \frac{gesamte\ Interaktionsfläche}{ebene\ projizierte\ Fläche}$ ist.

Nach der Wenzel-Gleichung wird Kontaktwinkel θ kleiner als θ_0 für hydrophile Oberflächen ($\cos\theta_0 > 0$) mit $R_f > 1$. Daneben wird er größer als θ_0 für hydrophobe, raue Oberflächen ($\cos\theta_0 < 0$). Das heißt, dass große Rauigkeitsfaktoren hydrophile Oberflächen hydrophiler und hydrophobe Oberflächen hydrophober machen [42].

1944 erweiterten Cassie und Baxter den von Wenzel definierten Zustand auf chemisch inhomogene Oberflächen: zum Beispiel gilt das Cassie-Baxter Modell für raue Oberflächen mit Lufteinschlüssen zwischen Festkörper und Flüssigkeitstropfen. In diesem Fall wird nur ein Teil der Festkörperoberfläche (f_{SL}) mit einer Flüssigkeit benetzt. Daher wird die Fläche der Festkörper-Flüssigkeits-Grenzfläche zu $R_f f_{SL}$. Da f_{SL} zwischen 0 und 1 variiert, ist der Anteil der Flüssigkeits-Luft-Grenzfläche ($1 - f_{SL}$). Damit werden die drei Grenzflächenenergien zu $R_f f_{SL}\gamma_{SL}$, $R_f f_{SL}\gamma_{SA}$ und $(1 - f_{SL})\gamma_{LA}$. Für solche Oberflächen wird der statische Kontaktwinkel (θ) nach der unten stehenden Cassie-Baxter-Gleichung berechnet [80]:

$$\cos\theta = R_f f_{SL} \cdot \cos\theta_0 - 1 + f_{SL} \qquad \text{(Gleichung 9)}$$

Nach den Wenzel- und Cassie-Gleichungen erhöht sich die Hydrophobie von hydrophoben Materialien durch eine erhöhte Rauigkeit. Um die sogenannte Superhydrophobie mit Kontaktwinkeln von höher als 130° zu erreichen, ist tatsächlich nicht nur eine hydrophobe Oberflächenchemie, sondern auch eine hohe Rauigkeit nötig [44]. Für die Beschreibung der Benetzungsmodi rauer, superhydrophoben Oberflächen werden am häufigsten die Modelle von Cassie (imprägnierter Cassie-Zustand bzw. Cassie-Baxter-Zustand) verwendet (siehe Abbildung 3.3). Zum Beispiel weisen die Blätter von *Nelumbo nucifera* (die Lotus Pflanze) ein bestimmtes superhydrophobes Benetzungsverhalten auf, das „Lotus-ähnlich superhydrophob" genannt wird. Sobald man einem Wassertropfen auf ein Lotus-Blatt gibt, rollt der Tropfen vom Blatt ab. Der Kontaktwinkel des Tropfens ist sehr hoch (~150°) und seine Adhäsion an die Oberfläche ist sehr schwach. Aufgrunddessen werden Lotus-Blätter und andere Lotus-ähnliche Oberflächen als „selbstreinigend" bezeichnet. Diese Art der Superhydrophobie ist ein besonderer Fall des Cassie-Zustands. Bei diesem Lotus-Modus der Benetzung besitzt die Oberfläche mehr Nanostrukturen als der normale -aus Mikrostrukturen bestehende- Cassie-Zustand.

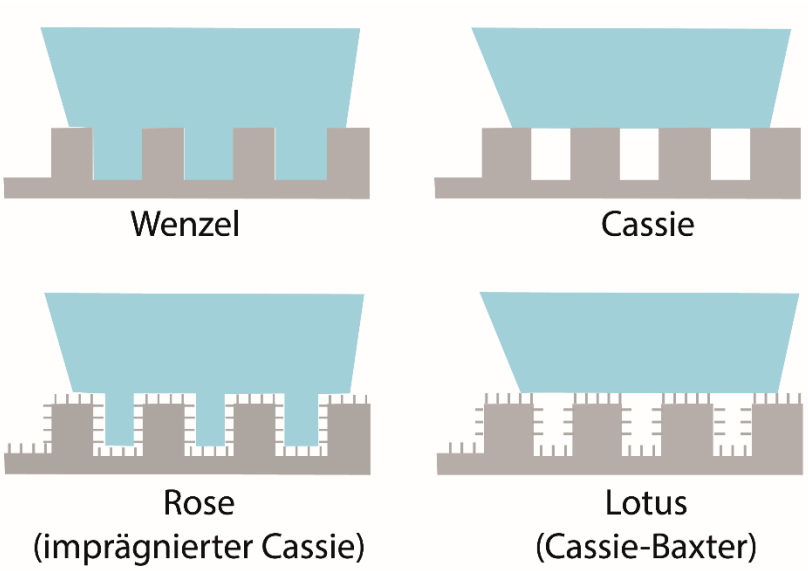

Abbildung 3.3. Benetzungsmodi der superhydrophoben Oberflächen. Rosen- oder Lotus- ähnliche Oberflächen sind besondere Fällen des Cassie-Zustands mit beteiligten Nanostrukturen.

Ein anderes Beispiel für einen superhydrophoben Zustand sind Rosen-Blütenblätter: Der Kontaktwinkel eines Wassertropfens auf einem Rosen-Blütenblatt ist zwar ebenfalls sehr hoch, aber der Tropfen bleibt auf dem Blütenblatt haften, auch wenn es auf den Kopf gestellt wird. Das Benetzungsverhalten dieser superhydrophoben und zugleich stark anhaftenden Oberflächen wird „Rosen-ähnlich superhydrophob" genannt und es ist ein Spezialfall des Cassie-Zustands: Bei diesem Zustand (imprägnierter Cassie-Zustand) werden die Makrostrukturen mit Wasser gefüllt, während die Luft in den Nanostrukturen eingeschlossen wird [43].

3.2.2 Kontaktwinkelhysterese

Auf einer perfekten (d. h. chemische homogenen und ebenen) Oberfläche gibt es nur einen Gleichgewichtszustand entlang der Dreiphasenkontaktlinie (siehe Abbildung 3.2), der den statischen Kontaktwinkel ergibt. Allerdings ermöglichen raue und/oder chemisch inhomogene Oberflächen vielfache Gleichgewichtszustände und damit verschiedene Kontaktwinkel. In solchen Fällen sind dynamische Kontaktwinkelmessungen nötigt, um das Benetzungsverhalten der Oberflächen zu identifizieren [43].

Dynamische Kontaktwinkelmessungen können auf zwei Arten durchgeführt werden (Abbildung 3.4). Für die erste Methode wird eine kleine Menge zusätzlicher Flüssigkeit einem festsitzenden Tropfen hinzugefügt. Dadurch schreitet die

Kontaktlinie des Tropfens voran und dies ergibt den voranschreitenden Kontaktwinkeln. Sobald die gleiche Menge Flüssigkeit wieder entfernt wird, bildet sich dagegen erneut eine andere Kontaktlinie aus und ein rückschreitender Kontaktwinkel wird gemessen. Die Differenz zwischen voranschreitendem und rückschreitendem Kontaktwinkel ergibt die Kontaktwinkelhysterese:

$$\Delta\theta = \theta_{vor} - \theta_{rück} \qquad \text{(Gleichung 10)}$$

Da der Unterschied zwischen der Benetzung und der Entnetzung einer Oberfläche durch Adhäsionshysterese erzeugt wird, gilt die Kontaktwinkelhysterese als ein Maß hierfür. Deswegen werden Kontaktwinkelhysteresemessungen zur Bestimmung der Benetzungsmodi superhydrophober Oberflächen verwendet. Zum Beispiel ergibt eine Rosen-ähnliche Oberfläche hohe Werte der Kontaktwinkelhysterese, weil die Adhäsion des Tropfens zur Oberfläche sehr stark ist. Dagegen weist eine Lotus-ähnliche Oberfläche eine geringe Kontaktwinkelhysterese auf.

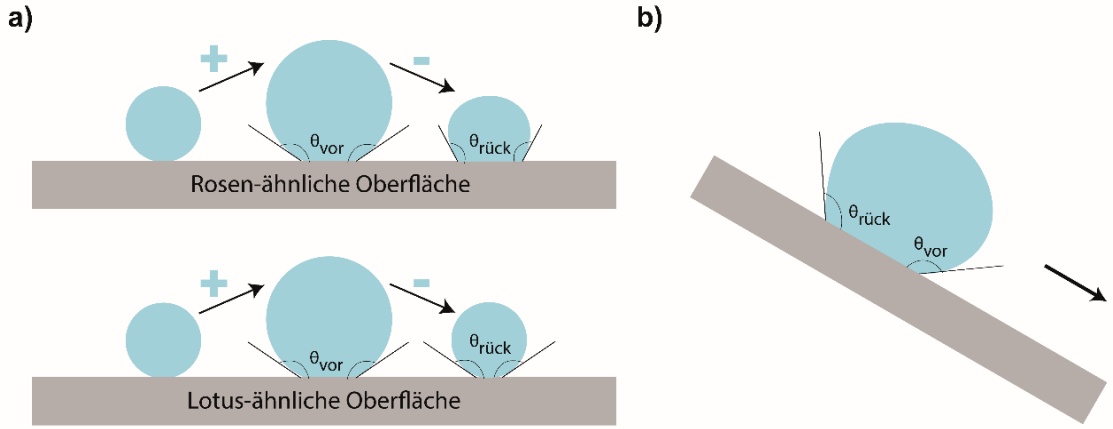

Abbildung 3.4. Kontaktwinkelhysteresemessungen. Der detaillierte Benetzungsmodus von superhydrophoben Oberflächen kann durch die Kontaktwinkelhysterese identifiziert werden. **a)** Während Benetzung und Entnetzung unterscheiden sich Rosen- und Lotus-ähnliche Oberflächen, und dieser Unterschied kann quantitativ gemessen werden. **b)** Die voran- und rückschreitenden Kontaktwinkel eines bewegenden Tropfens können gemessen werden oder man kann den Tropfen beobachten, ob er abrollt (Lotus-artig) oder anhaftet (Rosen-artig).

Bei der zweiten Methode wird der Tropfen entlang der Oberfläche bewegt. Dafür kann man zum Beispiel die Oberfläche neigen. Die Kontaktwinkel an der Vorderseite (d.h. voranschreitende Kontaktwinkel) und an der Rückseite (d.h. rückschreitende

Kontaktwinkel) des Tropfens werden gemessen und die Kontaktwinkelhysterese wie oben erwähnt berechnet. Mit dieser Methode können die Benetzungsmodi der superhydrophoben Oberflächen aber auch qualitativ bestimmt werden: man beobachtet, ob der Tropfen von der Oberfläche abrollt oder daran haftet. Somit unterscheidet man, ob das Benetzungsverhalten der Oberfläche der von Rosen-Blütenblättern oder Lotus-Blättern ähnelt [42,43].

3.3 Makrorheologie

Rheologie ist die Wissenschaft der Deformation und des Fließens der Materialien. Alle natürlichen oder synthetischen Materialien zeigen eine Reaktion, wenn eine Kraft auf sie einwirkt: Sie fließen oder verformen sich. Je nach Scherverhalten werden zwei Idealzustände für Materialien beschrieben: idealviskose Flüssigkeiten oder idealelastische Festkörper. Die idealviskosen Materialien beginnen zu fließen, wenn eine äußere Kraft auf sie einwirkt und sie bleiben verformt, sobald die Kraft wegfällt. Im Gegensatz dazu reagieren die idealelastischen Materialien sofort auf eine äußere einwirkende Kraft und die aufgetretene Verformung erholt sich vollständig, wenn diese Kraft weggenommen wird. Allerdings befinden die meisten Materialien sich in einem Zwischenzustand, der diese beiden Verhaltensweisen kombiniert. Solche Materialien werden „viskoelastisch“ genannt und weisen unterschiedliche Anteile der viskosen und elastischen Verhaltensformen auf [81].

Oszillationstests sind bekannte makrorheologische Methoden, die die Antwort einer Substanze auf einwirkende Kräfte beschreiben, indem sie das Fließ- und Deformationsverhalten der viskoelastischen Materialien messen. Zum Durchführen eines Oszillationstests wird eine Probe zwischen zwei parallele Platten gebracht; die obere Platte oszilliert hin- und her, während die untere Platte unbeweglich ist. Die auftretende Schubspannung (τ), wenn eine Kraft F auf die (Scher)fläche A der Probe einwirkt, ist dann:

$$\tau = F/A \qquad \text{(Gleichung 11)}$$

Im linearen Antwortbereich, wo das Verhältnis der Spannung und Dehnung (γ) unabhängig von der Größe der einwirkenden Kraft oder Deformation ist, gilt nach

dem Hooke'schen Gesetz, dass die Schubspannung direkt proportional zur Dehnung der Materialien ist:

$$\tau(t) = G^* \cdot \gamma(t) \qquad \text{(Gleichung 12)}$$

Hier tritt G* das komplexe Schubmodul auf und setzt sich aus einer viskosen und elastischen Komponente zusammen:

$$G^* = G' + i \cdot G'' \qquad \text{(Gleichung 13)}$$

Durch G' und G'' werden hier die elastische und viskose Komponente der Materialantwort dargestellt. Das Speichermodul (G') gilt als Maß für die gespeicherte Energie in dem Material während des Schervorgangs, die nachher zur Wiederherstellung dessen Form verwendet wird. Das Verlustmodul (G'') steht für die Energie, die während des Schervorgangs verloren geht. Diese Energie wird entweder für eine Veränderung der Materialienstruktur benutzt oder an die Umgebung abgegeben.

Während eines Oszillationstests wirkt eine sinusförmige Schubspannung auf die Probe ein:

$$\tau(t) = \tau_0 \sin(\omega t) \qquad \text{(Gleichung 14)}$$

Wobei $\omega = 2\pi \cdot f$ ist.

In diesem Fall tritt eine Dehnung zwar mit der gleichen Frequenz ω (bzw. *f*) auf, aber es gibt eine Phasenverschiebung von δ zwischen der Schubspannung und der Dehnung:

$$\gamma(t) = \gamma_0 \sin(\omega t + \delta) \qquad \text{(Gleichung 15)}$$

Der Winkel der Phasenverschiebung variiert zwischen 0° und 90°, und dessen Maß hängt von den viskoelastischen Eigenschaften der Materialien ab. Zum Beispiel ist er 0° für einen idealelastischen Festkörper, wohingegen idealviskose Flüssigkeiten eine Phasenverschiebung von 90° haben. Alle anderen nicht-idealen, d.h. viskoelastischen, Materialien weisen eine Phasenverschiebung von $0° < \delta < 90°$ zwischen der Schubspannung und der Dehnung auf. Mit diesem Winkel der Phasenverschiebung

können das Speichermodul (G') und das Verlustmodul (G'') der Probe berechnet werden [81]:

$$G'(f) = \frac{\tau_0}{\gamma^0}\cos\delta\,(f) \qquad \text{(Gleichung 16)}$$

$$G''(f) = \frac{\tau_0}{\gamma^0}\sin\delta\,(f) \qquad \text{(Gleichung 17)}$$

In dieser Arbeit wurden Frequenz-Sweep-Messungen zur Charakterisierung der Biofilme von *B. subtilis* NCIB 3610 und B-1 Bakterien durchgeführt. Infolge ihres reichen Polymer-Gehalts können die bakteriellen Biofilme als Polymer-Netzwerke behandelt werden. Das heißt, dass ihr viskoelastisches Verhalten abhängig von der Frequenz der Deformation ist [82,83]. Nach Lieleg *et al.* (2011) dominiert z. B. das Speichermodul von *Pseudomonas aeruginosa* Biofilmen über das Verlustmodul bei Frequenzen unter ~10 Hz. Allerdings wird das Verlustmodul dominant, wenn die Scherfrequenz über ~30 Hz erhöht wird. Darüber hinaus verändern sich die beide Module nicht bei Frequenzen zwischen 0.1 und 10 Hz [82]. Deswegen wurden die Messungen dieser Doktorarbeit auch in diesem Frequenzbereich vorgenommen. Da bei niedrigen Frequenzen das Speichermodul der Biofilme über das Verlustmodul dominierte, wurde die Biofilmsteifigkeit als Speichermodul bei einer mittleren Frequenz von 1 Hz angegeben.

Ein Einfluss der Viskoelastizität von verschiedenen Biofilmen auf ihren Widerstand gegen mechanische und chemische Belastungen wurde bereits beobachtet [10]. Weil die Biofilme der in dieser Arbeit verwendeten Bakterien unterschiedliche Matrixzusammensetzung haben, variiert erwartungsgemäß ihre Steifigkeit. Zum Beispiel haben Kretschmer *et al.* (2021) das Speichermodul der B-1 Biofilme als ~100 Pa bestimmt. Für NCIB 3610 Biofilme beträgt es dagegen ~1 kPa [84]. In ähnlicher Weise haben Kesel *et al.* (2016) eine 10-fach höhere Steifigkeit für NCIB 3610 Biofilme als für B-1 Biofilme berichtet [17]. Zusammen mit dem Benetzungsverhalten spielt die Steifigkeit eine wichtige Rolle für die Adhäsion, die Kohäsion [84] und den Erosionswiderstand [85] der Biofilme

4 Zusammenfassungen der Publikationen

4.1 Bacterial Materials: Applications of Natural and Modified Biofilms

Elif N. Hayta, *Marvin J. Ertelt, Martin Kretschmer,* und *Oliver Lieleg*

Biofilme sind viskoelastische, selbstheilende, gegen toxische Stoffe resistente, manchmal hydrophobe und robuste, lebendige Materialien. Zudem können manche Biofilme Strom erzeugen, indem sie Nährstoffe konvertieren. Einerseits verursacht diese Stabilität der Biofilme großen Schaden in industriellen oder medizinischen Einrichtungen, andererseits kann man von dieser Robustheit der Biofilme auch profitieren. Ferner können die entsprechenden Merkmale der Biofilme verstärkt werden und zusätzliche Funktionen hinzugefügt werden. Hierzu werden die Biofilme mit Nanopartikeln, Makromolekülen, Mineralen, Metallionen, Enzymen oder anderen Bakterien kombiniert.

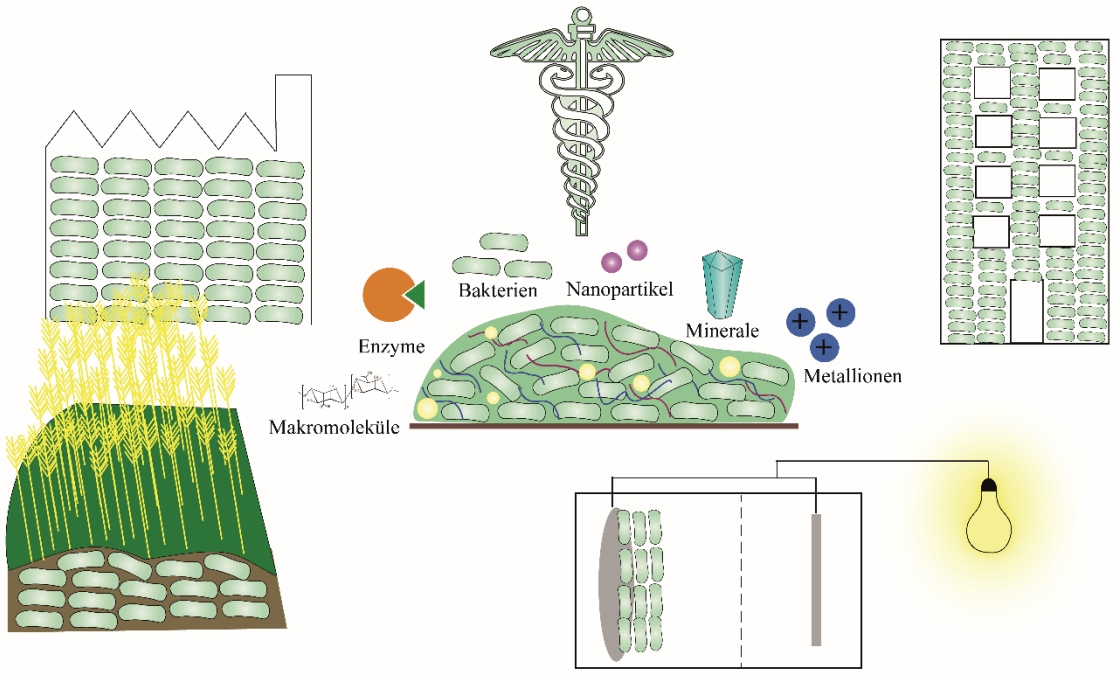

Abbildung 4. 1. Inhaltsübersichtsgrafik. Bakterielle Biofilme können mit Makromolekülen, Enzymen, Nanopartikeln, Mineralen, Metallionen oder mit anderen Bakterien kombiniert werden. Diese modifizierten Biofilme finden Anwendung in Bereichen wie landwirtschaftliche, industrielle oder Umwelt-Biotechnologie, Medizin und Bauwesen sowie Stromerzeugung.

Eine Immobilisierung von Enzymen oder von katalytischen Nanopartikeln in bakteriellen Biofilmen oder eine Ko-Kultivierung von Biofilm-bildenden Bakterien mit anderen, katalytischen Bakterien kombiniert den vom Biofilm gebotenen Schutz mit katalytischer Aktivität. Des Weiteren verändern sich die Materialeigenschaften eines Biofilms wie die Steifigkeit, die Viskoelastizität und die Oberflächen-topographie, wenn Metallionen, extrazellulär DNA, Minerale oder Polymere der Biofilmmatrix hinzugefügt werden. Somit kann man Biofilme mit erwünschten Eigenschaften erhalten. Zusätzlich können die Biofilme mit Polymeren oder Mineralen beschichtet werden, um die Beständigkeit der Biofilme zu verstärken.

Außerdem kann die Beimengung von Elektronenmediator-Molekülen, leitenden Polymeren, Kohlenstoff-Nanoröhrchen oder anderen Kohlenstoffbasierten Nano-partikeln nicht nur die Leitfähigkeit der Biofilme verstärken, sondern auch das Biofilmwachstum verbessern, weil hiermit die Elektronentransferfähigkeit und die Porosität der Biofilme erhöht wird und somit mehr Nährstoffe und Sauerstoffe im Volumen des Biofilms ankommen.

Darüber hinaus können zementartige Materialien durch Hinzufügung von Bakteriensuspensionen, Sporen, abgesonderten Makromolekülen, Zellfragmenten als auch ganzen Biofilmen verbessert werden. Zudem können hier toxische Stoffe durch bakterielle Zusatzstoffe ersetzt werden und die Bakterien können eine Biozementierung durchführen. Damit ist ein nachhaltiges und umweltfreundliches Bauwesen möglich.

Zusammenfasend werden in dieser Arbeit die Möglichkeiten der Anwendung von natürlichen oder veränderten Biofilmen als robuste, selbstheilende, lebendige Materialien in verschiedenen Bereichen wie (landwirtschaftliche, industrielle oder Umwelt-) Biotechnologie, Medizin und Bauwesen sowie Stromerzeugung dargestellt.

Einzelne Beiträge der Kandidatin: Ich habe an der Konzepterstellung dieser Arbeit mitgewirkt und den größten Teil des Manuskripts geschrieben.

4.2. Biopolymer-enriched *B. subtilis* NCIB 3610 biofilms exhibit increased erosion resistance

Elif N. Hayta und *Oliver Lieleg*

Mit der Biofilmbildung gewinnen Bakterien Beständigkeit gegenüber Erosion, die infolge von Scherkräften auftritt. Das verschafft einen großen Vorteil bei vielen biotechnologischen Anwendungen von Biofilmen, in welchen sie einer Strömung ausgesetzt sind. Bislang wurde festgestellt, dass die Erosionsbeständigkeit bakterieller Biofilme durch ihr Adhäsionsverhalten, ihre viskoelastischen Eigenschaften und ihre Benetzbarkeit bestimmt werden. In dieser Arbeit wird nun gezeigt, wie die Erosionsbeständigkeit von *B. subtilis* NCIB 3610 Biofilmen verbessert werden kann, indem fremde (Bio)Polymere wie Polyglutamat (PGA), Alginat und Polyethylen Glykol (PEG) während des Biofilmwachstums in die Biofilmmatrix integriert werden.

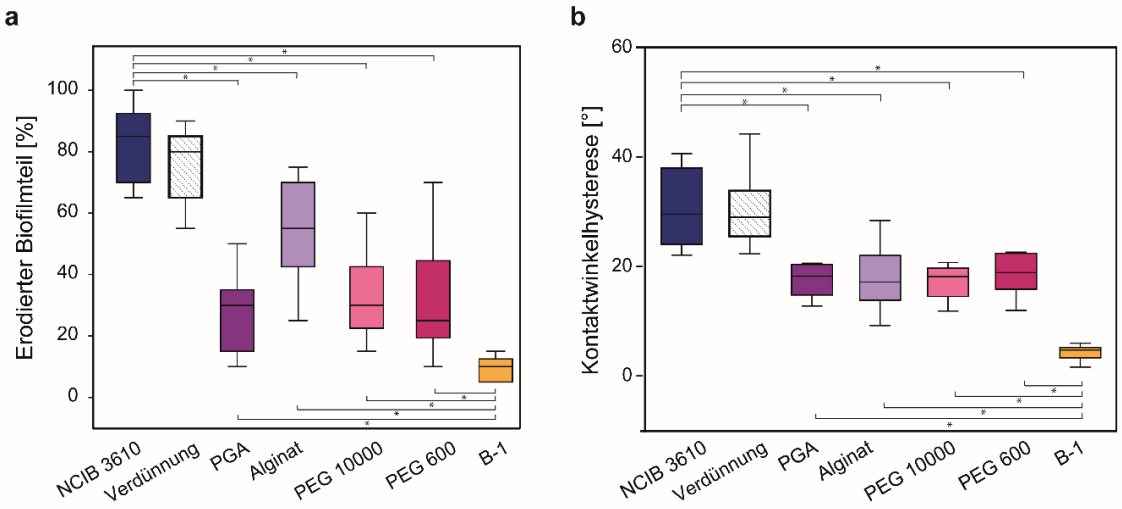

Abbildung 4.2. Einfluss der Beimengung von Biopolymeren auf a) Erosionsbeständigkeit und b) Benetzungsmodus der NCIB 3610 Biofilmen. Die Bezeichnungen "PGA", "Alginat", "PEG 600" und "PEG 10000" beziehen sich auf NCIB 3610-Biofilme, die mit diesen Biopolymeren angereichert sind. Die mit Puffer verdünnte NCIB 3610-Probe ist mit "Verdünnung" gekennzeichnet. Diese angereicherten Biofilme werden mit sowohl rosen-ähnlichen NCIB 3610 Biofilmen als auch lotus-ähnlichen, stark erosionsbeständigen B-1 Biofilmen verglicht.

Die künstliche Beigabe dieser Polymere zu NCIB 3610 Biofilmen führt zu einer deutlichen Erhöhung der Erosionsbeständigkeit aufgrund einer leichten Veränderung

der Oberflächentopographie: Infolge der Beimengung dieser Polymere verringern sich die Tiefe und das Volumen von Talstukturen an der Biofilmoberfläche, während die anderen Merkmale der Oberflächenrauigkeit unverändert bleiben. Das führt zu einer Änderung der Art der Superhydrophobie: der sich Rosen-ähnliche NCIB 3610 Biofilme erhalten einen Zwischenzustand, lotus-ähnlichen B-1 Biofilmen annähert. Die schwächere Wasseradhäsion erzeugten Biofilme (vergleichen mit Rosen-ähnlichen Biofilmen) lässt sich an den verringerten Werten der Kontaktwinkel-hysterese ablesen. Jedoch werden das viskoelastische Verhalten und die mikroskopischen Penetrationseigenschaften der Biofilme hierbei nicht beeinträchtigt.

Weiterhin werden ähnliche Ergebnisse mit mehreren getesteten Biopolymeren erzielt, die sich in Bezug auf Nettoladung und Molekulargewicht unterscheiden. Das deutet darauf hin, dass eine Vielzahl verschiedener (Bio)Polymere für einen ähnlichen Zweck eingesetzt werden kann.

Zusammenfassend stellt diese Arbeit dar, wie die Beimengung von verschiedenen Polymeren die Erosionsbeständigkeit von NCIB 3610 Biofilme verbessert. Die verminderten Täler der Biofilmoberfläche lassen zwar weniges Wasser an die Oberfläche haften, aber noch können im Wasser gelöste kleine Moleküle in den Biofilm diffundieren. Der hier vorgestellte Ansatz könnte neuartige Anwendungen von bakteriellen Biofilmen ermöglichen, bei denen sie stabiler gegen Scherkräfte aber gleichzeitig durchlässig für Nährstoffe oder andere Moleküle sein sollen.

Einzelne Beiträge der Kandidatin: Ich habe an der Konzepterstellung dieser Arbeit und der Planung der Versuche mitgewirkt, die Versuche durchgeführt, die Daten analysiert und das Manuskript verfasst.

4.3 Topography quantifications allow for identifying the contribution of parental strains to physical properties of co-cultured biofilms

Elif N. Hayta, *Carolin A. Rickert* und *Oliver Lieleg*

In der Biofilmerforschung werden meistens Biofilme untersucht, die von einzelnen Bakterien erzeugt wurden: in der Natur aber kommen in Biofilmen oft eine Kombination verschiedener Mikroorganismen vor. Solche Multi-Spezies-Biofilme weisen Merkmale und Eigenschaften auf, die durch die Mischung der beteiligten Stämme bedingt sind. Bislang wurden die möglichen biologischen Wechselwirkungen zwischen verschiedenen Bakterien in Multi-Spezies-Biofilmen bereits gründlich untersucht. Allerdings ist nur sehr wenig darüber bekannt, was die Materialeigenschaften eines Multi-Spezies-Biofilms bestimmt. In dieser Arbeit wird untersucht, wie die Ko-Kultivierung zweier *B. subtilis* Stämme die physikalischen Eigenschaften der Biofilmkolonien wie die Oberflächentopographie und das Benetzungsverhalten beeinflusst.

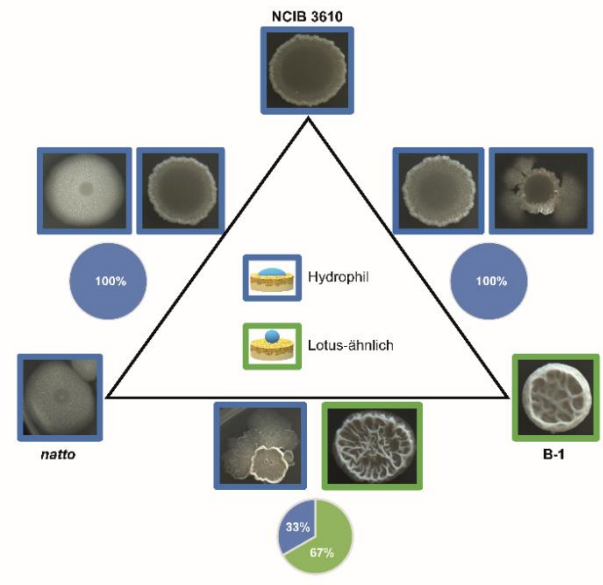

Abbildung 4. 3. Monokulturen und binäre Mischungen von ko-kultivierten *B. subtilis* NCIB 3610, *natto* und B-1 Biofilmkolonien, die auf LB-Agar angezüchtet wurden. In jeder Ecke des Dreiecks ist ein typisches Beispiel für eine Einzelstammkolonie abgebildet; dazwischen sind Beispielbilder von Mischkolonien zu sehen. Die Farbe der Bildrahmen gibt das Benetzungsverhalten der jeweiligen Biofilmkolonien an. Die Torten-diagramme unter den Bildern beschreiben die Häufigkeit, mit der die verschiedenen Benetzungsverhaltens bei den Mischkolonien auftreten.

Binäre Mischungen von *B. subtilis* NCIB 3610, *natto* und B-1 Stämmen ergeben Biofilmkolonien, die morphologisch je von einem „Eltern"-Stamm dominiert werden. Diese „Tochter"-Kolonien werden in Bezug auf ihre Morphologie durch ein Juroren-Panel als „NCIB 3610- ähnlich", „natto-ähnlich" oder „B-1-ähnlich" klassifiziert.

Zusätzlich bestimmen die dominierenden Eltern-Stämme auch das Benetzungsverhalten der Tochter-Biofilmkolonien: als „B-1 ähnlich“ klassifizierte Tochterkolonien weisen ein Benetzungsverhalten wie pure B-1 Biofilme (lotus-ähnlich superhydrophob) auf. Die Oberflächentopographie dieser Tochter-Kolonien unterscheidet sich jedoch geringfügig, aber signifikant von der des dominierenden Eltern-Stamms.

Die Ursache für den leichten Unterschied zwischen den Tochter-Kolonien und den Kolonien ihrer dominierenden Eltern-Stämme wird durch die Anwesenheit des anderen Eltern-Stammes erklärt. Durch Verwendung eines fluoreszenzmarkierten NCIB 3610 Stammes kann das Verhältnis der fluoreszierenden (=NCIB 3610) und nicht-fluoreszierenden (=*natto* oder B-1) Bakterien in den ko-kultivierten Kolonien bestimmt werden. Weiterhin werden ähnliche Ergebnisse erhalten, wenn die binären Mischungen dieser drei *B. subtilis* Stämmen auf einem anderen Nährstoffmedium gezüchtet werden.

Zusammenfassend zeigt diese Arbeit, dass ko-kultivierte Biofilmkolonien stets von einem der Eltern-Stämme dominiert werden und dieser dominierende Eltern-Stamm hauptsächlich die makro- und mikro-Morphologie der Biofilme bestimmt. Dennoch werden diese Tochter-Kolonien von dem anderen Eltern-Stamm signifikant beeinflusst. Die Anwesenheit des anderen Stammes innerhalb des Biofilms kann durch eine mikrotopographische Oberflächen-Analyse erkannt werden, nicht aber auf makro-morphologischen Bildern.

Einzelne Beiträge der Kandidatin: Ich habe an der Konzepterstellung dieser Arbeit und der Planung der Versuche mitgewirkt, die Versuche durchgeführt, die Daten analysiert und am Verfassen des Manuskripts mit

4.4 Machine Learning Approach to Analyze the Surface Properties of Biological Materials

Carolin A. Rickert, ***Elif N. Hayta****, Daniel M. Selle, Ioannis Kouroudis, Milan Harth, Alessio Gagliardi* und *Oliver Lieleg*

Viele Eigenschaften von Materialien wie ihr Benetzungsverhalten, Adhäsion, Reibung, Beständigkeit, elektrische Eigenschaften sowie Biokompatibilität hängen hauptsächlich von der chemischen Struktur und Morphologie der Oberflächen ab. Da die Beziehung zwischen diesen oberflächenbezogenen Eigenschaften und der Oberflächentopographie noch nicht gut erklärt ist, werden typischerweise zeitaufwändige Versuch-und-Irrtum-Ansätze verwendet, um erwünschtes Verhalten der Materialoberflächen zu erzielen. Hierzu kann das maschinelle Lernen helfen, die Optimierung eines Materialentwicklungsprozesses zu erleichtern. In dieser Arbeit werden die topographischen Merkmale von komplexen biologischen Materialien, die durch 21 metrologischen Parameter beschrieben werden, durch maschinelles Lernen analysiert. Verschiedene biologische Oberflächen wie Pflanzenblätter oder bakterielle Biofilme können in Bezug auf ihr Benetzungsverhalten erfolgreich klassifiziert werden, indem vier maschinelle Lern-Algorithmen (d.h. *k*-Nearest Neighbors, Gaussian naïve Bayes, Logistic Regression und Random Forest) mit mikrotopographischen Daten dieser Oberflächen konfrontiert werden.

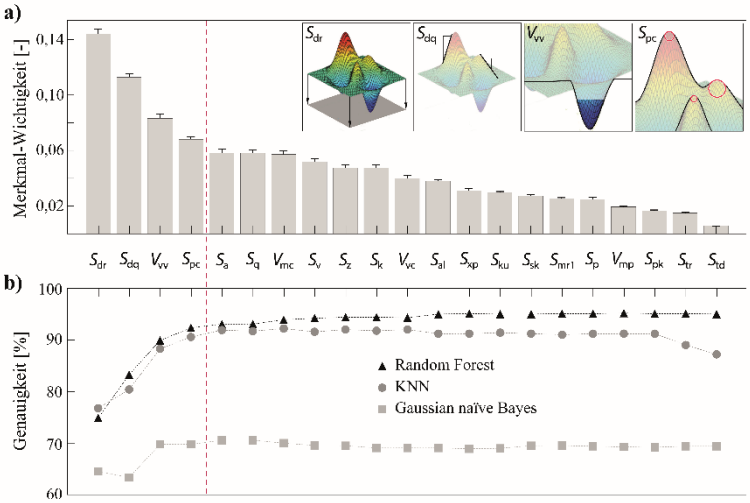

Abbildung 4.4. Dimensionsreduktion des gesammelten Datensatzes. Vier Parameter (S_{dr}, S_{dq}, V_{vv} und S_{pc}) sind für die Klassifizierung der biologischen Oberflächen in Bezug auf ihr Benetzungsverhalten ausreichend.

Auf MSgg Nährstoffmedium gebildete *B. subtilis* NCIB 3610 Biofilme weisen Rosen-ähnliche Superhydrophobie auf, während B-1 Biofilme Lotus-ähnlich superhydrophob und *natto* Biofilme hydrophil sind. Durch Wachstum auf LB Medium werden NCIB 3610 Biofilme hydrophil, das Benetzungsverhalten der anderen (B-1 und *natto*) Biofilme bleibt aber unverändert. Zuerst werden die Algorithmen mit MSgg-Daten trainiert und tatsächlich können die MSgg-Biofilme erfolgreich (d. h. mit hoher Genauigkeit, Spezifität und Sensitivität) klassifiziert werden. Die mit MSgg-Daten trainierten Algorithmen funktionieren auch gut, wenn auf LB Medium gewachsene Biofilme bezüglich ihres Benetzungsverhaltens klassifiziert werden. Das bedeutet konkret, dass NCIB 3610 Biofilme auf LB Medium als hydrophil (wie *natto* auf MSgg) erkannt werden. Wenn die Algorithmen mit topographischen Daten von verschiedenen Pflanzen mit dem gleichen Set von Benetzungsverhalten (d. h. hydrophil, Rosen-ähnlich superhydrophob und Lotus-ähnlich superhydrophob) trainiert werden, können sie die Biofilme jedoch nicht erfolgreich klassifizieren (und umgekehrt). Dennoch erzielen diese Algorithmen hohe Genauigkeitswerte, wenn Daten von beide Gruppen (von Biofilmen und Pflanzenblättern) für Training verwendet werden. Die höchste Genauigkeit für die Klassifizierung (~95 %) konnte mit dem Random Forest-Algorithmus erreicht werden. Hiermit wurden auch die wichtigsten Oberflächenmerkmale (d.h. Topographieparameter) durch eine Dimensionsreduktion bestimmt: Mit nur vier Parametern (S_{dr}, S_{dq}, V_{vv} und S_{pc}) kann dieser Algorithmus hydrophile, Rosen-ähnliche superhydrophobe und Lotus-ähnliche super-hydrophobe Oberflächen erfolgreich unterscheiden.

Zusammenfassend ermöglichen die in dieser Arbeit verwendeten Algorithmen die Vorhersage des Benetzungsverhaltens von komplexen, biologischen Oberflächen aufgrund der Oberflächentopographiedaten. Diese Erkenntnisse können für viele andere Materialforschungsprobleme hilfreich sein, z. B für Schadenbeurteilung sowie Adhäsion- oder Reibungsversuchen.

Einzelne Beiträge der Kandidatin: Ich habe an der Konzepterstellung dieser Arbeit, sowie der Planung und der Durchführung der Versuche mitgewirkt.

5 Diskussion

Bakterielle Biofilme sind eine großartige Kombination aus funktionellen, mikrobiellen Gemeinschaften und robusten, klebrigen, viskoelastischen Materialien. Mit ihren herausragenden Eigenschaften können sie einerseits als persistente, schädliche Kontaminationen, andererseits aber auch als beständige, biotechnologische Werkzeuge betrachtet werden. Wie bei klassischen Werkstoffen spielen die Oberflächenrauigkeit und das Benetzungsverhalten auch für diese lebendigen Materialien eine zentrale Rolle. Um ein besseres Verständnis für die Auswirkung der Rauigkeit auf das Benetzungsverhalten und die Klassifizierbarkeit von Biofilmen zu erhalten, fokussiert sich diese Doktorarbeit auf die quantitative Analyse der Oberflächentopographie von bakteriellen Biofilmen. Ferner werden die nützlichen Aspekte der Biofilme hier ausführlich dargestellt.

Die Erforschung von Biofilmen beschäftigt sich meistens mit negativen Folgen und mit der Entfernung der Biofilme [86,87]. Das große Potenzial der Biofilme wartet noch darauf, für vorteilhafte Anwendungen entdeckt zu werden. Bisher wurden nur manche Anwendungsbereiche von Biofilmen vorgestellt. Bei diesen Beispielen können die Biofilme entweder direkt verwendet werden oder sie werden manipuliert, um bestimmte, erwünschte Eigenschaften der Biofilme zu verbessern. Eine Möglichkeit, dieses Ziel zu erreichen, ist der Gebrauch gentechnischer Methoden. Diese Strategie wird bislang in verschiedenen Bereichen erfolgreich verwendet [83,88–90]. Durch gentechnische Veränderungen werden hier die Matrixkomponenten neu geordnet, um die gewollten Eigenschaften zu erzielen. Zum Beispiel ist *Shewanella oneidensis* ein weitverbreiteter Stamm, der bei vielen Anwendungen wie der Stromerzeugung oder der Bioremediation zum Einsatz kommt [90–93]. Mit Hilfe gentechnischer Mutationen können die Menge, die Kohäsion oder die extrazelluläre Elektrontransferfähigkeit dieser Biofilme reguliert werden [90]. Obwohl gentechnische Methoden präzise Eingriffe erlauben und relativ einfach zu kontrollieren sind, gibt es bei diesen Methoden auch Nachteile: Vor allem muss die genetische Struktur der Mikroorganismen gut bekannt sein. Sowohl die Bestimmung als auch die Veränderung des genetischen Materials von Organismen benötigen aufwändige Prozesse. Zudem muss diese Genanalyse für jeden einzelnen Organismus wiederholt werden, weil Mutationen spezifisch für den jeweiligen Mikroorganismus sind. Deswegen ist die Verwendung von gentechnischen Methoden nicht immer zielführend.

Eine einfachere Alternative für die Biofilmmanipulation ist die Veränderung der Matrixzusammensetzung von außen. Beispiele für das breite Anwendungsspektrum von Biofilmen und für mögliche Manipulationsmechanismen zur Integration von Zusatzstoffen in die Biofilmmatrix werden in Kapitel 4.1 vorgestellt. Das Hinzufügen von Metallionen, Nanopartikeln, Makromolekülen, Mineralien, Enzymen oder anderen Bakterien zu den Biofilmen verbessert entweder erwünschte Eigenschaften der Biofilme wie ihre Steifigkeit, Porosität und extrazelluläre Elektrontransferfähigkeit oder es erzeugt ganz neue Funktionen in den Biofilmen (siehe Abbildung 5.1). Zum Beispiel können nicht-exoelektrogene Bakterien durch Beimengung mit Elektron-leitenden Molekülen (d.h. Elektronenmediatoren) als bioelektrochemische Systeme verwendet werden. Außerdem können neue Fähigkeiten wie katalytische Aktivität durch Zugabe von Enzymen oder katalytischen Nanopartikeln zu Biofilmen erzeugt werden.

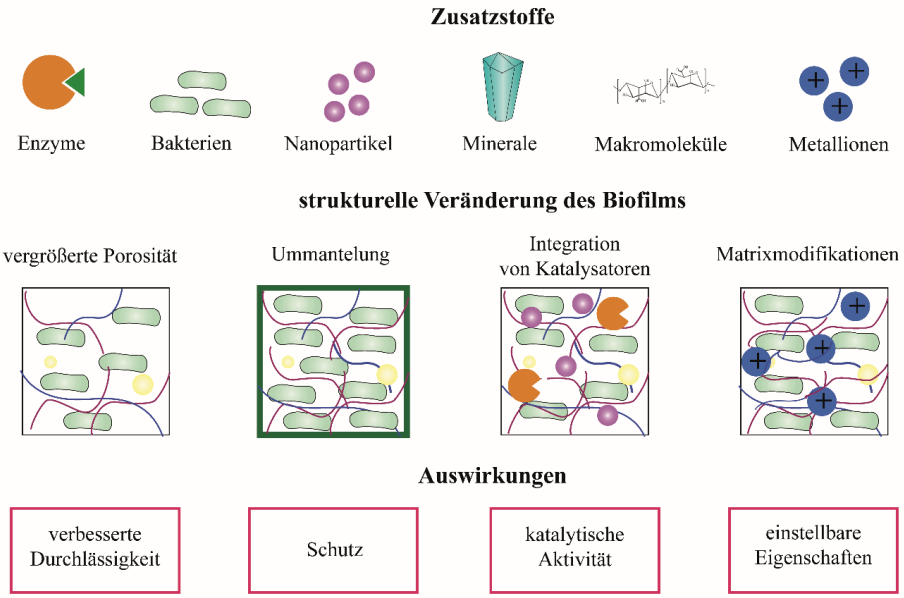

Abbildung 5.1. Manipulationsmechanismen von Biofilmen. Die Beimengung verschiedener Zusatzstoffe zu Biofilmen ermöglicht eine vergrößerte Porosität, die Integration von Katalysatoren wie Enzymen oder Nanopartikeln sowie Modifikation der Biofilmmatrix wie z. B Quervernetzung. Außerdem können manche Zusatzstoffe wie z. B. Polymere oder Minerale die Biofilme ummanteln. Diese Veränderungen lassen die Biofilme durchlässiger, lebensfähiger und belastbarer sein, und sie ermöglichen die Einstellung mancher Materialeigenschaften der Biofilme. Zudem können neue Funktionen wie katalytische Aktivitäten in die Biofilme eingebracht werden.

Die Beimengung solcher Zusatzstoffe in Biofilmen verändert oft die Matrixstruktur. Dadurch können die Viskoelastizität, die Durchlässigkeit, die Lebensfähigkeit und die

Belastbarkeit der Biofilme kontrolliert werden. Weiterhin decken manche Polymere die Biofilmoberfläche als eine Art von Beschichtung ab. Damit schützen sie die Biofilme vor Umgebungsstress oder Scherkräften. Eine Verstärkung der Materialeigenschaften der Biofilme führt zu robusteren und beständigeren Biofilmen, was für viele Anwendungen wichtig ist. Die hier dargestellten Anreicherungsmethoden bieten im Vergleich zu den gentechnischen Methoden eine einfachere Option zur Steuerung der Biofilmeigenschaften und sie ermöglichen die Verbesserungen bestimmter Biofilmeigenschaften nicht nur für die genetisch gut untersuchte, sondern für eine breitere Palette von Mikroorganismen.

In vielen biotechnologischen Einsatzgebieten werden die Biofilme Scherkräften ausgesetzt, die durch Wasser erzeugt werden. Aus diesem Grund bestimmt die Art der Wechselwirkung von Biofilmen mit Wasser viele ihrer Eigenschaften wie die Erosionsbeständigkeit oder Resistenz gegen wässerige toxische Stoffe. Die Benetzbarkeit einer Oberfläche hängt sowohl von der Chemie als auch der Rauigkeit ab [16], und beide werden durch die Matrixzusammensetzung von Biofilmen beeinflusst [45,94]. *B. subtilis* B-1 Biofilme weisen ein lotus-ähnliches superhydrophobes Benetzungsverhalten und stärke Erosionsbeständigkeit auf. Dagegen sind *B. subtilis* NCIB 3610 Biofilme Rosen-ähnlich superhydrophob und im Vergleich zu B-1 Biofilmen anfälliger gegen Scherkräfte. Zwar haben beide Biofilme das gleiche Beschichtungsprotein, *BslA*, auf ihren Oberflächen, aber die B-1 Biofilme enthalten PGA als Hauptbestandteil der Matrix [17]. Die Frage, was passiert, wenn dieses polyanionische Polymer zusätzlich zu NCIB 3610 Biofilmen zugegeben wird, wird in Kapitel 4.2 beantwortet. Durch Anreicherung der NCIB 3610 Biofilme mit PGA verändert sich die Erosionsbeständigkeit dieser Biofilme in einen Zustand der zwischen normalen NCIB 3610 und B-1 Biofilmen liegt (Abbildung 5.2). In ähnlicher Weise liegt die Kontaktwinkelhysterese (d.h. das Adhäsionsverhalten von Wasser auf der Oberfläche der Biofilme) dieser angereicherten NCIB 3610 Biofilmen zwischen der von nicht-modifizierten NCIB 3610 und der von B-1 Biofilmen, während sich die statische Kontaktwinkelwerte nicht verändern. Da die Steifigkeit der NCIB 3610 Biofilme durch die Anreicherung mit PGA unverändert bleibt, erklärt sich das verbesserte Erosionsverhalten der angereicherten NCIB 3610 Biofilme durch die leichte Veränderung der Wasseradhäsion auf der Oberfläche.

Der Benetzungswiderstand einer Oberfläche kann entweder durch eine Erhöhung der Oberflächenspannung (durch chemische Modifikationen) oder durch eine Erhöhung

der Oberflächenrauigkeit gesteigert werden [16]. Da das hier hinzugefügte Polymer (d.h. PGA) hydrophil ist, erwartet man nicht, dass die hydrophoben Eigenschaften der Oberfläche durch die Beimengung mit diesem Polymer chemisch verstärkt wurden. Aus diesem Grund wurde die Oberflächenrauigkeit der Biofilme detailliert untersucht. Die Ursache für das veränderte Benetzungsverhalten wird durch REM-Bilder der Biofilme deutlich: Infolge der Anwesenheit der zusätzlichen Polymere in der Matrix werden die tiefen Täler in der NCIB 3610 Biofilmoberfläche durch (B-1 ähnliche) flache Ausbeulungen ersetzt.

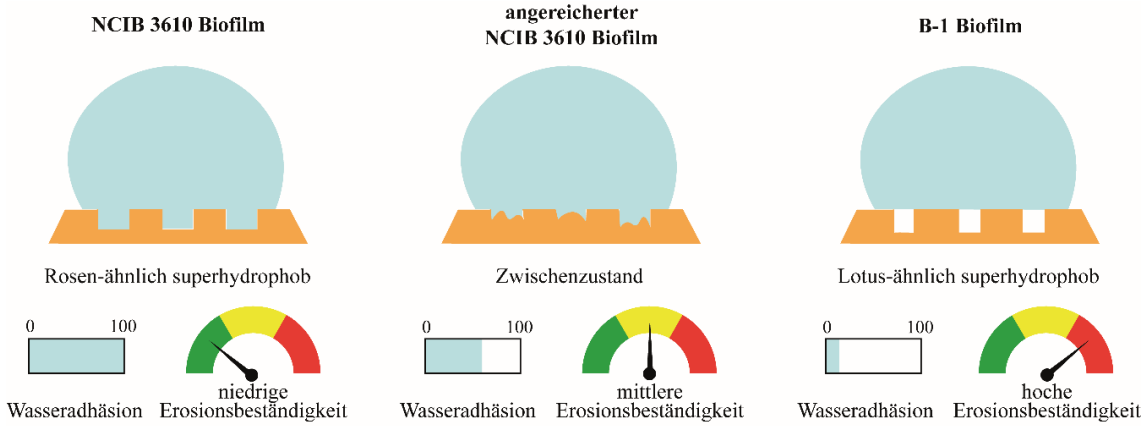

Abbildung 5.2. Vergleich der angereicherten NCIB 3610 Biofilmen mit normalen NICB 3610 und B-1 Biofilmen. Wegen der verringerten Wasseradhäsion durch Anreicherung mit Polymeren, zeigen angereicherte NCIB 3610 Biofilme eine Erosionsbeständigkeit, die zwischen der von nicht-angereicherten NCIB 3610 und B-1 Biofilmen liegt. Die Ursache für diese Veränderung ist die weniger ausgebeulte Talstruktur der angereicherten Biofilme.

Weiterhin belegt die quantitative Analyse der Oberflächentopographie diese Umwandlung der Talstruktur: Durch eine detaillierte Quantifizierung der Rauigkeit mit 3D-Laser- Rastermikroskopie (d. h. Profilometrie) werden die Veränderungen der Oberflächenmerkmale verdeutlicht: Alle talbezogenen Parameter (S_v, S_{vk}, V_{vv} und V_{vc}) sind bei den PGA-angereicherten NCIB 3610 Biofilmkolonien signifikant verringert. Diese verringerten Talstrukturen bieten nun ein kleineres Volumen für Wasser, um dort anzuhaften, weshalb das Wasser nun reduzierte Flüssigkeits-retentionskapazität der Oberflächen leichter abperlt [95].

Dennoch ist diese Veränderung nicht ausreichend, um eine Lotus-ähnliche Superhydrophobie zu erhalten, die einen Lufteinschluss zwischen der Festkörper-Flüssigkeitsgrenzflächen benötigt. Im hier dargestellten Fall steht der Wassertropfen noch in direktem Kontakt mit der Biofilmoberfläche. Das wird durch einen

Antibiotika-Empfindlichkeitstest deutlich: Es gibt hier keinen Unterschied zwischen PGA-angereicherten und nicht-modifizierten NCIB 3610 Biofilmen in Bezug auf ihre Antibiotikaresistenz. Dies bedeutet, dass sich die Durchlässigkeit dieser Biofilme durch die PGA-Anreicherung nicht verändert. Das ist ein großer Vorteil für biotechnologische Anwendungen, bei welchen Nährstoffe in den Biofilm hineindiffundieren sollen.

Für die Erzeugung mechanisch stärkerer Biofilme wurden bereits verschiedene Bemühungen unternommen. Hierzu wird meistens die Oberfläche der Trägermaterialien chemisch bearbeitet [96]. Bestimmte chemische Modifikationen dieser Oberflächen verstärken die bakterielle Anhaftung und infolgedessen werden die Biofilme widerstandsfähiger gegen Scherkräfte. Zum Beispiel beschichteten Lackner *et al.* die Oberfläche verschiedener Membranen mit modifizierten PEG-Molekülen und dann verwendeten sie diese Membranen zur biologischen Abwasserreinigung. Sie beobachteten mit diesen modifizierten Membranen eine bessere Anhaftung des Biofilms und eine stärkere Scherkraftresistenz. Die in Kapitel 4.2 vorgestellte Methode bietet im Vergleich zu Membranmodifikationen einen einfacheren Ansatz. Vor allem benötigt diese Methode keine Vorbereitung der Trägermaterialien und sie ist unabhängig vom Substrat, auf dem die Bakterien wachsen. Darüber hinaus kann ein breites Spektrum von Polymeren mit verschiedenen Nettoladen und Molekülgrößen für diese Methode verwendet werden (siehe Kapitel 2.3 für detaillierte Informationen über geeignete Polymere). Höchstwahrscheinlich fungieren diese Polymere als Bausteine innerhalb der Biofilmmatrix und infolge-dessen verändern sie leicht die Oberflächentopographie durch die Befüllung die Täler.

Neben Biopolymeren können auch andere Bakterien einen Biofilm anreichern. Das ist ein natürlicher Mechanismus, um stärkere oder funktionellere Biofilme zu erhalten. Hierzu leben mehrere Stämme zum ein- oder gegenseitigen Vorteil zusammen. Die meisten natürlichen Biofilme bestehen aus mehreren Mikroben: z. B. orale Biofilme oder die Darmflora. Außerdem kann diese Zusammenarbeit von Bakterien auch (im Labor) künstlich erzeugt werden, um die Wechselwirkungen zwischen den Mikroben in diesen Multi-Spezies-Biofilmen aufzuklären oder um erwünschte Eigenschaften von verschiedenen Mikroorganismen zu kombinieren. Dennoch ist zurzeit nur wenig bekannt, wie die Materialeigenschaften solcher Multispezies-Biofilme bestimmt werden. Deswegen wurden in dieser Doktorarbeit die Oberflächentopographie und das

Benetzungsverhalten von Biofilmen aus binären Mischungen von *B. subtilis* NCIB 3610, *natto* und B-1 Stämmen untersucht. In Kapitel 4.3 wird dargestellt, dass die makroskopische Morphologie der ko-kultivierten Tochterkolonien primär durch einen Elternstamm bestimmt wird. Zudem ist dieser morphologisch-dominierende Stamm auch innerhalb des Biofilms in großer Zahl vorhanden. Dennoch beeinflusst auch der andere Elternstamm die Biofilmeigenschaften, obwohl dies nicht makro-morphologisch erkennbar ist. Eine kleine Menge des anderen Elternstammes scheint jedoch für eine geringfügige, aber signifikante Veränderung der Mikrotopographie und der Benetzung der Tochterkolonien auszureichen und diese in Richtung der Eigenschaften des zweiten Elternstammes zu verschieben. Das bedeutet, dass so Merkmale aus verschiedenen Biofilmen kombiniert werden können. Solche Mischkolonien mit Hybrid-Merkmalen können für vielfältige biotechnologische Anwendungen hilfreich sein.

Da das Vorhandensein des morphologisch nicht-erkennbaren Stammes nur durch eine detaillierte mikroskopische Untersuchung der Biofilmoberfläche gezeigt werden konnten, hebt diese Doktorarbeit hervor, dass die quantitative Analyse der Oberflächenmikrotopographie mittels Profilometrie eine gute Methode für die Untersuchung von Multi-Spezies-Biofilmen sein kann. Es wurden auch bereits vielfaltige Methoden für die 3-D Abbildung von Biofilmen eingesetzt. Zum Beispiel wurden Elektronmikroskopie [97], konfokale Laser-Rastermikroskopie [98] oder Profilometrie [35] verwendet. Auch wurde die Anwesenheit unterschiedlicher Bakterien und ihrer EPS in einem oralen Biofilm durch Transmissions-elektronmikroskopie (TEM) gezeigt [99]. Die Autoren, Reese und Guggenheim, konnten hier die verschiedenen Bakterien in einem Multi-Spezies-Biofilm durch ihre Morphologie unterscheiden. Die verschiedenen EPS-Bestandteile, die durch unterschiedliche Bakterien abgesondert werden, waren ebenfalls unterscheidbar. Mit dieser Bilderfassungsmethode lassen sich die Komponenten der Multi-Spezies-Biofilme also erfolgreich erkennen, aber sie erfordert einen chemischen Vorbereitungsschritt. Nach Weber *et al.* stört dieser Vorbereitungsprozess (d.h., die nötige chemische Behandlung) die Probe, indem er die EPS-Struktur beeinflusst [100]. Zudem ermöglicht diese Methode nur qualitative Analysen. Mit Hilfe der Profilometrie kann man aber quantitative Messungen der Oberflächentopographie mit hoher Auflösung erhalten. Ferner benötigt die Profilometrie keine Vorbereitung oder Beschichtung der Proben, was den Arbeitsaufwand deutlich reduziert.

Die Möglichkeit zur quantitativen Analyse der Oberflächentopographie für die Erkennung des Beitrags von Bakterien in Mischkolonien zeigt, dass die 3D-Abbildung von Oberflächen ein mächtiges Werkzeug ist. In Kapitel 4.4 wird ferner die Rauigkeit von *B. subtilis* Biofilmen mit verschiedenen Benetzungsverhalten durch einen maschinellen Lernansatz untersucht. Da der Zusammenhang zwischen dem Benetzungsverhalten und der Oberflächentopographie von Biofilmen bereits bestimmt wurde [43,45], kann die Klassifizierung solcher Probe nach der Rauigkeit auch zur Bestimmung ihres Benetzungsverhaltens verwendet werden. Weiterhin können diese Algorithmen auch andere Biofilme und weitere biologische Oberflächen wie z. B. Pflanzenblätter mit hydrophilem, Rosen-ähnlich und Lotus-ähnlich superhydrophobem Benetzungsverhalten erfolgreich klassifizieren, indem sie Rauigkeitsparameter (d.h. topographische Daten) verwenden.

Werb *et al.* zeigten bereits, dass sich die Oberflächentopographie und das Benetzungsverhalten von *B. subtilis* NCIB 3610 Biofilmen ändern, wenn die Bakterien auf verschiedenen Medien gezüchtet werden [45]. Hier wurden Unterschiede zwischen den hydrophilen, Rosen-ähnlich und Lotus-ähnlich superhydrophoben Kolonien mit Hilfe der S_p, S_v, S_z, S_{al}, S_{dq} und S_{dr} Parameter gezeigt. Während hydrophile Biofilme die kleinsten Werte für diese Parametern ergaben, hatten die Lotus-ähnlichen Biofilme die größte Rauigkeit. Ein ähnliches Verhalten für die meisten Parameter wird auch in Kapitel 4.4. beobachtet.

Durch den hier dargestellten maschinellen Lernansatz kann die Beziehung zwischen Benetzungsverhalten und Topographie systematisch untersucht und verstanden werden. Bisher wurde diese Beziehung nur mit Versuch-und-Irrtum-Ansätzen überprüft. In früheren Arbeiten wurden zwar einige topographische Merkmale ausgewählt, um ihren Einfluss auf die Benetzbarkeit der Oberflächen zu untersuchen [23,45]. Allerdings ermöglichen die hier verwendeten computer-basierten Algorithmen eine allgemeine Untersuchung von Oberflächen, die alle möglichen Oberflächenmerkmale gleichzeitig aufweisen können. Deswegen ist der in Kapitel 4.4. dargestellte Ansatz für ein detailliertes Verständnis der Benetzungs-Topographie-Beziehung sehr hilfreich. Um unter allen berechneten Parametern die für das Benetzungsverhalten wichtigsten Oberflächenmerkmale zu ermitteln, wurde eine Dimensionsreduktion durchgeführt. Damit wurde gezeigt, dass im Wesentlichen vier Parameter (S_{dr}, S_{dq}, V_{vv} und S_{pc}) für die Unterscheidung der hydrophilen, Rosen-

ähnlich und Lotus-ähnliche superhydrophoben komplexen Oberflächen ausreichend sind (Abbildung 5.3).

Der Einfluss einiger dieser Parameter auf die Benetzbarkeit von Oberflächen wurde bereits in früheren Arbeiten erwähnt. Zum Beispiel wurde das entwickelte Übergangsflächenverhältnis (S_{dr}) in vielen Arbeiten als Vertreter der Oberflächenrauigkeit von Biofilmen verwendet [35,45,101,102]. Es quantifiziert die für die Wechselwirkung zwischen Oberfläche und Flüssigkeit verfügbare Gesamtfläche. Deswegen kann es als der wirksamste und universtellste Parameter für die Bestimmung des Benetzungverhaltens von Oberflächen betrachtet wurden [102]. Dennoch ist manchmal eine detailliertere Beschreibung von Oberflächen mit anderen Parameter auch wie in Kapitel 4.2 und 4.3 erwähnt für ein vollständiges Verständnis von Oberflächenmerkmalen nötig. Zusammen mit V_{vv} bestimmen der arithmetische Mittelwert der Spitzenkrümmung (S_{pc}) und der quadratischer Neigungsmittelwert (S_{dq}) die Hohlräume einer Oberfläche, die benetzt wird. Der Einfluss der Geometrie solcher Oberflächenmerkmale wurde auch bereits gezeigt [42,43,103,104]. Typischerweise wurden in diesen Arbeiten künstliche, regelmäßig strukturierte Oberflächen verwendet. Hier wird nun gezeigt, dass diese Modelle auch für komplexe, natürliche (biologische) Oberflächen gelten. Das ist eine wichtige Erkenntnis, da die meisten natürlichen Oberflächen komplexere topographische Strukturen als künstliche Materialien aufweisen.

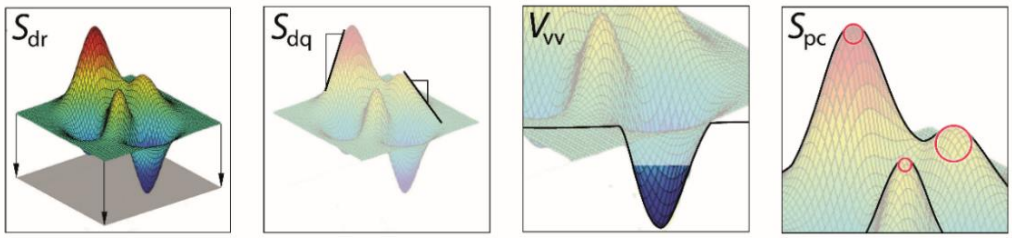

Abbildung 5. 3. Schematische Darstellung der für die Benetzbarkeit biologischer Proben vier wichtigsten Oberflächenmerkmale. Für die Klassifizierung biologischer Oberflächen bezüglich ihres Benetzungsverhaltens spielen diese topographische Oberflächenparameter eine zentrale Rolle. Siehe Kapitel 3.1.1. für eine detaillierte Beschreibung dieser Parameter.

Zusammenfassend wird in dieser Dissertation die zentrale Rolle der Oberflächentopographie von bakteriellen Biofilmen für das Benetzungsverhalten und andere anwendungsrelevante Eigenschaften wie z.B. die Erosionsresistenz untersucht.

Außerdem wird hier gezeigt, dass die mikro-topographischen Merkmale von Biofilmen Stamm-spezifisch sind. Dadurch kann die quantitative Analyse einer Biofilmoberfläche auch als eine ergänzende Methode zur Identifizierung der Bakterien verwendet werden, die den Biofilm bilden. Zudem ermöglichen topographischen Daten von Biofilmen deren Klassifizierung bezüglich ihres Benetzungsverhaltens mit Hilfe eines maschinellen Lernansatzes. In dieser Doktorarbeit werden Biofilme als nützliche, lebendige Biomaterialien betrachtet. Auch Bemühungen zur Verbesserung mancher Biofilmeigenschaften werden hier ausführlich vorgestellt. Das Verständnis dieser Eigenschaften von Biofilmen ist wesentlich, um von Biofilmen in biotechnologischen Anwendungen profitieren zu können.

6 Ausblick

In den letzten Jahrzehnten führte der zunehmende Bedarf an nachhaltigen und umweltfreundlichen Materialien und Produktionsverfahren zu großen Entwicklungen in der Biotechnologie. In Bereichen wie der Bioverfahrenstechnik, der Medizintechnik, der Stromerzeugung, der Landwirtschaft, dem Bauwesen sowie in der Umweltbiotechnologie finden heute Bakterien selbst oder bakterielle Produkte wie z. B. (Bio)Polymere und Enzyme aber auch bakterielle Biofilme Verwendung. Für solche Anwendungen kann ferner ein weites Spektrum von Zusatzstoffen verwendet werden, um die Eigenschaften oder Funktionalität von bakteriellen Biofilmen zu verbessern. In dieser Doktorarbeit wurden zahlreiche Beispiele für die Manipulation von bakteriellen Biofilmen vorgestellt. Diese breite Palette von Anwendungen und Zusatzstoffen kann aber sicher noch erweitert werden. Zum Beispiel wurden in Kapitel 4.2 vier Polymere mit unterschiedlicher Nettoladung und Molekülgröße zu NCIB 3610 Biofilmen gegeben. Da die verschiedenen Polymere hier die ähnlichen Wirkungen hatten, können wahrscheinlich anstelle der hier dargestellten, auch andere, günstigere oder leichter erhältliche Substanzen als Zusatzstoffe eingesetzt werden. Dadurch würden die Materialkosten sinken und die industrielle Einsetzbarkeit der hier beschriebenen Strategie erleichtert.

Eine andere Möglichkeit, um verbesserte Biofilme zu erhalten, ist die Ko-Kultivierung von mehreren Bakterien. Hier wurden nur binäre Mischungen von drei *B. subtilis* Stämmen untersucht. Da diese Bakterien der gleichen Spezies angehören, können sie auch die gleichen Nährstoffe umwandeln. Das führt zu Konkurrenz zwischen diesen Bakterien. Daher war der dominierte Stamm in der Mischung nur in kleiner Zahl anwesend, und dies beschränkt dessen Einfluss auf die Materialieneigenschaften des Biofilms. Möglicherweise können aber ausgewogene Mischkolonien aus Bakterien verschiedener Spezies erzeugt werden, bei denen die Anzahl der Bakterien in den Mischkolonien ungefähr gleich sind. Das könnte dann Hybrid-Kolonien mit kombinierten Eigenschaften ermöglichen, was das Anwendungsspektrum der Biofilme weiter verbreitern kann.

Außerdem wurde in dieser Arbeit die Anwesenheit der dominierten Stämme in den binären Mischkolonien durch eine quantitative Analyse der Oberflächenrauigkeit erkannt, obwohl deren Anzahl nur gering war. Dennoch konnte hiermit der Anteil der

verschiedenen Stämme in den gemischten Kolonien nicht bestimmt werden; dies erfordert eine manuelle Bestimmung der Kolonie-bildenden Einheiten jeder Bakterienspezies durch zeitaufwändige, traditionelle mikrobiologische Vereinzelungsversuche. In künftigen Arbeiten kann mit Hilfe computer-basierter Ansätze versucht werden, die Anteile der beigetragenden Stämme in Multi-Spezies-Biofilmen aus der Biofilmtopographie zu bestimmen, und erste Pilotversuche hierzu waren bereits vielversprechend (siehe Masterarbeit Daniel Selle, Professur für Biomechanik, Technische Universität München).

Wie in dieser Doktorarbeit gezeigt, können die Biofilme aber durch maschinelle Lernalgorithmen bezüglich ihres Benetzungsverhaltens gut klassifiziert werden, indem die Algorithmen topographische Daten verarbeiten. Hier wurde das Benetzungsverhalten der Proben als kategorische Variable verwendet. Als nächster Schritt kann nun eine quantitative Beziehung zwischen dem Benetzungsverhalten und der Rauigkeit erprobt werden. Dafür sollten sowohl statische Kontaktwinkel- als auch Kontaktwinkelhysterese-Messungen auf Oberflächen verschiedener Rauigkeit vorgenommen werden. Durch eine Modellierung von Kontaktwinkel(hysterese) durch die hier dargestellten vier Parameter (S_{dr}, S_{dq}, V_{vv} und S_{pc}) kann man die konkreten Beiträge dieser Parameter zum Benetzungsverhalten von (Bio)Materialien weiter aufschlüsseln. Solch ein Model kann dann sowohl auf künstlichen, regelmäßig strukturierten Oberflächen als auch auf natürlichen, komplexen Proben getestet werden.

Die in dieser Doktorarbeit dargestellte Ergebnisse können neue Wege in der Materialforschung eröffnen, indem die Rolle der Oberflächenrauigkeit für verschiedene Aspekte von Materialeigenschaften aufgezeigt war. Als robuste, lebendige Materialien bieten Biofilme außerdem viele Vorteile für die Menschheit. Für Biotechnologische Anwendungen von Biofilmen müssen ihre Materialeigenschaften aber gut verstanden und kontrollierbar sein. Diese Doktorarbeit bietet hilfreiche neue Informationen für ein besseres Verständnis von Biofilmen als Biomaterialien. Mit den hier vorgestellten Ansätzen können Biofilme so weiterentwickelt werden, dass ihre positiven Eigenschaften zukünftig noch breitere Anwendungen finden und wir Menschen von bakteriellen Materialien noch mehr profitieren als bisher.

Anhang

A. Publikationen

B. Lizenzen für die Publikationen

C. Vollständige Liste der Publikationen

A. Publikationen

A.1 Bacterial Materials: Applications of Natural and Modified Biofilms

REVIEW

ADVANCED MATERIALS INTERFACES
www.advmatinterfaces.de

Bacterial Materials: Applications of Natural and Modified Biofilms

*Elif N. Hayta, Marvin J. Ertelt, Martin Kretschmer, and Oliver Lieleg**

Over millennia, bacteria have developed clever strategies to build biopolymer-based communities in which they can survive even extremely challenging conditions. Such bacterial biofilms come with a broad range of fascinating material properties that—in settings such as medicine, food production, or other areas of industry—make it difficult to remove or inactivate them: they can stick to many surfaces, repel water and oils, and can even transport electrons. Inspired by the outstanding versatility and sturdiness of such bacterial biofilms, material scientists have set out to harness those properties and to create bacterial materials for different applications. However, as the range of technological applications employing biofilms keeps expanding, improved material properties or broader functionalities are desired. Here, such attempts where materials with improved properties were created by making use of either natural or modified bacterial biofilms are reviewed. The areas in which those bacterial materials may be used range from agriculture and (environmental) biotechnology over biomedical and electrical engineering to construction engineering.

1. Introduction

Bacterial biofilms are sticky and slimy substances that come with a variety of unique and sometimes annoying properties. In those biofilms, bacteria embed themselves into self-secreted, extracellular polymeric substances (EPSs).[1–6] Depending on the particular bacterial strain and the growth conditions during biofilm generation, the composition of this EPS can vary quite a bit.[7] Yet, in any case, these EPS crucially determine many biofilm properties and allow the resident bacteria to survive in challenging environments.[4,8]

E. N. Hayta, M. J. Ertelt, M. Kretschmer, O. Lieleg
Center for Protein Assemblies (CPA)
Technical University of Munich
Ernst-Otto-Fischer Straße 8, 85748 Garching, Germany
E-mail: oliver.lieleg@tum.de
E. N. Hayta, M. J. Ertelt, M. Kretschmer, O. Lieleg
Munich School of Bioengineering and Department of Mechanical Engineering
Technical University of Munich
Boltzmannstraße 15, 85748 Garching, Germany

The ORCID identification number(s) for the author(s) of this article can be found under https://doi.org/10.1002/admi.202101024.

DOI: 10.1002/admi.202101024

Biofilms can colonize a broad range of different surfaces including those of natural materials such as stones, teeth, and plant roots[9–11] as well as man-made objects including pipes, hulls, and catheters.[12–14] Yet, bacterial biofilms not only adhere well to the surface of objects they colonize; the upper surface of many biofilms is sticky as well, and this property enables biofilms to adhere to each other and to neighboring materials.[15–19]

Another central property of bacterial biofilms is their slimy consistency. In most cases, bacterial biofilms can be described as viscoelastic solids, i.e., materials that combine liquid-like and solid-like characteristics but are dominated by the latter.[8,20–26] Depending on the bacterial species, the stiffness of biofilms grown in the lab ranges from a few hundred to several kPa.[15,20,27] However, when exposed to certain metal ions, which can be part of the natural environment the biofilms grow in, those stiffness values can be increased up to 1000-fold.[15,20,21] This finding already indicates the high adaptability of this biomaterial. Even more curious is the ability of biofilms to self-heal: even after exposure to large shear forces, they are able to quickly and fully recover their initial viscoelastic properties.[20,22] Together, those properties enable biofilms to permanently settle on solid surfaces—even in the presence of shear forces.[21,28,29]

Another key property some bacterial biofilms are able to develop is the ability to efficiently repel a broad range of fluids ranging from water to oils.[30,31] With such a high wetting resistance, biofilms can withstand erosion by flowing or dripping water, and they can protect themselves from toxic substances (such as antibiotics or metal ions) dissolved in liquids.[21,31,32] Moreover, even if bacterial biofilms can be successfully wetted, they still can restrict the diffusive entry of molecules into their core.[33–35] The macromolecular network established by the bacterial EPS is mainly responsible for this effect: molecules (or particles) that bind to the EPS are prevented from reaching the bacteria—and this can limit the efficiency of antibiotics or other antibacterial substances.[21,36]

Of course, the viability and proliferation of biofilm bacteria requires the metabolic conversion of nutrients, and certain biofilms have developed a specific internal architecture to allow for their perfusion.[25,37] As a side product of their metabolic activity, a subset of biofilm bacteria liberate electrons, which originate from the chemical decomposition of organic substances;[38] and there are even conductive biofilms that are able to generate an electric current.[39]

Altogether, these properties render bacterial biofilms sturdy and unique materials. In many cases, typically in industrial or medical

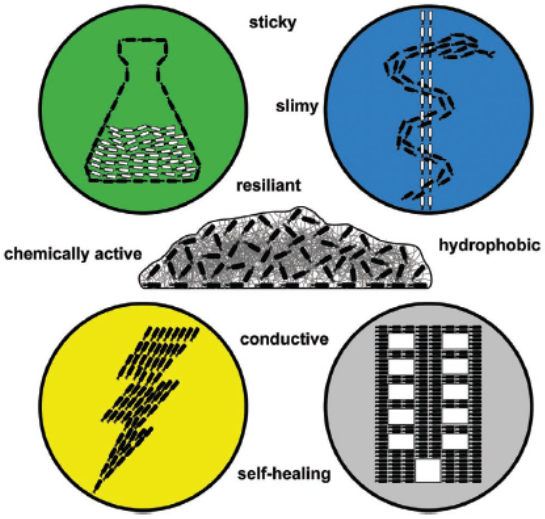

Figure 1. The multifaceted material properties of bacterial biofilms can be useful in different fields of application. Due to their unique material properties, bacterial biofilms and materials generated thereof have been tested in several areas including agriculture and (environmental) biotechnology (green), (bio)medicine (blue), electricity generation (yellow), and civil engineering (gray).

settings, biofilm growth has negative consequences for humans as the bacteria can contaminate food production processes or lead to infections.[4,40–43] With the range of properties discussed above, it is typically quite difficult to remove biofilms from the surfaces they colonize or to chemically inactivate bacteria residing within a protective biofilm matrix. However, from a material scientist's point of view, some of the unique properties of bacterial biofilms do not have to be a burden only—they also offer a variety of possibilities for applications in biotechnology, medicine, and even civil engineering (**Figure 1**). One option to make this happen is using genetic engineering tools, and there are many examples where this strategy was successfully implemented.[24,44,45] As an alternative approach, the properties of biofilms can also be modified by manipulating the composition of this biomaterial, e.g., by adding (bio)polymers, nanoparticles (NPs), small molecules, or other bacteria. In the following section, we highlight selected examples of the latter. There, either natural biofilms or artificial combinations of bacteria with microscopic objects have demonstrated high potential to serve mankind by doing exactly what they are good at: being resilient, sticky, and liquid-repellent as well as chemically converting molecules into other products.

2. Applications of Natural and Modified Biofilms in Different Fields

2.1. Biofilms for Agricultural, Environmental, and Industrial Biotechnology

Several biotechnological applications highly benefit from mankind's ability to make use of bacteria and their products. For instance, a large range of bacterial biocatalysts (enzymes or whole cells) have been developed to produce valuable molecules such as fine chemicals, pharmaceuticals, and ingredients of cosmetics.[46] In addition, bacteria themselves can be interesting products themselves, e.g., as food ingredients[47–49] or as additives to increase the sustainability of agriculture. The latter is achieved by the microorganisms acting as biocontrol agents,[50] plant-growth promoters,[51] or biofertilizers.[52] Of course, also bioremediation approaches heavily depend on microbial activity[53]—without them, wastewater treatment would be not efficient at all. In the following section, we highlight a few examples from those areas, where bacterial biofilms with dedicated properties were developed.

To obtain biofilms with tailored functionalities, synthetic biology tools can be employed, where genetic modifications on the bacterial genome are employed to change the biofilm properties.[24,45] Typically, such a strategy is based on the bacteria secreting additional (or altered) biofilm matrix components, enzymes, or other functional molecules. Alternatively, different bacterial strains can be combined with each other or with synthetic components (molecules, polymers, or nanoparticles) during biofilm cultivation (**Figure 2**). In nature, biofilms comprise multispecies microbial consortia, which follow a symbiotic life style to better adapt to the environment. Inspired by this natural collaboration, cocultivation of bacteria producing cellulose (e.g., acetic acid bacteria or acetobacteria) with other, catalytic microorganisms can result in functional, living materials with increased production efficiency. Here, the cellulose-environment generated by one bacterial strain can act as an encapsulation agent for the other strain and thus provides protection to the latter.[54,55] In another example where several additional functionalities were installed into a biofilm, the cellulose matrix secreted by the biofilm bacteria was modified by enzymes produced by yeast cells. There, engineered yeast cells were artificially integrated into the biofilm matrix by cocultivation, and this resulted in biofilms with altered mechanical properties: the biofilms were converted into viscoelastic fluids.[56]

A different strategy aims at immobilizing enzymes in biofilms to obtain an enhanced bioprocess performance such as increased activity, robustness toward alterations in pH and temperature, and reusability. For instance, Romero et al.[57] demonstrated how biofilm matrix components contribute to the immobilization of an extracellular bacterial enzyme. They showed that secreted lipase molecules are fully trapped in the biofilm matrix—there was no (undesired) loss of enzyme from the biofilm pellicle into the aqueous phase it was grown on. In the protected microenvironment of the biofilm matrix, the specific activity of this immobilized enzyme was increased, and the immobilized enzymes maintained 42% of their activity even after three catalytic cycles. Botyanszki et al.[58] achieved an immobilization of α-amylase onto the curli fibers of *Escherichia coli* biofilms; to make this possible, they used genetic tools to achieve site-specific binding to the curli fibers, and this entailed improved enzymatic activity: As a consequence of this immobilization, the pH range within which the enzyme has good activity, was increased and the biocatalyst maintained a high activity even in the presence of solvents. Such improvements and those building on them[59] may provide a big advantage in industrial applications, where organic solvents are necessary—

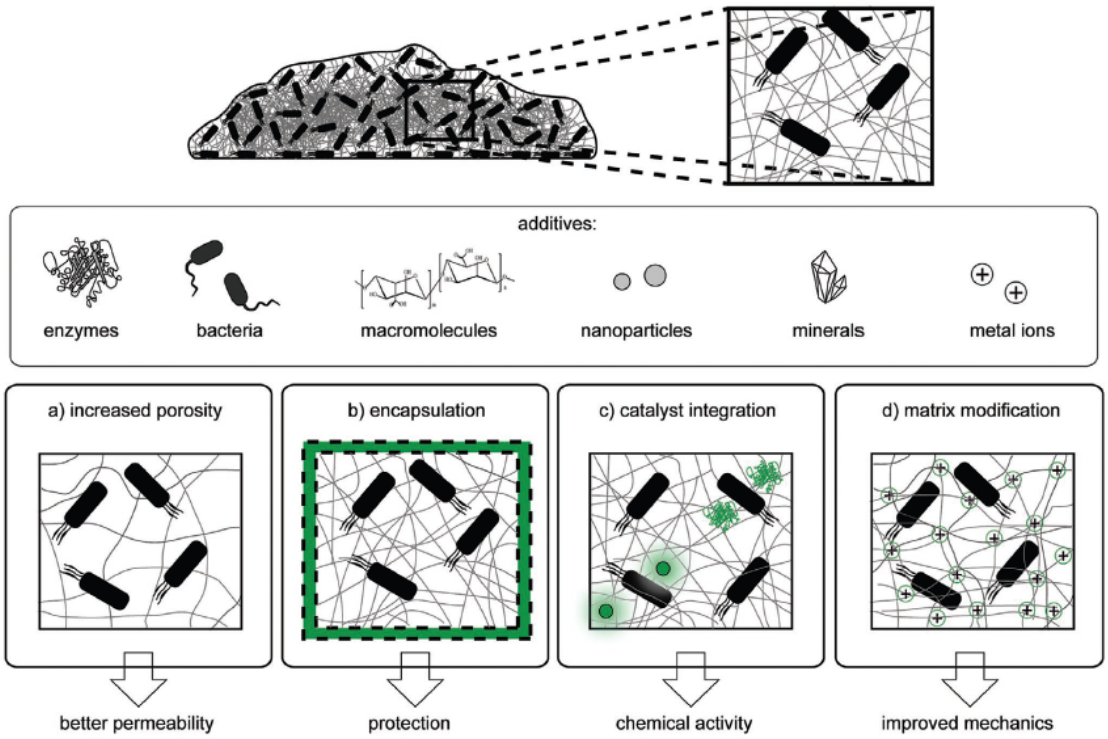

Figure 2. Strategies to obtain biofilms with improved properties. Integration of various entities such as (macro)molecules, nanoparticles, minerals, metal ions, enzymes, or other bacteria into the matrix can alter their properties such that they become better suitable for certain applications. a) For instance, increasing the porosity of the matrix improves the biofilm permeability toward nutrients and electrons, and this typically improves bacterial viability within the biofilm. b) Encapsulation of biofilms with polymers or minerals protects the bacteria from environmental stresses. c) By integrating enzymes or catalytic nanoparticles into the biofilm structure, the functionality of the biofilms can be broadened. d) Adding ionic compounds such as metal ions or extracellular DNA to the biofilm matrix induces crosslinking effects, which boosts the stiffness of the bacterial material.

thus broadening the range of possible applications. Similarly, Dong et al.[60] made use of a chemical immobilization strategy based on carbodiimide coupling to covalently link an enzyme to the EPS of a *Bacillus subtilis* biofilm matrix without reducing enzymatic activity. Moreover, in the same study, magnetic nanoparticles were added to the enzyme-enriched biofilm. The authors suggested that this second modification may help retrieving the biofilm by magnetic forces, e.g., after it has been added to a complex environment, in which it is supposed to perform its catalytic activity.

Of course, the benefit of including nanoparticles into biofilms can go beyond enabling material recovery. The antimicrobial properties of certain nanoparticles are well established, and there are many biotechnological applications where nanoparticles are combined with biofilms to harness this property.[61] In agriculture, nanoparticles have already been used quite often as biocontrol agents against plant pathogens.[62,63] Recently, Mahawar et al.[64] combined silver nanoparticles with cyanobacteria and observed improved plant growth as well as better resistance toward pathogens than when those two agents were applied individually. Timmusk et al.[65] formulated different bacterial inoculations with titanium dioxide (TiO_2) nanoparticles to improve the resilience of plants toward drought, salt, and pathogen stresses. Here, the addition of nanoparticles to the bacterial inoculates considerably amplified biofilm formation on the rhizosphere of the plant; consistently, NP-containing formulations performed better than bacterial fertilizers alone. Similarly, in a study conducted by Vishwakarma et al.,[66] combining rhizobacteria with silicon gave rise to better protection of plants against toxic effects than a rhizobacterial biofilm could provide itself.

Similar to equipping biofilms with enzymes, some nanoparticles can also convey catalytic activity to bacterial materials. For instance, Wang et al.[67] immobilized several nanomaterials in engineered *E. coli* biofilms to enable the reduction of polynitrophenol, the photocatalytic degradation of organic dyes, or photoinduced hydrogen production. In addition to establishing catalytic processes, nanoparticles can also boost the existing catalytic activity of a biofilm by enhancing existing extracellular electron transfer mechanisms. For instance, bioremediation of hexavalent chromium by *Shewanella oneidensis* biofilms formed in carbon nanotube (CNT)-enriched alginate beads was improved compared to biofilms formed without CNTs.[68] Adding quinone-based electron mediators to the CNT-enriched

biofilm materials further enhanced this effect, and the resulting bacterial material turned out to be useful for the bioremediation of uranium.[69]

For many biotechnological applications, e.g., for protein or metabolite biosynthesis, planktonic bacteria are highly suitable;[70] however, when other bacterial properties are required as part of a functional material, biofilms are typically preferred over planktonic cells.[71] To a large extent, this is due to the superior material properties of biofilms. Nevertheless, there are efforts to further improve these material properties, e.g., by incorporating functional entities (molecules, ions, minerals, or polymers) into the biofilm matrix. As one of the main components of natural biofilm matrices, extracellular DNA (eDNA) has been shown to play a crucial role in biofilm formation,[72] bacterial aggregation,[73] and adhesion;[74,75] moreover, eDNA can affect the mechanical strength and integrity of biofilms,[76–78] modulate extracellular electron transfer throughout the biofilm matrix,[79] and provide enhanced resistance against antibiotics.[80] In fact, Chaves et al.[81] suggested that tuning the viscoelastic properties and even surface topography of biofilms by controlling the amount of eDNA within the biofilm may offer opportunities in biotechnological applications—yet this still needs to be explored.

From a physicochemical point of view, interactions between eDNA and biofilm matrix components (or antibiotics) can be rationalized by electrostatic forces acting between the strongly anionic eDNA molecules and cationic groups from biofilm constituents.[82,83] Another strategy to alter the interactions between certain biofilm matrix components makes use of ionic crosslinks, which can be generated by incorporating cationic metal ions into the biofilm material.[20,21,84] Kretschmer and Lieleg[22] showed that the size and valency of the ions in combination with the molecular configuration of anionic residues on the biofilm matrix polymers dictates if and how strongly the stiffness of the biofilm is increased by this approach. The ability to boost the biofilm stiffness may open the door for novel applications: for instance, by adding Fe^{3+} ions to the biofilm matrix, Zhang et al.[85] could increase the internal mechanical strength of biofilms, which were genetically engineered to become highly sticky. With such a "living glue," surface damage could be successfully repaired. A similar self-healing activity accompanied by a strong anticorrosion protection was observed by Liu et al.[86] when they enriched a culture of cellulose-overproducing bacteria with Ca^{2+}. Here, calcite ($CaCO_3$) formation within the cellulose-rich biofilm provided improved stability of biofilm coatings. The authors suggested that such anticorrosive biocoatings could be useful tools to increase the life time of metallic objects in marine environments. A (reversibly) increased biofilm stiffness as achieved by the addition of metal ions can also result in enhanced erosion resistance[21,29]—and such a property can be a desirable feature for biotechnological applications. A similar result was obtained by Hayta and Lieleg;[28] yet, there, bacteria were allowed to establish a biofilm matrix in the presence of purified biopolymers. As a consequence, not the shear stiffness of the biofilm but its surface topography and thus its mode of interaction with water was modulated such that the stability of the biofilm toward erosion was enhanced.

Embedding bacteria with polymers is a strategy not only used by naturally occurring biofilms—the same can be achieved artificially. In fact, the effects of embedding bacteria into purified biopolymers present in the matrix of certain biofilms (such as alginate and cellulose) has already been extensively studied—both, with the goal to investigate the bacterial behavior in different polymeric matrixes[87,88] and to create more robust bacterial catalysts for biotechnological applications.[89–91] Recently, novel encapsulation techniques have been introduced to keep up with the latest developments in biotechnology. For instance, in a study conducted by Jaroch et al.,[92] in situ encapsulation of mature biofilms was achieved, and the biofilms were grown on a hollow fiber membrane. As a result, the encapsulated biofilm could better resist the shear forces it was exposed to in a bioreactor. Importantly, this covering layer was permeable to air and nutrients, which guaranteed good cell viability. A different approach was followed by Panchal et al.,[93] who filled liquid marbles generated from halloysite nanotubes with a bacterial culture. Here, the bacterial EPS produced inside the liquid marbles enhanced the mechanical strength of the spheres and stabilized their shape and volume by preventing evaporation. With these improvements, the encapsulated bacteria could be stored at room temperature for more than a week. Interestingly, a similar approach could be applied to nonbiofilm forming bacteria when the spheres were artificially enriched with polymers. A new, bioinspired method based on the self-assembly process of chitosan macromolecules was introduced by Park et al.[94] Here, tyrosinase-producing bacteria modified the chitosan biopolymers such that they bound to the bacteria and formed a network around them. Artificial biofilms produced this way showed better cell loading capacity and cellular viability than those obtained via conventional encapsulation strategies. Also here, an application has already been identified: The authors showed that these synthetic biofilms can be employed in the bioremediation of crude oil: within 28 days, they could remove ≈90% of oil from contaminated water.

Overall, those examples clearly highlight that, with further improvements in terms of production time, stability and recoverability, artificial biofilms have the potential to contribute to many other areas of biotechnology in the future.

2.2. Biofilms for Medical Applications

One of the natural habitats of bacterial biofilms is the gastrointestinal tract (GIT).[95] In fact, in humans, there are approximately ten times more procaryotic cells than eucaryotic ones. Commensal bacteria are not only crucial for regulating our metabolism and immune system, they can also protect us against pathogens. Hence, avoiding (and, if necessary, curing) GIT dysbiosis is increasingly considered as a therapeutic approach to deal with GIT disorders. To maintain or regain a balanced microflora in the GIT, diet regulation, antibiotic treatment, and consumption of prebiotics or probiotics may be needed.[96] The latter are living microorganisms which, when administered in adequate amounts, confer a health benefit to the host. More specifically, consumption of probiotics aims at regulating the gut microbiota by manipulating interspecies interactions.[97]

During the industrial production process that is required to turn bacteria into food products suitable for oral consumption,

the probiotics are exposed to harsh conditions such as heat or cold; after production is completed, the prolonged storage, e.g., in fridges or cooling cabinets (4 °C), is not ideal for the bacteria either. In addition, until they reach the desired area (i.e., the intestines), probiotics pass through the extreme environment of the stomach—yet they need to be viable in large numbers when arriving in the gut where they are supposed to take effect. Thus, those beneficial bacteria require protection. Microencapsulation of probiotic bacteria is a well-established method to produce functional probiotic food products,[98] and several biopolymers or smaller molecules (such as milk proteins) have been employed to achieve this.[97,99] However, also the natural shield produced by the bacteria, i.e., the EPS, can provide the required protection: biofilm-embedded bacteria exhibit better resistance against extreme conditions and trigger a better immune response in the host.[100,101]

Even though probiotics in biofilm form come with a range of advantages compared to their planktonic counterparts, they can still be further improved. For instance, Cheow and Hadinoto[102] encapsulated *Lactobacillus rhamnosus* bacteria into double-layered, chitosan-coated alginate or carrageenan polymeric beads and then further incubated these microcapsules to enable the formation of biofilms in their core. As expected, those shielded biofilms process showed superior freeze-drying resistance and thermotolerance. Moreover, bacterial release into the intestinal mucosa was higher for such encapsulated biofilms. In 2014, the same group of researchers improved their probiotic delivery system by adding locust bean gum to their chitosan-coated alginate formulation, which boosted the resilience of the probiotic.[103] Similarly, biofilm loaded calcium pectinate beads produced by Heumann et al.[104] lead to sturdier probiotics; from those biofilm-spheres, the bacteria were released to the colon as clusters which provided a better anti-inflammatory effect and protection against GIT disorders than other probiotic forms of this bacterial strain. A better release of biofilm bacteria was also achieved by Vega-Sagardía et al.,[105] who enriched their formulation with vegetal oil to increase the residence time of the probiotic biofilm in the stomach so that a *Helicobacter pylori* infection could be efficiently dealt with. A different approach proposed by Praveschotinunt et al.[106] aimed at enriching a probiotic biofilm with a therapeutic peptide to promote epithelial restitution. By introducing these modified biofilms, the authors were able to achieve mucosal healing and immunomodulation in vivo.

In addition to enriching the biofilm matrix, also fine-tuning the growth conditions of biofilms can render probiotics more resilient. For instance, Kiew et al.[107] examined the effect of biofilm age and growth medium affect the stress-resistance of biofilms. Moreover, also adjusting the detailed production process of encapsulated biofilms[108] and cocultivation with a second bacterial strain, e.g., combining lactic acid bacteria with *B. subtilis*[109] can improve the resilience of the probiotic. In the latter example, the EPS produced by *B. subtilis* is mainly responsible for the obtained protection effect. Importantly, the presence of this second bacterial strain comes with another advantage: in addition to their ability to secrete exopolymeric substances, *B. subtilis* bacteria have recently been reported to be able to help maintaining the balance of the GIT microbiota.[110,111] Another promising usage of biofilms in the GIT was described by Duraj-Thatte et al.[112] Here, a robust, self-regenerative hydrogel containing living bacteria was developed that showed an increased retention time in the GIT in vivo. Expression of mucin binding proteins by genetic modifications resulted in specific and strong adhesion of the bacteria-loaded hydrogels to the GIT tissue. Furthermore, the viscoelastic properties of this bacterial hydrogel could be adjusted by varying the type of mucoadhesive protein and the DNA content of the gel, and the authors suggested that such a system has the potential to serve as a drug delivery system.

However, the benefits of bacterial biofilms for our health are not limited to regulating the gut flora. Bacterial pellicles generated by certain bacteria belonging to the genera *Agrobacterium*, *Acetobacter*, *Pseudomonas*, *Rhizobium*, *Azotobacter*, *Alcaligenes*, *Achromobacter*, and *Sarcina* comprise almost exclusively bacterial cellulose (BC), and those have applications in biomedicine—with the bacteria being inactivated and washed out.[113,114] Owing to their high biocompatibility, water uptake capacity, permeability to gases and liquids, and desirable mechanical properties such as high tensile strength and flexibility, those BC materials have turned out to be good candidates for drug delivery systems[115] and wound treatment.[116,117] In addition, the structural similarity of BC-biofilms and human collagenous extracellular matrix enables the use of the former as tissue scaffolds.[118] Also here, the chemical and physical properties of BC-based materials can be further improved by incorporating polymers, nanoparticles, minerals, or functional molecules.[113,119,120]

More recently, engineered living materials have been introduced. Here, genetic engineering tools are combined with material science approaches to create novel materials for medical applications. For instance, Wang et al.[121] employed light-inducible biomineralization of hydroxyapatite to repair site-specific damages: *E. coli* biofilms expressing adhesins act as a glue that connects polystyrene microspheres thus creating a biohybrid filler material that autonomously solidifies via mineralization processes. Possible future applications of this technique could be in the field of bone regeneration. A similar *E. coli* biofilm producing adhesive molecules (adhesin and DOPA) was used by An et al.[122] to fight blood-leakage. In the lab, this already works: using a microfluidic setup mimicking a (slightly) bleeding blood vessel, it was shown that this living glue can autonomously repair small damages, and this is triggered by exposing the bacteria to the molecule heme. Although those examples still need to be developed further to be applicable in vivo, they present innovative new concepts of how bacterial biofilms could serve as promising tools for medical problems.

2.3. Biofilms with Enhanced Electrochemical Activity

Already in 1911, Potter could demonstrate that the decomposition of organic substances by bacteria or fungi can generate an electrical current.[38] However, this finding did not receive much attention until it was realized how the microbes make use of electron mediators in such a biological, electrogenic system:[123,124] Exoelectrogenic bacteria can transfer electrons directly to each other or to the surface of electrodes, and they

achieve this by employing outer membrane cytochromes, excreted mediators (i.e., electron shuttles) or biological "nanowires" (i.e., conductive pili).[39,123] Recent improvements in the electron transfer capability of microbial communities promoted the development of applications making use of them. Examples of such bioelectrochemical systems (BESs) include microbial fuel cells (MFCs),[124,125] microbial electrolysis cells (MECs),[126,127] biological photovoltaics (BPVs),[128,129] microbial desalination cells (MDCs),[130,131] microbial electrosynthesis (ME),[126,132,133] and microbial electrochemical biosensors (MEBs).[134]

In BESs, a diverse range of microorganisms (typically, those are bacteria; however, there are also examples where algae or fungi are used) can be employed—both as isolated strains and mixed cultures,[135] and either in form of planktonic cells[136] or as biofilms.[137] One of the major factors hindering the practical application of BESs is the low electron transfer efficiency at the electrode. To overcome this issue, biofilms can be a convenient solution as they come with the advantage that they can grow directly on the electrode surface; moreover, in protective biofilm matrix, the bacteria are well connected to each other, which facilitates the electron transfer process from one bacterium to another. However, when this biofilm matrix becomes too thick, it may become an obstacle that limits the diffusive transport of nutrients and electrons.[138] Hence, there is still a need to maximize the transport properties within biofilms as well as the electron transfer efficiency at the biofilm–electrode interface.

To improve the electron transfer process to electrodes, researchers have pursued several approaches, and they can be divided into two groups: the first strategy is based on a manipulation of biofilm growth to increase both, biofilm formation and the electroactivity of the biofilm bacteria. The latter is typically achieved by creating more options to transfer electrons from donors to acceptors. One option to achieve this is to increase the number of extracellular electron carriers (cytochromes, flavin- or quinone-based mediators, or conductive pili) by means genetic engineering.[44,139] Of course, maximizing the number of microbial cells producing these carriers, e.g., by nutrient optimization, has a similar effect.[139,140] An alternative approach aims at manufacturing electrodes with enhanced conductivity of with larger surface areas. Here, lots of effort has been made to investigate various electrode materials and surface treatments.[123,141]

The second strategy aims at improving extracellular electron transfer through the BESs by integrating artificial components into either the liquid part of the BES (containing planktonic bacteria) or into the biofilm matrix—and the latter is typically achieved by growing the biofilms in the presence of those artificial objects. The first steps taken in this area were based on the addition of soluble electron mediators to the bacterial culture during microbial growth. Flavin and quinone containing compounds such as riboflavin, Neutral Red, Brilliant Blue, Methyl Violegene, and humic acid have been approved as electron mediators for indirect electron transfer purposes.[124,142–145] Wu et al.[146] have studied the performance of a BES making use of a *S. oneidensis* strain in combination with five different mediators. They observed that, after 4 days of incubation, the current generated by the mediator-enriched samples was 20–60 times higher than the one generated in the control sample. Furthermore, they showed that it was indeed the biofilm formed on the anode in combination with the artificially supplied electron mediators that was responsible for the obtained effect—and that the contribution of planktonic cells was weak. Moreover, in this particular setting, supplying the mediators did not only promote the electron shuttling process, but also enhanced biofilm formation by a factor of >15. Arinda et al.[147] added riboflavin-functionalized magnetic beads to biofilms to enable recovery and reusage of the mediators. However, the effect of riboflavin on biofilm formation and current generation was weaker than when it was added in its free, unbound form.

In addition to electron mediators, several polymers have been employed to improve the performance of a BES, and examples include both, biological and synthetic polymers.[79,148–152] In a recent study, Zhang et al.[153] mixed a bacterial culture of *S. oneidensis* with the conductive polymer PMNT (poly(3-(3′-*N*,*N*,*N*-triethyloamino-1′-propyloxy)-4methyl2,5-thiophene hydrochloride)). There, a combination of electrostatic and hydrophobic interactions between PMNT and *S. oneidensis* cells was suggested to help the bacteria transfer electrons between each other and to the electrodes. This enhanced bidirectional electron transfer throughout the biofilm was also suggested to help obtaining thicker biofilm layers with improved bacterial viability (even within the inner layers of biofilm); probably, this was made possible by boosting the metabolic activity of bacteria, which—otherwise—would be limited by diffusion. An additional advantage brought about by this PMNT enrichment was that the lifetime of the biofilm electrodes was prolonged from 100 to 250 h. Another example of how polymer incorporation improves the functionality of a BES was described by Du et al.[154] Here, the researchers could produce a robust BES by encapsulating a mature biofilm with polydopamine (PDA): even at strongly acidic conditions, this PDA-coated bioelectrode contained a very high density of viable cells—and in such extreme environments, unprotected bacteria would die.

Similar to conductive polymers, also carbon-based materials have been used—either as electrode materials or as components for artificial biofilms. Due to their chemical stability, high conductivity, high specific surface area, and good biocompatibility, graphene and CNTs have been widely used in BESs.[155] By growing bacteria on graphene oxide (GO) nanosheets in situ, Yong et al.[156] produced an *S. oneidensis* biofilm with an increased pore size of 10–200 µm. Yuan et al.[157] showed that that such a GO-enriched biofilm with increased porosity not only exhibits improved transport of nutrients but also enhanced kinetics of electrochemical activity. An application of such GO-enriched biofilms was demonstrated by Song et al.:[158] here, within 48 h, these semiartificial biofilms could remove all Cr(IV) from wastewater; the control sample was only half as efficient. Carbon-based additives to electrode biofilms resulted in similar results.[155] Also here, wastewater treatment benefitted from those engineered biofilms as they allowed for rapidly determining the biological oxygen demand (BOD).[159] Of course, there also combined approaches where both, graphene-type and carbon-type objects were added to enhance the properties of the enriched biofilm.[160–162] Finally, using similar strategies as described above, it is even possible to create a conductive biofilm from nonexoelectrogenic bacteria.[149,163–165] This demonstrates the great potential that combining microbes with artificial objects holds.

2.4. Bacterial Construction Materials

Creating more sustainable building materials is one of the major goals in the field of civil engineering;[166] especially alternatives for cementitious construction materials are needed to reduce the CO_2 emission originating from the production of cement.[167] Interestingly, bacteria and bacterial products can also help here.[168,169] Even though the chemical conditions inside cementitious materials (such as the high pH levels occurring during the hydration reaction and the lack of nutrients) are not ideal for promoting bacterial growth, innovative concepts have been introduced that improve the functionality of construction materials by using bacterial additives (**Figure 3**).

One reason why biobased admixtures derived from bacterial sources have attracted lots of interest is their ability to replace commonly used, partially noxious or even toxic additives; at the same time, those biological additives can often be produced such that their environmental impact is comparably low. Prominent examples for such bacterial products are biopolymers generated by bacterial fermentation: examples include welan gum[170–172] or xanthan gum,[173–175] both of which are used as viscosity modifying agents in concrete.[176,177] Similar effects were obtained with other bacterial additives, such as extracellular polysaccharides,[178] bacterial cell walls,[179] whole prokaryotic cells,[180,181] or bacterial biofilms.[182] This is important as the viscosity determines the workability of the uncured construction material—and this parameter often needs to be adjusted to meet the requirements of different applications.

In the literature, the viscosity-increasing effect of bacterial additives was attributed to a combination of different mechanisms:[183] First, water molecules can be bound by the additives via hydrogen bonds, and this can increase the viscosity of the hybrid material. Second, long polysaccharide chains present in the bacterial additives can, in combination with water, create a gel-like structure, and this boosts the viscosity. Third, bacterial additives are often charged; different anionic motifs from a polymer chain can interact with several positively charged cement particles, leading to bridging flocculation, and also this effect can tune the viscosity of the material.

In addition to modifying the viscosity of cementitious materials, a second important effect brought about by bacterial additives aims at improving the properties of the cured material. For a variety of different bacterial additives, e.g., bacterial cell walls,[184] and bacterial solutions,[185,186] such an improvement of the mechanical competence of the final, cured material has been reported.[187–189] Moreover, bacterial additives can enhance the corrosion resistance of load-bearing steel elements in reinforced concrete[190–192]—and this increases the durability and

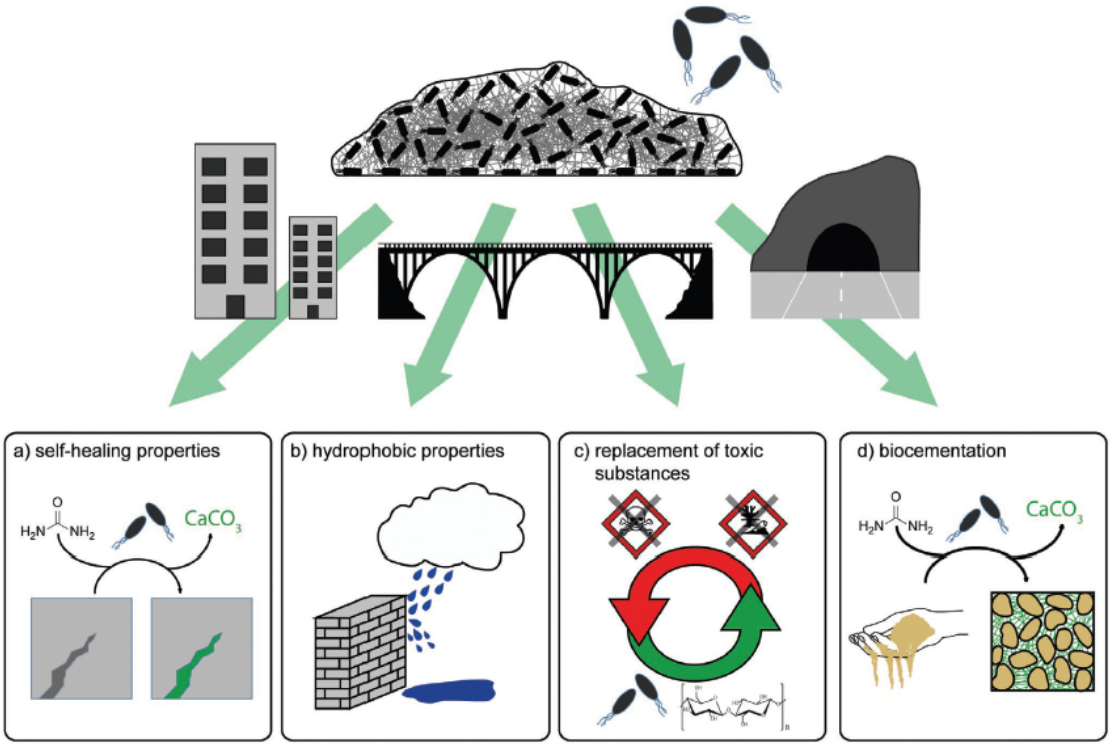

Figure 3. Benefits obtained by using bacterial additives in construction materials. Bacterial additives such as bacterial suspensions, spores, secreted macromolecules or cell fragments, as well as whole biofilms have been shown to improve the functionality of cementitious materials. For instance, a) self-healing of microcracks and b) water repellency was achieved. Moreover, c) by replacing toxic chemicals with bacterial ingredients and d) by enabling biocementation processes, more sustainable construction materials were developed.

thus lifetime of objects making use of this class of building materials, e.g., bridge pillars, walls in high rise buildings, and tunnel constructions.

The microscopic mechanisms responsible for these properties can be as follows: as the porosity and the strength of cementitious materials are related,[193] strength improvement is often achieved by calcite precipitation, which reduces the porosity. In addition, precipitated calcite can act as a diffusion barrier and therefore protect steel elements in concrete from corrosion, and reduced rates of oxygen ingress can contribute to a higher corrosion resistance as well.[194]

Corrosion of steel elements in concrete is driven by the ingress of chloride and sulfate ions into the bulk of the material—and this is made possible by invading water transporting the ions. The latter can occur via rain or water splashes, or it can originate from capillary water uprise when cementitious structures are erected in moist environments. Importantly, also in this context, bacterial additives have turned out to be extremely helpful: both, the external wetting resistance of mortar and the suppression of the capillary water uptake into the material can be enhanced using fresh[195,196] or freeze-dried bacterial biofilm,[197] bacterial solutions,[197] or bacterial spores.[198]

In those cases, it was suggested that a modification of the microstructure of the mortar material is responsible for the increased water resistance: increased roughness features on the inner and outer surface of the mortar as well as alterations in the density of the material were observed when bacterial additives were used. Yet, it remains to be shown which particular microarchitecture of bacterial hybrid mortar provides the overall optimal set of material properties—and how this ideal microstructure can be achieved.

Increasing the service life of cementitious structures is certainly a great step toward more sustainable building concepts. Yet, emerging trends from this field aim at developing cement-free building materials to completely erase the greenhouse gas emission caused by the cement production. Here, alternative binders, e.g., alkali activated slag, may offer a possible option.[199] One limitation of this approach is the considerable material shrinkage triggered by alkali activation as well as insufficient containment of moisture in the material volume. Again, by using bacterial biofilm as an additive, those two issues could be successfully addressed.[200]

Whereas, in the examples discussed above, a modification of the material properties was directly achieved by the addition of bacteria or bacterial products, a second strategy employed in the area of civil engineering aims at exploiting the unique ability of bacteria to take part in, control, or initiate biomineralization processes.[201] Indeed, also this approach has led to many new developments toward the creation of more sustainable building materials,[202] and most of them make use of microbial-induced calcite precipitation. One prominent example from this area is the concept of self-healing cementitious materials.[203–205] In this approach, bacterial spores are added to the bulk of concrete. Due to their unique structure, bacterial spores can withstand harsh conditions without losing their viability.[206,207] Instead, they remain dormant without any perceivable metabolic activity until they are reactivated by contact with moisture and oxygen. The latter is made possible when cracks have formed in the material through which water and air can enter. In other words, damage to the material serves as a "wake-up call" which then triggers autonomous repair: The metabolic activity of the reactivated bacteria induces calcite precipitation,[201] and this, in turn, can seal microcracks (in the range of 0.46 mm).[208] For such self-healing concrete, different types of bacteria have been identified,[209] and they utilize different precipitation mechanisms[210] to achieve this effect.

Bacterial precipitation is also the basis for the patented concept of "biocementation."[211,212] Here, instead of sealing cracks in the cured construction material, bacteria are employed to produce calcium carbonate, and this mineral can solidify sand or other gravel particles without the need of a binding agent.[213] The properties of such "bacterial soil" depend on several factors including the concentration of added bacteria and urea, and the grain size distribution.[214,215] However, real-life applications of this idea have not been tested yet. Along the same lines—yet taking this idea one step further—the concept of "living building materials" is discussed by Heveran et al.[216] As the name already suggests, microorganisms inside such a material remain viable and thus can react to alterations in environmental conditions such as temperature and humidity by switching on (or off) material growth.

For such a novel class of living buildings, it was even suggested that—once the end of the service life of the building is reached—the material can be largely recycled. Whether or not this is really possible, future research will have to show. Overall, the results we highlight above clearly demonstrate the great potential innovative bacterial materials hold for developing a novel, more sustainable class of construction materials with improved properties.

3. Outlook

Bacterial biofilms have the potential to be so much more than just a nuisance. The examples we highlight here stem from selected areas of bioprocess, biomedical, agricultural, environmental, electrical, and civil engineering and demonstrate how different material properties of biofilms can be used to generate objects with tailored functionalities. Together with fundamental insights into how those material properties can be further boosted or modified, a broad range of applications have already been identified that make use of bacterial materials. With the current improvements in additive manufacturing techniques,[217–219] our ability to control the composition, architecture and shape of objects is improving day by day.

Indeed, there are already a few recent examples where such advanced manufacturing methods have been applied to create bacterial materials.[220–222] For the purpose of wastewater treatment, an artificial biofilm was printed into a grid-like structure to obtain an object with a very high surface area. As a bacterial strain for this particular application, *Pseudomonas putida* was selected, which is capable of degrading phenol and converting it into biomass.[223] As an example of a medical application, we would like to highlight 3D-printed *Acetobacter xylinum* bacteria, which—once embedded into a hydrogel matrix—produced cellulose.[223] Once enough cellulose was secreted, the bacteria and the hydrogel were removed by washing leaving a cellulose

scaffold in a predefined shape as realized by the printing process. Such cellulose scaffolds were suggested to support the wound healing process—especially in areas having complex shapes such as the face. Also in electrical engineering, 3D-printing of bacterial structures has been attempted and living anodes for microbial fuel cells were produced. With this technique, bioelectrodes could be fabricated with a high level of control in terms of geometry and porosity.[224] A different approach was realized by Moser et al.,[225] who used light signals to pattern *E. coli* on solid surfaces to induce the biofilm formation in a desired shape.

To arrange any printable material into a dedicated 3D shape, the viscoelastic properties of the "ink" need to be just right—and the same holds true when attempting to print biofilms. During printing, the biofilm needs to have the properties of a liquid; yet afterward, it has to stay in place and maintain its shape which requires elastic properties. Owing to their viscoelasticity and stickiness in combination with their self-healing abilities, "naturally grown" bacterial biofilms meet these requirements. However, when specific functions are desired, artificial biofilms are preferred and a viscoelastic matrix (typically a hydrogel comprising either alginate, hyaluronic acid, carrageenan, or fumed silica) is loaded with the bacteria of choice[223,226] or the expression of bacterial EPS is manipulated.[227] Here, the artificial biofilm matrix not only needs to provide the required mechanical stability but has also to ensure bacterial survival and metabolic activity. Duraj-Thatte et al.[228] used a nanofiber gel produced by bacteria as a matrix for 3D-printing. Then, the original bacteria were removed from the gel by washing and replaced with different bacterial cells and selected additives.

In addition to 3D-printing, several other methods have been reported to control the structure of cellulose-based biofilms and to create complex shapes. For instance, biofilm spheres could be produced by adding PTFE nanoparticles,[229] by employing microfluidics methods using alginate–agarose as a shell structure,[230] or by making use of water-in-oil emulsions.[231–233] With this range of methods, spherical biofilms with tunable sizes can be produced which might be useful for encapsulation purposes in food engineering and biomedical applications.

At this point, material science, microbiology, and manufacturing science meet and open up a plethora of new avenues that still need to be explored. Considering the huge variety of bacterial species and our growing ability to control the properties of bacterial biofilms, many new and exciting developments are possible in this area.

Acknowledgements

The authors acknowledge funding by the Deutsche Forschungsgemeinschaft (DFG, German Research Foundation) -SFB 863, Projekt B11 - 111166240. In addition, E.N.H. thankfully acknowledges a fellowship granted by the Turkish Ministry of Education.

Open access funding enabled and organized by Projekt DEAL.

Conflict of Interest

The authors declare no conflict of interest.

Keywords

bacterial additives in construction materials, bacterial biofilms, biofilms for medical applications, biofilms in agriculture, biofilms with electrochemical activity

Received: June 18, 2021
Revised: July 30, 2021
Published online: October 10, 2021

[1] H. Vlamakis, Y. Chai, P. Beauregard, R. Losick, R. Kolter, *Nat. Rev. Microbiol.* **2013**, *11*, 157.
[2] S. S. Branda, Å. Vik, L. Friedman, R. Kolter, *Trends Microbiol.* **2005**, *13*, 20.
[3] K. Sauer, A. H. Rickard, D. G. Davies, *Microbe* **2007**, *2*, 347.
[4] L. Hall-Stoodley, J. W. Costerton, P. Stoodley, *Nat. Rev. Microbiol.* **2004**, *2*, 95.
[5] Z. Xue, V. R. Sendamangalam, C. L. Gruden, Y. Seo, *Environ. Sci. Technol.* **2012**, *46*, 13212.
[6] T. Li, R. Bai, J. Liu, *J. Biotechnol.* **2008**, *135*, 52.
[7] M. Tallawi, M. Opitz, O. Lieleg, *Biomater. Sci.* **2017**, *5*, 887.
[8] H. C. Flemming, J. Wingender, *Nat. Rev. Microbiol.* **2010**, *8*, 623.
[9] R. C. Thompson, P. S. Moschella, S. R. Jenkins, T. A. Norton, S. J. Hawkins, *Mar. Ecol.: Prog. Ser.* **2005**, *296*, 53.
[10] J. F. Siqueira, I. N. Rôças, D. Ricucci, *Endod. Top.* **2012**, *22*, 33.
[11] A. Pandit, A. Adholeya, D. Cahill, L. Brau, M. Kochar, *J. Appl. Microbiol.* **2020**, *129*, 199.
[12] J. Yu, D. Kim, T. Lee, *Water Sci. Technol.* **2010**, *61*, 163.
[13] M. Salta, J. A. Wharton, Y. Blache, K. R. Stokes, J. F. Briand, *Environ. Microbiol.* **2013**, *15*, 2879.
[14] M. Gominet, F. Compain, C. Beloin, D. Lebeaux, *APMIS* **2017**, *125*, 365.
[15] M. Kretschmer, C. A. Schüßler, O. Lieleg, *Adv. Mater. Interfaces* **2021**, *8*, 2001658.
[16] J. Yan, A. Moreau, S. Khodaparast, A. Perazzo, J. Feng, C. Fei, S. Mao, S. Mukherjee, A. Košmrlj, N. S. Wingreen, B. L. Bassler, H. A. Stone, *Adv. Mater.* **2018**, *30*, 1804153.
[17] M. J. Chen, Z. Zhang, T. R. Bott, *Biotechnol. Tech.* **1998**, *12*, 875.
[18] W. M. Dunne, *Clin. Microbiol. Rev.* **2002**, *15*, 155.
[19] T. R. Garrett, M. Bhakoo, Z. Zhang, *Prog. Nat. Sci.* **2008**, *18*, 1049.
[20] K. Lieleg, O. Caldara, M. Baumgärtel, R. Ribbeck, *Soft Matter* **2011**, *7*, 3307.
[21] S. Grumbein, M. Opitz, O. Lieleg, *Metallomics* **2014**, *6*, 1441.
[22] M. Kretschmer, O. Lieleg, *Biomater. Sci.* **2020**, *8*, 1923.
[23] L. Pavlovsky, J. G. Younger, M. J. Solomon, *Soft Matter* **2013**, *9*, 122.
[24] S. G. V. Charlton, M. A. White, S. Jana, L. E. Eland, P. G. Jayathilake, J. G. Burgess, J. Chen, A. Wipat, T. P. Curtis, *J. Bacteriol.* **2019**, *201*, 00101.
[25] J. N. Wilking, T. E. Angelini, A. Seminara, M. P. Brenner, D. A. Weitz, *MRS Bull.* **2011**, *36*, 385.
[26] E. S. Gloag, G. K. German, P. Stoodley, D. J. Wozniak, *Sci. Rep.* **2018**, *8*, 9691.
[27] Y. Shen, P. C. Huang, C. Huang, P. Sun, G. L. Monroy, W. Wu, J. Lin, R. M. Espinosa-Marzal, S. A. Boppart, W. T. Liu, T. H. Nguyen, *npj Biofilms Microbiomes* **2018**, *4*, 15.
[28] E. N. Hayta, O. Lieleg, *Biomater. Sci.* **2019**, *7*, 4675.
[29] M. Klotz, M. Kretschmer, A. Goetz, S. Ezendam, O. Lieleg, M. Opitz, *RSC Adv.* **2019**, *9*, 11521.
[30] A. K. Epstein, B. Pokroy, A. Seminara, J. Aizenberg, *Proc. Natl. Acad. Sci. USA* **2011**, *108*, 995.
[31] C. Falcón García, F. Stangl, A. Götz, W. Zhao, S. A. Sieber, M. Opitz, O. Lieleg, *Biomater. Sci.* **2019**, *7*, 220.
[32] C. Falcón García, M. Kretschmer, C. N. Lozano-Andrade, M. Schönleitner, A. Dragoš, Á. T. Kovács, O. Lieleg, *npj Biofilms Microbiomes* **2020**, *6*, 1.

[33] S. Singh, S. K. Singh, I. Chowdhury, R. Singh, *Open Microbiol. J.* **2017**, *11*, 53.
[34] P. S. Stewart, *Int. J. Med. Microbiol.* **2002**, *292*, 107.
[35] W. W. Nichols, *Rev. Med. Microbiol.* **1991**, *2*, 177.
[36] M. Marguerettaz, G. Dieppois, Y. A. Que, V. Ducret, S. Zuchuat, K. Perron, *Microb. Pathog.* **2014**, *77*, 36.
[37] J. D. Seymour, S. L. Codd, E. L. Gjersing, P. S. Stewart, *J. Magn. Reson.* **2004**, *167*, 322.
[38] M. C. Potter, *Proc. R. Soc. London, Ser. B* **1911**, *84*, 260.
[39] B. E. Logan, *Nat. Rev. Microbiol.* **2009**, *7*, 375.
[40] J. D. Brooks, S. H. Flint, *Int. J. Food Sci. Technol.* **2008**, *43*, 2163.
[41] C. G. Kumar, S. K. Anand, *Int. J. Food Microbiol.* **1998**, *42*, 9.
[42] S. Galié, C. García-Gutiérrez, E. M. Miguélez, C. J. Villar, F. Lombó, *Front. Microbiol.* **2018**, *9*, 898.
[43] J. W. Costerton, P. S. Stewart, E. P. Greenberg, *Science* **1999**, *284*, 1318.
[44] M. J. Angelaalincy, R. Navanietha Krishnaraj, G. Shakambari, B. Ashokkumar, S. Kathiresan, P. Varalakshmi, *Front. Energy Res.* **2018**, *6*, 63.
[45] Y. Hu, M. Mukherjee, B. Cao, *ACS Symp. Ser.* **2019**, *1323*, 59.
[46] S. Heux, I. Meynial-Salles, M. J. O'Donohue, C. Dumon, *Biotechnol. Adv.* **2015**, *33*, 1653.
[47] E. Dimidi, S. Cox, M. Rossi, K. Whelan, *Nutrients* **2019**, *11*, 1806.
[48] G. Campbell-Platt, *Food Res. Int.* **1994**, *27*, 253.
[49] M. N. Hasan, M. Z. Sultan, M. Mar-E-Um, *J. Sci. Res.* **2014**, *6*, 373.
[50] M. Morikawa, *J. Biosci. Bioeng.* **2006**, *101*, 1.
[51] R. Bhatia, D. Gulati, G. Sethi, *Folia Microbiol.* **2021**, *66*, 159.
[52] T. Parween, P. Bhandari, Z. H. Siddiqui, S. Jan, T. Fatma, P. K. Patanjali, in *Mycoremediation and Environmental Sustainability*, Vol. *1* (Eds: R. Prasad), Springer, Cham, Switzerland **2017**, Ch. 3.
[53] R. Singh, D. Paul, R. K. Jain, *Trends Microbiol.* **2006**, *14*, 389.
[54] A. A. K. Das, J. Bovill, M. Ayesh, S. D. Stoyanov, V. N. Paunov, *J. Mater. Chem. B* **2016**, *4*, 3685.
[55] D. P. Birnbaum, A. Manjula-Basavanna, A. Kan, B. L. Tardy, N. S. Joshi, *Adv. Sci.* **2020**, *8*, 2004699.
[56] C. Gilbert, T. C. Tang, W. Ott, B. A. Dorr, W. M. Shaw, G. L. Sun, T. K. Lu, T. Ellis, *Nat. Mater.* **2021**, *20*, 691.
[57] C. M. Romero, P. V. Martorell, A. G. López, C. G. N. Peñalver, S. Chaves, M. Mechetti, *Colloids Surf., B* **2018**, *162*, 246.
[58] Z. Botyanszki, P. K. R. Tay, P. Q. Nguyen, M. G. Nussbaumer, N. S. Joshi, *Biotechnol. Bioeng.* **2015**, *112*, 2016.
[59] M. G. Nussbaumer, P. Q. Nguyen, P. K. R. Tay, A. Naydich, E. Hysi, Z. Botyanszki, N. S. Joshi, *ChemCatChem* **2017**, *9*, 4328.
[60] H. Dong, W. Zhang, Y. Wang, D. Liu, P. Wang, *J. Agric. Food Chem.* **2020**, *68*, 1373.
[61] C. K. Ng, A. Mohanty, B. Cao, in *Bio-Nanoparticles: Biosynthesis and Sustainable Biotechnological Implications* (Ed: O. V. Singh), John Wiley & Sons Inc., Hoboken, NJ **2015**, pp. 83–99.
[62] J. M. Rajwade, R. G. Chikte, K. M. Paknikar, *Appl. Microbiol. Biotechnol.* **2020**, *104*, 1437.
[63] S. Dwivedi, Q. Saquib, A. A. Al-Khedhairy, J. Musarrat, in *Microbial Inoculants in Sustainable Agricultural Productivity* (Eds: D. P. Singh, H. B. Singh, R. Prabha), Springer India, New Delhi **2016**, pp. 271–288.
[64] H. Mahawar, R. Prasanna, R. Gogoi, S. B. Singh, G. Chawla, A. Kumar, *3 Biotech* **2020**, *10*, 102.
[65] S. Timmusk, G. Seisenbaeva, L. Behers, *Sci. Rep.* **2018**, *8*, 617.
[66] K. Vishwakarma, V. P. Singh, S. M. Prasad, D. K. Chauhan, D. K. Tripathi, S. Sharma, *J. Hazard. Mater.* **2020**, *390*, 121806.
[67] X. Wang, J. Pu, Y. Liu, F. Ba, M. Cui, K. Li, Y. Xie, Y. Nie, Q. Mi, T. Li, L. Liu, M. Zhu, C. Zhong, *Natl. Sci. Rev.* **2019**, *6*, 929.
[68] F. F. Yan, C. Wu, Y. Y. Cheng, Y. R. He, W. W. Li, H. Q. Yu, *Biochem. Eng. J.* **2013**, *77*, 183.
[69] W. Wang, Y. Feng, X. Tang, H. Li, Z. Du, A. Yi, X. Zhang, *J. Environ. Sci.* **2015**, *31*, 68.
[70] T. Hermann, *J. Biotechnol.* **2003**, *104*, 155.
[71] N. Mangwani, S. K. Shukla, S. Kumari, S. Das, T. S. Rao, *RSC Adv.* **2016**, *6*, 57540.
[72] C. B. Whitchurch, T. Tolker-Nielsen, P. C. Ragas, J. S. Mattick, *Science* **2002**, *295*, 1487.
[73] T. Das, B. P. Krom, H. C. Van Der Mei, H. J. Busscher, P. K. Sharma, *Soft Matter* **2011**, *7*, 2927.
[74] S. Vilain, J. M. Pretorius, J. Theron, V. S. Brözel, *Appl. Environ. Microbiol.* **2009**, *75*, 2861.
[75] T. Das, P. K. Sharma, B. P. Krom, H. C. Van Der Mei, H. J. Busscher, *Langmuir* **2011**, *27*, 10113.
[76] A. Kanampalliwar, D. V. Singh, *Environ. Microbiol. Rep.* **2020**, *12*, 594.
[77] B. Stojković, S. Sretenovic, I. Dogsa, I. Poberaj, D. Stopar, *Biophys. J.* **2015**, *108*, 758.
[78] K. Schwartz, M. Ganesan, D. E. Payne, M. J. Solomon, B. R. Boles, *Mol. Microbiol.* **2016**, *99*, 123.
[79] S. H. Saunders, E. C. M. Tse, M. D. Yates, F. J. Otero, S. A. Trammell, E. D. A. Stemp, J. K. Barton, L. M. Tender, D. K. Newman, *Cell* **2020**, *182*, 919.
[80] E. A. Jones, G. McGillivary, L. O. Bakaletz, *J. Innate Immun.* **2013**, *5*, 24.
[81] S. Chaves, M. Longo, A. Gómez López, F. del V Loto, M. Mechetti, C. M. Romero, *Colloids Surf., B* **2020**, *194*, 111201.
[82] M. Okshevsky, R. L. Meyer, *Crit. Rev. Microbiol.* **2015**, *41*, 341.
[83] J. S. Kavanaugh, C. E. Flack, J. Lister, E. B. Ricker, C. B. Ibberson, C. Jenul, D. E. Moormeier, E. A. Delmain, K. W. Bayles, A. R. Horswill, *mBio* **2019**, *10*, 01137.
[84] W. L. Jones, M. P. Sutton, L. Mckittrick, P. S. Stewart, *Biofouling* **2011**, *27*, 207.
[85] C. Zhang, J. Huang, J. Zhang, S. Liu, M. Cui, B. An, X. Wang, J. Pu, T. Zhao, C. Fan, T. K. Lu, C. Zhong, *Mater. Today* **2019**, *28*, 40.
[86] T. Liu, Z. Guo, Z. Zeng, N. Guo, Y. Lei, T. Liu, S. Sun, X. Chang, Y. Yin, X. Wang, *ACS Appl. Mater. Interfaces* **2018**, *10*, 40317.
[87] M. Sønderholm, K. N. Kragh, K. Koren, T. H. Jakobsen, S. E. Darch, M. Alhede, P. Ø. Jensen, M. Whiteley, M. Kühl, T. Bjarnsholt, *Appl. Environ. Microbiol.* **2017**, *83*, 00113.
[88] B. Pabst, B. Pitts, E. Lauchnor, P. S. Stewart, *Antimicrob. Agents Chemother.* **2016**, *60*, 6294.
[89] Z. B. Bouabidi, M. H. El-Naas, Z. Zhang, *Environ. Chem. Lett.* **2019**, *17*, 241.
[90] Z. Bayat, M. Hassanshahian, S. Cappello, *Open Microbiol. J.* **2015**, *9*, 48.
[91] Y. Kourkoutas, A. Bekatorou, I. M. Banat, R. Marchant, A. A. Koutinas, *Food Microbiol.* **2004**, *21*, 377.
[92] D. Jaroch, E. Mclamore, W. Zhang, J. Shi, J. Garland, M. K. Banks, D. M. Porterfield, J. L. Rickus, *Biotechnol. Bioeng.* **2011**, *108*, 2249.
[93] A. Panchal, N. Rahman, S. Konnova, R. Fakhrullin, D. Zhang, D. Blake, V. John, E. Ivanov, Y. Lvov, *ACS Appl. Nano Mater.* **2020**, *3*, 1263.
[94] J. P. Park, M. Do, S. H. Hong, J. Ryu, D. Kang, K. Rho, J. H. Ahn, H. Lee, *Adv. Mater. Interfaces* **2019**, *6*, 1900379.
[95] S. Macfarlane, J. F. Dillon, *J. Appl. Microbiol.* **2007**, *102*, 1187.
[96] E. Thursby, N. Juge, *Biochem. J.* **2017**, *474*, 1823.
[97] V. H. Ozyurt, S. Ötles, *Acta Sci. Pol., Technol. Aliment.* **2014**, *13*, 413.
[98] J. Burgain, C. Gaiani, M. Linder, J. Scher, *J. Food Eng.* **2011**, *104*, 467.
[99] M. de Araújo Etchepare, G. L. Nunes, B. R. Nicoloso, J. S. Barin, E. M. Moraes Flores, R. de Oliveira Mello, C. Ragagnin de Menezes, *LWT* **2020**, *117*, 108601.
[100] A. Rieu, N. Aoudia, G. Jego, J. Chluba, N. Yousfi, R. Briandet, J. Deschamps, B. Gasquet, V. Monedero, C. Garrido, J. Guzzo, *Cell. Microbiol.* **2014**, *16*, 1836.
[101] H. Kubota, S. Senda, N. Nomura, H. Tokuda, H. Uchiyama, *J. Biosci. Bioeng.* **2008**, *106*, 381.

[102] W. S. Cheow, K. Hadinoto, *Biomacromolecules* **2013**, *14*, 3214.
[103] W. S. Cheow, T. Y. Kiew, K. Hadinoto, *Carbohydr. Polym.* **2014**, *103*, 587.
[104] A. Heumann, A. Assifaoui, D. Da Silva Barreira, C. Thomas, R. Briandet, J. Laurent, L. Beney, P. Lapaquette, J. Guzzo, A. Rieu, *npj Biofilms Microbiomes* **2020**, *6*, 44.
[105] M. Vega-Sagardía, J. Rocha, K. Sáez, C. T. Smith, C. Gutierrez-Zamorano, A. García-Cancino, *J. Funct. Foods* **2018**, *46*, 504.
[106] P. Praveschotinunt, A. M. Duraj-Thatte, I. Gelfat, F. Bahl, D. B. Chou, N. S. Joshi, *Nat. Commun.* **2019**, *10*, 5580.
[107] T. Y. Kiew, W. S. Cheow, K. Hadinoto, *LWT–Food Sci. Technol.* **2014**, *59*, 956.
[108] N. Jiang, G. Dev Kumar, J. Chen, A. Mishra, K. Mis Solval, *LWT* **2020**, *124*, 109200.
[109] S. Yahav, Z. Berkovich, I. Ostrov, R. Reifen, M. Shemesh, *Artif. Cells, Nanomed. Biotechnol.* **2018**, *46*, 974.
[110] J. Jeżewska-Frąckowiak, K. Seroczyńska, J. Banaszczyk, G. Jedrzejczak, A. Zylicz-Stachula, P. M. Skowron, *Acta Biochim. Pol.* **2018**, *65*, 509.
[111] C. Szlufman, M. Shemesh, *Front. Microbiol.* **2021**, *12*, 638830.
[112] A. M. Duraj-Thatte, N. M. Dorval Courchesne, P. Praveschotinunt, J. Rutledge, Y. Lee, J. M. Karp, N. S. Joshi, *Adv. Mater.* **2019**, *31*, 1901826.
[113] N. Eslahi, A. Mahmoodi, N. Mahmoudi, N. Zandi, A. Simchi, *Polym. Rev.* **2020**, *60*, 144.
[114] S. Gea, C. T. Reynolds, N. Roohpour, B. Wirjosentono, N. Soykeabkaew, E. Bilotti, T. Peijs, *Bioresour. Technol.* **2011**, *102*, 9105.
[115] M. M. Abeer, M. C. I. Mohd Amin, C. Martin, *J. Pharm. Pharmacol.* **2014**, *66*, 1047.
[116] I. Sulaeva, U. Henniges, T. Rosenau, A. Potthast, *Biotechnol. Adv.* **2015**, *33*, 1547.
[117] J. Kucińska-Lipka, I. Gubanska, H. Janik, *Polym. Bull.* **2015**, *72*, 2399.
[118] J. M. Dugan, J. E. Gough, S. J. Eichhorn, *Nanomedicine* **2013**, *8*, 287.
[119] W. Liu, H. Du, M. Zhang, K. Liu, H. Liu, H. Xie, X. Zhang, C. Si, *ACS Sustainable Chem. Eng.* **2020**, *8*, 7536.
[120] N. Petersen, P. Gatenholm, *Appl. Microbiol. Biotechnol.* **2011**, *91*, 1277.
[121] Y. Wang, B. An, B. Xue, J. Pu, X. Zhang, Y. Huang, Y. Yu, Y. Cao, C. Zhong, *Nat. Chem. Biol.* **2021**, *17*, 351.
[122] B. An, Y. Wang, X. Jiang, C. Ma, M. Mimee, F. Moser, K. Li, X. Wang, T. C. Tang, Y. Huang, Y. Liu, T. K. Lu, C. Zhong, *Matter* **2020**, *3*, 2080.
[123] A. Pareek, S. V. Mohan, *Bioelectrochemical Interface Engineering*, John Wiley & Sons, Inc., Hoboken, NJ **2019**, p. 165.
[124] K. Rabaey, W. Verstraete, *Trends Biotechnol.* **2005**, *23*, 291.
[125] B. E. Logan, B. Hamelers, R. Rozendal, U. Schröder, J. Keller, S. Freguia, P. Aelterman, W. Verstraete, K. Rabaey, *Environ. Sci. Technol.* **2006**, *40*, 5181.
[126] D. Call, B. E. Logan, *Environ. Sci. Technol.* **2008**, *42*, 3401.
[127] E. S. Heidrich, S. R. Edwards, J. Dolfing, S. E. Cotterill, T. P. Curtis, *Bioresour. Technol.* **2014**, *173*, 87.
[128] P. Bombelli, T. Müller, T. W. Herling, C. J. Howe, T. P. J. Knowles, *Adv. Energy Mater.* **2015**, *5*, 1401299.
[129] K. Ocakoglu, T. Krupnik, B. Van Den Bosch, E. Harputlu, M. P. Gullo, J. D. J. Olmos, S. Yildirimcan, R. K. Gupta, F. Yakuphanoglu, A. Barbieri, J. N. H. Reek, J. Kargul, *Adv. Funct. Mater.* **2014**, *24*, 7467.
[130] H. Luo, P. Xu, T. M. Roane, P. E. Jenkins, Z. Ren, *Bioresour. Technol.* **2012**, *105*, 60.
[131] M. Mehanna, T. Saito, J. Yan, M. Hickner, X. Cao, X. Huang, B. E. Logan, *Energy Environ. Sci.* **2010**, *3*, 1114.
[132] J. S. Deutzmann, A. M. Spormann, *ISME J.* **2017**, *11*, 704.
[133] C. W. Marshall, D. E. Ross, E. B. Fichot, R. S. Norman, H. D. May, *Environ. Sci. Technol.* **2013**, *47*, 6023.
[134] M. B. Santiago, G. A. Daniel, A. David, B. Casañas, G. Hernández, A. R. Guadalupe, J. L. Clón, *Electroanalysis* **2010**, *22*, 1097.
[135] G. D. Saratale, R. G. Saratale, M. K. Shahid, G. Zhen, G. Kumar, H.-S. Shin, Y.-G. Choi, S.-H. Kim, *Chemosphere* **2017**, *178*, 534.
[136] T. Utesch, W. Sabra, C. Prescher, J. Baur, P. Arbter, A. P. Zeng, *Biotechnol. Bioeng.* **2019**, *116*, 1627.
[137] J. Babauta, R. Renslow, Z. Lewandowski, H. Beyenal, *Biofouling* **2012**, *28*, 789.
[138] S. C. Popat, C. I. Torres, *Bioresour. Technol.* **2016**, *215*, 265.
[139] M. Li, M. Zhou, X. Tian, C. Tan, C. T. McDaniel, D. J. Hassett, T. Gu, *Biotechnol. Adv.* **2018**, *36*, 1316.
[140] Y. Yuan, S. Zhou, N. Xu, L. Zhuang, *Colloids Surf., B* **2011**, *82*, 641.
[141] M. Zhou, M. Chi, J. Luo, H. He, T. Jin, *J. Power Sources* **2011**, *196*, 4427.
[142] D. K. Newman, R. Kolter, *Nature* **2000**, *405*, 94.
[143] M. E. Hernandez, D. K. Newman, *Cell. Mol. Life Sci.* **2001**, *58*, 1562.
[144] C. J. Sund, S. McMasters, S. R. Crittenden, L. E. Harrell, J. J. Sumner, *Appl. Microbiol. Biotechnol.* **2007**, *76*, 561.
[145] S. B. Velasquez-Orta, I. M. Head, T. P. Curtis, K. Scott, J. R. Lloyd, H. Von Canstein, *Appl. Microbiol. Biotechnol.* **2010**, *85*, 1373.
[146] Y. Wu, X. Luo, X. Luo, X. Luo, B. Qin, F. Li, M. M. Häggblom, T. Liu, T. Liu, *Environ. Sci. Technol.* **2020**, *54*, 7217.
[147] T. Arinda, L. A. Philipp, D. Rehnlund, M. Edel, J. Chodorski, M. Stöckl, D. Holtmann, R. Ulber, J. Gescher, K. Sturm-Richter, *Front. Microbiol.* **2019**, *10*, 126.
[148] Y. Hu, D. Rehnlund, E. Klein, J. Gescher, C. M. Niemeyer, *ACS Appl. Mater. Interfaces* **2020**, *12*, 14806.
[149] G. Pankratova, K. Hasan, D. Leech, L. Hederstedt, L. Gorton, *Electrochem. Commun.* **2017**, *75*, 56.
[150] S. A. Patil, K. Hasan, D. Leech, C. Hägerhäll, L. Gorton, *Chem. Commun.* **2012**, *48*, 10183.
[151] Y. Yuan, H. Shin, C. Kang, S. Kim, *Bioelectrochemistry* **2016**, *108*, 8.
[152] K. Hasan, H. Bekir Yildiz, E. Sperling, P. Ó Conghaile, M. A. Packer, D. Leech, C. Hägerhäll, L. Gorton, *Phys. Chem. Chem. Phys.* **2014**, *16*, 24676.
[153] P. Zhang, X. Zhou, R. Qi, P. Gai, L. Liu, F. Lv, S. Wang, *Adv. Electron. Mater.* **2019**, *5*, 1900320.
[154] Q. Du, T. Li, N. Li, X. Wang, *Environ. Sci. Technol. Lett.* **2017**, *4*, 345.
[155] Y. Zhang, L. Liu, B. Van Der Bruggen, F. Yang, *J. Mater. Chem. A* **2017**, *5*, 12673.
[156] Y. C. Yong, Y. Y. Yu, X. Zhang, H. Song, *Angew. Chem., Int. Ed.* **2014**, *53*, 4480.
[157] Y. Yuan, S. Zhou, B. Zhao, L. Zhuang, Y. Wang, *Bioresour. Technol.* **2012**, *116*, 453.
[158] T.-s. Song, Y. Jin, J. Bao, D. Kang, J. Xie, *J. Hazard. Mater.* **2016**, *317*, 73.
[159] J. Chen, Z. Yu, J. Sun, J. Jia, G. Li, *Water Environ. Res.* **2008**, *80*, 699.
[160] C. K. Ngaw, C.-e Zhao, V. B. Wang, S. Kjelleberg, T. T. Yang Tan, Q. Zhang, S. C. Joachim Loo, *Sustainable Energy Fuels* **2017**, *1*, 191.
[161] C.e Zhao, J. Wu, Y. Ding, V. B. Wang, Y. Zhang, S. Kjelleberg, J. S. C. Loo, B. Cao, Q. Zhang, *ChemElectroChem* **2015**, *2*, 654.
[162] Y. Y. Yu, H. L. Chen, Y. C. Yong, D. H. Kim, H. Song, *Chem. Commun.* **2011**, *47*, 12825.
[163] C. E. Milliken, H. D. May, *Appl. Microbiol. Biotechnol.* **2007**, *73*, 1180.
[164] K. Hasan, S. A. Patil, K. Górecki, D. Leech, C. Hägerhäll, L. Gorton, *Bioelectrochemistry* **2013**, *93*, 30.
[165] E. Zhang, Y. Cai, Y. Luo, Z. Piao, *Can. J. Microbiol.* **2014**, *60*, 753.
[166] K. L. Scrivener, V. M. John, E. M. Gartner, *Cem. Concr. Res.* **2018**, *114*, 2.
[167] S. A. Miller, F. C. Moore, *Nat. Clim. Change* **2020**, *10*, 439.
[168] N. De Belie, *RILEM Tech. Lett.* **2016**, *1*, 56.
[169] J. Wang, Y. C. Ersan, N. Boon, N. De Belie, *Appl. Microbiol. Biotechnol.* **2016**, *100*, 2993.

[170] H. Ai, M. Liu, P. Yu, S. Zhang, Y. Suo, P. Luo, S. Li, J. Wang, *Carbohydr. Polym.* **2015**, *129*, 35.
[171] M. Lachemi, K. M. A. Hossain, V. Lambros, P. C. Nkinamubanzi, N. Bouzoubaâ, *Cem. Concr. Res.* **2004**, *34*, 917.
[172] V. Kaur, M. B. Bera, P. S. Panesar, H. Kumar, J. F. Kennedy, *Int. J. Biol. Macromol.* **2014**, *65*, 454.
[173] B. Katzbauer, *Polym. Degrad. Stab.* **1998**, *59*, 81.
[174] B. Urlacher, O. Noble, in *Thickening and Gelling Agents for Food* (Ed: A. P. Imeson), Springer US, Boston, MA **1997**, pp. 284–311.
[175] G. Sworn, in *Handbook of Hydrocolloids*, Elsevier, Amsterdam **2021**, pp. 833–853.
[176] A. Leemann, F. Winnefeld, *Cem. Concr. Compos.* **2007**, *29*, 341.
[177] I. E. Isik, M. H. Ozkul, *Constr. Build. Mater.* **2014**, *72*, 239.
[178] G. G. Kahng, S. H. Lim, H. D. Yun, W. T. Seo, *Biotechnol. Bioprocess Eng.* **2001**, *6*, 112.
[179] R. Pei, J. Liu, S. Wang, *Cem. Concr. Compos.* **2015**, *55*, 186.
[180] M. Azima, Z. Başaran Bundur, in *Rheology and Processing of Construction Materials* (Eds: V. Mechtcherine, K. Khayat, E. Secrieru), Springer, Cham **2020**, pp. 79–86.
[181] M. Azima, Z. B. Bundur, *Constr. Build. Mater.* **2019**, *225*, 1086.
[182] M. Azima, A. G. Guldogan, Z. B. Bundur, **2019**, *37*, 142.
[183] M. Palacios, R. J. Flatt, in *Science and Technology of Concrete Admixtures* (Eds: P.-C. Aïtcin, R. J. Flatt), Elsevier, Amsterdam **2016**, pp. 415–432.
[184] R. Pei, J. Liu, S. Wang, M. Yang, *Cem. Concr. Compos.* **2013**, *39*, 122.
[185] M. V. S. Rao, V. S. Reddy, C. Sasikala, *J. Inst. Eng.: Ser. A* **2017**, *98*, 501.
[186] S. Mondal, P. Das, A. Kumar Chakraborty, *Mater. Today: Proc.* **2017**, *4*, 9833.
[187] N. Nain, R. Surabhi, N. V. Yathish, V. Krishnamurthy, T. Deepa, S. Tharannum, *Constr. Build. Mater.* **2019**, *202*, 904.
[188] R. Andalib, M. Z. Abd Majid, M. W. Hussin, M. Ponraj, A. Keyvanfar, J. Mirza, H. S. Lee, *Constr. Build. Mater.* **2016**, *118*, 180.
[189] P. Ghosh, S. Mandal, B. D. Chattopadhyay, S. Pal, *Cem. Concr. Res.* **2005**, *35*, 1980.
[190] B. Tayebani, D. Mostofinejad, *J. Mater. Civ. Eng.* **2019**, *31*, 04019002.
[191] K. Kawaai, T. Nishida, A. Saito, I. Ujike, S. Fujioka, *Cem. Concr. Res.* **2019**, *124*, 105822.
[192] F. Feugeas, M. Tran, S. Chakri, in *Eco-efficient Repair and Rehabilitation of Concrete Infrastructures*, Elsevier, Amsterdam **2018**, pp. 569–587.
[193] X. Chen, S. Wu, J. Zhou, *Constr. Build. Mater.* **2013**, *40*, 869.
[194] Q. Chunxiang, W. Jianyun, W. Ruixing, C. Liang, *Mater. Sci. Eng., C* **2009**, *29*, 1273.
[195] S. Grumbein, D. Minev, M. Tallawi, K. Boettcher, F. Prade, F. Pfeiffer, C. U. Grosse, O. Lieleg, *Adv. Mater.* **2016**, *28*, 8138.
[196] O. Lieleg, D. Minev, C. Grosse, US10604448B2, **2020**.
[197] M. J. Ertelt, M. Raith, J. Eisinger, C. U. Grosse, O. Lieleg, *ACS Sustainable Chem. Eng.* **2020**, *8*, 5704.
[198] M. J. Ertelt, L. Bubendorfer, C. U. Grosse, O. Lieleg, *Cem. Concr. Compos.* **2021**, *120*, 104002.
[199] S. A. Miller, R. J. Myers, *Environ. Sci. Technol.* **2020**, *54*, 677.
[200] Z. Y. Qu, Q. Yu, Y. D. Ji, F. Gauvin, I. K. Voets, *Cem. Concr. Res.* **2020**, *138*, 106234.
[201] M. J. Castro-Alonso, L. E. Montañez-Hernandez, M. A. Sanchez-Muñoz, M. R. Macias Franco, R. Narayanasamy, N. Balagurusamy, *Front. Mater.* **2019**, *6*, 126.
[202] V. Achal, A. Mukherjee, *Constr. Build. Mater.* **2015**, *93*, 1224.
[203] H. M. Jonkers, in *Self Healing Materials* (Ed: S. van derZwaag), Springer, Dordrecht, The Netherlands **2007**, pp. 195–204.
[204] H. M. Jonkers, US8460458B2, **2013**.
[205] H. M. Jonkers, *HERON* **2011**, *56*, 1.
[206] M. J. Leggett, G. Mcdonnell, S. P. Denyer, P. Setlow, J. Y. Maillard, *J. Appl. Microbiol.* **2012**, *113*, 485.
[207] P. T. Mckenney, A. Driks, P. Eichenberger, *Nat. Rev. Microbiol.* **2013**, *11*, 33.
[208] V. Wiktor, H. M. Jonkers, *Cem. Concr. Compos.* **2011**, *33*, 763.
[209] K. Vijay, M. Murmu, S. V. Deo, *Constr. Build. Mater.* **2017**, *152*, 1008.
[210] Y. S. Lee, W. Park, *Appl. Microbiol. Biotechnol.* **2018**, *102*, 3059.
[211] E. S. Kucharski, R. Cord-Ruwisch, V. Whiffin, S. M. Al-Thawadi, US8182604B2, **2012**.
[212] D. Mujah, M. A. Shahin, L. Cheng, *Geomicrobiol. J.* **2017**, *34*, 524.
[213] L. Cheng, T. Kobayashi, M. A. Shahin, *Constr. Build. Mater.* **2020**, *231*, 117095.
[214] Q. Zhao, L. Li, C. Li, M. Li, F. Amini, H. Zhang, *J. Mater. Civ. Eng.* **2014**, *26*, 04014094.
[215] A. Mahawish, A. Bouazza, W. P. Gates, *Acta Geotech.* **2018**, *13*, 1019.
[216] C. M. Heveran, S. L. Williams, J. Qiu, J. Artier, M. H. Hubler, S. M. Cook, J. C. Cameron, W. V. Srubar, *Matter* **2020**, *2*, 481.
[217] T. D. Ngo, A. Kashani, G. Imbalzano, K. T. Q. Nguyen, D. Hui, *Composites, Part B* **2018**, *143*, 172.
[218] S. Li, H. Bai, R. F. Shepherd, H. Zhao, *Angew. Chem., Int. Ed.* **2019**, *58*, 11182.
[219] M. K. Mohan, A. V. Rahul, G. De Schutter, K. Van Tittelboom, *Cem. Concr. Compos.* **2021**, *115*, 103855.
[220] S. Kyle, *Trends Biotechnol.* **2018**, *36*, 340.
[221] L. Hsu, X. Jiang, *Trends Biotechnol.* **2019**, *37*, 795.
[222] S. Balasubramanian, M. E. Aubin-Tam, A. S. Meyer, *ACS Synth. Biol.* **2019**, *8*, 1564.
[223] M. Schaffner, P. A. Rühs, F. Coulter, S. Kilcher, A. R. Studart, *Sci. Adv.* **2017**, *3*, eaao6804.
[224] M. C. Freyman, T. Kou, S. Wang, Y. Li, *Nano Res.* **2020**, *13*, 1318.
[225] F. Moser, E. Tham, L. M. González, T. K. Lu, C. A. Voigt, *Adv. Funct. Mater.* **2019**, *29*, 1901788.
[226] B. A. E. Lehner, D. T. Schmieden, A. S. Meyer, *ACS Synth. Biol.* **2017**, *6*, 1124.
[227] J. Huang, S. Liu, C. Zhang, X. Wang, J. Pu, F. Ba, S. Xue, H. Ye, T. Zhao, K. Li, Y. Wang, J. Zhang, L. Wang, C. Fan, T. K. Lu, C. Zhong, *Nat. Chem. Biol.* **2019**, *15*, 34.
[228] A. M. Duraj-Thatte, A. Manjula-Basavanna, J. Rutledge, J. Xia, S. Hassan, A. Sourlis, A. G. Rubio, A. Lesha, M. Zenk, A. Kan, D. A. Weitz, Y. S. Zhang, N. S. Joshi, *bioRxiv, Synth. Biol.* **2021**, 440538, https://doi.org/10.1101/2021.04.19.440538.
[229] L. G. Greca, J. Lehtonen, B. L. Tardy, J. Guo, O. J. Rojas, *Mater. Horiz.* **2018**, *5*, 408.
[230] J. Yu, T. R. Huang, Z. H. Lim, R. Luo, R. R. Pasula, L. De Liao, S. Lim, C. H. Chen, *Adv. Healthcare Mater.* **2016**, *5*, 2983.
[231] M. Pepicelli, M. R. Binelli, A. R. Studart, P. A. Rühs, P. Fischer, *ACS Biomater. Sci. Eng.* **2021**, *7*, 3221.
[232] J. Song, F. Babayekhorasani, P. T. Spicer, *Biomacromolecules* **2019**, *20*, 4437.
[233] G. Subbiahdoss, E. Reimhult, *Colloids Surf., B* **2020**, *194*, 111163.

Elif N. Hayta is a bioengineer who received her M.Sc. degree in chemical engineering from Istanbul Technical University in 2014. Since 2018, she has been conducting her Ph.D. studies in the lab of Prof. Lieleg. Her research focuses on the material properties of semisynthetic and cocultured biofilms and the relation between their surface topography and wetting behavior.

Marvin J. Ertelt received his M.Sc. degree in chemistry from Ludwig Maximilian University of Munich (LMU) in 2018. Since then, he has been working as a research associate in the lab of Prof. Lieleg at the Technical University of Munich (TUM). His research focuses on bacterial additives to cementitious materials to increase their sustainability.

Martin Kretschmer received his M.Sc. degree in production engineering from the University of Bremen in 2017. Since then, he has been working as a research associate in the lab of Prof. Lieleg at the Technical University of Munich (TUM). His research focuses on the material properties of bacterial biofilms and hydrogels.

Oliver Lieleg is a trained biophysicist who completed his Ph.D. at the Technical University of Munich (TUM) in 2008. After a postdoctoral phase at Harvard and MIT, he returned to TUM in 2011, where he has been an associate professor for biomechanics since. His research focuses on the selective permeability and viscoelastic properties of soft biological materials such as mucus and bacterial biofilms as well as biopolymer-based nanoparticles and coatings for applications in biomedical engineering.

A.2 Biopolymer-enriched *B. subtilis* NCIB 3610 biofilms exhibit increased erosion resistance

Biomaterials Science

PAPER

View Article Online
View Journal

Cite this: DOI: 10.1039/c9bm00927b

Biopolymer-enriched *B. subtilis* NCIB 3610 biofilms exhibit increased erosion resistance†

Elif N. Hayta and Oliver Lieleg *

The erosion resistance of bacterial biofilms can be a double-edged sword: it hampers the removal of undesired biofilms in biomedical settings, but it is necessary for beneficial biofilms to be used in aqueous environments for biotechnological applications. Whether or not a bacterial biofilm exhibits this material property depends on the bacterial species and the detailed composition of the biofilm matrix. Here, we demonstrate how the erosion resistance of *B. subtilis* NCIB 3610 biofilms can be enhanced by integrating foreign (bio)polymers into the matrix during biofilm growth. As a result of this artificial macromolecule addition, the engineered biofilm colonies show changes in their surface topography which, in turn, cause an alteration in the mode of surface superhydrophobicity. Surprisingly, the viscoelastic properties and permeability of the biofilms towards antibiotics remain unaffected. The method introduced here may present a promising strategy for engineering beneficial biofilms such, that they become more stable towards shear forces caused by flowing water but, at the same time, remain permeable to nutrients or other molecules.

Received 14th June 2019,
Accepted 25th August 2019

DOI: 10.1039/c9bm00927b

rsc.li/biomaterials-science

Introduction

Erosion by water is a process that occurs on very different length scales – from continental erosion reducing the mass of land, to microscopic erosion washing off paint particles from house walls.[1–3] Whereas erosion of soil on coastal shores can be a serious threat for the environment, many cleaning methods used in our daily life are based on the sensitivity of biomatter to be worn away by ongoing shear forces induced by flowing water. However, there are some biological materials which have developed very clever mechanisms to resist such water-based erosion, and bacterial biofilms belong to those erosion-resistant materials.[4–8]

Because of their high mechanical sturdiness, the removal of undesired biofilms from surfaces such as teeth or the inside of water pipes in cooling towers can be very difficult; often, either mechanical scraping or the application of harsh chemicals is necessary to detach bacterial biofilms from the surface they have colonized. However, biofilms are not always harmful. The biofilms covering plant leaves and roots or colonizing the mucosal membranes of the human intestinal tract provide protection against pathogenic invaders and help with the utilization of certain nutrients.[9–11] In industrial settings, such surface attached communities of microbes are also employed in many beneficial applications including the bioremediation of toxic compounds, wastewater treatment, and acting as biocatalyzers in many biotechnological processes.[12–15]

So far, several mechanistic contributions have been identified that establish or enhance the erosion resistance of bacterial biofilms: their adhesion behavior, viscoelastic properties and wetting resistance.[6,16–18] All of these biofilm properties are critically related to the extracellular polymeric substances (EPS) the bacteria are embedded into.[19–21] However, the composition of the biofilm matrix can be very different, even for biofilms generated by related species. For instance, the matrix of *B. subtilis* B-1 biofilms mainly comprises γ-polyglutamate (PGA).[22] In contrast, *B. subtilis* NCIB 3610 biofilms are mainly composed of an exopolysaccharide expressed by *epsA-O* operon; an amyloid-fiber-forming protein, *TasA*; and a surface layer hydrophobin, *BslA*.[23–25] The BslA protein has been reported to form a hydrophobic surface coating on NCIB 3610 biofilms and contributes to the liquid repellency of the biofilms.[25] However, the wetting resistance of biofilms does not solely depend on their surface chemistry. In addition to this chemical contribution, as for many other materials,[26,27] also the nano- and microscopic surface roughness critically affects the wetting properties of biofilms. In Werb *et al.*,[28] it was demonstrated that there are two modes of superhydrophobicity for *B. subtilis* NCIB 3610 biofilms when the bacteria are grown on different media. There, it was also shown that changes in the growth medium alter the biofilm matrix composition and – as a consequence – the surface topography of the biofilms.

Munich School of Bioengineering and Department of Mechanical Engineering, Technical University of Munich, 85748 Garching, Germany.
E-mail: oliver.lieleg@tum.de; Fax: +49 89 289 10801; Tel: +49 89 289 10952

†Electronic supplementary information (ESI) available. See DOI: 10.1039/c9bm00927b

The details in the surface topography of a material – be it a biofilm or an artificial, man-made surface – affect not only the macroscopic wetting properties of the surface (as quantified by contact angle measurements) but also the microscopic mode of interaction between the surface and the wetting liquid. The latter defines the difference between two well-known modes of superhydrophobicity, *i.e.* lotus-like and rose-like behavior. On lotus-like surfaces, there is a Cassie–Baxter-state, *i.e.* microscopic air bubbles are trapped between the roughness features of the surface. Due to this complex material/liquid interface, most of the solid surface is separated from the wetting liquid by the air pockets.[29,30] As a result, those lotus-like surfaces exhibit negligible adhesion forces towards water, and biofilms with lotus-like surface properties show a high erosion resistance.[17] In turn, rose-like superhydrophobicity allows for microscopic contact between the rough surface features of a material and the wetting liquid, as an impregnated Cassie state (similar to a Wenzel state) is observed here. As a consequence, biofilms with rose-like surface properties – although also classified as superhydrophobic – are much more vulnerable to erosion by water than their lotus-like counterparts.[17]

Here, we show that the erosion resistance of superhydrophobic *B. subtilis* NCIB 3610 biofilms can be drastically increased by incorporating synthetic or purified macromolecules into their biofilm matrix. This is achieved by growing the biofilm bacteria in the presence of those synthetic or purified macromolecules. Surprisingly, the increased erosion resistance we observe is neither due to a change in the contact angle determined on the biofilm surface nor to a change in biofilm stiffness. Instead, we find a correlation between the erosion behavior of the biofilm colonies and the contact angle hysteresis of the biofilm surfaces, the latter of which is a measure for the detailed mode of superhydrophobicity. An optical analysis of surfaces of polymer-enriched biofilm samples suggests that subtle changes in the surface topography are responsible for establishing a non-wetting state that is located somewhere in between rose-like and lotus-like superhydrophobicity. Our results implicate that the integration of 'foreign' (bio)polymers into the matrix of *B. subtilis* NCIB 3610 biofilms can sensitively modulate the wetting resistance of the biofilm colonies and thus improves their resilience towards erosion by water while maintaining their other material properties.

Experimental

Polyglutamate purification

PGA was extracted from *B. subtilis* B-1 liquid cultures as described in the literature[31] with slight modifications. First, a piece of frozen *B. subtilis* B-1 glycerol stock was inoculated in 10 mL of sterile 2.5% LB (Luria/Miller) medium (Carl-Roth, Karlsruhe, Germany) and incubated overnight at 37 °C at a shaking speed of 300 rpm (Unimax1010 and Incubator 1000, Heidolph Instruments, Schwabach, Germany). The overnight culture was then spread onto Medium E plates containing 1.5% (w/v) agar. Medium E contains 25.6 g sodium-L-glutamate monohydrate (Applichem, Darmstadt, Germany), 18.7 g trisodium citrate dihydrate (Carl-Roth, Karlsruhe, Germany), 7 g NH_4Cl (Applichem, Darmstadt, Germany), 0.5 g K_2HPO_4, 0.5 g $MgSO_4{\cdot}7H_2O$ (Carl-Roth, Karlsruhe, Germany), 63.4 g glycerol, 40 mg $FeCl_3{\cdot}6H_2O$ (Applichem, Darmstadt, Germany), 150 mg $CaCl_2{\cdot}2H_2O$ (Carl-Roth, Karlsruhe, Germany), 104 mg $MnSO_4{\cdot}H_2O$ (Applichem, Darmstadt, Germany) and 1 mg $ZnSO_4{\cdot}7H_2O$ (Carl-Roth, Karlsruhe, Germany), per 1 L. After incubation at 30 °C for a day, the slimiest (*i.e.*, strongest PGA-producing) colony was selected, inoculated in 10 mL of medium E and incubated at 30 °C for 12–15 h to generate an efficient PGA-producing *B. subtilis* B-1 liquid culture. For scaling up of this liquid culture, 250 mL medium E was inoculated with 5 mL of this overnight culture and incubated in a 1 L baffled flask at 30 °C at a shaking speed of 100 rpm (Certomat BS-1, Sartorius AG, Göttingen, Germany). The turbidity of the culture was measured with an OD reader (Genequant Pro, Amersham Biosciences Inc.) at 600 nm every hour until the bacterial growth reached a stationary phase (which occurred after ~2 days). Then, the incubation was continued for additional 10 h to allow for efficient PGA production.

For PGA purification from this bacterial liquid culture, the liquid culture was mixed with ice in a volume ratio of 2 : 1 and homogenized with an immersion blender for 3–4 minutes. When the ice had fully thawed, the mixture was centrifuged (Optima LE-70 Ultracentrifuge, Beckman Coulter Inc., Krefeld, Germany) for 1 h at 3000*g* and 4 °C to remove the cells. 4 times volume of ice-cold 96% (w/v) ethanol was added to the PGA containing supernatant during stirring, and the mixture was incubated at −20 °C for 48 h. The rubber like precipitate was separated, dried at 37 °C and dissolved in 100 mL of distilled water. The obtained polymer solution was dialyzed against distilled water at 4 °C for 48 h. Prior to dialysis, the dialysis membrane (MWCO: 12–14 kDa, Spectra/Por 4, Spectrum Labs) was pretreated to avoid membrane clogging: for this purpose, the membrane was boiled in 500 mL of an aqueous solution containing 2% $NaHCO_3$ and 1 mM ethylenediaminetetraacetic acid, then boiled again for 10 min in ~2 L of distilled water and washed for several times. After dialysis, the polymer solution was centrifuged at 100 000*g* and 4 °C for 4 h. The supernatant was frozen at −20 °C and lyophilized for 48 h.

The purified PGA was further analyzed by gel filtration chromatography and compared to commercial PGA (MW: >750 000 by MALLS). For this purpose, 30 mL solutions of both commercial and purified PGA at a concentration of 0.05% (w/v) were prepared in distilled water. Then, the solutions were run through a Sepharose 6FF XK50/100 column using phosphate-buffered saline (PBS, pH 7.0) as a running buffer. Both PGA variants were detected by absorbance at 220 nm. Also, the absorbance of the samples at 280 nm wavelength was monitored to detect putative protein-based impurities or non-specific absorbance. Both commercial and purified PGA samples exhibit similar peaks at 220 nm and at similar

retention times. No other significant peaks were observed at both wavelengths, which indicates that both PGA variants have comparable purity (Fig. S1†).

All other used molecules were obtained from commercial suppliers. If not stated otherwise, chemicals were purchased from Sigma Aldrich (St Louis, USA).

Biofilm formation

For generating liquid cultures of planktonic cells, a piece of frozen bacterial glycerol stock was inoculated in 10 mL of sterile 2.5% LB (Luria/Miller) medium (Carl-Roth, Karlsruhe, Germany). Both, NCIB 3610 and B-1 cultures were incubated at 37 °C overnight using shaking speeds of 90 and 300 rpm, respectively (Certomat BS-1, Sartorius AG, Göttingen, Germany; Unimax1010 and Incubator 1000, Heidolph Instruments, Schwabach, Germany). To obtain standard *B. subtilis* B-1 and NCIB 3610 biofilm colonies, three separate 10 μL drops of bacterial overnight culture were placed onto 1.5% (w/v) agar plates enriched with MSgg (Minimal Salts Glycerol Glutamate) medium and incubated at 30 °C and ~23% humidity for 24 h. This MSgg medium contained 5 mM potassium phosphate, 100 mM 3-(*N*-Morpholino)propanesulfonic acid (MOPS) (Carl-Roth, Karlsruhe, Germany), 2 mM $MgCl_2$, 700 μM $CaCl_2$, 50 μM $MnCl_2$, 50 μM $FeCl_3$, 1 μM $ZnCl_2$, 2 μM thiamine, 0.5% (v/v) glycerol, 0.5% (w/v) glutamate, 50 μg mL^{-1} L-tryptophan, 50 μg mL^{-1} L-phenylalanine, and 50 μg mL^{-1} threonine.[23] To prepare biomolecule-enriched biofilm colonies, either PGA, sodium alginate, polyethyleneglycol (with two different molecular weights, *i.e.*, PEG 10 000 and PEG 600; Merck, Darmstadt, Germany) was dissolved in buffer (100 mM phosphate and 150 mM NaCl, pH 7.2) at a concentration of 20 mg mL^{-1}; then, each of these solutions was mixed with a NCIB 3610 overnight culture in a volumetric ratio of 1 : 1. Due to the significant differences in the molecular weights of the different polymers, the final mass concentration of added (bio)polymers was set to 10 mg mL^{-1} in each inoculation mixture. Finally, 10 μL of those biomolecule-enriched liquid cultures were spotted onto MSgg agar plates, which were incubated as described above.

Erosion assay

The erosion tests performed here follow a methodology introduced in ref. 18 and 21, but were slightly modified as follows: tailored polytetrafluorethylene (PTFE) chips were crafted in a workshop, and each of those PTFE chips contained 10 cylindrical wells with a diameter of 6 mm and depth of 3 mm (Fig. 1a). Those PTFE chips were autoclaved, and the sterilized wells were filled with 100 μL of MSgg agar. Right after the agar had solidified, 5 μL of either standard or biomolecule-enriched bacterial liquid cultures were spread over the agar surfaces of each well. Each of these inoculated chips were placed into a Petri dish and inside a plastic bag to avoid drying of the agar substrate, and they were incubated at 30 °C for 24 h to generate biofilm colonies. On each PTFE chip, all 10 wells were inoculated with the same sample type, *i.e.* a new chip was used for each different simple.

To carry out the erosion tests, the inoculated PTFE chips were placed into falcon tubes filled with 45 mL distilled water (Fig. 1b), and the mature biofilm colonies were exposed to shear forces by shaking the filled falcon tubes at 300 rpm for 1 h (Unimax1010, Heidolph Instruments, Schwabach, Germany). The erosion process of the biofilms was then determined in time intervals of 10 min; after each inspection, the PTFE chips were placed back into the falcon tubes and subjected to further shear treatment. The amount of eroded biofilm mass was evaluated by a trinary grading system: following an optical inspection of the samples, a score of 0 points was assigned if no erosion was visible, a score of 0.5 points was assigned to partially eroded biofilm samples, and 1 point was assigned to fully eroded biofilm samples. Then, the total score obtained on a given PTFE chip was normalized to 10. For example, if on a given chip, one biofilm sample was partially eroded and another one was fully eroded at a certain time point, this chip was assigned a cumulative score of 1.5 points, which returns a normalized erosion efficiency of 15%.

Rheological characterization

Rheological measurements were performed on a commercial rheometer (MCR 302, Anton Paar GmbH, Graz, Austria) using a 25 mm plate-plate geometry (PP25, Anton Paar) and a plate separation of 500 μm. Standard and macromolecule-enriched biofilm colonies were grown as described above. Then, mature biofilm colonies were removed from the agar substrate by manual scraping, pooled until a sufficient amount was collected (*i.e.*, at least 1 mL for one measurement) and placed onto the stationary sample plate of the rheometer. Shear measurements were conducted in a frequency range from 0.1 to 10 Hz at a temperature of 21 °C. To ensure linear material response, the frequency spectra were acquired using small torques (~1 μNm).

Topographical characterization

To examine the surface topography of the biofilms, light profilometry images were acquired using a 3D laser scanning confocal microscope (VK-X1000 series, Keyence Corporation, Osaka, Japan). Pictures were obtained at 20× magnification resulting in topographical images with an area of 529 × 705 μm. The obtained topographical data was evaluated with the software MultiFileAnalyzer (Version 2.1.3.89, Keyence Corporation, Osaka, Japan).

To quantify the surface topography of the biofilms, different topographical parameters were calculated, which are all defined in the ISO norm 25178. The developed interfacial surface ratio,

$$\mathrm{Sdr} = \frac{1}{A}\left[\iint_A \left(\sqrt{\left[1+\left(\frac{\partial z(x,y)}{\partial x}\right)^2+\left(\frac{\partial z(x,y)}{\partial y}\right)^2\right]}-1\right)\mathrm{d}x\mathrm{d}y\right],$$

describes the percentage of measured surface area (as established by the surface texture) with respect to the (perfectly flat) definition area. The root mean square height, $\mathrm{Sq} = \sqrt{\frac{1}{A}\iint_A Z^2(x,y)\mathrm{d}x\mathrm{d}y}$, is equivalent to the standard deviation of the *z*-coordinates. The maximum height, Sz = Sp + Sv, denotes

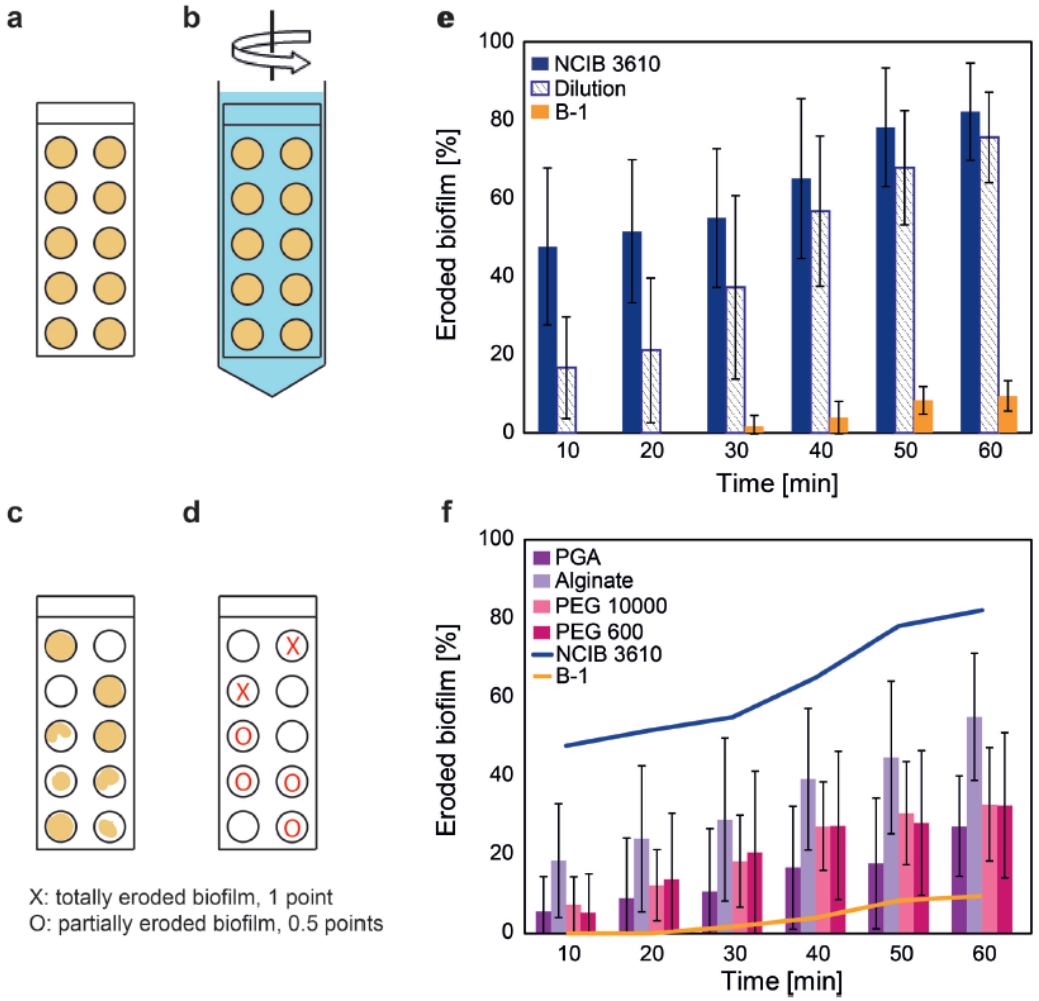

Fig. 1 Erosion behavior of different *B. subtilis* biofilm variants. A schematic representation of the biofilm erosion assay is depicted in (a)–(d). Each of the 10 wells of a given PTFE chip was inoculated with the same sample. The time-dependent erosion process of *B. subtilis* B-1, *B. subtilis* NCIB 3610 biofilms and polymer-enriched variants of the latter is depicted in (e) and (f). "PGA", "Alginate", "PEG 600" and "PEG 10000" labels refer to NCIB 3610 biofilms enriched with these (bio)polymers. The buffer-diluted NCIB 3610 sample is labelled as "Dilution". The error bars denote the standard deviation as obtained from $n = 9$ independent PTFE chips on which biofilms were generated from $N = 3$ different growth batches.

the sum of the largest peak height, Sp = $\max_A z(x,y)$, and the largest valley depth, Sv = $|\min_A z(x,y)|$, within the investigated area. However, its two components, the maximum pit height, Sv, and the maximum peak height, Sp, can sometimes return misleading results, *e.g.*, if the surface height is dominated by a few extreme pits or peaks. Thus, as explained in the main text, we examined the surface texture in more detail. The core height, Sk, is calculated by subtracting the minimum height from the maximum height of the core surface and represents the surface roughness after removal of predominant peaks and valleys. Thus, Sk more reliably takes into account information from the whole surface without being overwhelmingly influenced by extreme points. A related parameter, the reduced dale height, Svk, denotes the arithmetical mean of the valley depth below the core roughness. Surface parameters reflecting the valley depth such as Sv and Svk are suggested to be related to the liquid retention capacity of a surface.[32–34] However, height parameters alone may not be sufficient to understand a complex 3-dimensional scenario such as liquid retention. Hence, to better define the effect of valleys on surface wetting in three dimensions (*i.e.* in volumetric terms), we also calculated the core void volume, Vvc, and the dale void volume, Vvv, of the biofilm surfaces. Vvc represents the void

volume of the surface, which is between 10 and 80% of the areal material ratio, and Vvv represents the void volume of the dale, where the areal material ratio of the reduced valleys to the core surface is 80%.

Scanning electron microscopy

Similar to what we had described previously,[28] we prepared biofilm samples for scanning electron microscopy (SEM) imaging without sample fixation. Instead, biofilm colonies were shock-frozen by exposure to liquid nitrogen and dried by lyophilization for at least 48 h. The dried colonies were placed onto aluminum sample holders and sputtered twice (40 s pre round) with gold (MED 020, BAL-TEC, Balzers, Liechtenstein). Images were acquired at 3500 times magnification with a scanning electron microscope (JEOL-JSM-6060LV, Jeol, Eching, Germany) operated at an acceleration voltage of 5 kV and a ~25 mm working distance.

Contact angle measurements

The wetting behavior of the biofilms was determined by contact angle (CA) and contact angle hysteresis measurements. To measure the static contact angle, 10 μL of distilled water was placed onto the biofilms, and a transversal image was acquired using a high resolution camera (Point Gray Research, Richmond, Canada). The acquired images were processed with the "drop snake" plug-in of the software "Image J" to determine the contact angle values. Contact angle hysteresis was calculated as the difference between the advancing and receding contact angles as follows: first, a drop of 5 μL water was placed onto the biofilms. Then, the advancing CA was obtained by adding 5 μL of water onto this droplet and determining the CA afterwards; similarly, the receding CA was determined by removing 5 μL of water again from the 10 μL drop and measuring the CA afterwards (Fig. S2†).

Antibiotic treatment

The antibiotic susceptibility of the biofilm bacteria was tested by exposing them to kanamycin and tetracycline, respectively, *i.e.*, two examples of antibiotics which are reported to be efficient towards several *Bacillus* species.[35–38] Kanamycin sulfate (Carl-Roth, Karlsruhe, Germany) and tetracycline hydrochloride (Applichem, Darmstadt, Germany), respectively, were dissolved in sterile distilled water at a concentration of 1.25 mg mL^{-1}, which is ~150 times higher than the reported MIC_{90} of kanamycin and tetracycline (8 μg mL^{-1}) for planktonic *B. subtilis* species.[36] Then, the surfaces of mature biofilm colonies were covered with 100 μL of antibiotic solutions for 2 h. At the end of this treatment period, the remaining antibiotic solution was removed from the biofilm surface. A piece of biomass obtained from the center of the biofilm was suspended in 100 μL sterile distilled water and dissolved by vortexing for at least 10 s to allow individual bacterial cells to disperse in the suspension. 50 μL of this suspension (without any perceivable biofilm residues) were then used to determine the cell viability using a commercial LIVE/DEAD BacLight bacterial viability kit L7012 (Thermo Fischer, MA, USA). Different from the manufacturer's guidelines, propidium iodide (PI) and SYTO 9 dyes were mixed in a 4 : 1 volumetric ratio to avoid staining of dead cells with SYTO 9.[39] The bacterial cell suspension was mixed with the dye mixture in a volumetric ratio of 100 : 1 and incubated in the dark for 15 min. Then, 5 μL of this stained sample was placed onto a μ-slide well (Ibidi, Planegg, Germany) and covered with an agarose patch of ~600 μm thickness. The stained bacterial cells were then visualized with an inverse fluorescence microscope (Leica Biosystems, Hesse, Germany) at 63× magnification and using a digital camera (Orca Flash 4.0 C11440-22C, Hamamatsu, Japan) at 2 × 2 binning. Texas red (TXR) and FITC filters were used for imaging the PI and SYTO 9 dyes, respectively. The acquired images were processed with Image J. First, the background values of both images taken with TXR and FITC filters were removed. Then, the brightness intensities of the two images were equalized, these images were merged, and the composed image was converted into RGB values. Cells stained in red or green were identified using color threshold and counted using the particle analysis plug-in of ImageJ.

Based on this analysis, a percentage of dead cells before and after antibiotic treatment was calculated. Then, to account for slight variations in the percentage of dead cells prior to antibiotic treatment, the efficiency of the antibiotic exposure was calculated with the following equation:

$$\%\,\text{antibiotic efficiency} = 100 \times \frac{DR_t - DR_u}{100 - DR_u} \quad (1)$$

Here, DR_t denotes the percentage of dead bacteria after antibiotic treatment and DR_u the percentage of dead bacteria in untreated biofilm samples.

Sample sizes and statistical analysis

For all experiments shown, we obtained data from three independent growth batches. As mentioned above, for erosion tests, a total of 10 identical samples were analyzed per PTFE chip, and 3 PTFE chips were evaluated per growth batch. Rheological measurements were performed with 5 individual samples per batch, and each measured sample contained material from ~20 biofilm colonies. For all other experiments, data was obtained from 3 technical replicates of 9 individual samples, and those were created from 3 distinct growth batches.

A statistical analysis of the data was performed using the software SigmaPlot 12.5 (Systat Inc., San Jose, CA, USA). Statistical significance between samples was assessed by performing two-sample *t*-tests assuming a two-tailed alternative hypothesis with a confidence level of 95%. The assumptions of normal distribution and equal variances were also tested with this software ($p = 0.05$).

Results and discussion

When *B. subtilis* NCIB 3610 bacteria are grown on MSgg agar at 30 °C for 1 day, the obtained biofilm colonies are much more

sensitive to erosion than *B. subtilis* B-1 biofilm colonies grown at the same conditions (Fig. 1): *B. subtilis* NCIB 3610 biofilm colonies show a quick response to shear forces, and almost half of the biofilm mass is removed from the agar substrate within 10 min.

After ~1 h of exposure to shear forces, the eroded biofilm mass saturates at ~80%. In contrast, first detachment of B-1 biofilms is observed after ~30 min only, and less than 10% of the biofilm mass is removed during the time of the whole experiment. Also, while NCIB 3610 biofilms tend to detach from the agar surface as a whole (*i.e.* as a continuous layer), B-1 biofilms are removed from the surface in small pieces.

However, when *B. subtilis* NCIB 3610 bacteria are cultivated in the presence of purified PGA, the obtained PGA-enriched NCIB 3610 biofilm colonies exhibit an erosion resistance behavior that is very different from that of standard NCIB 3610 biofilms. The PGA-enriched colonies are quite stable during the first 30 min, and the maximum of eroded biofilm mass after 1 h of treatment time is with ~27% significantly lower than the value obtained for standard NCIB 3610 colonies (Fig. 2a). However, this value is still significantly higher than that obtained for B-1 colonies. Together, this suggests that artificially including PGA into the matrix of NCIB 3610 biofilms increases the erosion resistance of the biofilm colony – albeit less efficiently than when the bacteria themselves integrate this macromolecule into the matrix.

Of course, by mixing the bacterial overnight culture with a PGA solution the density of the bacteria is reduced by half. To assess a putative influence of this dilution process on the properties of the developed colonies, we perform a control experiment where NCIB 3610 cultures are mixed with a buffer solution devoid of PGA. For this control group, we detect a moder-

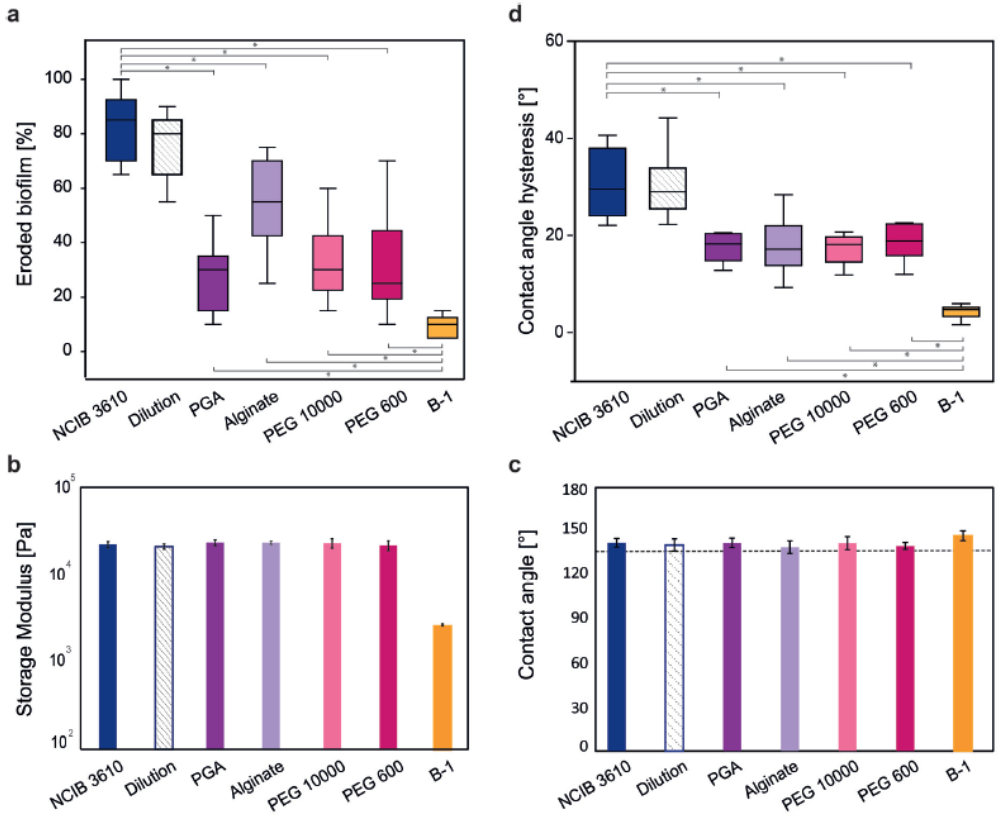

Fig. 2 Influence of (bio)polymer integration into NCIB 3610 biofilms on (a) biofilm erosion, (b) biofilm shear stiffness, and (c, d) biofilm wetting. Wetting experiments are performed with distilled water, and the static contact angle is depicted in (c) whereas contact angle hysteresis is shown in (d). "PGA", "Alginate", "PEG 600" and "PEG 10000" labels refer to NCIB 3610 biofilms enriched with these (bio)polymers. The buffer-diluted NCIB 3610 sample is labelled as "Dilution". The whiskers in (a) and (d) denote the first and the fourth quartile, respectively, of the pooled data obtained from 9 independent samples, which were created from $N = 3$ different growth batches. Error bars in (b) and (c) denote the standard deviation as obtained from 5 or 9 independent samples, respectively, created from $N = 3$ distinct growth batches each. Asterisks in (a) and (d) denote statistical significance considering a p-value of $p = 0.05$.

ately increased erosion resistance at early time points of the experiments (*i.e.*, for erosion times below 30 min) (Fig. 1e). However, at the end of the experiment, the amount of eroded biofilm mass reaches ~75% for those control samples, which is not significantly different from the value obtained for biofilm colonies generated from undiluted NCIB 3610 cultures (Fig. 2a). From this control experiment, we conclude that the strong increase in erosion resistance observed for the PGA-enriched colonies is indeed caused by the addition of PGA into the biofilm matrix.

It was shown before[18] that the shear stiffness of biofilms and their erosion resistance are often related. Thus, in a next step, we ask if the addition of PGA increases the stiffness of NCIB 3610 biofilm colonies. For comparing the mechanical properties of standard and PGA-enriched NCIB 3610 biofilms, we choose the dynamic shear modulus – a material parameter which describes the elastic part of the viscoelastic response of a material to applied shear forces. Since all tested biofilm samples show viscoelastic properties which are largely independent of the probing frequency (Fig. S3†), we focus on the storage modulus determined at an intermediate frequency range and refer to this quantity as 'biofilm stiffness' from now on. Surprisingly, the stiffness of standard and PGA-enriched NCIB 3610 biofilms is almost identical with ~23 kPa each (Fig. 2b). This demonstrates that the artificial PGA integration into the biofilm matrix does not significantly affect this biofilm property – at least at the PGA concentrations used here. In contrast, the stiffness of B-1 biofilm colonies is one order of magnitude lower ($G' \sim 2.6$ kPa), which illustrates that, for the conditions studied here, the biofilm stiffness is not mainly responsible for the observed difference in erosion behavior.

At this point, it is important to recall that the shear forces driving the erosion process are created by agitated water. As a consequence, the wetting properties of the biofilm colonies can be an important parameter influencing their erosion resistance. Yet, both standard and PGA-enriched NCIB 3610 as well as B-1 biofilm colonies exhibit superhydrophobic surfaces with very similar contact angles in the range of 140° (Fig. 2c and Fig. S2†). This seems to challenge the idea that differences in the biofilm wetting behavior might be responsible for the differences in erosion properties. However, despite having similar contact angles, the wetting properties of superhydrophobic materials can differ,[30] and this also holds true for biofilms.[28] B-1 biofilm colonies repel water more efficiently than NCIB 3610 biofilms: on the former, water droplets roll off the surface when the biofilm sample is tilted (lotus-like behavior); on the latter, the biofilm exhibits strong adhesive forces towards water which makes a droplet stick when the sample is tilted or turned upside down (rose-like behavior). Previous experiments have demonstrated that it is possible to alter the mode of biofilm wetting from lotus-like to rose-like by exposing the biofilm to concentrated ionic solutions.[17] Thus, the opposite behavior might occur here as a result of PGA integration into the biofilm matrix.

Indeed, when performing wetting tests with the different colonies, we experience that PGA-enriched samples show intermediate properties compared to both, lotus- and rose-like biofilms, respectively. On those PGA-enriched colonies, the water droplets can be restrictedly moved across the surface of the biofilm colony by pushing them manually, but they stick again once the pushing force subsides. To quantify this impression and to clarify the mode of superhydrophobicity, we measure the contact angle hysteresis of the samples by subtracting the receding contact angle from the advancing contact angle (see Methods for details). Standard NCIB 3610 biofilm colonies exhibit a relatively large contact angle hysteresis of (31 ± 7)°, which indicates strong adhesion towards water (Fig. 2d and Fig. S2†). This agrees with previous results obtained for those biofilms grown at the conditions studied here[28] and is typical for rose-like hydrophobicity. In contrast, lotus-like surfaces exhibit negligible contact angle hysteresis representing very low adhesion towards water, and this is what we observe for *B. subtilis* B-1 colonies (Fig. 2d and Fig. S2†). Interestingly, incorporating PGA into NCIB 3610 biofilm colonies lowers the contact angle hysteresis to 18 ± 3° (Fig. 2d and Fig. S2†). This is quite surprising considering that PGA is a hydrophilic, even hygroscopic molecule. However, even though this reduction in contact angle hysteresis is significant, the hysteresis value is still significantly higher than what we determine on *B. subtilis* B-1 colonies – which underscores the qualitative impression described above. Also here, control samples demonstrate that the observed effect is due to the PGA addition, as we measure an equally high hysteresis value on biofilms grown from diluted NCIB 3610 liquid culture as for standard NCIB 3610 biofilm colonies. From the experiments conducted so far, we conclude that the artificial incorporation of PGA into the matrix of NCIB 3610 biofilm colonies affects both, the mode of biofilm wetting and the biofilm erosion resistance.

Our next goal is to understand how PGA incorporation alters the detailed mode of hydrophobicity of NCIB 3610 biofilms. The wetting resistance of a surface can be increased by either increasing the surface tension *via* chemical modification or by increasing the surface roughness.[27] Since it is extremely unlikely that the integration of a hydrophilic polymer were to boost the hydrophobic properties of the biofilm colonies through chemical effects, we investigate the surface topography of the biofilm. For this purpose, 3-D images of the biofilm surfaces are acquired using light profilometry (Fig. 3a). From those images, it becomes immediately clear that *B. subtilis* B-1 biofilms have a much higher surface roughness than all the other biofilm variants. This impression can be quantified by calculating classical ISO roughness parameters from the topographical images: the root mean square roughness, Sq, the developed interfacial surface ratio, Sdr, and the maximum height, Sz, all return significantly larger values for B-1 biofilm colonies than for standard NCIB 3610 colonies (Fig. 3b). For the PGA-enriched samples, both the Sq and Sz values are significantly altered compared to standard NCIB 3610 colonies. This result seems to underscore our notion that topographical alterations are responsible for the observed change in wetting mode. However, both Sq and Sz are *decreased* for the PGA-enriched samples, which seems counter-

a

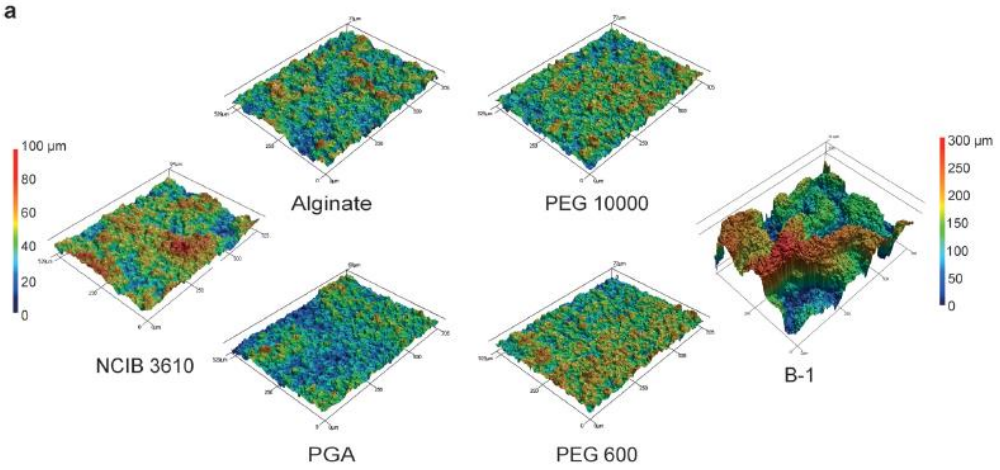

b

	Sdr [%]	Sq [µm]	Sz [µm]	Sp [µm]	Sv [µm]	Sk [µm]	Svk [µm]	Vvv [mL/m^2]	Vvc [mL/m^2]
NCIB 3610	157 ± 11	12 ± 2	92 ± 14	45 ± 7	47 ± 7	30 ± 4	11 ± 2	1.31 ± 0.23	14.7 ± 2.2
Dilution	161 ± 6	12 ± 2	86 ± 10	42 ± 6	44 ± 6	29 ± 4	11 ± 2	1.25 ± 0.16	14.1 ± 2.1
PGA	147 ± 20	10 ± 1*	79 ± 6*	41 ± 3	39 ± 4*	26 ± 2*	9 ± 1*	1.10 ± 0.12*	12.6 ± 0.9*
Alginate	151 ± 22	11 ± 2	80 ± 8*	40 ± 6	40 ± 4*	27 ± 3	10 ± 2	1.19 ± 0.18	13.1 ± 2.2
PEG 10000	150 ± 4	10 ± 1*	77 ± 9*	38 ± 5*	39 ± 6*	26 ± 4*	9 ± 2	1.11 ± 0.15*	12.6 ± 1.6*
PEG 600	146 ± 20	10 ± 3	76 ± 17*	38 ± 10	38 ± 8*	27 ± 7	9 ± 2	1.11 ± 0.28	12.9 ± 3.8
B-1	919 ± 526*	70 ± 25*	333 ± 95*	180 ± 55*	153 ± 44*	171 ± 45*	33 ± 13*	5.21 ± 1.74*	98 ± 39*

c

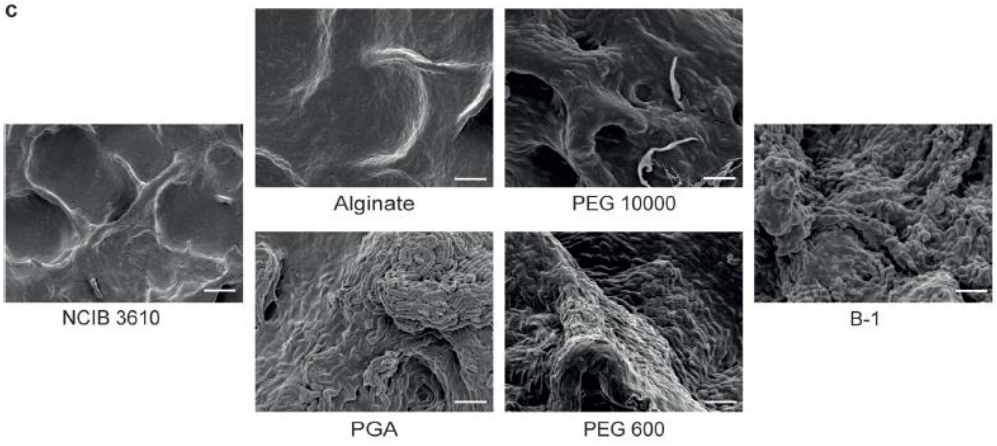

Fig. 3 Comparison of surface features from different *B. subtilis* biofilm variants. "PGA", "Alginate", "PEG 600" and "PEG 10000" labels refer to NCIB 3610 biofilms enriched with these (bio)polymers. The buffer-diluted NCIB 3610 sample is labelled as "Dilution". (a) Images of biofilm surfaces as obtained *via* profilometry at 20× magnification. The scale bar on the left applies to all images with the exception of the B-1 sample which the scale bar in the right is included for. (b) Metrological parameters were calculated from a total of 9 profilometric images per condition (3 images per sample, n = 3 different biofilm samples obtained on N = 3 different growth batches). Asterisks denote statistical significance between the modified biofilm samples and standard NCIB 3610 biofilm colonies considering a p-value of p = 0.05. In addition, all of the modified NCIB 3610 samples were significantly different from the B-1 samples. (c) SEM images of biofilm surfaces at 3500× magnification. The scale bar represents 5 µm and applies to all SEM images shown.

intuitive considering that those samples exhibit a more lotus-like superhydrophobicity.

To obtain more detailed information about the surface topography of the different biofilm colonies, SEM images are acquired at 3500× magnification (Fig. 3c and Fig. S4†). Also on this length scale, *B. subtilis* B-1 biofilms exhibit a rougher surface than NCIB 3610 biofilms. Individual cells are very well visible in the B-1 biofilm where they stand out from the biofilm surface. In contrast, most bacteria appear to be embedded into the biofilm matrix of NCIB 3610 biofilms which – as a consequence – has a much smoother texture than B-1 biofilm colonies. In a good agreement with the surface images obtained by light profilometry, SEM images of NCIB 3610 colonies reveal relatively large cavities with flat, smooth bottoms. Those cavities are absent on B-1 colonies and are not present on PGA-enriched NCIB 3610 biofilms either. Instead, on those PGA-enriched colonies, the individual bacteria are clearly visible and stand out from the biofilm matrix. Thus, also at this higher magnification, there are clear structural surface features in which PGA-enriched biofilms resemble B-1 colonies. With this visual impression in mind, we reexamine the topographical images obtained with light profilometry by calculating more specific metrological parameters which characterize cavities/valley structures.

Above, we have already mentioned the Sz value – a parameter that measures the maximum peak height reaching from the deepest valley to the highest peak. Mathematically, this parameter can be split into two contributions, the maximum peak height, Sp, and the maximum pit height, Sv. By analyzing those two contributing parameters individually, we expect to find differences in the valley structure of the biofilms, but not necessarily in their peak structure. In full agreement with this expectation, the Sv value is significantly decreased for PGA-enriched biofilms compared to standard NCIB 3610 biofilms, which underscores our visual impression from the SEM images. Also, there is no significant difference between standard and PGA-enriched biofilms in terms of Sp. In retrospect, this explains why we found a reduced value in the total peak height of PGA-enriched biofilms: this is caused by a reduction of the valley depths. Additional metrological parameters which quantify surface features related to cavities/valleys (such as Sk, Svk, Vvv and Vvc – see Methods for details) underscore this analysis and all return significant differences between unmodified and PGA-enriched colonies.

How can the disappearance of cavities alter the mode of biofilm superhydrophobicity? A reduced contact angle hysteresis indicates that the adhesive forces towards water (as typical for rose-like superhydrophobicity) are weakened. In a model picture describing the physical wetting state related to rose-like superhydrophobicity (*i.e.*, the impregnated Cassie state), the water is thought to penetrate into pits located between roughness feature structures, and this efficient contact between water and the substrate gives rise to the adhesive forces pinning water droplets onto the surface.

On the biofilms we examine here, such pits are present on NCIB 3610 biofilms showing rose-like superhydrophobicity, but not on B-1 biofilms showing lotus-like superhydrophobicity. In agreement with this picture, also PGA-enriched biofilm colonies lack this feature, which could explain why the contact angle hysteresis determined on those modified biofilms is reduced. From the topographical analysis of our biofilm colonies, we conclude that incorporating PGA into NCIB 3610 biofilms does not increase the surface roughness of the biofilm colonies but has a more subtle influence on the surface structure: it fills the pits and valleys in between elevated surface structures and thus reduces the surface cavities a water droplet can adhere to. In turn, the mode of superhydrophobicity is slightly altered and – on a macroscopic level – the erosion resistance of the biofilm colony is strongly increased.

Previous experiments on hydrophobic biofilm colonies have shown that the detailed mode of superhydrophobicity also affects the resilience of bacterial biofilm colonies towards topical treatment with aqueous antibiotic solutions. Thus, in a next step, we ask if PGA-integration into NCIB 3610 biofilms affects the susceptibility of the embedded bacteria towards antibiotics (see Methods). We chose two model antibiotics, kanamycin and tetracycline, which are both efficient towards planktonic *B. subtilis* bacteria.[36] However, as expected, we obtain different results when we challenge NCIB 3610 and B-1 biofilms with those antibiotics. When *B. subtilis* biofilms are exposed to solutions of kanamycin or tetracycline, respectively, after 2 h of incubation the fraction of dead bacterial cells in rose-like NCIB 3610 biofilms is increased from initially ~48% to ~90%. In contrast, this increase is much smaller for lotus-like B-1 biofilms, where the fraction of dead cells is ~31% before the antibiotic challenge and ~53% afterwards. This difference in susceptibility is – to a certain extent – due to the differences in surface superhydrophobicity.

To account for different levels of initially dead cells before the antibiotic challenge, we calculate an antibiotic efficiency, *i.e.*, the relative percentage of bacteria killed by the antibiotics (see Methods for detail) (Fig. 4). For standard NCIB 3610 biofilms using the numbers listed above, this killing efficiency is (83 ± 18)% for kanamycin and (77 ± 15)% for tetracycline treatment, respectively. For lotus-like *B. subtilis* B-1 biofilms, both antibiotics have a similar efficiency of only ~30%. In a next step, we ask if the integration of PGA affects this outcome. Importantly, we find similar fractions of initially dead bacterial cells in standard, diluted and PGA-enriched NCIB 3610 biofilms; this guarantees that a (putative) observed increase in bacterial death would be caused by the antibiotics and not by our modification of the biofilm matrix (Fig. S5†). However, the incorporation of PGA into the NCIB 3610 biofilm matrix does not cause a significant change in this efficiency, as we determine (79 ± 10)% for kanamycin treatment and (74 ± 10)% for tetracycline treatment.

Although this result appears to be somewhat disappointing, it further underscores that the PGA-enriched biofilms have not reached a real lotus-like wetting resistance yet. Whereas a reduced depth of cavities on the surface of PGA-enriched NCIB 3610 biofilms seems to be sufficient to weaken the attractive forces between liquids and the surface thus affecting contact

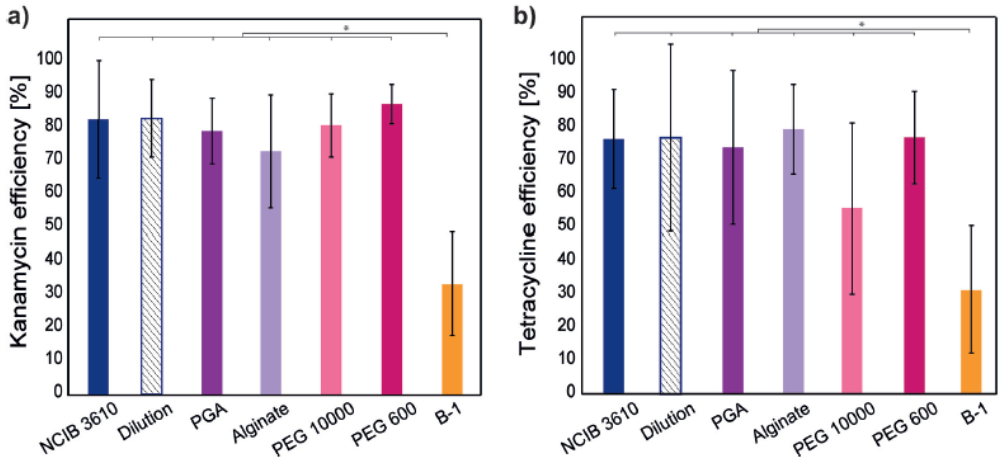

Fig. 4 Efficiency of (a) kanamycin and (b) tetracycline treatment of different *B. subtilis* biofilms. "PGA", "Alginate", "PEG 600" and "PEG 10000" labels refer to NCIB 3610 biofilms enriched with these (bio)polymers. The buffer-diluted NCIB 3610 sample is labelled as "Dilution". The values shown describe the relative killing efficiency of the two antibiotics considering slight sample-to-sample variations in the content of dead bacterial biofilm cells prior to antibiotic treatment (see Methods for details). The error bars denote the standard deviation as obtained from $n = 9$ independent samples, which were created from $N = 3$ distinct growth batches. Asterisks denote statistical significance between the results obtained for B-1 biofilm colonies and the different variants of NCIB 3610-derived biofilm colonies considering a p-value of $p = 0.05$.

angle hysteresis and biofilm erosion, this modification is not strong enough to prevent microscopic contact of liquids with the biofilm surface. For lotus-like biofilms, there are microscopic air pockets on the biofilm surface which constitute a physical barrier between the liquid phase and the biofilm surface, and this restricts the liquid–biofilm interaction. Thus, we conclude that the surface of PGA-enriched NCIB 3610 biofilm is still largely in direct contact with the antibiotic solution, and the antibiotics may very well enter the biofilm matrix by diffusion. Of course, the resilience of biofilm bacteria towards antibiotics depends on many factors, including the diffusion barrier effect of the biofilm matrix.[40] The permeability of a biofilm was suggested to be related to its mechanical properties *via* the biofilm porosity.[41] However, as we mentioned it above, the addition of PGA into NCIB 3610 biofilms does not alter the biofilm stiffness; thus, we speculate that the microscopic permeability of those PGA-enriched biofilms is not strongly altered either.

In a last step, we ask whether the effects described so far are specific for PGA, or if integrating a different macromolecule into the matrix of NCIB 3610 biofilms can have a similar effect. PGA is a hydrophilic, polyanionic macromolecule with strongly hygroscopic properties.[42] Another example of such a hydrophilic, polyanionic macromolecule is alginate, a biopolymer which is the main constituent of, *e.g.*, the biofilm matrix of *Pseudomonas aeruginosa*. When we analyze the erosion behavior of alginate-enriched NCIB 3610 biofilm colonies, we find that ~55% of the biofilm mass is eroded after exposure to shear forces for 60 min (Fig. 2a). This value is higher than what we described for B-1 and PGA-enriched NCIB 3610 biofilms, but still lower than what we obtained for standard NCIB 3610 biofilms. Moreover, for those alginate-enriched NCIB 3610 biofilms, the shear stiffness is comparable to that of standard NCIB 3610 biofilms (Fig. 2b), and also the static contact angle (Fig. 2c and Fig. S2†) and the contact angle hysteresis (Fig. 2d and Fig. S2†) of alginate-enriched samples return similar results as we obtained for PGA-enriched biofilms. Thus, it appears that alginate integration into the biofilm matrix has a similar effect on the mode of biofilm superhydrophobicity as PGA integration. When we quantify the surface topography of alginate-enriched biofilms, we find similar topographical alterations as for PGA-enriched biofilms, but – overall – less pronounced (Fig. 3a, c and Fig. S4†). This can be attributed to heterogeneous results, *i.e.*, some alginate-enriched samples show similarly strong alterations as the PGA-enriched samples, but some do not. We attribute this high sample-to-sample variation to experimental challenges during the sample preparation, *i.e.* difficulties with fully dissolving alginate in the buffer and increased uncertainties arising from pipetting small amounts of the highly viscous alginate solution. SEM images reveal that alginate-enriched and standard NCIB 3610 biofilms look similar on a microscopic scale (Fig. 3c and Fig. S4†). Thus, it is not surprising that an antibiotic treatment of alginate-enriched biofilms returns similar results as for standard NCIB 3610 biofilm colonies (Fig. 4).

So far, we showed that the integration of polyanionic, hydrophilic biomacromolecules such as PGA or alginate has a similar effect on the erosion and wetting behavior of NCIB 3610 biofilms. Surprisingly, very similar results are obtained

when an uncharged, synthetic macromolecule such as PEG is added to the biofilm. As depicted in Fig. 1–4 (see also Fig. S2–5†), both, PEG macromolecules with high (PEG 10 000, MW: 9000 g mol^{-1}) and low (PEG 600, MW: ~600 g mol^{-1}) molecular weight lead to very similar effects as PGA or alginate do. Thus, we conclude that the artificial incorporation of a macromolecule into the matrix of *B. subtilis* NCIB 3610 biofilms affects the biofilm surface topography and – as a direct consequence – alters the mode of superhydrophobicity and increases the erosion resistance of the biofilm. Surprisingly, the detailed biochemical properties of the added macromolecules seem not to matter much, and similar results can be obtained with a set of very different (bio)polymers. This indicates that the incorporated (bio)polymers do not specifically interact with the bacteria or the existing biofilm matrix components. Instead, they most likely act as additional 'building blocks' which are used by the bacteria to construct the biofilm, *e.g.*, as 'fillers' thus reducing the depth of the surface cavities.

There is increasing evidence that the material properties of bacterial biofilms depend strongly on the detailed composition of the matrix the bacteria are embedded in – and only to a lesser degree on the bacteria themselves, who have created this matrix. Here, we have demonstrated that growing the identical strain of *B. subtilis* NCIB 3610 bacteria in the presence of 'foreign' biomolecules results in very different material properties of the resulting biofilm colonies. In particular, we have observed a strongly enhanced erosion resistance for the biopolymer-enriched samples. Our data suggests that this enhancement in erosion resilience is enabled by a subtle alteration in the mode of superhydrophobicity, which seems to be due to a reduction of cavity depths on the surface of the biofilm colonies.

The well-known relation between surface topography and superhydrophobicity as described for plant leaves[26,27,29,30,43] and the existence of both, lotus-like and rose-like behavior, has been validated before for bacterial biofilms created by different bacterial species.[17,28] However, we here detected a type of superhydrophobicity with properties in between those of rose-like and lotus-like wetting resistance. This intermediate level of non-wetting combines properties from the two other, traditional superhydrophobic states, *i.e.*, a high erosion resistance as typical for lotus-like biofilms and microscopic contact to water as typical for rose-like biofilms.

Conclusions

Creating biofilms with a special variant of superhydrophobicity as described here could be highly interesting for biotechnological applications: if beneficial biofilms are constantly exposed to flowing water from which they need to access molecules, *i.e.* for detoxification or metabolic conversion, they can be more efficiently used if they remain stable and are not eroded easily. Existing efforts to enhance the erosion resistance of beneficial biofilms used in wastewater treatment rely on modifying the membrane substrate the biofilms are grown.[44] The strategy we introduce here is independent of the substrate the biofilms are grown on. Moreover, since a wide range of different (bio)polymers can be used to achieve this effect, our approach could open new avenues for novel applications of biofilm-forming bacteria in biotechnology.

Author contributions

ENH and OL planned the experiments, which were conducted and analyzed by ENH. The manuscript was written by ENH and OL.

Conflicts of interest

There are no conflicts of interest to declare.

Acknowledgements

We thank Carolina Falcón García for assistance with the experiments and helpful discussions. This work was supported by the Deutsche Forschungsgemeinschaft (DFG) through project B11 in the framework of SFB863. ENH acknowledges a fellowship granted by the Turkish Ministry of Education.

References

1 P. Pinet and M. Souriau, *Tectonics*, 1988, 7, 563–582.
2 S. R. Runnels, *J. Electrochem. Soc.*, 2006, 141, 1900–1904.
3 G. I. Parslow, D. J. Stephenson, J. E. Strutt and S. Tetlow, *Wear*, 1997, 212, 103–109.
4 J. L. Lister and A. R. Horswill, *Front. Cell. Infect. Microbiol.*, 2014, 4, 1–9.
5 L. Hall-Stoodley and P. Stoodley, *Trends Microbiol.*, 2005, 13, 7–10.
6 A. Ohashi, T. Koyama, K. Syutsuba and H. Harada, *Water Sci. Technol.*, 1999, 39, 261–268.
7 C. Picioreanu, M. C. M. Van Loosdrecht and J. J. Heijnen, *Biotechnol. Bioeng.*, 2001, 72, 205–218.
8 B. D'Acunto, L. Frunzo, I. Klapper, M. R. Mattei and P. Stoodley, *Math. Biosci.*, 2019, 307, 70–87.
9 S. C. Chew and L. Yang, in *Encyclopedia of Food and Health*, Academic Press, 2016, pp. 407–415.
10 A. Hashem, B. Tabassum and E. Fathi Abd_Allah, *Saudi J. Biol. Sci.*, DOI: 10.1016/j.sjbs.2019.05.004.
11 J. Jeżewska-Frąckowiak, K. Seroczyńska, J. Banaszczyk, G. Jedrzejczak, A. Żylicz-Stachula and P. M. Skowron, *Acta Biochim. Pol.*, 2018, 65, 509–519.
12 M. Morikawa, *J. Biosci. Bioeng.*, 2006, 101, 1–8.
13 T. K. Wood, S. H. Hong and Q. Ma, *Trends Biotechnol.*, 2011, 29, 87–94.
14 C. K. Ng, A. Mohanty and B. Cao, in *Bio-Nanoparticles: Biosynthesis and Sustainable Biotechnological Implications*,

ed. O. V. Singh, John Wiley & Sons Inc., 1st edn, 2015, pp. 83–99.
15 F. Costa, B. Silva and T. Tavares, in *Current Developments in Biotechnology and Bioengineering: Bioprocesses, Bioreactors and Controls*, 2016, pp. 143–175.
16 S. J. Pogorzelski, A. Z. Mazurek and A. Szczepanska, *J. Mar. Syst.*, 2013, **119–120**, 50–60.
17 C. Falcón García, F. Stangl, A. Götz, W. Zhao, S. A. Sieber, M. Opitz and O. Lieleg, *Biomater. Sci.*, 2019, 7, 220–232.
18 S. Grumbein, M. Opitz and O. Lieleg, *Metallomics*, 2014, 6, 1441–1450.
19 M. A. Demeter, J. A. Lemire, R. J. Turner and J. J. Harrison, in *Biofilms in Bioremediation: Current Research and Emerging Technologies*, ed. G. Lear, Caister Academic Press, Norfolk, UK, 2016, pp. 43–57.
20 S. Kesel, S. Grumbein, M. Tallawi, A. Marel, O. Lieleg and M. Opitz, *Appl. Environ. Microbiol.*, 2016, 82, 2424–2432.
21 M. Klotz, M. Kretschmer, A. Goetz, S. Ezendam, O. Lieleg and M. Opitz, *RSC Adv.*, 2019, 9, 11521–11529.
22 M. Morikawa, S. Kagihiro, M. Haruki, K. Takano, S. Branda, R. Kolter and S. Kanaya, *Microbiology*, 2006, 152, 2801–2807.
23 R. Branda, S. S. González-Pastor, J. E. Ben-Yehuda, S. Losick and R. Kolter, *Proc. Natl. Acad. Sci. U. S. A.*, 2001, 98, 11621–11626.
24 S. S. Branda, F. Chu, D. B. Kearns, R. Losick and R. Kolter, *Mol. Microbiol.*, 2006, 59, 1229–1238.
25 K. Kobayashi and M. Iwano, *Mol. Microbiol.*, 2012, 85, 51–66.
26 M. Nosonovsky and B. Bhushan, *Ultramicroscopy*, 2007, 107, 969–979.
27 H. Y. Erbil, A. L. Demirel, Y. Avci and O. Mert, *Science*, 2011, 299, 1377–1380.
28 M. Werb, C. Falcón García, N. C. Bach, S. Grumbein, S. A. Sieber, M. Opitz and O. Lieleg, *npj Biofilms Microbiomes*, 2017, 3, 1–10.
29 B. Bhushan and M. Nosonovsky, *Philos. Trans. R. Soc., A*, 2010, 368, 4713–4728.
30 S. Wang and L. Jiang, *Adv. Mater.*, 2007, 19, 3423–3424.
31 R. A. Gross, in *Biopolymers from Renewable Resources*, ed. D. L. Kaplan, Springer, 1st edn, 1998, pp. 195–217.
32 Michigan metrology, https://www.michmet.com/3d_s_functional_parameters_spksksvksmr1smr2.htm, (accessed 14 June 2019).
33 Michigan metrology, https://www.michmet.com/3d_s_height_parameters_spsvsz.htm.
34 Introduction to roughness, https://www.keyence.com/ss/products/microscope/roughness/surface/svk-reduced-dale-height.jsp.
35 P. Trieu-Cuot, A. Klier and P. Courvalin, *MGG, Mol. Gen. Genet.*, 1985, 198, 348–352.
36 D. B. Adimpong, K. I. Sørensen, L. Thorsen, B. Stuer-Lauridsen, W. S. Abdelgadir, D. S. Nielsen, P. M. F. Derkx and L. Jespersen, *Appl. Environ. Microbiol.*, 2012, 78, 7903–7914.
37 D. J. Weber, S. M. Saviteer, W. A. Rutala and C. A. Thomann, *Antimicrob. Agents Chemother.*, 1988, 32, 642–645.
38 J. D. Coonrod, P. J. Leadley and T. C. Eickhoff, *J. Infect. Dis.*, 1971, 123, 102–105.
39 S. M. Stocks, *Cytometry, Part A*, 2004, 61, 189–195.
40 R. Singh, S. Sahore, P. Kaur, A. Rani and P. Ray, *Pathog. Dis.*, 2016, 74, 1–6.
41 N. Billings, A. Birjiniuk, T. S. Samad, P. S. Doyle and K. Ribbeck, *Rep. Prog. Phys.*, 2015, 78, 36601.
42 T. Candela and A. Fouet, *Mol. Microbiol.*, 2006, 60, 1091–1098.
43 C. Yang, U. Tartaglino and B. N. J. Persson, *Phys. Rev. Lett.*, 2006, 97, 1–4.
44 S. Lackner, M. Holmberg, A. Terada, P. Kingshott and B. F. Smets, *Water Res.*, 2009, 43, 3469–3478.

Electronic Supplementary Material (ESI) for Biomaterials Science.

Supplementary Information for

Biopolymer-enriched *B. subtilis* NCIB 3610 biofilms exhibit increased erosion resistance

Elif N. Hayta and Oliver Lieleg#

Munich School of Bioengineering and Department of Mechanical Engineering,
Technical University of Munich, 85748 Garching, Germany

Corresponding author:

Prof. Dr. Oliver Lieleg

Department of Mechanical Engineering and Munich School of Bioengineering,

Technical University of Munich,

Boltzmannstraße 11, 85748 Garching, Germany

e-mail: oliver.lieleg@tum.de,

phone: +49 89 289 10952, fax: + 49 89 289 10801

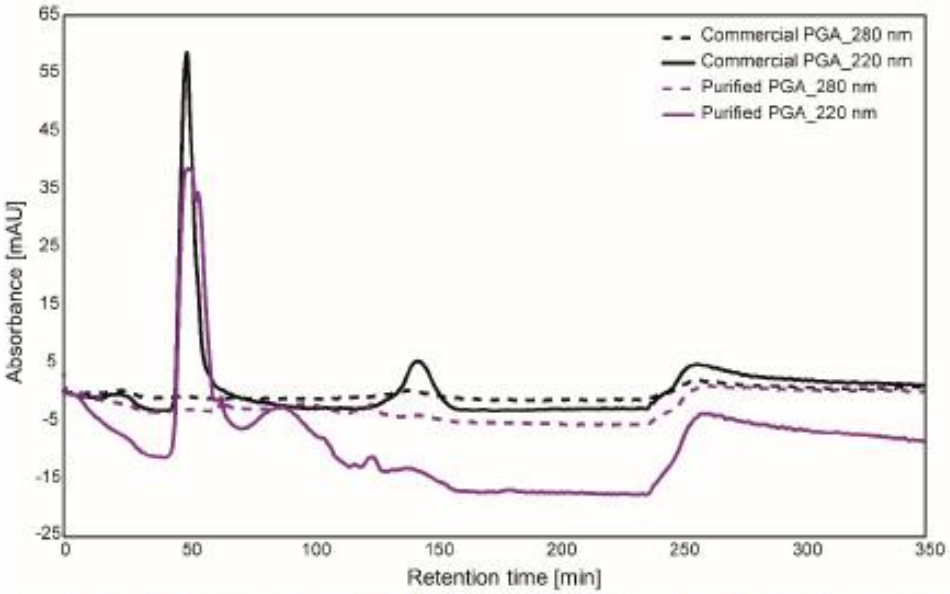

Figure S1. Gel filtration chromatograms of commercial and in-lab purified PGA. The same amount of a commercial or purified PGA solution (concentration 0.05% (w/v)) was run through a Sepharose 6FF XK50/100 column, and the absorbance at 220 nm and 280 nm was compared. Both PGA variants give a strong peak at 220 nm and at the same retention time. Moreover, neither sample exhibits significant absorption at 280 nm, which shows that the purity of both samples is comparable.

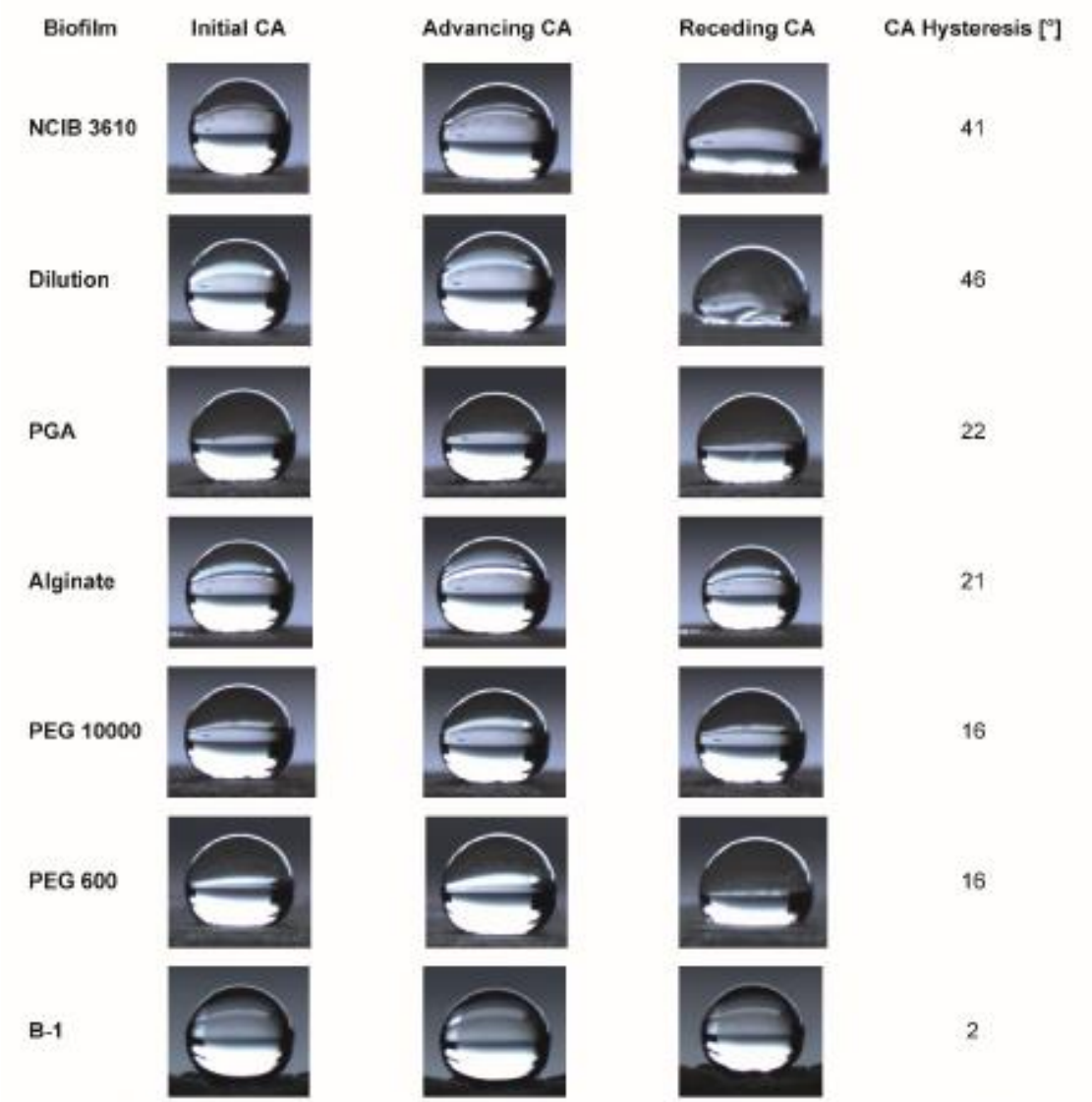

Figure S2. Exemplary images of water droplets on biofilm samples as used for the determination of contact angles. Initial (5 µL), advancing (10 µL) and receding (5 µL) contact angle images of water droplets on each biofilm colony were acquired, and the contact angle hysteresis was calculated by subtracting the receding contact angle from the advancing contact angle.

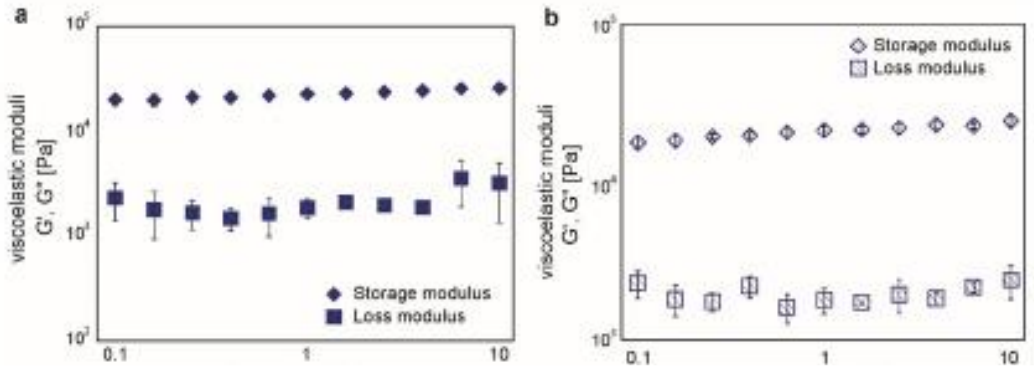

Figure S3. Viscoelastic properties of different *B. subtilis* biofilms. Frequency spectra showing the storage (*G'*) and loss (*G''*) moduli of **a)** standard, **b)** diluted, as well as **c)** PGA-, **d)** alginate-, **e)** PEG 10000-, or **f)** PEG 600-enriched NCIB 3610 and **g)** B-1 biofilms. The error bars denote the standard deviation as obtained from $n = 5$ independent samples which were generated from $N = 3$ different growth batches.

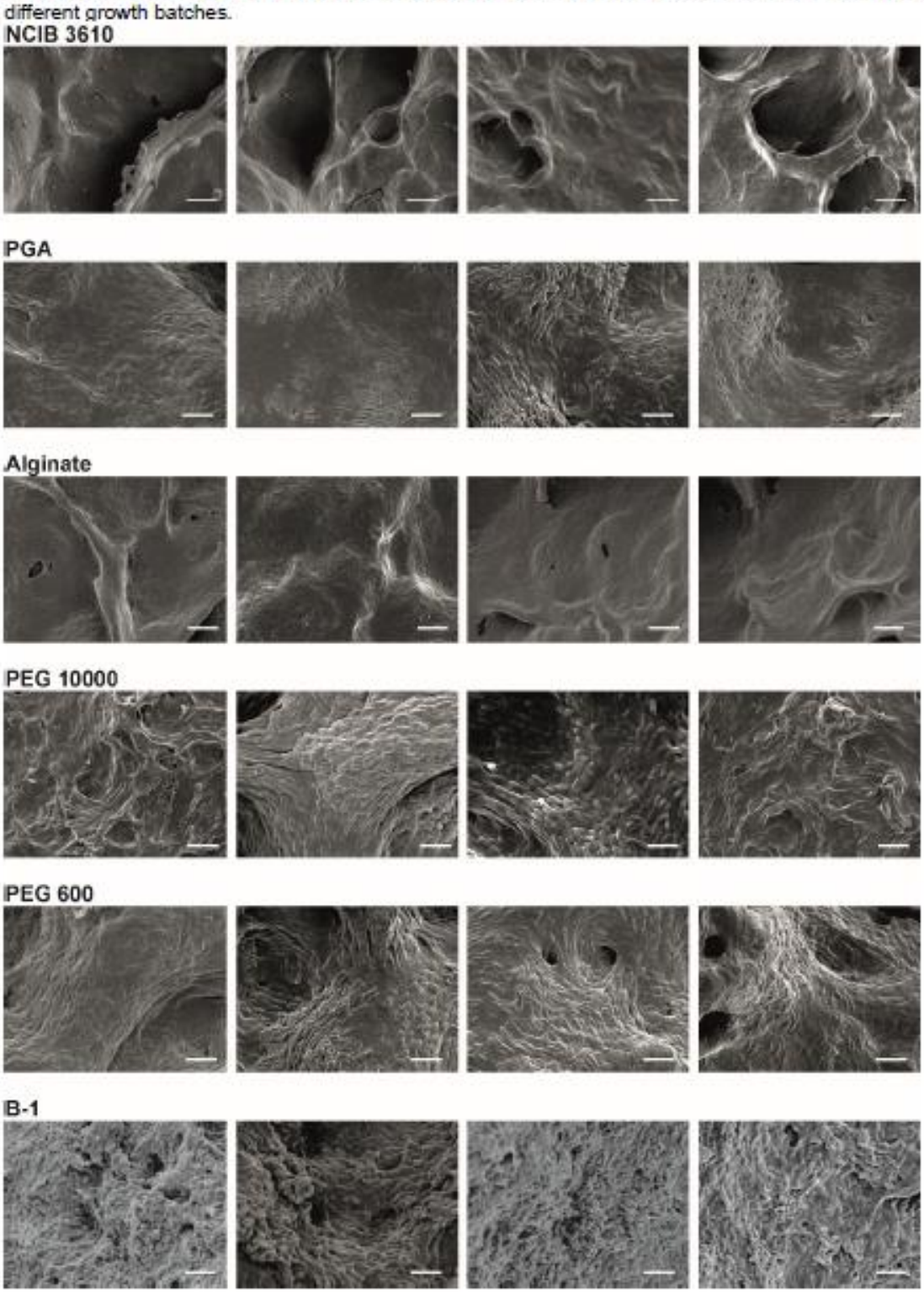

Figure S4. SEM images of obtained from the surface of different *B. subtilis* biofilm variants. All images shown were acquired at 3500x magnification; the scale bars represent 5 µm. "PGA", "Alginate", "PEG 600" and "PEG 10000" labels refer to NCIB 3610 biofilms enriched with these

(bio)polymers.

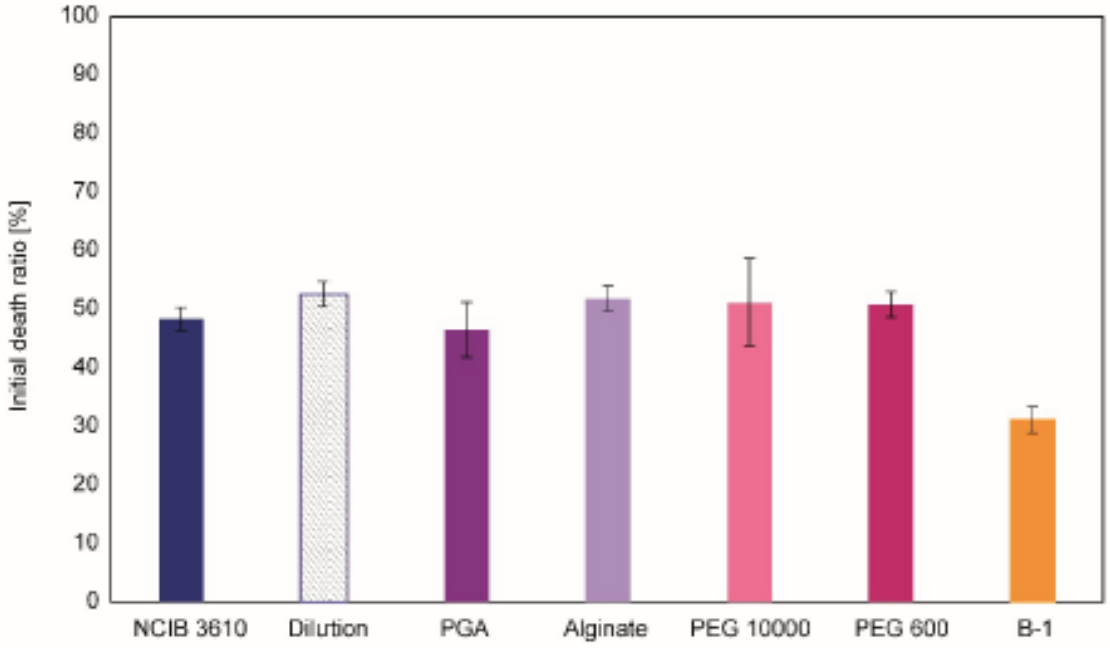

Figure S5. Fraction of dead biofilm cells before antibiotic treatment. The viability of the bacterial cells was tested by a two-color staining method using a LIVE/DEAD BacLight viability kit (see main paper for details). "PGA", "Alginate", "PEG 600" and "PEG 10000" labels refer to NCIB 3610 biofilms enriched with these (bio)polymers. The buffer-diluted NCIB 3610 sample is labelled as "Dilution". The error bars denote the standard deviation as obtained from $n = 9$ independent samples, created from $N = 3$ distinct growth batches each.

A.3 Topography quantifications allow for identifying the contribution of parental strains to physical properties of co-cultured biofilms

Biofilm 3 (2021) 100044

Contents lists available at ScienceDirect

Biofilm

journal homepage: www.elsevier.com/locate/biofilm

Topography quantifications allow for identifying the contribution of parental strains to physical properties of co-cultured biofilms

Elif N. Hayta [a,b], Carolin A. Rickert [a,b], Oliver Lieleg [a,b,*]

[a] Munich School of Bioengineering and Department of Mechanical Engineering, Technical University of Munich, 85748, Garching, Germany
[b] Center for Protein Assemblies (CPA), Technical University of Munich, Ernst-Otto-Fischer Straße 8, 85748, Garching, Germany

ARTICLE INFO

Keywords:
Biofilms
Topography
Wetting behavior
Synergy
Feature detection
Computational image classification

ABSTRACT

Most biofilm research has so far focused on investigating biofilms generated by single bacterial strains. However, such single-species biofilms are rare in nature where bacteria typically coexist with other microorganisms. Although, from a biological view, the possible interactions occurring between different bacteria are well studied, little is known about what determines the material properties of a multi-species biofilm. Here, we ask how the co-cultivation of two *B. subtilis* strains affects certain important biofilm properties such as surface topography and wetting behavior. We find that, even though each daughter colony typically resembles one of the parent colonies in terms of morphology and wetting, it nevertheless exhibits a significantly different surface topography. Yet, this difference is only detectable via a quantitative metrological analysis of the biofilm surface. Furthermore, we show that this difference is due to the presence of bacteria belonging to the 'other' parent strain, which does not dominate the biofilm features. The findings presented here may pinpoint new strategies for how biofilms with hybrid properties could be generated from two different bacterial strains. In such engineered biofilms, it might be possible to combine desired properties from two strains by co-cultivation.

Introduction

With the first cry of a baby, an endless debate starts: Does he/she resemble mom or dad? Not only seem all relatives to have a different opinion on this topic, the question itself appears to be ill-conceived. Clearly, every child has inherited certain traits from both of his parents, and subjective 'morphological' classifications by an 'expert panel' are not sufficient to detect the parents' contributions. Similarly, simple morphological descriptions of other biological entities can be misleading. For instance, *Myrmarachne formicaria*, an animal known as ant-like jumping spider (which was chosen as the "spider of the year 2019" by the European Society of Arachnology) is famous for its incredible capability of mimicking ants [1]. Often enough, those spiders cannot be distinguished from ants by an unexperienced observer, and sometimes even quantitative approaches are required to assign them correctly [2].

A famous case from material science, where a quantitative characterization is required to achieve a correct categorization is the wetting properties of superhydrophobic surfaces. For instance, both rose petals and lotus leaves exhibit superhydrophobic surfaces with extremely high contact angles; yet, they are still different from each other in terms of droplet adhesion: water droplets strongly adhere to rose petals but easily roll off from lotus leaves [3]. Whereas this is a qualitative criterion, a more detailed quantification procedure (i.e., a contact angle hysteresis measurement) correctly classify a surface as rose-like or lotus-like [3,4].

The wetting behavior of a material is dictated by a combination of surface chemistry and topography [5,6]. For a superhydrophobic surface, low surface energy and hierarchical roughness features in the micro- and nanoscale are required [6,7]. A detailed relation between the wetting behavior and the surface topography has also been demonstrated for biofilms – a special form of surface-attached bacteria which are embedded into a matrix of secreted macromolecules [8]. Also, the susceptibility of biofilms towards antibiotic solutions, their resilience to other chemical stresses and the erosion resistance of biofilms were shown to be related to the surface topography of those soft materials [9,10]. In fact, in recent years, quantitative topographical analyses of biofilms have become a well-established and useful tool in biofilm research [8,10–15].

The vast majority of biofilm properties studied to date is critically related to the extracellular polymeric substances (EPS) secreted by the bacteria [11,16,17]. Interestingly, even when bacterial strains belong to the same species, the biofilms they produce may differ in terms of EPS

* Corresponding author. Department of Mechanical Engineering and Munich School of Bioengineering, Technical University of Munich, Boltzmannstraße 11, 85748, Garching, Germany.
E-mail address: oliver.lieleg@tum.de (O. Lieleg).

https://doi.org/10.1016/j.bioflm.2021.100044
Received 1 September 2020; Received in revised form 25 January 2021; Accepted 25 January 2021
Available online 6 February 2021

composition. For instance, the matrix of *B. subtilis* NCIB 3610 biofilms contains exopolysaccharides expressed by the *eps*A-O operon [18], an amyloid-fiber-forming protein *Tas*A [19,20], and a surface layer hydrophobin, *Bsl*A [21,22] – the latter of which is required for the biofilms to develop hydrophobic properties. In contrast, *B. subtilis natto* and B-1 biofilms are mostly composed of γ-polyglutamate [23,24]. Previous studies demonstrated that those different matrix components affect biofilm properties in different ways, and biofilms generated by different variants of *B. subtilis* bacteria show very different physical properties – which is due to their unique matrix compositions and surface topographies [8,11,22].

Whereas biofilms cultivated in the lab for research purposes are typically generated from one particular bacterial strain only, naturally occurring biofilms such as dental plaques or biofilms used in biotechnology, e.g. for wastewater treatment, typically contain a multitude of several bacterial strains [25–30]. Such multi-species biofilms, i.e., microbial communities, where more than one strain is present at the same time, will exhibit features and properties which are brought about by the detailed mixture of strains involved [28]. Hence, throughout this manuscript, we use the phrase 'parent' to describe single strains contributing to the properties of co-cultured colonies; following the same logic, those co-culture colonies are referred to as 'daughters' to indicate that they possess hybrid properties brought about by the 'parents'. We emphasize that those terms are not supposed to indicate an inter-generation dependency of the strains used here.

Interspecies interactions within co-cultured biofilms have already been investigated in detail, and different aspects such as the spatial organization of colonies, quorum sensing, evolution or biofilm control by competing bacteria have been analyzed [31–40]. Paul et al. (2019) [41] investigated the inter-colony interactions of two 'sibling' *B. subtilis* colonies by qualitatively analyzing their morphology; they concluded that these sibling colonies either merge or form demarcation lines – depending on how the detailed nutrient supply and starting distance of the sibling colonies were chosen. However, a follow-up study conducted at the cellular level by Matoz-Fernandez et al. (2020) [42] showed that the two sibling strains actually did not merge but remained spatially separated. Together, these studies indicated that attempting colony classifications based on macro-scale information alone might be insufficient.

Here, we show that the binary mixtures of *B. subtilis* NCIB 3610, *natto* and B-1 strains exhibit microscopic surface topographies and wetting behavior that are similar to those of their morphologically dominating parent colonies – but still distinct from them. However, this distinctiveness of the daughter colonies is not obvious enough to be detected by a macromorphological evaluation via computational image comparison approaches or by an untrained examination panel. In contrast, it requires a metrological quantification of the colony surfaces on the microscopic level. Interestingly, in all but one mixtures, the parent strain dominating the daughter colony properties is also found in larger numbers than the other, dominated parent strain. Our findings suggest that topographical analyses as we conduct them here can be a helpful tool to investigate the properties of co-cultured biofilm colonies, where the behavior of the colonies is determined by the detailed mixture of bacterial strains generating the biofilm colony.

Materials and methods

If not stated otherwise, chemicals were purchased from Sigma Aldrich (St Louis, USA).

Biofilm colony formation

Planktonic cultures were generated as described in the SI. To obtain biofilm colonies, 16 h old planktonic cultures were first diluted to an OD_{600} of 0.6 using fresh LB medium. For creating binary mixtures of NCIB 3610/*natto*, NCIB 3610/B-1 and *natto*/B-1, respectively, the diluted planktonic cultures were mixed at a volumetric ratio of 1:2, 1:4 and 1:2, respectively; those mixture ratios were chosen to obtain mixtures containing equal numbers of viable cells from each strain (see main text). By doing so, we aim to create fair conditions where both bacterial strains have equal chances to contribute to the properties of the co-cultured biofilm colony. Then, five separate 5 μL drops of these mixtures (or standard cultures of NCIB 3610, natto and B-1 diluted to the same OD_{600}) were placed onto 1.5% (w/v) agar plates enriched with either 2.5% (w/v) of LB or MSgg (Minimal Salts Glycerol Glutamate) media. The MSgg medium contained 5 mM potassium phosphate, 100 mM 3-(N-Morpholino)propanesulfonic acid (MOPS) (Carl-Roth, Karlsruhe, Germany), 2 mM $MgCl_2$, 700 μM $CaCl_2$, 50 μM $MnCl_2$, 50 μM $FeCl_3$, 1 μM $ZnCl_2$, 2 μM thiamine, 0.5% (v/v) glycerol, 0.5% (w/v) glutamate, 50 μg/mL L-tryptophan, 50 μg/mL L-phenylalanine, and 50 μg/mL threonine. The inoculated agar plates were incubated at 37 °C and ~25% humidity for 1 day, and we conducted all analyses on these 1 day old colonies to obtain colonies that are large enough for accurate contact angle and surface topography measurements. These co-cultured colonies were not studied at later time points of cultivation to avoid bacterial competition effects within the colony – which would further increase the complexity of the experimental outcome.

Biofilm colony classification based on macromorphological appearance

To assign a morphologically dominating 'parent' to each of the co-cultured biofilm colonies, a panel comprising nine people was asked to select the most similar 'parent' colony among three single strain colonies of *B. subtilis* NCIB 3610, *natto* and B-1 strains. The strain that had received the most votes was then selected as the 'dominating parent'; in the case of tied votings, the respective co-cultured colonies were classified as 'inconclusive'.

Similar to the panel survey, three different computational approaches were employed to classify the images of the co-cultured biofilms according to their similarity to pure, one-strain 'parent' colonies. In detail, all images were subjected to a pairwise comparison with one of three reference colony images (one per bacterial 'parent' strain), and the best-matching parent colony was considered as the algorithm's decision. For this comparison, the following methods were applied: First, the structural similarity [43] metric was used, which performs a generic image comparison that estimates the perceived difference of two images; second, template matching based on correlation coefficients was conducted; third, oriented FAST and rotated BRIEF (ORB [44]) – a robust local feature detector based on the FAST [45] (Features from Accelerated Segments Test) key point detector and a modified version of the visual descriptor BRIEF [46] (Binary Robust Independent Elementary Features) – was used (for more detailed information please see the Supplementary Information). All algorithms were programmed and executed with Python (version 3.8.3, Python Software Foundation, Wilmington Delaware, USA) including the NumPy [47] (version 1.19.2) extension for numerical calculations. For image handling and preprocessing, OpenCV [48] (Open Source Computer Vision Library, version 4.4.0), Pillow [49] (version 8.0.1) and Scikit-image [50] (version 0.17.2) Toolboxes were used.

Biofilm wetting properties

To determine the wetting behavior of the center of biofilm colonies, water droplets (2.5 μL or 5 μL in volume; the volume of the droplets had to be adjusted in dependency of the hydrophobicity and size of the biofilm colonies) were placed onto the surface of NCIB 3610, *natto* and B-1 biofilms, respectively. Then, transversal images of those water droplets were acquired using a high-resolution camera (Point Grey Research, Richmond, Canada). Finally, contact angle values were determined by processing the images with the "drop snake" plug-in of the OpenSource software ImageJ.

To distinguish between rose-like and lotus-like superhydrophobicity, the biofilm colonies were tilted after the contact angle measurement. The

colonies were designated as rose-like if the droplet remained attached to the biofilm surface during tilting; conversely, the colonies were rated lotus-like when the droplet rolled-off upon sample tilting.

Topographical biofilm characterization on the micro-scale

As in previous work, the microscopic surface topography of the biofilm colonies was characterized using optical profilometry [8,10]. In detail, topographical images were acquired from the central areas of the biofilm colonies using a 3D laser scanning confocal microscope (VK-X1000 series, Keyence Corporation, Osaka, Japan) at 20× magnification resulting in image sizes of 529 μm × 705 μm comprising 2048 × 1536 pixels. The step size in z was 0.5 μm, and the corresponding resolution in this dimension (based on fitting algorithms employed by the software) was 0.5 nm. The obtained topographical data was then evaluated with the software MultiFileAnalyzer (Version 2.1.3.89, Keyence Corporation, Osaka, Japan).

To quantify the surface topography of the biofilm colonies, different topographical parameters were calculated, which are all defined in ISO norm 25178. In this study, we mainly focus on the developed interfacial surface ratio,

$$Sdr = \frac{1}{A}\left[\iint_A \left(\sqrt{\left[1+\left(\frac{\partial z(x,y)}{\partial x}\right)^2+\left(\frac{\partial z(x,y)}{\partial y}\right)^2\right]}-1\right)dxdy\right],$$

which describes the ratio of the measured surface area (as established by the surface texture) with respect to the (perfectly flat) definition area. This *Sdr* parameter was previously shown to be suitable to differentiate between different complex topographies of biofilms, which are related to differences in their wetting properties [8]. However, for some specific cases, a more in-depth analysis employing additional metrological parameters were required (see supplement for details).

Optical microscopy

The presence of *B. subtilis* NCIB 3610, *natto* and B-1 bacteria within co-cultured colonies was investigated by a combination of fluorescence and phase-contrast microscopy. In those experiments, we used a modified NCIB 3610 strain that expresses the green fluorescent protein (GFP). As similar GFP-expressing *natto* and B-1 strains were not available to us, only binary mixtures containing NCIB 3610 could be studied. Prior to preparing fluorescently labeled colonies, we quantified the number of viable NCIB 3610-GFP bacteria at an OD_{600} of 0.6 and compared this value to numbers obtained for standard NCIB 3610 bacteria grown at the same conditions. There was no significant difference ($p = 0.155$) between wild-type and GFP expressing ((3.9 ± 0.3) x 10^8 CFU/mL) strains. Also, both variants of this bacterial strain exhibit similar growth kinetics in LB and MSgg media (Fig. S3). Co-cultured biofilm colonies of NCIB 3610-GFP/B-1 and NCIB 3610-GFP/*natto* were obtained as described above. Then, a piece of biofilm sample was taken from the center of the colonies, transferred into 100 μL of distilled water and vortexed to ensure a homogeneous bacterial solution. 5 μL of this homogenized bacterial suspension was then placed onto μ-slide wells (Ibidi, Planegg, Germany) and covered with an agarose patch of 600 μm thickness. The mixture of fluorescent (NCIB 3610) and non-fluorescent (either *natto* or B-1) bacterial cells was then visualized on an inverse light microscope (Leica Biosystems, Hesse, Germany) at 63× magnification using a digital camera (Orca Flash 4.0 C11440–22C, Hamamatsu, Japan) at 2 × 2 binning in two ways: first, using a FITC filter; second, in phase-contrast mode. The acquired images were then processed with Image J as follows: First, the backgrounds of both images were removed. Their brightness intensities were equalized, and the images were merged and converted into RGB values. Then, the composed images were split again, and any unevenness resulting from the background of the phase-contrast images was smoothened by applying a bandpass filter. These grey-scaled phase-contrast images were colored by Lookup Tables (LUT), and then the LUT was inverted. The brightness of the images was adjusted to select cells. The total number of cells was determined using a color threshold and the particle analysis plug-in of ImageJ. Then, GFP-expressing (=NCIB 3610) cells were identified from the merged images and counted. The number of non-fluorescent bacteria (= *natto* or B-1) was obtained by subtracting the number of fluorescent (NCIB 3610) cells from the total number of bacteria.

Sample sizes and statistics

For morphological observations, surface topography analysis and contact angle measurements, we obtained data from 15 individual samples generated from three independent growth batches. For fluorescence imaging, all data was obtained from 10 individual samples created from two distinct growth batches. For all sample subgroups (e.g., *natto*-like samples, 3610-like samples, B-1-like samples), data from at least 3 technical replicates and a minimum of 5 individual samples was collected and analyzed.

A statistical analysis of the data was performed using the software SigmaPlot 12.5 (Systat Inc, San Jose, CA, USA). Statistically significant differences between samples were assessed by performing two-sample t-tests assuming a two-tailed alternative hypothesis with a confidence level of 95%. The assumptions of normal distribution and equal variances were also tested with this software ($p = 0.05$).

To assign a 'least different' parent strain to each of the individual co-cultured colonies generated from NCIB 3610/*natto* mixtures, we applied pairwise *t*-tests using the open source software R. Then, we compared the *Sdr* or contact angle data obtained from 3 technical replicates for each individual co-cultured colony to those of three single strain 'parent' colonies. Holm's method was employed to control the family-wise error [51]. Different from standard *t*-tests, here, we then applied a reverse approach, i.e., we identified the highest *p*-value within each set of compared samples of 'parent' and 'daughter' colonies and selected the corresponding 'parent' strain, accordingly. The corresponding results are shown in the SI.

Results

When three different strains of *B. subtilis* are grown separately on LB agar (at 37 °C with ~25% humidity for 1 d), the obtained colonies differ in terms of morphology and wetting behavior (Fig. 1). Whereas *B. subtilis* NCIB 3610 and *natto* strains form hydrophilic colonies with smooth surfaces, *B. subtilis* B-1 colonies exhibit extremely liquid repellent (= superhydrophobic lotus-like) surfaces with micro- and macroscopic roughness features. We here ask if mixtures of those strains would generate colonies with new surface features, or if the properties of one of the 'mother' colonies were to dominate the outcome.

To obtain a controlled mixture of *B. subtilis* NCIB 3610, *natto* and B-1 strains, one possibility would be to adjust the densities of the overnight cultures to the same value before mixing. However, this approach does not necessarily guarantee similar amounts of living cells in these suspensions: when bacterial liquid cultures reach the stationary phase, they contain not only living and dead cells but also microbial debris and secreted metabolites – and all of these components may contribute to the optical density of the culture [52]. Thus, to obtain starting conditions that allow us to mix similar numbers of bacteria generated from the three different strains, we first determine the CFUs of bacterial overnight cultures at different optical densities (Fig. S2). Indeed, 16 h old cultures of *B. subtilis* NCIB 3610, *natto* and B-1 diluted to an OD_{600} of 0.6 contain (4.4 ± 0.5) x 10^8, (2.0 ± 0.4) x 10^8 and (1.3 ± 0.4) x 10^8 CFU/mL, respectively. Even though those differences are not huge, this result demonstrates that mixing bacterial cultures at the same optical density would create somewhat unfair starting conditions within the colony as always one strain would be present in larger numbers. To compensate for this, we here mixed the different overnight cultures such that similar

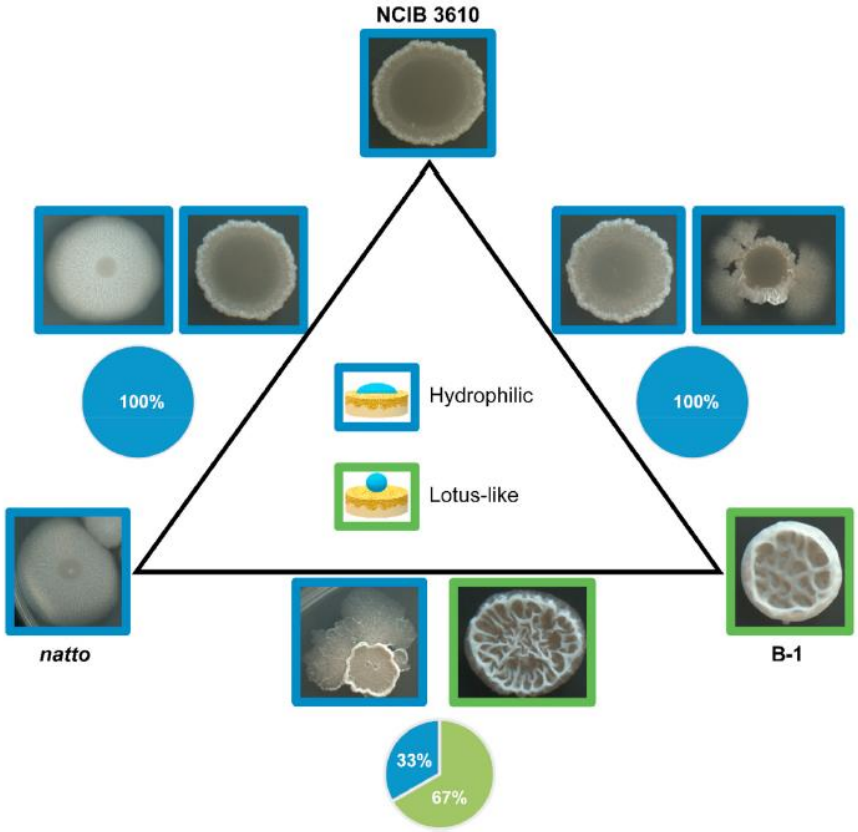

Fig. 1. Overview of single-species and binary mixtures of co-cultured *B. subtilis* NCIB 3610, *natto* and B-1 biofilm colonies grown on LB agar. In each corner of the triangle, a typical example of a single strain colony is shown; in between, example images of mixture colonies are shown. The color of the image frames denotes the wetting behavior of the respective biofilm colonies; hydrophilic biofilms are indicated in blue and lotus-like superhydrophobic biofilms in green, respectively. The pie charts below the images describe the frequency at which the different wetting behaviors occur. Wetting tests on co-cultivated biofilm samples are conducted on 15 colonies grown from 3 different batches. (For interpretation of the references to color in this figure legend, the reader is referred to the Web version of this article.)

numbers of CFUs from each strain were added to the inoculation mix. With this approach, we generate all possible binary mixtures of *B. subtilis* NCIB 3610, *natto* and B-1 bacteria.

For the colonies produced by those mixtures, a panel consisting of nine people (none of whom took part in the experiments shown here) is asked to classify the morphology of the colonies (Table S1) by comparing their macroscopic appearance to that of colonies generated by one of the 'parent' strains. In addition to the panel survey, we also employ computational approaches to select the most similar 'parent' strain for each co-cultured daughter colony (see Methods section and supplementary information). Among these three image categorization approaches (i.e., algorithms applying 'structural similarity', 'template matching' and 'feature detection' methods), we consider the 'feature detection' approach to be the most reliable one. This assessment is based on our observation that this particular algorithm returns the lowest amount of clearly wrong assignments, i.e., it only rarely selects 'dominant' strains that are not even present in the co-cultured biofilm colonies. Interestingly, such a clearly wrong assignment never occurred in the panel decisions. Based on this result, we conclude that the panel assessments are more reasonable than the algorithm-based categorization results – yet, the panel decisions are not fully correct either (Fig. 2). Nevertheless, for the remainder of this article, we use the categorizations obtained by the panel evaluations to sort the 'daughter' colonies for further micromorphological investigations.

As depicted in Table S1, binary mixtures containing *B. subtilis* NCIB 3610 and B-1 bacteria are all rated by the panel to be dominated by the NCIB 3610 strain. In agreement with this panel assessment, all those colonies show hydrophilic surfaces with contact angles typical for pure NCIB 3610 colonies cultivated at those conditions (Fig. 3a).

Of course, all information discussed so far has been obtained on a macroscopic scale. Yet, it has been shown in several previous studies, that the wetting properties of bacterial biofilms are controlled on a microscopic level which cannot be visualized by simple, macroscopic camera images. Yet, microscopic imaging techniques such as laser scanning profilometry (a variant of confocal light microscopy) allow for accessing this microscopic length scale, and they provide topographical information that can be quantified by metrological parameters. Examples of such topographical images of both, single-strain 'parent' colonies and mixed 'daughter' colonies are shown in Fig. S4. A quantification of the microscopic surface topographies of mixed colonies returns roughness values (represented by the *Sdr* parameter) that are very similar to those determined for pure NCIB 3610 colonies (Fig. 3d). Taken together, this shows that, for this particular mixture of strains, the panel evaluation can correctly identify the main contributor responsible for the surface

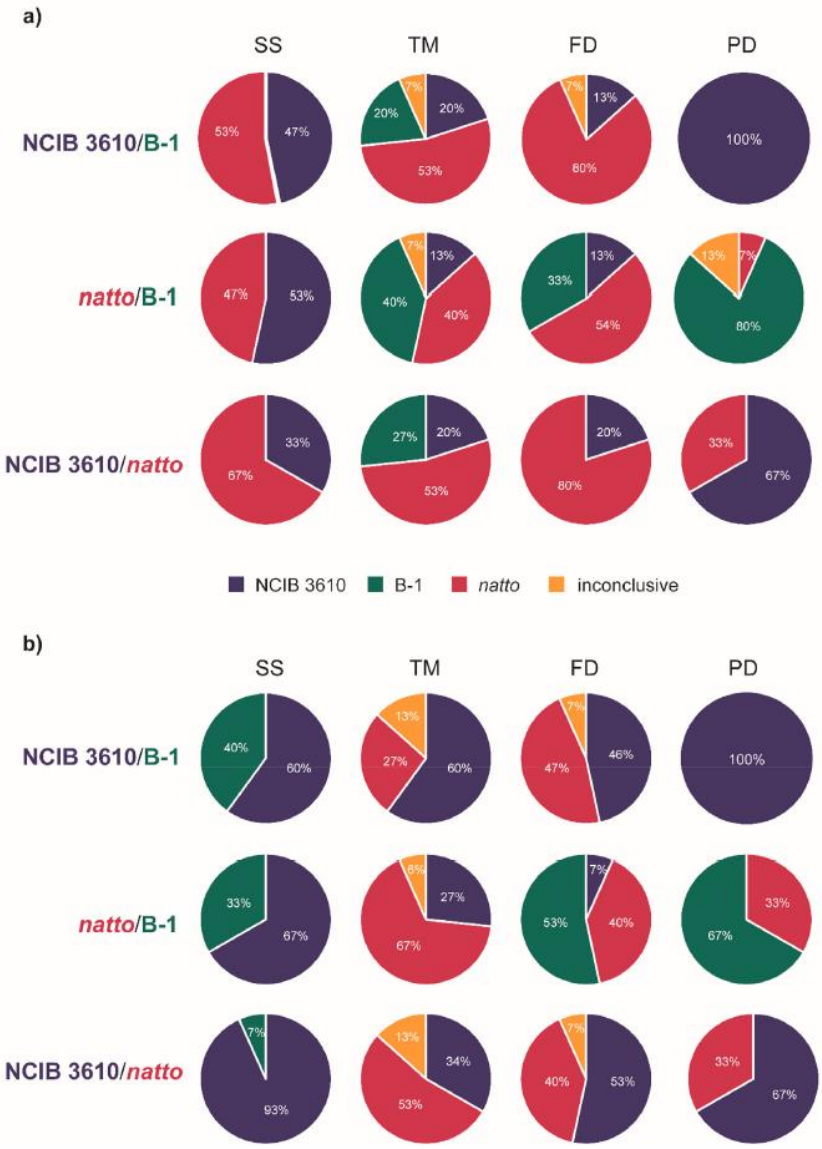

Fig. 2. Biofilm colony classifications based on panel decisions (PD) and computational methods evaluating the macromorphological appearance of the co-cultured colonies. The three algorithms make use of structural similarity (SS), template matching (TM) and feature detection (FD) equations (see SI for details). The pie charts depict pooled results from 15 co-cultured colonies grown on LB (a) and MSgg agar (b).

properties of the mixed colony. For binary mixtures of *natto* and B-1 bacteria, a more complex picture emerges. Here, whereas the majority of colonies seems to be morphologically dominated by B-1, the panel rates some colonies as "*natto*-like" or even "NCIB 3610-like" (Table S1). This result shows that, for colonies generated by this mixture of bacterial strains, a more detailed analysis is required. A wetting analysis of the colonies shows that the majority of colonies have hydrophobic surfaces similar to those present on pure B-1 colonies; however, a subset of samples has hydrophilic surface properties similar to those of pure *natto* colonies (Figs. 1 and 3b). In agreement with this observation, also an analysis of the microscopic surface topography of the mixed colonies allows for sorting them into two sub-groups: the hydrophilic (*natto*-like) colonies have low *Sdr* values around 100% whereas the hydrophobic (B-1-like) colonies exhibit high *Sdr* values on the order of ~1000%. Interestingly, we find a significant increase in this microscopic surface roughness parameter for the *natto*-like mixture colonies compared to pure *natto* colonies (Fig. 3e). Similarly, the average contact angle of B-1-like colonies is slightly but significantly lower than the corresponding

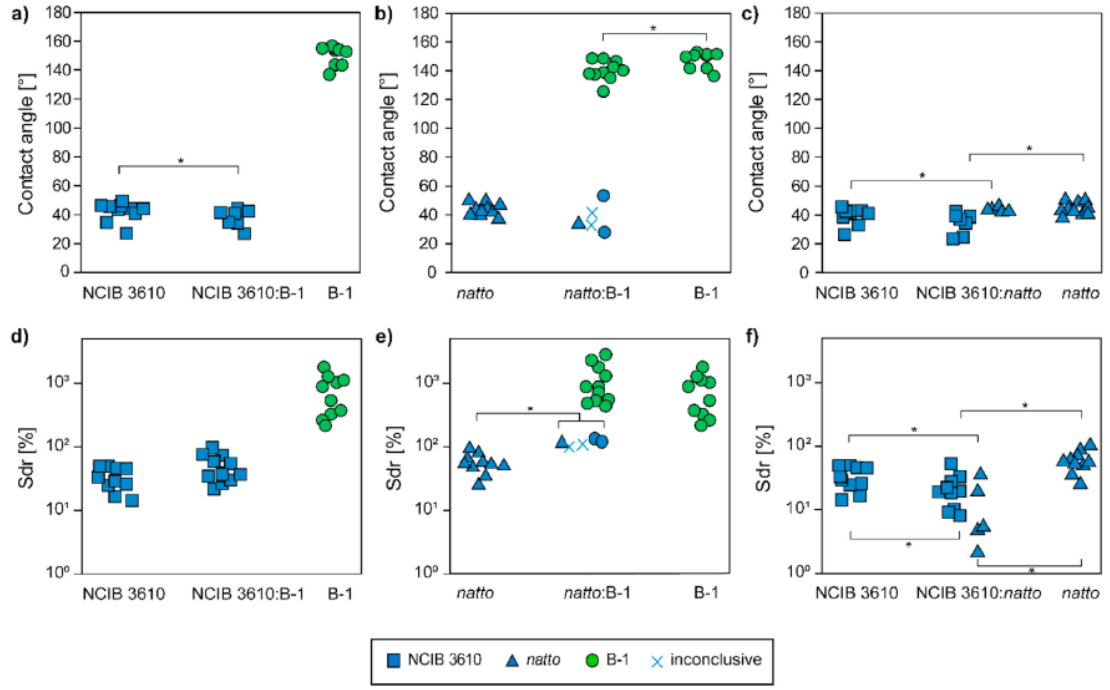

Fig. 3. Quantitative characterization of different biofilm colonies grown on LB agar. Contact angle and surface roughness (*Sdr*) values are obtained on the center biofilm colonies generated from co-cultured NCIB 3610/B-1 (**a**,**d**), *natto*/B-1 (**b**,**e**) and NCIB 3610/natto (**c**,**f**) colonies and compared to values obtained from single-strain colonies. Each symbol denotes the average value of three technical replicates obtained from one colony. The data is sorted according to the panel decision regarding the morphological dominance of either NCIB 3610 (□), *natto* (Δ) or B-1 (○) in the co-cultured colonies. If the panel voting did not lead to a conclusive result, those colonies are indicated by a cross (X). The detailed wetting behavior of the biofilm colonies is indicated by the color of the marker: green color represents lotus-like superhydrophobic behavior and blue color represents hydrophilic behavior. Asterisks denote statistical significances based on a *p*-value of $p = 0.05$. Even though we find significant differences between the contact angles and *Sdr* values of all single-strain 'parent' colonies (when compared pair-wise), this is not marked in the figure for simplicity. (For interpretation of the references to color in this figure legend, the reader is referred to the Web version of this article.)

value we determine for pure B-1 colonies (Fig. 3b). Together, this indicates that, in this particular mixture scenario, there are two possible experimental outcomes: either *natto* or B-1 can dominate in the 'daughter' colonies. Moreover, even though the main contributor to the colony properties can be clearly identified in both cases, the presence of the other bacterial strain influences the colony properties as well – albeit subtly.

The third binary mixture we study is a co-cultivation of *B. subtilis* NCIB 3610 and *natto* bacteria. Here, the panel considers 2/3 of the 'daughter' colonies to be morphologically dominated by NCIB 3610, and the remaining third mostly as *natto*-dominated (Table S1). Since both 'parent' colonies are hydrophilic, so are all the daughter colonies (Fig. 1). Still, the contact angles we determine on the daughter colonies allow for a categorization into 3610-like (CA = 38° ± 5°) and *natto*-like (CA = 43° ± 4°), with the average CA value of each subpopulation being significantly different from the CA-value typical for the 'other' (= not dominant) parent (Fig. 3c). Interestingly, both of the daughter colony variants exhibit less pronounced surface roughness features (*Sdr*) than their parents (Fig. 3f). This is somewhat unexpected as the contact angles of the two daughter subpopulations agree very well with those determined for the dominating parent colony. Moreover, with a reverse approach, i.e., by conducting a pair-wise comparison of contact angles determined for both, individual NCIB 3610/*natto* mixture colonies and each of the three putative mother strain colonies, good agreement with the panel decisions is obtained (Table S2). In contrast, when the *Sdr* data is used for a similar identification approach, lots of wrong assignments are obtained. This indicates that, for such a reverse assignment of parent strains, a more detailed analysis of the surface topography is required – most likely including more than only one metrological parameter. A more detailed analysis of the surface features of those daughter colonies suggests the following explanation: as the daughter and parent colonies have very similar peak, core and valley heights but the peak density is lower for the daughter colonies, the same wetting behavior occurs even though the surface roughness parameter *Sdr* is reduced (Table S3).

So far, we have shown that binary mixtures of *B. subtilis* NCIB 3610, *natto* and B-1 strains generate biofilm colonies with surface features (contact angles and surface roughness) that resemble those of one of their parent colonies but are nevertheless significantly different. This suggests that the other, morphologically non-dominant parent strain has a relevant influence on the colony properties. For this influence to manifest, of course, the 'other' parent strain has to be present in the daughter colony, i.e., it must not be outgrown by the second strain it is co-cultured with. Indeed, growth curves obtained for the three *B. subtilis* strains in liquid LB medium (Fig. 4a) already indicate that this is most likely not the case: when grown in parallel at identical conditions, NCIB 3610 bacteria do not possess a growth advantage over the other strains; yet, they clearly dominate the properties of, e.g., colonies where they are mixed with B-1 bacteria. Similarly, the growth curve we obtain for B-1 bacteria indicates slightly slower growth kinetics than what we obtain for *natto* - but mixed colonies created from those two strains tend to be morphologically dominated by B-1.

Hence, as a next step, we aim to verify the coexistence of both parent

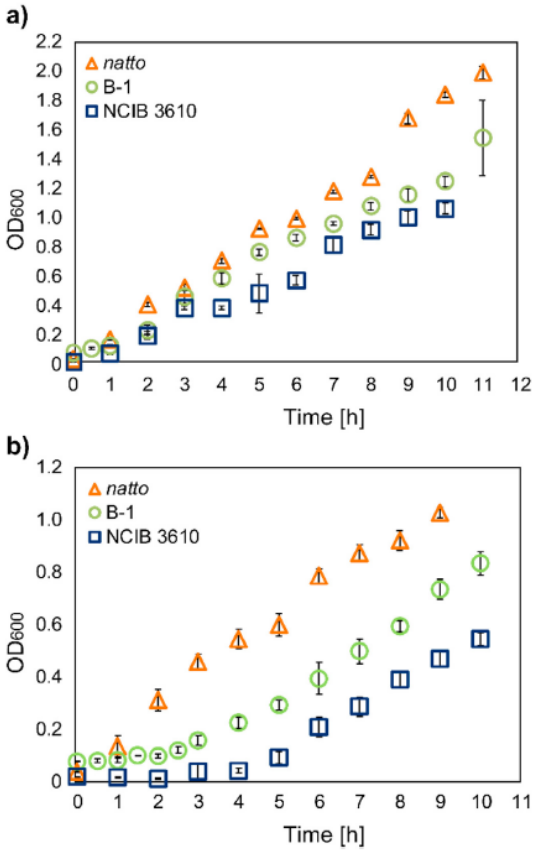

Fig. 4. Microbial growth of planktonic *B. subtilis* NCIB 3610, *natto* and B-1 bacteria at 37 °C. Growth in LB (a) and MSgg (b) media is quantified by determining the optical density (OD_{600}). Error bars indicate the standard deviation as obtained from 3 biological replicates.

strains in the daughter colonies by using a fluorescent (GFP expressing) NCIB 3610 strain. Both, in colonies created from NCIB 3610/B-1 and NCIB 3610/*natto* mixtures, the strongly green appearance of the colonies already demonstrates the presence of the NCIB 3610 strain – in full agreement with our expectation (as this strain was the dominant parent in both cases). Moreover, when we quantify the ratio of GFP-labeled (= NCIB 3610) to non-fluorescent (= either *natto* or B-1) bacteria in the center of each colony by a combination of fluorescence and phase-contrast microscopy (see Methods), we can always detect a significant content of the second parent strain: for NCIB 3610/B-1 colonies, this content can vary between 1% and 22%; although this is very low, it seems to be sufficient to influence the surface properties of the daughter colonies. For NCIB 3610/*natto* mixtures, the relative content of the 'other' parent (= *natto*) is much higher and ranges from 24% to 79% (Fig. 5a). This variation is quite high which may seem surprising. However, when the results are sorted into the same two subpopulations we identified above, this large variation in the relative content of the two bacteria agrees very well with our previous assessment: '*natto*-like' daughter colonies contain predominantly *natto* bacteria, whereas 'NCIB 3610-like' colonies contain mostly NCIB 3610 bacteria.

To investigate whether the two parent strains still co-exist at the periphery of the daughter colonies, we quantify the ratio of GFP-labeled

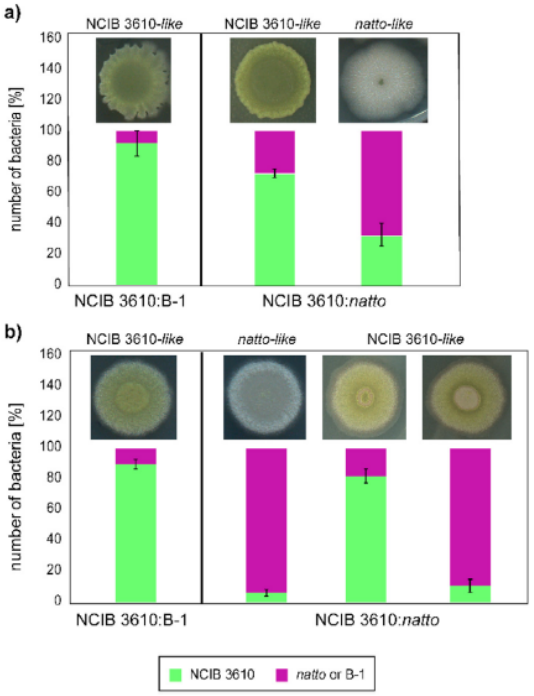

Fig. 5. Strain identification in the center of co-cultured *B. subtilis* biofilm colonies as assessed by fluorescence microscopy. The coexistence ratio of fluorescent NCIB 3610 bacteria and another, non-fluorescent strain (either *natto* or B-1) is shown for different sub-groups (see main text) of co-cultured biofilm colonies grown on LB (a) and MSgg (b) agar. Error bars represent the standard deviation as obtained from at least 5 different colonies.

and other bacteria at the peripheral part of such daughter colonies, where we detect a different macroscopic structure than in the colony center (Fig. S5). By doing so, we find that the morphologically dominating strain is also present at higher numbers in those colony peripheries. Furthermore, similar to what we described above for the central areas of co-cultured biofilm colonies, we find clear indications that, also in those peripheral regions, both strains contribute to the surface roughness features of the daughter colony (Fig. S5).

So far, we showed that the coexistence of both parent strains in the daughter colonies leads to biofilms with hybrid surface properties that are brought about by both parent strains. In the experiments discussed above, a nutrient-rich medium, i.e., LB, was chosen for biofilm growth. However, a different scenario might emerge when the range of available nutrients is limited [53]: the range of nutrients available during biofilm growth not only affects bacterial interactions [31], also the properties of single strain *B. subtilis* biofilms depend on the nutrient conditions: for instance, biofilms can show different surface topographies and wetting behaviors when generated at nutrient-rich and limiting nutrient conditions, respectively [8]. Hence, in a next step, we repeated the co-cultivation experiments using MSgg medium as a nutrient source.

As expected, we observe a different growth behavior for the planktonic bacteria in MSgg medium, where the only carbon source is glycerol. As for B-1 bacteria, the planktonic growth of NCIB 3610 bacteria shows a long (~5 h) lag phase at the conditions chosen here (see Methods). The limited nutrient sources available in MSgg medium increase the gaps between the planktonic growth curves of *B. subtilis* NCIB 3610, *natto* and B-1 strains (Fig. 4b); overall, *natto* bacteria seem to have a clear

advantage over the other strains (due to the short lag-phase). Thus, naively, one might assume that *natto* bacteria will always dominate the other two strains in co-cultured biofilm colonies; however, as we show below, this is not necessarily the case.

When the three *B. subtilis* strains are individually grown on MSgg agar, the generated colonies show three different modes of wetting (Fig. 6): B-1 colonies again exhibit lotus-like superhydrophobic surfaces with very high contact angles (CA = 142° ± 6°) and *Sdr* values in the range of ~1000% (Fig. 7). Also *natto* colonies have similar (= hydrophilic) surface properties as when grown on LB agar, with both, low *Sdr* and CA values alike. NCIB 3610 colonies, however, now possess strongly hydrophobic surfaces (CA = 138° ± 4°) with water-adhesive properties – a combination that is referred to as 'rose-like' superhydrophobicity [3]. Consistent with previous results, this is reflected by intermediate surface roughness values (*Sdr* =(120 ± 7)%), which are significantly different from both, the surface roughness of B-1 and *natto* colonies grown on MSgg agar at the conditions chosen here. We would like to mention, that the capability of NCIB 3610 and B-1 strains to generate superhydrophobic colonies is intimately linked to their ability to express the hydrophobic surface layer protein *BslA* [11] – a property that *natto* bacteria lack. Here, we tested the contribution of this hydrophobin *BslA* to the surface hydrophobicity of co-cultured colonies by employing a NCIB 3610 mutant strain unable to produce *BslA* (*ΔBslA*). Indeed, in full agreement with results described in the literature [12,21,22,54–58], co-cultivation of *ΔBslA* with one of the other strains results in hydrophilic daughter colonies (Fig. S7).

For biofilm colonies grown from binary strain mixtures on MSgg agar, we obtain an outcome that supports our findings obtained on LB agar: daughter colonies that morphologically resemble one of their mother colonies also show wetting properties that agree with this morphological similarity (Fig. 6). However, now, the panel participants are able to identify the dominating 'mother' strain with higher accuracy (Table S1). A more detailed analysis of the colony properties shows that the contact angles we measure for co-cultured colonies are always virtually identical to those we measure on the dominating 'mother' colony (Fig. 7a–c). As determining static contact angles is not sufficient to distinguish between rose-like and lotus-like superhydrophobic surfaces [3,4], the categorization applied to samples showing high contact angles >120° is conducted by tilting the samples with a wetting droplet on their surface (as described above). Yet, based on this contact angle analysis alone, a clear contribution of the non-dominant parent strain is, so far, not evident.

Such a contribution, however, becomes detectable when the microscopic surface roughness of the colonies is analyzed. Similar to when they are grown on LB agar, NCIB 3610-like and *natto*-like daughter colonies grown on MSgg agar exhibit a slightly (but significantly) different surface topography compared to colonies formed by their dominating parent. For NCIB-3610/B-1 mixtures and *natto*/B-1 mixtures, analyzing the *Sdr* values is sufficient to make this statement (Fig. 7d–f); for NCIB 3610/*natto* mixtures, however, the topography of the daughter colonies is more complicated and requires the analysis of more complex metrological surface parameters to identify the contribution of the non-dominating parent (Table S4). Only for B-1-like daughter colonies, we cannot detect such a clear contribution of the non-dominating parent (Fig. 7d and e); we speculate that this is due to wide distribution of *Sdr* values (and other roughness parameters) we obtain for those lotus-like colonies. As in previous studies, where the surface roughness of B-1 biofilm colonies was quantified, the *Sdr* values obtained from those particular biofilms cover a very broad range [10,11]. In addition to the occurrence of roughness features on several length scales, another main reason for the wide distribution of those values is the random selection of areas on the

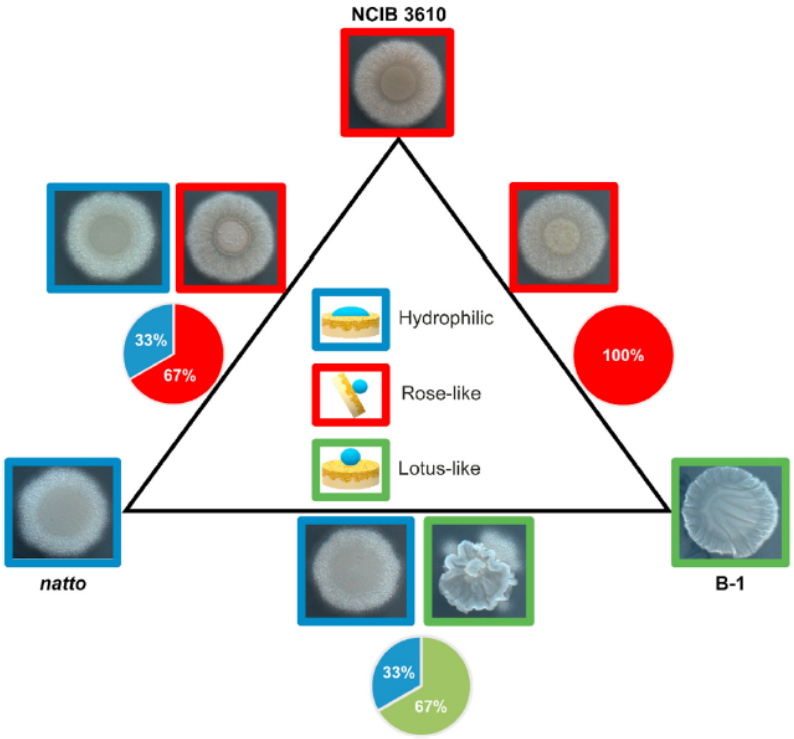

Fig. 6. Overview of single-species and binary mixtures of co-cultured *B. subtilis* NCIB 3610, *natto* and B-1 biofilm colonies grown on MSgg agar. In each corner of the triangle, a typical example of a single strain colony is shown; in between, example images of mixture colonies are shown. The color of the image frames denotes the wetting behavior of the respective biofilm colonies; hydrophilic biofilms are indicated in blue, rose-like superhydrophobic biofilms in red, and lotus-like superhydrophobic biofilms in green. The pie charts below the images describe the frequency at which the different wetting behaviors occur. Wetting tests on co-cultivated biofilm samples are conducted on at least 15 colonies grown from 3 different batches. (For interpretation of the references to color in this figure legend, the reader is referred to the Web version of this article.)

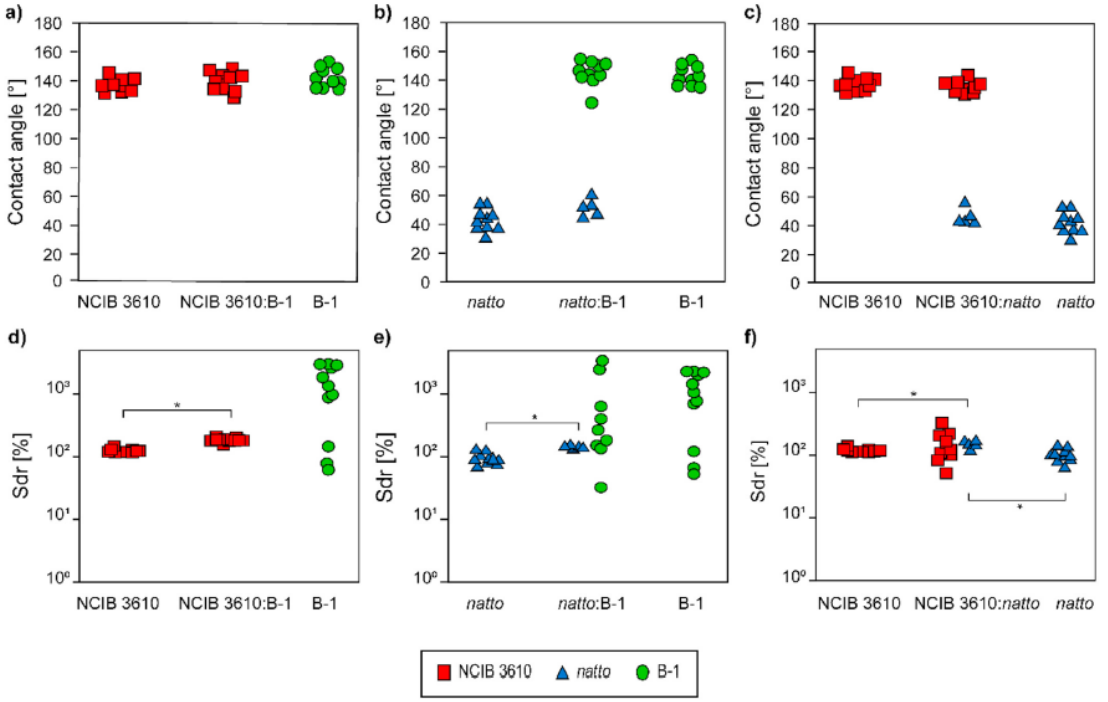

Fig. 7. Quantitative characterization of different biofilm colonies grown on MSgg agar. Contact angle and surface roughness (*Sdr*) values are obtained on the center biofilm colonies generated from co-cultured NCIB 3610/B-1 (**a**,**d**), *natto*/B-1 (**b**,**e**) and NCIB 3610/natto (**c**,**f**) colonies and compared to values obtained from single-strain colonies. Each symbol denotes the average value of three technical replicates obtained from one colony. The data is sorted according to the panel decision regarding the morphological dominance of either NCIB 3610 (□), *natto* (Δ) or B-1 (○) in the co-cultured colonies. The detailed wetting behavior of the biofilm colonies is indicated by the color of the marker: green color represents lotus-like superhydrophobic behavior, red color indicates rose-like superhydrophobic behavior, and blue color represents hydrophilic behavior. Asterisks denote statistical significances based on a *p*-value of $p = 0.05$. Even though we find significant differences between the contact angles and *Sdr* values of all single-strain 'parent' colonies (when compared pair-wise), this is not marked in the figure for simplicity. (For interpretation of the references to color in this figure legend, the reader is referred to the Web version of this article.)

biofilm colony for microscopic surface roughness analysis – some of which took place on local valleys of the macroscopic waves, some of which on the top of those macro-structures.

As for the results we discuss above for colonies grown on LB agar, also for co-cultured colonies grown on MSgg agar we can confirm that both parent strains coexist (Fig. 5b). Interestingly, we find two realizations of NCIB 3610-like daughters of NCIB 3610/*natto* mixtures: in one case, the mixture contains mainly (i.e., ~82%) NCIB 3610 bacteria. However, in a second subgroup, we detected mostly (i.e., ~89%) *natto* bacteria (Fig. 5b). Most likely, the panel rated both of those colony variants generated by this particular mixture as 'NCIB 3610-like' since the periphery structure of those colonies shows a macroscopic morphology typical for NCIB 3610 colonies (Table S1). Moreover, the wetting behavior of both of those subgroups is identical to that of NCIB 3610 colonies, i.e. rose-like with a wide distribution of *Sdr* values (Fig. 7c, f). Thus, in this particular case, although it 'looks like a duck and swims like a duck and quacks like a duck – it's a goose-duck' [59].

Conclusions

For the conditions we study here, co-cultured biofilm colonies are always – in terms of numbers – dominated by one parent strain, and this dominating strain is mostly responsible for the macro- and microscopic morphology of the daughter colony. However, these daughter colonies are also significantly (and measurably) influenced by the other parent strain. These findings show that the presence of a second bacterial strain – even at relatively small amounts – may cause slight but significant changes in the properties of a biofilm. Whether or not the two co-cultured bacteria are well-mixed on a microscopic scale, or if they grow in local niches (e.g., on top of each other), is – at this point of research, not clear yet. Nevertheless, our insights may provide useful stimuli for biotechnological applications where biofilms are engineered to possess dedicated properties: As we show it here for using *B. subtilis* bacteria, a desired property present in a single-strain biofilm may be transferred to a multi-species biofilm by co-cultivation of different bacteria – provided that the different bacteria can exist together without extinguishing each other.

CRediT authorship contribution statement

Elif N. Hayta: Conceptualization, Methodology, Investigation, Formal analysis, Writing - original draft, Visualization, Funding acquisition. **Carolin A. Rickert:** Software, Formal analysis, Writing - original draft. **Oliver Lieleg:** Conceptualization, Methodology, Resources, Writing - review & editing, Visualization, Supervision, Funding acquisition.

Declaration of competing interest

The authors declare that they have no known competing financial interests or personal relationships that could have appeared to influence the work reported in this paper.

Acknowledgements

The authors thank to Dr. Madeleine Opitz and Turgut Refik Caglar for their helpful discussions. ENH thankfully acknowledges a fellowship granted by the Turkish Ministry of Education. In addition, this project was partially supported by the Deutsche Forschungsgemeinschaft (DFG, German Research Foundation) – SFB 863, project B11 – 111166240.

Appendix A. Supplementary data

Supplementary data to this article can be found online at https://doi.org/10.1016/j.bioflm.2021.100044.

References

[1] Edmunds M. On the association between Myrmarachne spp. (Salticidae) and ants. Bull Br Arachnol Soc 1978;4:149–60.
[2] Shamble PS, Hoy RR, Cohen I, Beatus T. Walking like an ant: a quantitative and experimental approach to understanding locomotor mimicry in the jumping spider Myrmarachne formicaria. Proc R Soc B Biol Sci 2017;284:20170308. https://doi.org/10.1098/rspb.2017.0308.
[3] Bhushan B, Nosonovsky M. The rose petal effect and the modes of superhydrophobicity. Philos Trans R Soc A Math Phys Eng Sci 2010;368:4713–28. https://doi.org/10.1098/rsta.2010.0203.
[4] Wang S, Jiang L. Definition of superhydrophobic states. Adv Mater 2007;19:3423–4. https://doi.org/10.1002/adma.200700934.
[5] Shim MH, Kim J, Park CH. The effects of surface energy and roughness on the hydrophobicity of woven fabrics. Textil Res J 2014;84:1268–78. https://doi.org/10.1177/0040517513495945.
[6] Erbil HY, Demirel AL, Avci Y, Mert O. Transformation of a simple plastic into a superhydrophobic surface. Science 2003;299:1377–80. https://doi.org/10.1126/science.1078365. 80.
[7] Nosonovsky M, Bhushan B. Hierarchical roughness optimization for biomimetic superhydrophobic surfaces. Ultramicroscopy 2007;107:969–79. https://doi.org/10.1016/j.ultramic.2007.04.011.
[8] Werb M, Falcón García C, Bach NC, Grumbein S, Sieber SA, Opitz M, Lieleg O. Surface topology affects wetting behavior of Bacillus subtilis biofilms. Npj Biofilms Microbiomes 2017;3:11. https://doi.org/10.1038/s41522-017-0018-1.
[9] Hayta EN, Lieleg O. Biopolymer-enriched: B. subtilis NCIB 3610 biofilms exhibit increased erosion resistance. Biomater Sci 2019;7:4675–86. https://doi.org/10.1039/c9bm00927b.
[10] Falcón García C, Stangl F, Götz A, Zhao W, Sieber SA, Opitz M, Lieleg O. Topographical alterations render bacterial biofilms susceptible to chemical and mechanical stress. Biomater Sci 2019;7:220–32. https://doi.org/10.1039/c8bm00987b.
[11] Kesel S, Grumbein S, Tallawi M, Marel A, Lieleg O, Opitz M. Direct comparison of physical properties of Bacillus subtilis NCIB 3610 and B-1 biofilms. Appl Environ Microbiol 2016;82:2424–32. https://doi.org/10.1128/AEM.03957-15.
[12] Kesel S, Von Bronk B, Falcón García C, Götz A, Lieleg O, Opitz M. Matrix composition determines the dimensions of: Bacillus subtilis NCIB 3610 biofilm colonies grown on LB agar. RSC Adv 2017;7:31886–98. https://doi.org/10.1039/c7ra05559e.
[13] Raab N, Bachelet I. Resolving biofilm topography by native scanning electron microscopy. J Biol Methods 2017;4:70. https://doi.org/10.14440/jbm.2017.173.
[14] Huang Y, Chakraborty S, Liang H. Methods to probe the formation of biofilms: applications in foods and related surfaces. Anal Methods 2020;12:416–32. https://doi.org/10.1039/c9ay02214g.
[15] Schiebel J, Noack J, Rödiger S, Kammel A, Menzel F, Schwibbert K, Weise M, Weiss R, Böhm A, Nitschke J, Elimport A, Roggenbuck D, Schierack P. Analysis of three-dimensional biofilms on different material surfaces. Biomater Sci 2020;8:3500–10. https://doi.org/10.1039/d0bm00455c.
[16] Klotz M, Kretschmer M, Goetz A, Ezendam S, Lieleg O, Opitz M. Importance of the biofilm matrix for the erosion stability of Bacillus subtilis NCIB 3610 biofilms. RSC Adv 2019;9:11521–9. https://doi.org/10.1039/C9RA01955C.
[17] T RJ, Marc JH, Demeter A, Lemire Joseph A. Biofilm survival strategies in polluted environments. In: Lear G, editor. Biofilms Bioremediation Curr. Res. Emerg. Technol., Caister Academic Press, Norfolk, UK; 2016. p. 43–57.
[18] Branda SS, Chu F, Kearns DB, Losick R, Kolter R. A major protein component of the Bacillus subtilis biofilm matrix. Mol Microbiol 2006;59:1229–38. https://doi.org/10.1111/j.1365-2958.2005.05020.x.
[19] Kearns DB, Chu F, Branda SS, Kolter R, Losick R. A master regulator for biofilm formation by Bacillus subtilis. Mol Microbiol 2005;55:739–49. https://doi.org/10.1111/j.1365-2958.2004.04440.x.
[20] Romero D, Aguilar C, Losick R, Kolter R. Amyloid fibers provide structural integrity to Bacillus subtilis biofilms. Proc Natl Acad Sci USA 2010;107:2230–4. https://doi.org/10.1073/pnas.0910560107.
[21] Kobayashi K, Iwano M. BslA(YuaB) forms a hydrophobic layer on the surface of Bacillus subtilis biofilms. Mol Microbiol 2012;85:51–66. https://doi.org/10.1111/j.1365-2958.2012.08094.x.
[22] Hobley L, Ostrowski A, Rao FV, Bromley KM, Porter M, Prescott AR, MacPhee CE, Van Aalten DMF, Stanley-Wall NR. BslA is a self-assembling bacterial hydrophobin that coats the Bacillus subtilis biofilm. Proc Natl Acad Sci USA 2013;110:13600–5. https://doi.org/10.1073/pnas.1306390110.
[23] Morikawa M, Kagihiro S, Haruki M, Takano K, Branda S, Kolter R, Kanaya S. Biofilm formation by a Bacillus subtilis strain that produces γ-polyglutamate. Microbiology 2006;152:2801–7. https://doi.org/10.1099/mic.0.29060-0.
[24] Kimura K, Phan Tran LS, Do TH, Itoh Y. Expression of the pgsB Encoding the poly-gamma-DL-glutamate synthetase of bacillus subtilis (natto). Biosci Biotechnol Biochem 2009;73:1149–55. https://doi.org/10.1271/bbb.80913.
[25] Bowen WH, Burne RA, Wu H, Koo H. Oral biofilms: pathogens, matrix, and polymicrobial interactions in microenvironments. Trends Microbiol 2018;26:229–42. https://doi.org/10.1016/j.tim.2017.09.008.
[26] Lamont RJ, Hajishengallis G. Polymicrobial synergy and dysbiosis in inflammatory disease. Trends Mol Med 2015;21:172–83. https://doi.org/10.1016/j.molmed.2014.11.004.
[27] Marsh PD, Head DA, Devine DA. Dental plaque as a biofilm and a microbial community - implications for treatment. J Oral Biosci 2015;57:185–91. https://doi.org/10.1016/j.job.2015.08.002.
[28] Karygianni L, Ren Z, Koo H, Thurnheer T. Biofilm matrixome: extracellular components in structured microbial communities. Trends Microbiol 2020;28:668–81. https://doi.org/10.1016/j.tim.2020.03.016.
[29] Lazarova V, Manem J. Biofilm characterization and activity analysis in water and wastewater treatment. Water Res 1995;29:2227–45. https://doi.org/10.1016/0043-1354(95)00054-O.
[30] Hassard F, Biddle J, Cartmell E, Jefferson B, Tyrrel S, Stephenson T. Rotating biological contactors for wastewater treatment - a review. Process Saf Environ Protect 2015;94:285–306. https://doi.org/10.1016/j.psep.2014.07.003.
[31] Ghoul M, Mitri S. The ecology and evolution of microbial competition. Trends Microbiol 2016;24:833–45. https://doi.org/10.1016/j.tim.2016.06.011.
[32] Røder HL, Sørensen SJ, Burmølle M. Studying bacterial multispecies biofilms: where to start? Trends Microbiol 2016;24:503–13. https://doi.org/10.1016/j.tim.2016.02.019.
[33] Burmølle M, Ren D, Bjarnsholt T, Sørensen SJ. Interactions in multispecies biofilms: do they actually matter? Trends Microbiol 2014;22:84–91. https://doi.org/10.1016/j.tim.2013.12.004.
[34] Zuo R, Wood TK. Inhibiting mild steel corrosion from sulfate-reducing and iron-oxidizing bacteria using gramicidin-S-producing biofilms. Appl Microbiol Biotechnol 2004;65:747–53. https://doi.org/10.1007/s00253-004-1651-1.
[35] Jayaraman A, Hallock PJ, Carson RM, Lee CC, Mansfeld FB, Wood TK. Inhibiting sulfate-reducing bacteria in biofilms on steel with antimicrobial peptides generated in situ. Appl Microbiol Biotechnol 1999;52:267–75. https://doi.org/10.1007/s002530051520.
[36] Singh R, Sahore S, Kaur P, Rani A, Ray P. Penetration barrier contributes to bacterial biofilm-associated resistance against only select antibiotics, and exhibits genus-, strain- and antibiotic-specific differences. Pathog Dis 2016;74:2–7. https://doi.org/10.1093/femspd/ftw056.
[37] Kinkel LL, Schlatter DC, Xiao K, Baines AD. Sympatric inhibition and niche differentiation suggest alternative coevolutionary trajectories among Streptomycetes. ISME J 2014;8:249–56. https://doi.org/10.1038/ismej.2013.175.
[38] Coyte KZ, Tabuteau H, Gaffney EA, Fostera KR, Durham WM. Microbial competition in porous environments can select against rapid biofilm growth. Proc Natl Acad Sci USA 2017;114:E161–70. https://doi.org/10.1073/pnas.1525228113.
[39] Liu J, Prindle A, Humphries J, Gabalda-Sagarra M, Asally M, Lee DYD, Ly S, Garcia-Ojalvo J, Süel GM. Metabolic co-dependence gives rise to collective oscillations within biofilms. Nature 2015;523:550–4. https://doi.org/10.1038/nature14660.
[40] Liu W, Røder HL, Madsen JS, Bjarnsholt T, Sørensen SJ, Burmølle M. Interspecific bacterial interactions are reflected in multispecies biofilm spatial organization. Front Microbiol 2016;7:1–8. https://doi.org/10.3389/fmicb.2016.01366.
[41] Paul R, Ghosh T, Tang T, Kumar A. Rivalry in: Bacillus subtilis colonies: enemy or family? Soft Matter 2019;15:5400–11. https://doi.org/10.1039/c9sm00794f.
[42] Matoz-Fernandez D, Arnaouteli S, Porter M, MacPhee CE, Stanley-Wall NR, Davidson FA. Comment on "rivalry in: Bacillus subtilis colonies: enemy or family? Soft Matter 2020;16:3344–6. https://doi.org/10.1039/c9sm02141h.
[43] Wang Z, Bovik AC, Sheikh HR, Simoncelli EP. Image quality assessment: from error visibility to structural similarity. IEEE Trans Image Process 2004;13:600–12. https://doi.org/10.1109/TIP.2003.819861.
[44] Rublee E, Rabaud V, Konolige K, Bradski G. ORB: an efficient alternative to SIFT or SURF. In: Int. Conf. Comput. Vis. IEEE, Barcelona; 2011. p. 2564–71. https://doi.org/10.1109/ICCV.2011.6126544.
[45] Viswanathan DG. Features from accelerated segment test (FAST). In: Proc. 10th work. Image anal. Multimed. Interact. Serv.; 2009. London, UK.
[46] Calonder M, Lepetit V, Strecha C, Fua P. BRIEF: binary robust independent elementary features. Lect Notes Comput Sci (Including Subser Lect Notes Artif Intell Lect Notes Bioinformatics). 6314 LNCS 2010:778–92. https://doi.org/10.1007/978-3-642-15561-1_56.
[47] Harris CR, Millman KJ, van der Walt SJ, Gommers R, Virtanen P, Cournapeau D, Wieser E, Taylor J, Berg S, Smith NJ, Kern R, Picus M, Hoyer S, van Kerkwijk MH, Brett M, Haldane A, del Río JF, Wiebe M, Peterson P, Gérard-Marchant P, Sheppard K, Reddy T, Weckesser W, Abbasi H, Gohlke C, Oliphant TE. Array programming with NumPy. Nature 2020;585:357–62. https://doi.org/10.1038/s41586-020-2649-2.
[48] Bradski G. The OpenCV library. Dr. Dobb's J Softw Tools 2000;25:120–5.
[49] Clark A. Pillow (PIL fork) documentation release 3.1.2. 2020.
[50] van der Walt SJ, Schönberger JL, Nunez-Iglesias J, Boulogne F, Warner JD, Yager N, Gouillart E, Yu T. Scikit-image: image processing in python. PeerJ 2014:1–18. https://doi.org/10.7717/peerj.453. 2014.

[51] Holm S. Board of the foundation of the scandinavian journal of statistics A simple sequentially rejective multiple test procedure author (s): sture holm published by : wiley on behalf of board of the foundation of the scandinavian journal of statistics stable U. Scand J Stat 1978;6:65–70.
[52] Schuler ML, Kargi F. Bioprocess engineering: basic concepts. second ed. Upper Saddle River, NJ: Prentice Hall; 2002.
[53] Gallegos-Monterrosa R, Mhatre E, Kovács ÁT. Specific Bacillus subtilis 168 variants form biofilms on nutrient-rich medium. Microbiol (United Kingdom) 2016;162:1922–32. https://doi.org/10.1099/mic.0.000371.
[54] Arnaouteli S, MacPhee CE, Stanley-Wall NR. Just in case it rains: building a hydrophobic biofilm the Bacillus subtilis way. Curr Opin Microbiol 2016;34:7–12. https://doi.org/10.1016/j.mib.2016.07.012.
[55] Bromley KM, Morris RJ, Hobley L, Brandani G, Gillespie RMC, McCluskey M, Zachariae U, Marenduzzo D, Stanley-Wall NR, MacPhee CE. Interfacial self-assembly of a bacterial hydrophobin. Proc Natl Acad Sci USA 2015;112:5419–24. https://doi.org/10.1073/pnas.1419016112.
[56] Morris RJ, Schor M, Gillespie RMC, Ferreira AS, Baldauf L, Earl C, Ostrowski A, Hobley L, Bromley KM, Sukhodub T, Arnaouteli S, Stanley-Wall NR, MacPhee CE. Natural variations in the biofilm-associated protein BslA from the genus Bacillus. Sci Rep 2017;7:1–13. https://doi.org/10.1038/s41598-017-06786-9.
[57] Liu W, Li S, Wang Z, Yan ECY, Leblanc RM. Characterization of surface-active biofilm protein BslA in self-assembling Langmuir monolayer at the air-water interface. Langmuir 2017;33:7548–55. https://doi.org/10.1021/acs.langmuir.7b01739.
[58] Kovács ÁT, van Gestel J, Kuipers OP. The protective layer of biofilm: a repellent function for a new class of amphiphilic proteins. Mol Microbiol 2012;85:8–11. https://doi.org/10.1111/j.1365-2958.2012.08101.x.
[59] Riley JW. Poems & Prose Sketches: "When I see a bird that walks like a duck and swims like a duck and quacks like a duck, I call that bird a duck.," Portable Poetry. 2017.

Supplementary Information for

Topography quantifications allow for identifying the contribution of parental strains to physical properties of co-cultured biofilms

Elif N. Hayta, Carolin A. Rickert and Oliver Lieleg#

Munich School of Bioengineering and Department of Mechanical Engineering,
Technical University of Munich, 85748, Garching, Germany

Center for Protein Assemblies (CPA), Technical University of Munich,
Ernst-Otto-Fischer Straße 8, 85748, Garching, Germany

Corresponding author:

Prof. Dr. Oliver Lieleg

Department of Mechanical Engineering and Munich School of Bioengineering,

Technical University of Munich,

Boltzmannstraße 11, 85748 Garching, Germany

e-mail: oliver.lieleg@tum.de,

1. Planktonic growth of *B. subtilis* bacteria

For preparing liquid (= planktonic) cultures of each strain, a piece of a frozen bacterial glycerol stock was inoculated in 10 mL of sterile 2.5% (w/v) LB (Luria/Miller) medium (Carl-Roth, Karlsruhe, Germany). All *B. subtilis* NCIB 3610[1], *natto*[2] and B-1[3] cultures were incubated at 37 °C overnight at a shaking speed of 200 rpm (Certomat BS-1, Sartorius AG, Göttingen, Germany). After 16 h of incubation phase-contrast microscopy images of planktonic cultures were obtained with an inverse light microscope (Leica Biosystems, Nußloch, Germany) at a 63x magnification using a digital camera (Orca flash 4.0 C11440-22C, Hamamatsu, Japan) using 2x2 binning; this step was added to test for the occurrence of sporulation events of these three *B. subtilis* strains. Yet, we did not observe considerable amounts of spores (which would be recognizable by a thicker coat and their smaller size compared to vegetative cells) in any of the three planktonic cultures (**Fig. S1**).

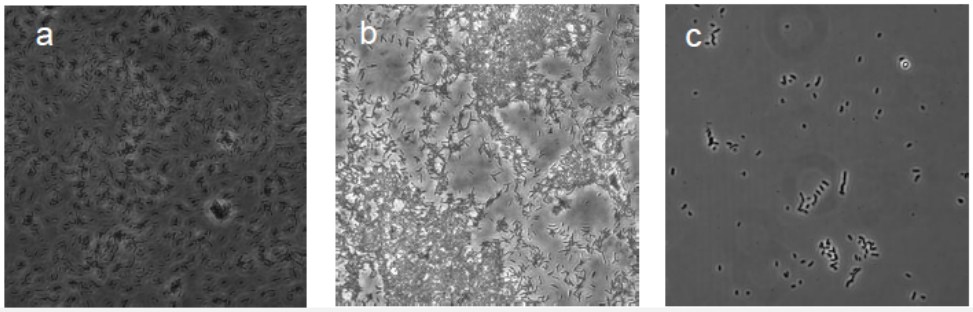

Figure S1. Phase contrast microscopy images of planktonic cultures of a) *B. subtilis* NCIB 3610, b) *B. subtilis natto,* and c) *B. subtilis* B-1 strains. The images were acquired from 16 h old planktonic cultures at 63x magnification.

The optical densities of the planktonic cultures were measured at 600 nm (GeneQuant pro, Amersham Biosciences, Little Chalfont, UK) to avoid the interference with components from the growth medium. To determine the number of viable bacteria at a certain optical density (OD), bacterial liquid cultures were first generated over night and then diluted to a certain OD value (i.e., 0.3, 0.6 or 0.9) with fresh LB medium. Then, serial dilutions were obtained in physiological saline solution (9% NaCl) and 100 µL of the last two dilutions (10^{-5} and 10^{-6}) were inoculated on readily prepared LB agar plates (in triplicates) and distributed across the plates with glass beads. The inoculated agar plates were then incubated (either at RT for 3 d or at 37 °C for 1 d), and colony forming units per mL (CFU/mL) were calculated for each sample (**Fig. S2**).

---

[1] *Bacillus subtilis* NCIB 3610 was kindly supplied by Roberto Kolter.
[2] *Bacillus subtilis natto* (27E3) was obtained from the Bacillus Genetic Stock Center (BGSC).
[3] *Bacillus subtilis* B-1 strain was kindly supplied by Masaaki Morikawa.

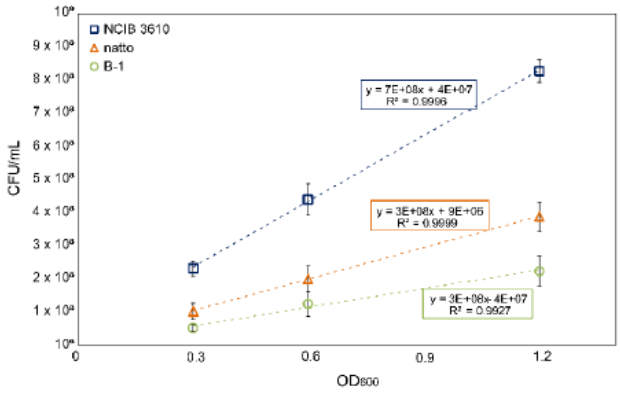

Figure S2. Colony forming unit content (per mL) from overnight cultures grown to certain optical densities. The number of viable bacteria in 16 h old overnight cultures of *B. subtilis* NCIB 3610, *natto* and B-1 strains were measured at OD_{600} of 0.3, 0.6 and 1.2. The error bars denote the standard deviation as obtained from three independent growth batches.

To investigate the growth kinetics of the three different *B. subtilis* strains at planktonic conditions, first overnight cultures were obtained as described above and diluted to an OD_{600} of 0.6. Then, an inoculation volume for a new round of planktonic growth was selected such that it contained the same number of viable bacteria (~$2x10^9$ CFU) for each strain. For planktonic growth in MSgg medium, the diluted overnight cultures were first centrifuged at 5000 rpm for 10 min and the pellet was resuspended in fresh MSgg medium. 150 mL of freshly inoculated cultures were filled into 250 mL Erlenmeyer flasks and incubated at 37 °C at a shaking speed of 200 rpm (to guarantee sufficient aeration). At intervals of 1 h, 1 mL samples were removed from this liquid culture to monitor their growth behavior by measuring the optical density at 600 nm (**Fig. S3**).

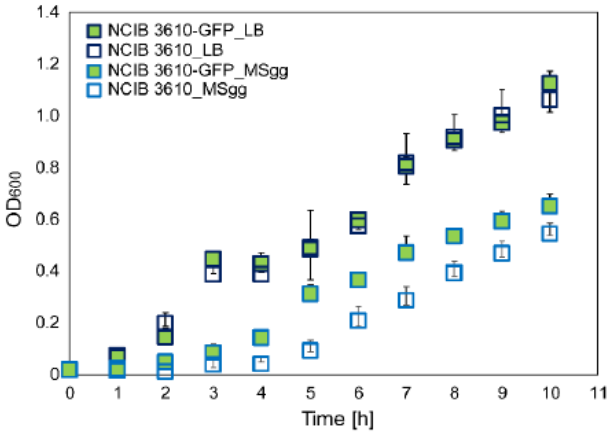

Figure S3. Microbial growth curves of planktonic wild-type and GFP expressing NCIB 3610 bacteria in LB and MSgg media. The error bars denote the standard deviation as obtained from three different growth batches.

2. Classification of macroscopic colony images with Python

To classify the macroscopic images obtained for co-cultured biofilms, three different computational approaches were employed. All algorithms were programmed and executed with Python (version 3.8.3, Python Software Foundation, Wilmington Delaware, USA) including the NumPy[1] (version 1.19.2) extension for numerical calculations. For image handling and preprocessing, OpenCV[2] (Open Source Computer Vision Library, version 4.4.0), Pillow[3] (version 8.0.1) and Scikit-image[4] (version 0.17.2) toolboxes were used. In all algorithms, the images were subjected to a pair-wise comparison with one of three reference colony images (one per bacterial 'mother' strain), and the best-matching parent colony was considered as the algorithm's decision.

2.1 Structural Similarity Index

First, a generic image comparison was performed by calculating the Structural Similarity Index (SSIM) as established by *Wang et al.*[5]. The SSIM is a metric that quantifies the perceived difference of two images by taking into account the structural information of the images based on luminance and contrast (equation S1):

$$SSIM(x,y) = \frac{(2\mu_x\mu_y + c_1)(2\sigma_{xy} + c_2)}{(\mu_x^2 + \mu_y^2 + c_1)(\sigma_x^2 + \sigma_y^2 + c_2)} \tag{S1}$$

Here, μ_x and μ_y correspond to the mean intensities of the luminance in *x* and *y* direction, respectively:

$$\mu_x = \frac{1}{N}\sum_{i=1}^{N} x_i, \qquad \mu_y = \frac{1}{N}\sum_{i=1}^{N} y_i \tag{S2}$$

Furthermore, σ_x and σ_y denote the signal contrast as calculated from the square root of the luminance variance (equations S3), whereas σ_{xy} represents the combination of those two parameters according to equation S4:

$$\sigma_x = \sqrt{\frac{1}{N-1}\sum_{i=1}^{N}(x_i - \mu_x)^2}, \qquad \sigma_y = \sqrt{\frac{1}{N-1}\sum_{i=1}^{N}(y_i - \mu_y)^2} \tag{S3}$$

$$\sigma_{xy} = \frac{1}{N-1}\sum_{i=1}^{N}(x_i - \mu_x)(y_i - \mu_y) \tag{S4}$$

In addition, the two constants c_1 and c_2 are included to avoid mathematical instability when either $\mu_x^2 + \mu_y^2$ or $\sigma_x^2 + \sigma_y^2$ are close to zero. These constants are calculated by considering the dynamic range L of the pixel values (which is 255 for 8-bit grayscale images as used here) and $K_1, K_2 << 1$ (automatically selected by the algorithm) as follows:

$$c_1 = (K_1 L)^2 \qquad c_2 = (K_2 L)^2 \tag{S5}$$

To reliably apply the described calculations, the images were preprocessed by first converting RGB colors to grayscale and then rescaling the images to a uniform size. Finally, SSIM values were calculated using the structural_similarity metric of the Scikit-image toolbox. Those SSIM values can range from 0 to 1, where 1 indicates perfect similarity between two analyzed images and 0 indicates full dissimilarity.

2.2 Template Matching

As an alternative quantification tool that actually makes use of an object detection approach instead of applying a generic image comparison only, template matching was performed[6]. Here, the reference images of the three bacterial 'mother' colonies were used as templates and the system iterated over the target images (i.e. the images of the co-cultured biofilms) to find all objects that match the template. Also for this algorithm, the images were preprocessed from RGB into grayscale and reshaped to a uniform size. To match the grey scale values of the target images I with those of the templates T, a probability map was created based on normalized correlation coefficients (cv2.TM_CCOEFF_NORMED) that are defined as follows:

$$R(x,y) = \frac{\sum_{x',y'}(T'(x',y') * I'(x+x',y+y'))}{\sqrt{\sum_{x',y'} T'(x',y')^2 * \sum_{x',y'} I'(x+x',y+y')}} \tag{S6}$$

where

$$T'(x',y') = T(x',y') - \frac{1}{w*h} * \sum_{x'',y''} T(x'',y'') \tag{S7}$$

and

$$I'(x+x',y+y') = I(x+x',y+y') - \frac{1}{w*h} * \sum_{x'',y''} I(x+x'',y+y''). \tag{S8}$$

Here, w denotes the width of the template image whereas h is the height, i.e., the length of the image in the other dimension.

The created probability matrix was then compared to a defined probability threshold value between 0 and 1 (1 corresponds to perfect similarity and 0 to full dissimilarity) to find all locations were the matching probability exceeded the threshold. Here, to eliminate inaccuracies arising from this manually defined threshold, the threshold was increased in a stepwise (step size: 0.02) manner from 0.5 to 1 and the number of the identified matching areas was summed up. Threshold values below 0.5 were ignored to avoid unspecific matching. The thus obtained matching numbers can range from 0 to 50, where 50 denotes perfect similarity.

2.3 Feature Detection: Oriented FAST and Rotated BRIEF (ORB)

In a third approach, the ORB method[7] was used to compare target images with the given templates. This method – in general terms – is a fusion of the FAST (Features from Accelerated Segments Test) key point detector and the BRIEF (Binary Robust Independent Elementary Features) detection methods. In brief, FAST is first used to find key points within both, a template image and a target image, by analyzing local changes in brightness[8]. To reach partial scale-invariance, this key point detection is not only performed with the original image, but also with a multiscale image pyramid – a representation, that contains down-sampled versions of the image at different levels. Furthermore, a Harris corner filter[9] is applied to reject edges and to guarantee a reasonable score. In a next step, the orientation of every key point is determined using the *intensity centroid*[10] measure. Therefore, first the *p*-th and *q*-th moments of the key point patches are calculated as

$$m_{pq} = \sum_{x,y} x^p y^q I(x,y), \tag{S9}$$

where *I* denotes the greyscale values of the target and template image, respectively. Based on these moments, the intensity weighted centroid *C* (i.e. the "center of the mass") of each patch (equation S10) and a vector pointing from the center *O* towards the centroid *OC* (equation S11) are calculated, and a canonical rotation is computed for the key point descriptor to obtain rotational invariance.

$$C = \left(\frac{m_{10}}{m_{00}}, \frac{m_{01}}{m_{00}}\right) \tag{S10}$$

$$\theta = atan2(m_{01}, m_{10}) \tag{S11}$$

Afterwards, the BRIEF algorithm is employed to convert all identified key points into a binary feature vector[11]. Therefore, after smoothing the image using a Gaussian kernel to prevent sensitivity towards

high-frequency noise, a set of binary tests τ (equation S12) is performed for all key point patches based on the pixel intensities p. Each feature is then defined as a vector (equation S13) of n such binary tests resulting in a 2xn matrix (equation S14) containing the test locations.

$$\tau(p; x, y) = \begin{cases} 1: & p(x) < p(y) \\ 0: & p(x) \geq p(y) \end{cases} \quad \text{(S12)}$$

$$f(n) = \sum_{1<i<n} 2^{i-1} \tau(p; x_i, y_i) \quad \text{(S13)}$$

$$S = \begin{pmatrix} x_1, \dots, x_n \\ y_1, \dots, y_n \end{pmatrix} \quad \text{(S14)}$$

For the BRIEF algorithm to be invariant to in-plane rotation, a "steered" version of the matrix is calculated (equation S15) by rotating S by the angle θ (which is the same angle determined earlier during the patch orientation step):

$$S_\theta = R_\theta S \quad \text{(S15)}$$

Then, the BRIEF operator is defined as described in equation S16:

$$g_n(p, \theta) := f_n(p) | (x_i, y_i) \in S_\theta \quad \text{(S16)}$$

To compensate for the loss of variance caused by the rotation of the feature patch, a more reliable subset of binary tests is chosen. This is achieved by conducting a search among all possible binary tests to find those that exhibit both, a high variance as well as a negligible degree of correlation. Finally, using those processed feature patches, a Hamming Distance[12] operator is used to match the descriptors by performing brute-force matching to find the best-matching correspondence.

With the processes described above, the 500 strongest key points of the template images were determined and compared to the 500 strongest key points of the test images. The number of matching key points then served as a measure for similarity (in other words, a score of 500 corresponds to perfect similarity).

For each co-cultured colony, the strain determined as the 'most similar parent' is shown in **Table S1**, both for algorithm-based decisions and panel tests. Those results are summarized in Fig. 2 of the main paper.

Table S1. Categorization results of algorithm-based and panel-based decisions regarding the macromorphological appearance of different biofilm colonies. The images shown below represent the following co-cultures: NCIB 3610/B-1 grown on LB (a) and MSgg (d) agar, *natto*/B-1 grown on LB (b) and MSgg (e) agar, NCIB 3610/*natto* grown on LB (c) and MSgg (f) agar. (SS = Structural Similarity, TM = Template Matching, ORB = Oriented FAST and Rotated BRIEF, PD= Panel Decisions)

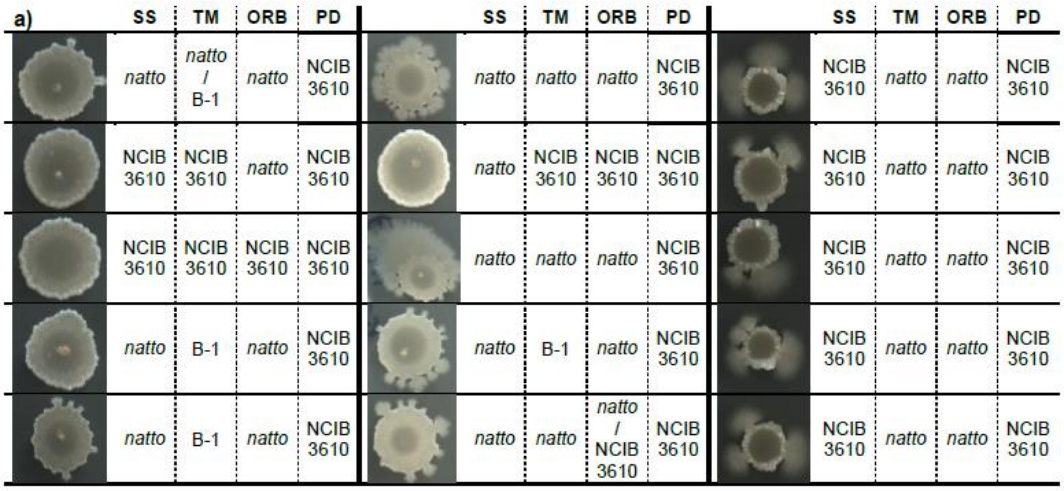

a)	SS	TM	ORB	PD		SS	TM	ORB	PD		SS	TM	ORB	PD
	natto	*natto* / B-1	*natto*	NCIB 3610		*natto*	*natto*	*natto*	NCIB 3610		NCIB 3610	*natto*	*natto*	NCIB 3610
	NCIB 3610	NCIB 3610	*natto*	NCIB 3610		*natto*	NCIB 3610	NCIB 3610	NCIB 3610		NCIB 3610	*natto*	*natto*	NCIB 3610
	NCIB 3610	NCIB 3610	NCIB 3610	NCIB 3610		*natto*	*natto*	*natto*	NCIB 3610		NCIB 3610	*natto*	*natto*	NCIB 3610
	natto	B-1	*natto*	NCIB 3610		*natto*	B-1	*natto*	NCIB 3610		NCIB 3610	*natto*	*natto*	NCIB 3610
	natto	B-1	*natto*	NCIB 3610		*natto*	*natto*	*natto* / NCIB 3610	NCIB 3610		NCIB 3610	*natto*	*natto*	NCIB 3610

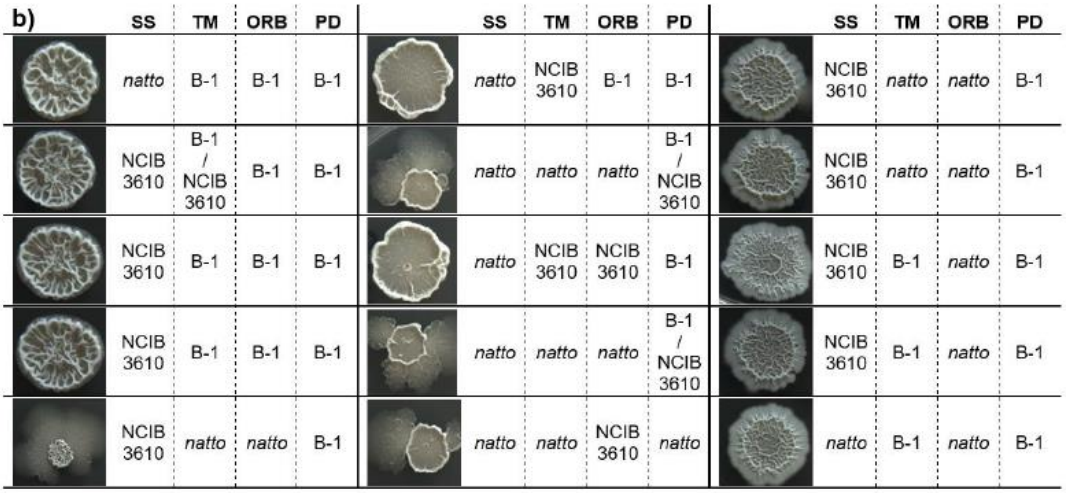

b)	SS	TM	ORB	PD		SS	TM	ORB	PD		SS	TM	ORB	PD
	natto	B-1	B-1	B-1		*natto*	NCIB 3610	B-1	B-1		NCIB 3610	*natto*	*natto*	B-1
	NCIB 3610	B-1 / NCIB 3610	B-1	B-1		*natto*	*natto*	*natto*	B-1 / NCIB 3610		NCIB 3610	*natto*	*natto*	B-1
	NCIB 3610	B-1	B-1	B-1		*natto*	NCIB 3610	NCIB 3610	B-1		NCIB 3610	B-1	*natto*	B-1
	NCIB 3610	B-1	B-1	B-1		*natto*	*natto*	*natto*	B-1 / NCIB 3610		NCIB 3610	B-1	*natto*	B-1
	NCIB 3610	*natto*	*natto*	B-1		*natto*	*natto*	NCIB 3610	*natto*		*natto*	B-1	*natto*	B-1

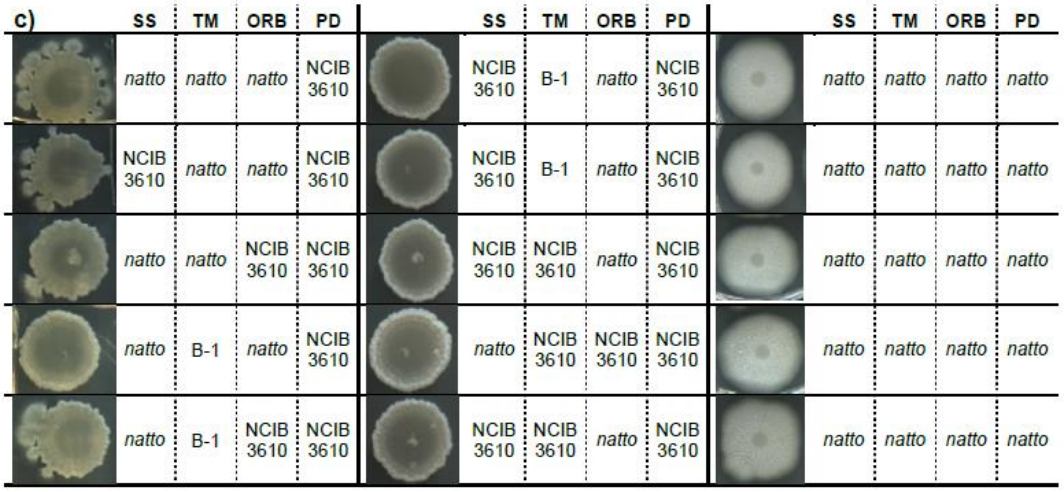

c)	SS	TM	ORB	PD		SS	TM	ORB	PD		SS	TM	ORB	PD
	natto	*natto*	*natto*	NCIB 3610		NCIB 3610	B-1	*natto*	NCIB 3610		*natto*	*natto*	*natto*	*natto*
	NCIB 3610	*natto*	*natto*	NCIB 3610		NCIB 3610	B-1	*natto*	NCIB 3610		*natto*	*natto*	*natto*	*natto*
	natto	*natto*	NCIB 3610	NCIB 3610		NCIB 3610	NCIB 3610	*natto*	NCIB 3610		*natto*	*natto*	*natto*	*natto*
	natto	B-1	*natto*	NCIB 3610		*natto*	NCIB 3610	NCIB 3610	NCIB 3610		*natto*	*natto*	*natto*	*natto*
	natto	B-1	NCIB 3610	NCIB 3610		NCIB 3610	NCIB 3610	*natto*	NCIB 3610		*natto*	*natto*	*natto*	*natto*

d)

SS	TM	ORB	PD
NCIB 3610	NCIB 3610	NCIB 3610	NCIB 3610
NCIB 3610	NCIB 3610	*natto*	NCIB 3610
NCIB 3610	NCIB 3610	NCIB 3610	NCIB 3610
NCIB 3610	*natto*	NCIB 3610	NCIB 3610
NCIB 3610	NCIB 3610	NCIB 3610	NCIB 3610

SS	TM	ORB	PD
B-1	NCIB 3610 / *natto*	*natto*	NCIB 3610
B-1	NCIB 3610	*natto*	NCIB 3610
B-1	*natto*	*natto*	NCIB 3610
B-1	*natto*	*natto*	NCIB 3610
B-1	NCIB 3610 / *natto*	NCIB 3610	NCIB 3610

SS	TM	ORB	PD
B-1	NCIB 3610	NCIB 3610 / *natto*	NCIB 3610
NCIB 3610	NCIB 3610	NCIB 3610	NCIB 3610
NCIB 3610	*natto*	*natto*	NCIB 3610
NCIB 3610	NCIB 3610	*natto*	NCIB 3610
NCIB 3610	NCIB 3610	NCIB 3610	NCIB 3610

e)

SS	TM	ORB	PD
NCIB 3610	*natto*	*natto*	B-1
B-1	*natto*	B-1	B-1
B-1	*natto*	B-1	B-1
B-1	*natto*	B-1	B-1
NCIB 3610	*natto*	*natto*	B-1

SS	TM	ORB	PD
B-1	*natto*	*natto*	*natto*
NCIB 3610	*natto*	*natto*	*natto*
NCIB 3610	*natto*	*natto*	*natto*
NCIB 3610	*natto*	*natto*	*natto*
B-1	*natto*	NCIB 3610	*natto*

SS	TM	ORB	PD
NCIB 3610	NCIB 3610	B-1	B-1
NCIB 3610	NCIB 3610	B-1	B-1
NCIB 3610	NCIB 3610	B-1	B-1
NCIB 3610	NCIB 3610 / *natto*	B-1	B-1
NCIB 3610	NCIB 3610	B-1	B-1

f)

SS	TM	ORB	PD
NCIB 3610	NCIB 3610	NCIB 3610	NCIB 3610
NCIB 3610	NCIB 3610	NCIB 3610	NCIB 3610
NCIB 3610	NCIB 3610	*natto*	NCIB 3610
B-1	NCIB 3610	NCIB 3610	NCIB 3610
NCIB 3610	NCIB 3610	NCIB 3610	NCIB 3610

SS	TM	ORB	PD
NCIB 3610	*natto*	*natto*	*natto*
NCIB 3610	*natto*	NCIB 3610	*natto*
NCIB 3610	*natto*	NCIB 3610	*natto*
NCIB 3610	NCIB 3610 / *natto*	NCIB 3610	*natto*
NCIB 3610	NCIB 3610 / *natto*	*natto*	*natto*

SS	TM	ORB	PD
NCIB 3610	*natto*	*natto*	NCIB 3610
NCIB 3610	*natto*	*natto*	NCIB 3610
NCIB 3610	*natto*	*natto*	NCIB 3610
NCIB 3610	*natto*	NCIB 3610	NCIB 3610
NCIB 3610	*natto*	NCIB 3610 / *natto*	NCIB 3610

3. Classification of different biofilm colonies based on microtopographical properties

3.1 Laser scanning microscopy images visualizing the microscopic surface features of biofilms

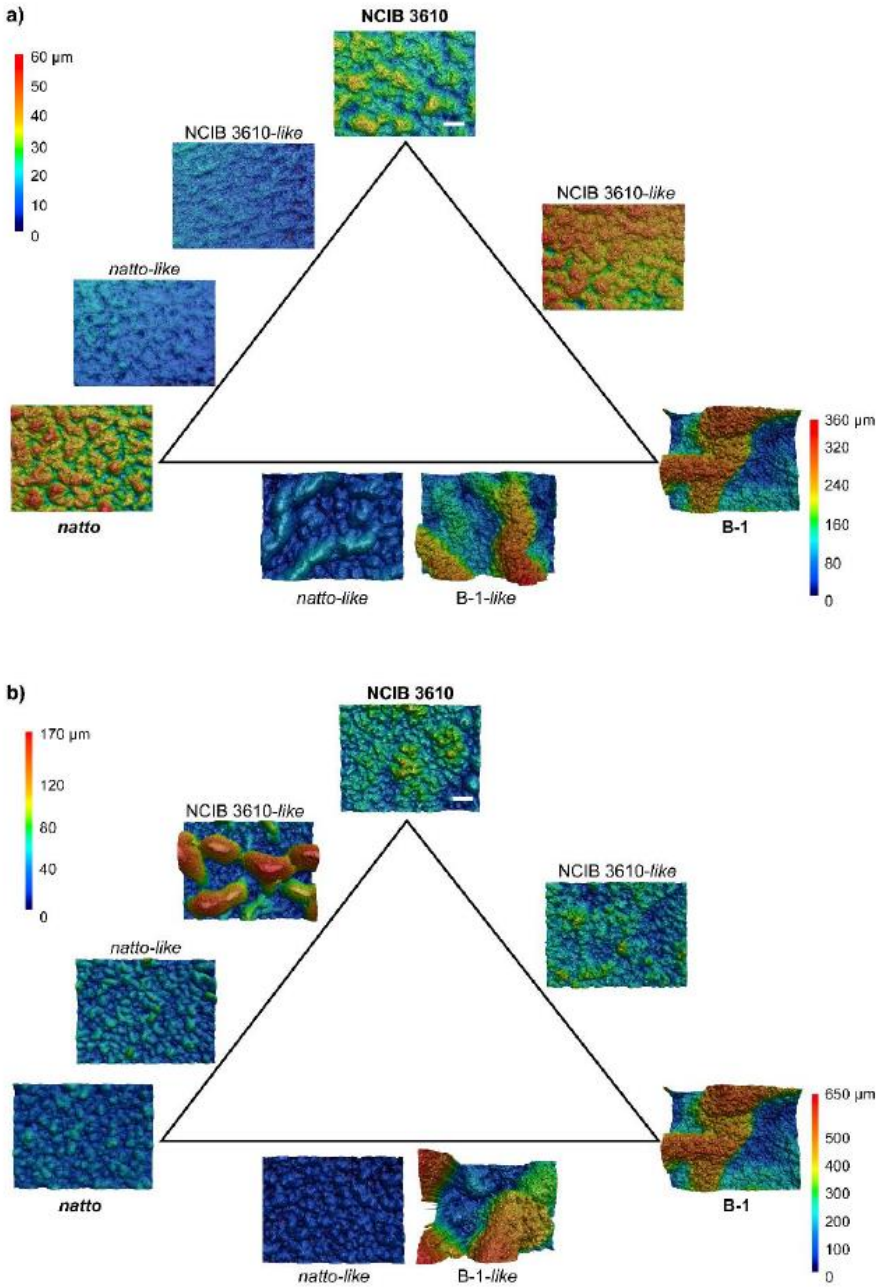

Figure S4. Exemplary topographical images of single strain and co-cultured biofilm colonies grown on LB (a) and MSgg (b) agar. Images were acquired by using light profilometry at a 20x magnification. The color scale on the left applies to all images with the exception of the images exhibiting a higher surface roughness: for single strain B-1 and both *natto*/B-1 co-cultured samples, the color scale shown on the right was applied. The lateral scale bar shown in the NCIB 3610 (a) images represents 100 µm and applies to all images in this figure.

3.2 Parent strain identification attempt based on contact angle (CA) and microscopic biofilm surface roughness (Sdr)

Table S2. Comparison of individual co-cultured NCIB 3610/*natto* colonies grown on LB (a) and MSgg (b) agar to the three possible single-strain 'parent' colonies (generated by either NCIB 3610, *natto* or B-1) in terms of microscopic surface roughness (*Sdr*) and wetting behavior (CA). The result of the panel decisions (PD) regarding the dominant strain is listed for each sample. Paired *t*-tests were conducted and the calculated *p*-values are shown. The largest *p*-value obtained for each sample type is depicted in bold print. The corresponding strain can be interpreted as the 'least different' variant.

a)		*Sdr*			Contact angle		
Sample	PD	$p_{NCIB\ 3610}$	p_{natto}	p_{B-1}	$p_{NCIB\ 3610}$	p_{natto}	p_{B-1}
1	NCIB 3610	0.00083	0.00014	**0.00251**	0.045	**0.868**	1.80E-13
2	NCIB 3610	0.00043	0.00011	**0.00246**	**0.7973**	0.5313	0.0013
3	NCIB 3610	0.0017	8.80E-05	**0.0025**	**0.5644**	2.60E-03	9.00E-14
4	NCIB 3610	**0.203**	**0.203**	0.025	**0.018**	6.70E-12	0.003
5	NCIB 3610	**0.01304**	0.00054	0.00335	**0.06344**	**0.06344**	0.00045
6	NCIB 3610	0.019	**0.0522**	0.0046	**0.9457**	0.8723	0.0057
7	NCIB 3610	**0.5982**	0.0045	0.0045	**0.2675**	0.14139	0.00012
8	NCIB 3610	**0.01003**	0.00052	0.00337	**0.376**	0.063	6.80E-08
9	NCIB 3610	**0.1163**	0.0025	0.0036	**1**	**1**	0.00049
10	NCIB 3610	**0.01428**	0.00092	0.00346	**0.932**	0.379	5.70E-05
11	*natto*	**0.5277**	0.0412	0.0043	0.089	**0.951**	4.40E-11
12	*natto*	6.80E-05	4.20E-05	**0.0023**	0.05	**0.75**	1.20E-12
13	*natto*	**0.00565**	0.00033	0.00328	0.0045	**0.151**	8.50E-13
14	*natto*	0.00053	3.50E-05	**0.00236**	0.165	**0.262**	6.50E-14
15	*natto*	0.0002	3.80E-05	**0.0024**	**0.75468**	**0.75468**	0.00026

b)		*Sdr*			Contact angle		
Sample	PD	$p_{NCIB\ 3610}$	p_{natto}	p_{B-1}	$p_{NCIB\ 3610}$	p_{natto}	p_{B-1}
1	NCIB 3610	0.421	**0.614**	0.031	**0.39**	0.058	**0.39**
2	NCIB 3610	**1**	**1**	0.031	**0.5825**	0.0013	0.4909
3	NCIB 3610	**0.258**	0.221	0.031	**0.3417**	0.0021	0.3091
4	NCIB 3610	**0.00472**	0.00068	0.00339	**0.044**	**0.044**	9.60E-05
5	NCIB 3610	**0.992**	**0.992**	0.029	**0.0088**	4.90E-11	0.0033
6	*natto*	**0.06**	**0.06**	0.038	**0.43**	1.30E-08	0.18
7	*natto*	**0.035**	0.026	**0.035**	**0.91**	6.70E-07	0.53
8	*natto*	**0.441**	0.04	0.031	**0.97**	1.60E-08	0.34
9	*natto*	**0.135**	**0.135**	0.036	**0.88**	0.13	**0.88**
10	*natto*	**0.067**	0.034	0.031	**0.68**	0.11	**0.68**
11	NCIB 3610	**0.075**	0.048	0.031	0.00233	**0.43318**	0.00073
12	NCIB 3610	9.50E-05	0.00058	**0.02085**	2.20E-14	**0.00057**	1.90E-12
13	NCIB 3610	**0.164**	0.1	0.031	0.00221	**0.95637**	0.00071
14	NCIB 3610	**0.0396**	0.0036	0.0261	0.01	**0.8975**	0.0079
15	NCIB 3610	**0.042**	0.03	0.03	1.30E-12	**0.15**	4.33E-12

3.3 Detailed surface microtopography analysis of co-cultured biofilms employing a broader set of metrological parameters

The parameters we used for an in-depth characterization of different biofilm surface properties are as follows: The root mean square height, $Sq = \sqrt{\frac{1}{A}\iint_A Z^2(x,y)dxdy}$, is a common parameter in surface science and is equivalent to the standard deviation of the z-coordinates.

To investigate the peak properties of biofilm surfaces, we measured the largest peak height, $Sp = \max_A z(x,y)$, the reduced peak height, *Spk*, which describes the height above the core surface, and the peak material volume, *Vmp*, which is a measure of the volume of reduced peak structures.

The core surface was described by the core height, *Sk*, the core material volume, *Vmc,* and the core void volume, *Vvc*. The core height, *Sk*, was calculated by subtracting the minimum height from the maximum height of the core surface and represents the surface roughness after removal of predominant peaks and valleys. *Vmc* and *Vvc* were calculated using standard settings (p = 10%, q = 80%); those parameters represent the material and void volume of a core surface, respectively.

For a detailed investigation of valley structures, the largest valley depth, $Sv = \left|\min_A z(x,y)\right|$, within the investigated area and the valley void volume, *Vvv*, which represents the void volume of the dale were calculated.

The surface peak density, *Spd*, was employed to measure the number of peaks per unit area, and the sparseness of the peaks estimated by the *Sal*, parameter, which is based on the auto-correlation length. In detail, *Sal* represents the horizontal distance in the direction in which the auto-correlation function, $f_{ACF}(t_x,t_y) = \frac{\iint_A z(x,y)z(x-t_x,y-t_y)dxdy}{\iint_A z^2(x,y)dxdy}$ decays to a value of 0.2 the fastest; this represents the distance one can move away from a certain surface texture feature until the local topography significantly differs from that of the original location.

With this extended set of metrological parameters, co-cultured NCIB 3160/*natto* colonies were characterized in more detail. The corresponding values are listed below in **Table S3** and **S4** for biofilm cultivation on LB agar (**Table S3**) and MSgg agar (**Table S4**), respectively.

Table S3. Overview of different metrological surface parameters determined for co-cultured NCIB 3610/*natto* colonies grown on LB agar. The data was obtained from 15 measurements generated from 3 different growth batches. Asterisks (*) denote significant differences compared to pure NCIB 3610 colonies, and hash symbols (#) denote significant differences compared to pure *natto* colonies (p=0.05).

	Parameters	NCIB 3610	NCIB 3610-like	*natto*-like	*natto*
	***Sq* [µm]**	4.7 ± 1.1$^{\#}$	5.7 ± 1.1	5.1 ± 1.6	6.2 ± 1.6*
Peak	***Sp* [µm]**	16 ± 6$^{\#}$	18 ± 4	14 ± 4$^{\#}$	22 ± 6*
	***Spk* [µm]**	3.7 ± 1.3$^{\#}$	4.4 ± 2.1	3.4 ± 0.8$^{\#}$	5.3 ± 1.6*
	***Vmp* [mL/mm^2]**	0.19 ± 0.07$^{\#}$	0.22 ± 0.06	0.18 ± 0.05$^{\#}$	0.34 ± 0.19*
Core	***Sk* [µm]**	14 ± 6	15 ± 4	15 ± 6	18 ± 7
	***Vmc* [mL/mm^2]**	5.0 ± 2.0	5.5 ± 1.2	5.0 ± 1.7	7.8 ± 2.1
	***Vvc* [mL/mm^2]**	5.6 ± 1.3$^{\#}$	6.9 ± 1.8	6.5 ± 2.1	7.8 ± 2.1*
Pit	***Sv* [µm]**	20 ± 6	18 ± 3	15 ± 5$^{\#}$	22 ± 5
	***Vvv* [mL/mm^2]**	0.54 ± 0.14	0.59 ±0.11	0.51 ± 0.16	0.64 ± 0.14
Density	***Sal* [µm]**	77 ± 23	99 ± 19*	110 ± 21$^{\#}$	73 ± 28
	***Spd* [10^3/mm^2]**	91 ± 19	51 ± 29*	34 ± 24 $^{\#}$	79 ± 24

Table S4. Overview of different metrological surface parameters determined for co-cultured NCIB 3610/*natto* colonies grown on MSgg agar. The data was obtained from 15 measurements generated from 3 different growth batches. Asterisks (*) denote significant differences compared to pure NCIB 3610 colonies, and hash symbols (#) denote significant differences compared to pure *natto* colonies (p=0.05).

	Parameters	NCIB 3610	NCIB 3610-like	*natto*-like	*natto*
	***Sq* [µm]**	17.4 ± 4.2$^{\#}$	28.0 ± 8.1*	12.3 ± 0.8*	13.0 ± 5.3*
Peak	***Sp* [µm]**	53.2 ± 9.6$^{\#}$	81.6 ± 19.6*	44.7 ± 3.0	43.8 ± 8.0*
	***Spk* [µm]**	15.2 ± 2.2$^{\#}$	42.2 ± 22.9*	13.3 ± 1.3	12.2 ± 2.0*
	***Vmp* [mL/mm^2]**	0.75 ± 0.12$^{\#}$	1.36 ± 0.53*	0.65 ± 0.69	0.61 ± 0.11*
Core	***Sk* [µm]**	46.2 ± 12.7$^{\#}$	56.3 ± 14.0	31.8 ± 2.2	34.6 ± 11.7*
	***Vmc* [mL/mm^2]**	16.2 ± 4.4$^{\#}$	24.0 ± 8.3*	11.1 ± 0.8	12.0 ± 3.8
	***Vvc* [mL/mm^2]**	21.8 ± 4.7$^{\#}$	38.4 ± 15.7*	15.7 ± 0.9*	16.5 ± 4.8*
Pit	***Sv* [µm]**	61.3 ± 17.5$^{\#}$	69.9 ± 14.6	42.4 ± 4.0*	44.9 ± 10.6
	***Vvv* [mL/mm^2]**	1.83 ± 0.50$^{\#}$	2.34 ± 0.81	1.19 ± 0.13*	1.32 ± 0.39
Density	***Sal* [µm]**	57.3 ± 5.4$^{\#}$	69.2 ± 9.6*	27.0 ± 1.5$^{\#,*}$	50.4 ± 26.4*
	***Spd* [10^3/mm^2]**	47 ± 3$^{\#}$	27 ± 4*	20 ± 1*	30 ± 13*

3.4 Microscopic characterization of biofilm peripheries

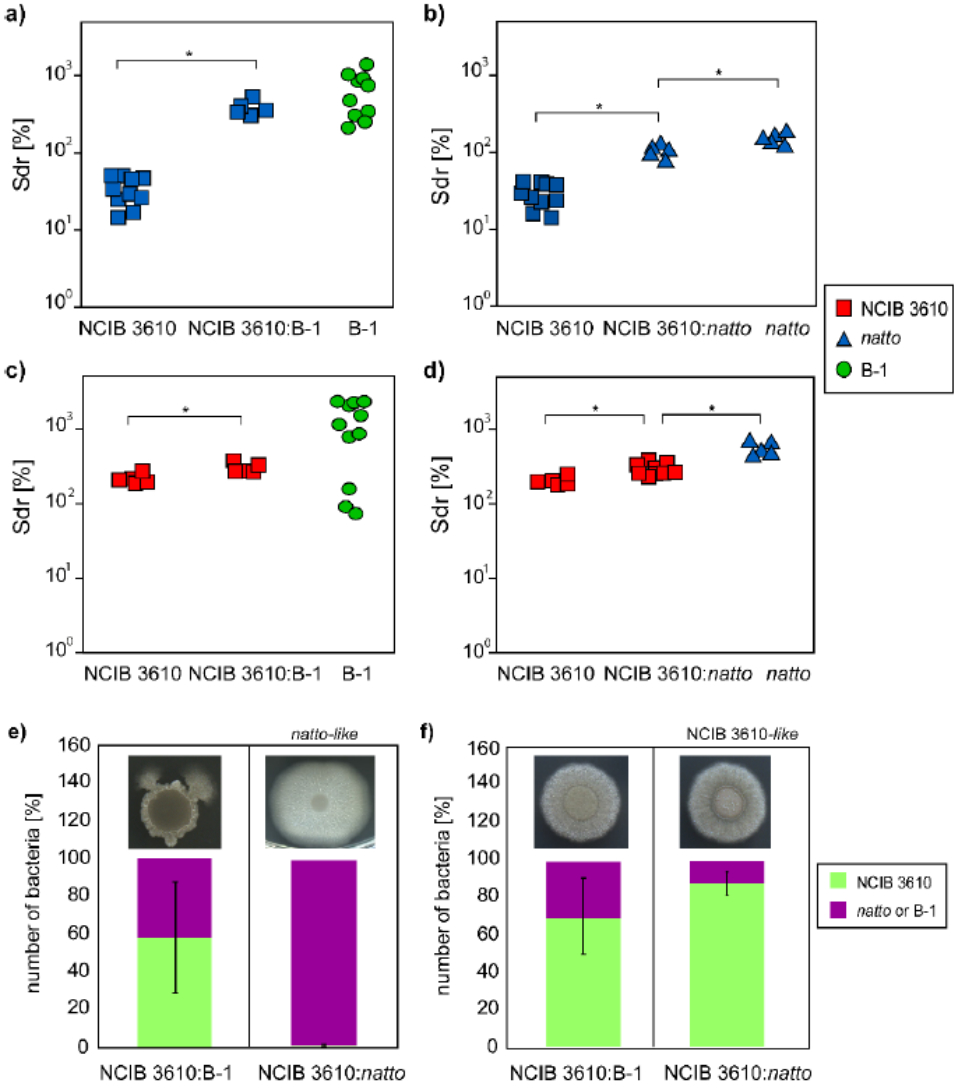

Figure S5. Quantitative surface characterization and strain identification of the peripheries of different biofilm colonies. Surface roughness (*Sdr*) values were obtained from the peripheries of the co-cultured NCIB 3610/B1 (a, c) and NCIB 3610/*natto* (b, d) biofilm colonies grown on LB (a, b) and MSgg (c, d) agar, respectively. The data is sorted according to the panel decisions regarding the morphological dominance of either NCIB 3610 (□), *natto* (Δ) or B-1 (○) in the co-cultured colonies. The wetting behavior in the biofilm periphery is indicated by the color of the marker: green color represents lotus-like superhydrophobic behavior, red color indicates rose-like superhydrophobicity, and blue color represents hydrophilic behavior. Asterisks denote statistical significances based on a *p*-value of $p = 0.05$. Even though we find significant differences between the contact angles and *Sdr* values of all single-strain 'parent' colonies (when compared pair-wise), this is not marked in the figure for simplicity. The co-existence ratio of fluorescent NCIB 3610 bacteria and another, non-fluorescent strain (either *natto* or B-1) is shown for periphery structures of co-cultured colonies grown on either LB (e) or MSgg (f) agar, respectively. Error bars represent the standard deviation as obtained from at least five different colonies.

4. Experimental results obtained with biofilm colonies involving a NCIB 3610 mutant strain unable to produce *BslA*

One of the main biofilm matrix components of *B. subtilis* NCIB 3610 bacteria is *BslA*, which is an amphiphilic hydrophobin. In previous studies[13–20] it was shown that *BslA* coats the biofilm and conveys hydrophobicity to the biofilm surface. Here, to verify that the biofilm colonies we study in the main paper do correctly express this *BslA* protein, we conducted control experiments with a mutant strain unable to produce this hydropohobin. Thus, we assessed the wetting behavior and surface topography of co-cultured biofilm colonies which we obtained by mixing either *natto* or B-1 bacteria with this NCIB 3610 mutant strain (*ΔBslA*). To also secure fair starting conditions between the involved bacteria in those experiments, we first determined the viable cell amount at an optical density of 0.6 as we describe it for wild type NCIB 3610 in the main text. Since we found that planktonic *ΔBslA* cultures contained (3.3 ± 1.5) x 10^8 CFU/mL, the mixing volumes were adjusted to achieve a 1:1 CFU ratio in each mixture. Moreover, we found that the growth kinetics of this NCIB 3610 mutant strain in LB and MSgg media is similar to that of the wild-type strain (**Fig. S6**).

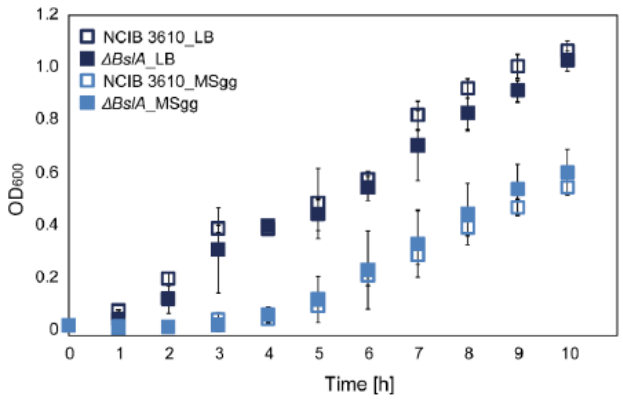

Figure S6. Microbial growth curves of NCIB 3610 wild type and mutant strains in LB and MSgg media. The error bars denote the standard deviation as obtained from three different growth batches.

As depicted below, biofilm colonies generated from pure *ΔBslA* cultures on MSgg agar showed low contact angles (and thus hydrophilic properties) – which is fully consistent with our expectation based on literature (**Fig. S7**). Moreover, as can be seen in **Fig. S7b** and **Fig. S7d**, co-cultured colonies of *natto* and *ΔBslA* exhibit properties that are different from those of both 'parent' strains; this is again in full agreement with the results we present and discuss in the main text. For the *ΔBslA*/B-1 mixtures, neither CA data nor *Sdr* data alone is sufficient to detect the contribution of the 'other' (non-dominant) parent

strain; probably, similar to what we show in **Table S3** and **S4**, a more detailed analysis of the biofilm microtopography would be required again to reveal this contribution of the second parent strain.

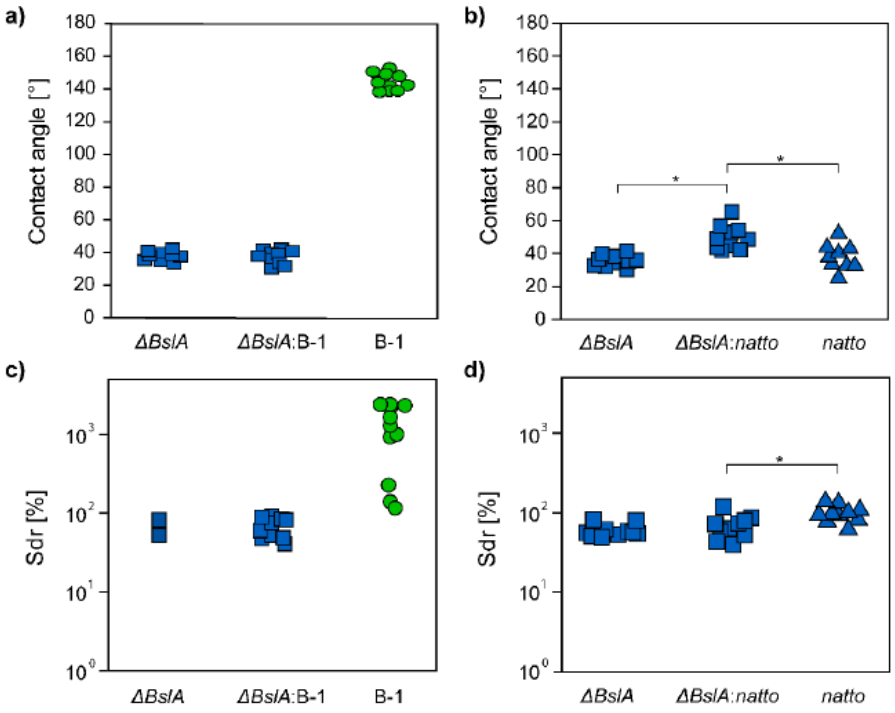

Figure S7: Quantitative surface topography characterization of biofilm colonies generated by co-culturing either B-1 or *natto* with *ΔBslA* . Surface roughness (*Sdr*) values are obtained from the center of the co-cultured *ΔBslA*/B1 (a, c) and *ΔBslA/natto* (b, d) biofilm colonies grown on MSgg agar. The data is sorted regarding the morphological dominance of either *ΔBslA* (□), *natto* (Δ) or B-1 (○) in the co-cultured colonies. The wetting behavior of the biofilm colonies is indicated by the color of the marker: green color represents lotus-like superhydrophobic behavior and blue color represents hydrophilic behavior. Asterisks denote statistical significances based on a *p*-value of $p = 0.05$. Even though we find significant differences between the contact angles and *Sdr* values of all single-strain 'parent' colonies (when compared pair-wise), this is not marked in the figure for simplicity.

References

1. Harris, C.R., Millman, K.J., van der Walt, S.J., Gommers, R., Virtanen, P., Cournapeau, D., Wieser, E., Taylor, J., Berg, S., Smith, N.J., *et al.* (2020). Array programming with NumPy. Nature *585*, 357–362. Available at: http://dx.doi.org/10.1038/s41586-020-2649-2.

2. Bradski, G. (2000). The OpenCV Library. Dr. Dobb's J. Softw. Tools. 25, 120-125.

3. Clark, A. (2020). Pillow (PIL Fork) Documentation Release 3.1.2.

4. van der Walt, S.J., Schönberger, J.L., Nunez-Iglesias, J., Boulogne, F., Warner, J.D., Yager, N., Gouillart, E., and Yu, T. (2014). Scikit-image: Image processing in python. PeerJ *2014*, 1–18.

5. Wang, Z., Bovik, A.C., Sheikh, H.R., and Simoncelli, E.P. (2004). Image quality assessment: From error visibility to structural similarity. IEEE Trans. Image Process. *13*, 600–612.

6. Culjak, I., Abram, D., Pribanic, T., Dzapo, H., and Cifrek, M. (2012). A brief introduction to OpenCV. In 2012 Proceedings of the 35th International Convention MIPRO (Opatija), pp. 1725–1730.

7. Rublee, E., Rabaud, V., Konolige, K., and Bradski, G. (2011). ORB: an efficient alternative to SIFT or SURF. In International conference on computer vision (Barcelona: IEEE), pp. 2564–2571.

8. Viswanathan, D.G. (2009). Features from Accelerated Segment Test (FAST). In Proceedings of the 10th workshop on Image Analysis for Multimedia Interactive Services (London, UK).

9. Harris, C., and Stephens, M. (2013). A Combined Corner and Edge Detector. 23.1-23.6.

10. Rosin, P.L. (1999). Measuring Corner Properties. Comput. Vis. Image Underst. *73*, 291–307.

11. Calonder, M., Lepetit, V., Strecha, C., and Fua, P. (2010). BRIEF: Binary robust independent elementary features. Lect. Notes Comput. Sci. (including Subser. Lect. Notes Artif. Intell. Lect. Notes Bioinformatics) *6314 LNCS*, 778–792.

12. Norouzi, M., Fleet, D.J., and Salakhutdinov, R. (2012). Hamming distance metric learning. Adv. Neural Inf. Process. Syst. *2*, 1061–1069.

13. Kesel, S., Von Bronk, B., Falcón García, C., Götz, A., Lieleg, O., and Opitz, M. (2017). Matrix composition determines the dimensions of: Bacillus subtilis NCIB 3610 biofilm colonies grown on LB agar. RSC Adv. *7*, 31886–31898.

14. Kovács, Á.T., van Gestel, J., and Kuipers, O.P. (2012). The protective layer of biofilm: A repellent function for a new class of amphiphilic proteins. Mol. Microbiol. *85*, 8–11.

15. Bromley, K.M., Morris, R.J., Hobley, L., Brandani, G., Gillespie, R.M.C., McCluskey, M., Zachariae, U., Marenduzzo, D., Stanley-Wall, N.R., and MacPhee, C.E. (2015). Interfacial self-assembly of a bacterial hydrophobin. Proc. Natl. Acad. Sci. U. S. A. *112*, 5419–5424.

16. Arnaouteli, S., MacPhee, C.E., and Stanley-Wall, N.R. (2016). Just in case it rains: building a hydrophobic biofilm the Bacillus subtilis way. Curr. Opin. Microbiol. *34*, 7–12. Available at: http://dx.doi.org/10.1016/j.mib.2016.07.012.

17. Hobley, L., Ostrowski, A., Rao, F. V., Bromley, K.M., Porter, M., Prescott, A.R., MacPhee, C.E., Van Aalten, D.M.F., and Stanley-Wall, N.R. (2013). BslA is a self-assembling bacterial hydrophobin that coats the Bacillus subtilis biofilm. Proc. Natl. Acad. Sci. U. S. A. *110*, 13600–13605.

18. Kobayashi, K., and Iwano, M. (2012). BslA(YuaB) forms a hydrophobic layer on the surface of Bacillus subtilis biofilms. Mol. Microbiol. *85*, 51–66.

19. Morris, R.J., Schor, M., Gillespie, R.M.C., Ferreira, A.S., Baldauf, L., Earl, C., Ostrowski, A., Hobley, L., Bromley, K.M., Sukhodub, T., *et al.* (2017). Natural variations in the biofilm-associated protein BslA from the genus Bacillus. Sci. Rep. *7*, 1–13.

20. Liu, W., Li, S., Wang, Z., Yan, E.C.Y., and Leblanc, R.M. (2017). Characterization of Surface-Active Biofilm Protein BslA in Self-Assembling Langmuir Monolayer at the Air-Water Interface. Langmuir *33*, 7548–7555.

A.4 Machine Learning Approach to Analyze the Surface Properties of Biological Materials

ACS Biomaterials SCIENCE & ENGINEERING

pubs.acs.org/journal/abseba Article

Machine Learning Approach to Analyze the Surface Properties of Biological Materials

Carolin A. Rickert, Elif N. Hayta, Daniel M. Selle, Ioannis Kouroudis, Milan Harth, Alessio Gagliardi, and Oliver Lieleg*

Cite This: *ACS Biomater. Sci. Eng.* 2021, 7, 4614–4625 Read Online

ACCESS | Metrics & More | Article Recommendations | Supporting Information

ABSTRACT: Similar to how CRISPR has revolutionized the field of molecular biology, machine learning may drastically boost research in the area of materials science. Machine learning is a fast-evolving method that allows for analyzing big data and unveiling correlations that otherwise would remain undiscovered. It may hold invaluable potential to engineer novel functional materials with desired properties, a field, which is currently limited by time-consuming trial and error approaches and our limited understanding of how different material properties depend on each other. Here, we apply machine learning algorithms to classify complex biological materials based on their microtopography. With this approach, the surfaces of different variants of biofilms and plant leaves can not only be distinguished but also correctly classified according to their wettability. Furthermore, an importance ranking provided by one of the algorithms allows us to identify those surface features that are critical for a successful sample classification. Our study exemplifies how machine learning can contribute to the analysis and categorization of complex surfaces, a tool, which can be highly useful for other areas of materials science, such as damage assessment as well as adhesion or friction studies.

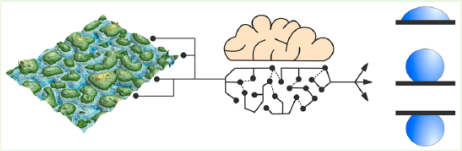

KEYWORDS: *supervised learning, deep learning, hydrophobicity, wettability, topography*

■ INTRODUCTION

Although the bulk volume constitutes the majority of a material, many properties relevant for applications are determined by its surface. Often, biological examples serve as inspiration for the development of novel surface structures with astonishing properties. A famous example from this area of materials science is given by nanotextured graphene surfaces with maximal light absorbance properties,[1] similar to the ultrablack structures found in snakes[2] or butterflies.[3] Also artificial omniphobic surfaces draw inspiration from nature,[4] and they allow for repelling a broad range of liquids including blood,[5] oil, and sticky fluids such as ketchup.[6] To obtain surfaces with dedicated properties in terms of wetting,[7,8] adhesion,[9,10] friction,[11] stability,[12] electrical properties,[13,14] or biocompatibility,[15] the chemical composition, morphology, and functionalization of material surfaces needs to be adjusted. However, such targeted tailoring of a surface behavior typically relies on time-consuming trial and error approaches. To a large extent, this is due to our limited knowledge of how distinct surface properties depend on each other and, in particular, on the surface topography. This topography, which *inter alia* includes different surface features and the ensuing surface roughness, can critically determine the behavior of an object in terms of friction,[16,17] wettability[18] and interaction with molecules.[19] A strong correlation between the surface topography and the wettability was, for instance, observed for bacterial biofilms (surface attached bacterial communities). Whether such a biofilm behaves as hydrophilic or hydrophobic is mostly attributed to the presence of the surface hydrophobin BslA,[20,21] that is, the chemical composition of the biofilm. However, the type of biofilm hydrophobicity can differ, even for biofilms of similar chemical composition; when tilted, some of them efficiently repel water, as known for lotus leaves, while others show high contact angles but a strong adhesion toward water droplets. This variation in the hydrophobic behavior of biofilms was shown to be dictated by the surface topography.[22]

When more than one surface property of a material needs to be optimized, the ensuing high complexity further increases the experimental workload and renders the design of new functional materials challenging. Here, machine learning may provide a remedy that can help reduce the time required to optimize a material development process. With machine learning methods, multidimensional data sets can be analyzed; then, patterns in those big data sets can be automatically recognized to form generalized, descriptive models that otherwise the human mind can hardly identify. On the basis of these models, additional samples can be evaluated, and the

Received: July 1, 2021
Accepted: August 9, 2021
Published: August 20, 2021

https://doi.org/10.1021/acsbiomaterials.1c00869
ACS Biomater. Sci. Eng. 2021, 7, 4614–4625

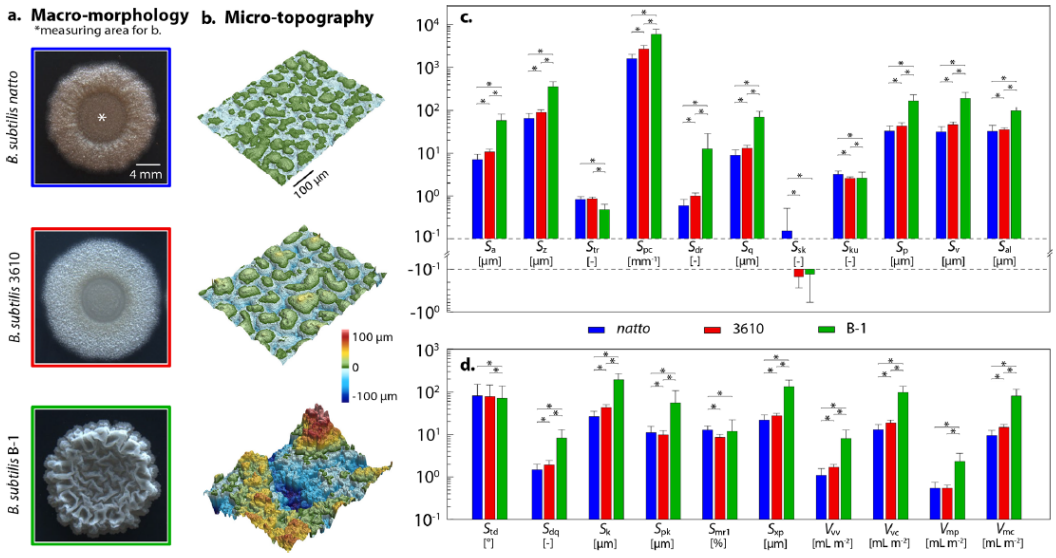

Figure 1. Surface structure of different bacterial biofilms. Macroscopic colony images (a), microscopic profilometric images (b), and metrological surface parameters (c,d) as determined from the latter are shown for biofilms generated by *B. subtilis natto* (blue, n = 705), *B. subtilis* NCIB 3610 (red, n = 592), and *B. subtilis* B-1 (green, n = 491) bacteria cultivated on MSgg agar. The scale bars in (a,b) apply to all three images within the respective subfigure. The error bars in (c) and (d) denote the standard deviation as obtained from $n \geq 491$ images each. Asterisks indicate statistical differences as assessed with a Wilcoxon−Mann−Whitney test applying a p-value of 0.05.

model can be used to predict their properties. Such approaches were already successfully implemented to predict the efficacy of anticancer drugs,[23] to identify ideal process parameters in 3D bioprinting,[24] or to direct material synthesis toward ultraincompressible behavior.[25]

In this study, we use machine learning to analyze the topographical features of complex biological surfaces. We show that, when fed microtopographical information, several algorithms can classify different biological surfaces regarding their wetting behavior. Moreover, we demonstrate how the dimensionality of the data set can be reduced by identifying a subset of parameters that contributes most strongly to the classification procedure. Several other surface-related questions in material science, such as adhesion or friction studies or damage assessments, could benefit from a similar approach as we introduce it here.

RESULTS AND DISCUSSION

Machine Learning Algorithms Can Discriminate the Topographies of Different Bacterial Biofilms. As an initial step toward our goal to apply machine learning methods for analyzing the surface properties of complex biological materials, we aim at obtaining a broad overview of the topographical features of biosurfaces with different morphological characteristics. For this purpose, we first analyze surface-bound bacterial colonies (so-called biofilms). This particular biomaterial comes with the advantage that its surface properties can be broadly varied by selecting different bacterial strains and/or growth conditions for biofilm generation. In this first step, three different *Bacillus subtilis* variants that are closely related are cultivated on MSgg agar and analyzed after 24 h of incubation (this incubation time is customary when mature biofilms are desired;[26] Figure 1a,b). Macroscopically, the central areas of biofilm colonies generated by *B. subtilis natto* and *B. subtilis* NCIB 3610 bacteria are both fairly flat; their microtopographies, however, appear different, as the latter biofilms exhibit somewhat bigger structures on this microscopic length scale. *B. subtilis* B-1 biofilms have a very diverse appearance, both on the macro- and microscale; they exhibit large-scale wrinkles and, locally, wavelike features.

For all biofilm variants mentioned above, profilometric images (approximately 500 per strain; for example images, please refer to Supporting Information, Section S13.1) acquired at the microscale are evaluated further. In detail, 21 different metrological surface parameters (a broad potpourri of height, spatial, hybrid, functional, and functional volume parameters according to EN ISO 25178, see Figure 1c,d) are calculated from those images to quantify different aspects of their surface topography (for details, please refer to the Supporting Information, Section S2). For the majority of those parameters, significant differences are obtained that allow for distinguishing the three different biofilm types. Overall, for most parameters we find the highest absolute values for lotuslike B-1 biofilm surfaces; in contrast, hydrophilic *natto* biofilms tend to return the lowest values, yet this is only a general trend and does not provide a strict sorting criterion.

Thus, in the next step we attempt an algorithm-based classification of the topographical biofilm images based on those metrological parameters. In detail, we ask whether or not an automized classification procedure can reliably decide what biofilm variant a parameter set obtained from a particular image belongs to. For this purpose, we select four different machine learning methods of different complexity and abstraction levels (Figure 2). Each of those algorithms is first trained and then tested with the data set shown in Figure 1. For this purpose, the accuracies of the categorization decisions

https://doi.org/10.1021/acsbiomaterials.1c00869
ACS Biomater. Sci. Eng. 2021, 7, 4614−4625

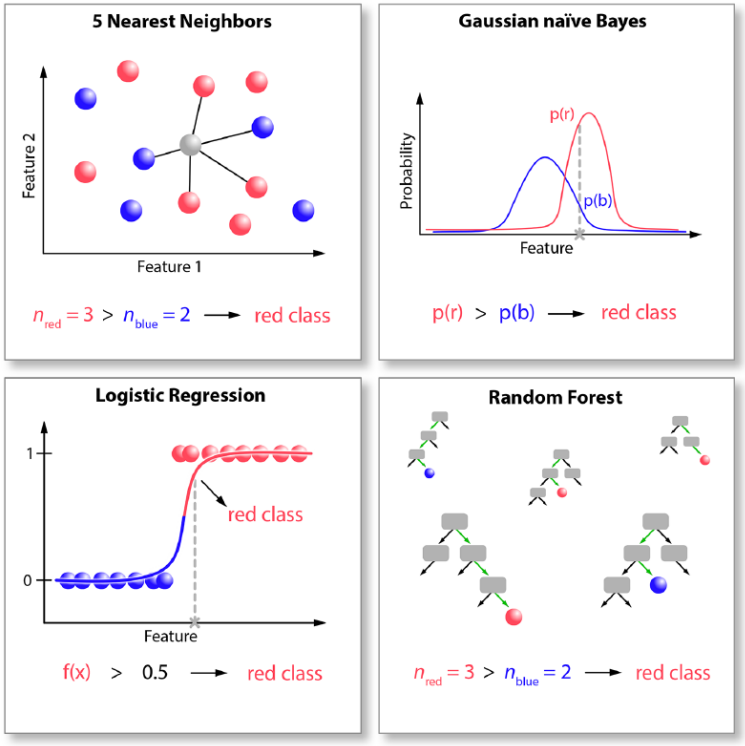

Figure 2. Schematic illustration of the four machine learning algorithms used in this study. The *k* nearest neighbor (KNN) classifier (a) identifies the *k* samples that are closest to the query point in an *n* dimensional space (*n* equals the number of features) and assigns the query sample to that class which has the highest number of representatives (within those *k* samples). The Gaussian naïve Bayes algorithm (b) calculates conditional probabilities and categorizes samples based on a "fits better" principle. The logistic regression algorithm (c) models the probability of classes by assigning importance weights and fitting a sigmoid function through all features. The Random Forest classifier (d) performs predictions in a popular-vote-like manner considering the decision of a large number of random, uncorrelated decision trees.

made by the four algorithms are determined by applying a repeated stratified 5-fold cross-validation; in other words, the data set (a total of ∼1500 images comprising >500 images per biofilm variant) is repetitively separated into training data (80%) and test data (20%, for details see Materials and Methods).

We begin with a rather basic approach and apply a KNN (*k* nearest neighbors) classifier. Here, classification is performed based on a spatial comparison of the test data with the training data. When applying this method to the data set described above, this KNN classifier achieves a prediction accuracy of approximately 98% (Figure 3a). Similarly high accuracies are obtained with the other three algorithms (see Materials and Methods for details). The Gaussian naïve Bayes classifier (Figure 3b) calculates conditional probabilities based on the simplified assumptions that all features are independent, normally distributed and equally contributing. The multinomial logistic regression (Figure 3c) determines the logarithmic odds of each class as a linear combination of the feature variables. The Random Forest classifier (Figure 3d) makes predictions based on the most popular decision of a large number of randomly generated, uncorrelated decision trees. Moreover, in all cases tested here, the calculated specificity and sensitivity values are above 90% (see SI Section S7.1). As we obtain very high classification accuracies with each of the four algorithms, we conclude that the biofilms generated by the three different bacterial strains on MSgg agar can indeed be clearly classified with the set of topographical parameters calculated here.

One major challenge when trying to apply machine learning approaches to experimentally obtained data is the rather small amount of available data points; typically, the number of such experimental repetitions is much smaller than the 500 topographical images we captured here for the different biofilm variants. Thus, in the next step we test the robustness of our machine learning approach when smaller, lab-scaled data sets are used. In detail, we challenge the same algorithms employed so far with a drastically reduced size of training data (Figure 3e−h). Surprisingly, in all four cases even a much smaller number of training data entails categorization accuracies above 90%. Whereas 5 training images per biofilm variant are not sufficient (here, all four algorithms return fluctuating decisions with accuracies between ∼80−95%), data sets calculated from 10 distinct images are enough to obtain stable and reliable results. This is remarkable considering that the data set comprises images of biofilms grown on different days; it thus encompasses a significant level of (typical) biological variability.

https://doi.org/10.1021/acsbiomaterials.1c00869
ACS Biomater. Sci. Eng. 2021, 7, 4614−4625

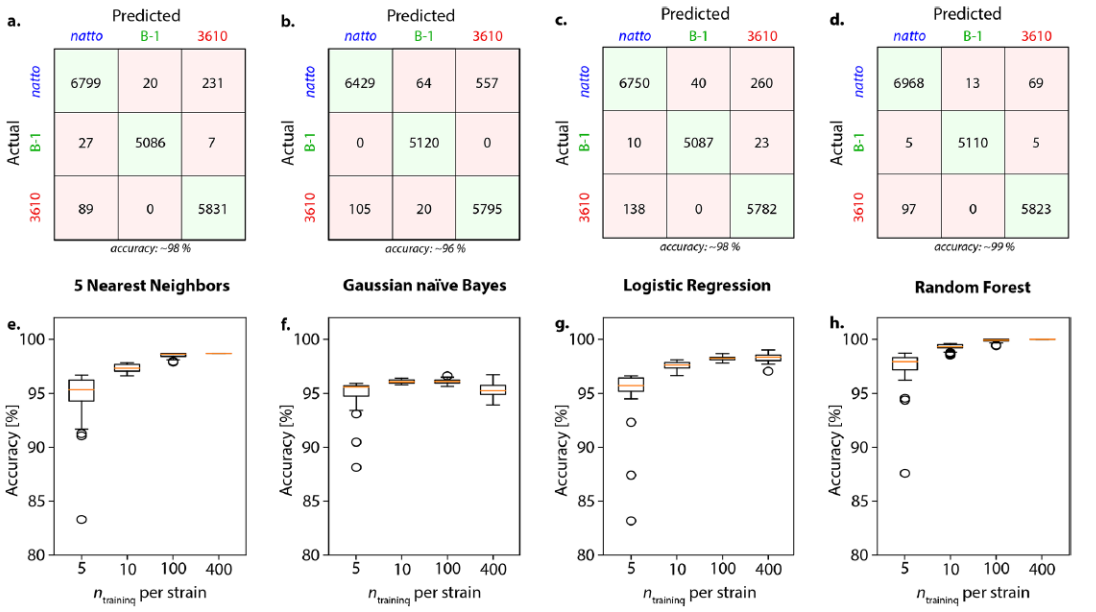

Figure 3. Categorization results obtained with four different machine learning algorithms fed with biofilm data obtained on MSgg agar. The confusion matrices (a–d) compare the actual classes (i.e., the names of the bacterial strains where the biofilms were grown) with the predicted classes when a 5 nearest neighbor classifier (a), a Gaussian naïve Bayes model (b), multinomial logistic regression (c), and a Random Forest classifier (d) are applied to the data. The evaluation was performed by repeated (10 times) 5-fold cross validation with shuffling the data set before each iteration, that is, each sample was used as a test sample 10 times with differently trained algorithms. The main diagonal (green boxes) contains the numbers of correctly classified samples whereas all other boxes represent wrongly assigned samples. The accuracy values below the confusion matrices denote the total proportion of correctly classified samples. Furthermore, the accuracy of the four algorithms is shown as a function of the training set size in (e–h, data obtained from n = 50 runs).

Machine Learning Algorithms Can Also Classify "Unknown" Biofilms and Mixed Biofilm/Plant Data. Having verified that the selected algorithms can make reliable predictions based on the given set of topographical parameters, we next challenge those classifiers in a different way. In detail, we ask them to classify biofilms that were grown at different conditions than the biofilm samples with which the algorithms are trained. At this point, it is important to realize that the three biofilm variants we compared so far not only differ in terms of their surface characteristics but also with regard to a physical property, which is intimately related to the surface topography of a material: the surface wettability.[22] Indeed, we had chosen the growth conditions for cultivating the three *B. subtilis* variants such that the generated biofilms exhibit different wetting behaviors: *B. subtilis natto* biofilms have a hydrophilic surface; *B. subtilis* NCIB 3610 biofilms have superhydrophobic surfaces similar to rose petals; and *B. subtilis* B-1 biofilms have superhydrophobic surfaces similar to lotus leaves (for contact angle measurements and details on how a classification into rose-vs-lotus like behavior was conducted, please refer to Supporting Information, Section S7.2). The key difference between the latter two variants of superhydrophobic behavior can be identified when a water droplet is placed onto a tilted surface: on roselike surfaces, the droplet sticks; in contrast, on lotuslike surfaces the droplet rolls off. In previous studies, these differences in surface wettability were found to mainly depend on two factors: the chemical composition and the surface topography of the sample.[27,28] With the same set of bacterial strains used so far, biofilms with different wetting profiles can be obtained by changing the growth medium from MSgg to LB (see Materials and Methods). As a consequence of this alteration in nutrient availability, biofilms with a different macro-morphological appearance are created (Figure 4a).

Also for this new set of biofilm colonies, profilometric images are acquired on the microscale (Figure 4b) and the same metrological parameters are calculated as for the biofilm samples discussed above (for an overview of this data, see SI Section S8.1). One interesting aspect is that for the strain 3610 not only has the visual appearance of the biofilm colonies changed when biofilm growth is conducted on LB agar but also the wetting behavior of the biofilm colonies differs: now, hydrophilic surfaces are obtained (see SI Section S8.2) and not roselike superhydrophobic surfaces anymore. In contrast, biofilm colonies grown from *B. subtilis natto* and B-1 bacteria exhibit the same wettability on LB agar as they do on MSgg agar, *i.e.*, they show hydrophilic and lotuslike behavior, respectively. Consequently, this new set of samples does not contain any biofilms with roselike surface properties.

When the four algorithms trained with data obtained for biofilm colonies grown on MSgg agar are used to classify the biofilms grown on LB agar (Figure 4c), we observe two items. First, three out of four algorithms correctly and accurately classify *natto* and B-1 biofilms; only the logistic regression approach misinterprets the majority of images acquired from *natto* biofilms and assigns them to 3610 biofilms. This shows that those three classifiers are generalized enough to classify samples even if they differ from the training set in terms of macromorphological and microtopographical appearance. The

https://doi.org/10.1021/acsbiomaterials.1c00869
ACS Biomater. Sci. Eng. 2021, 7, 4614–4625

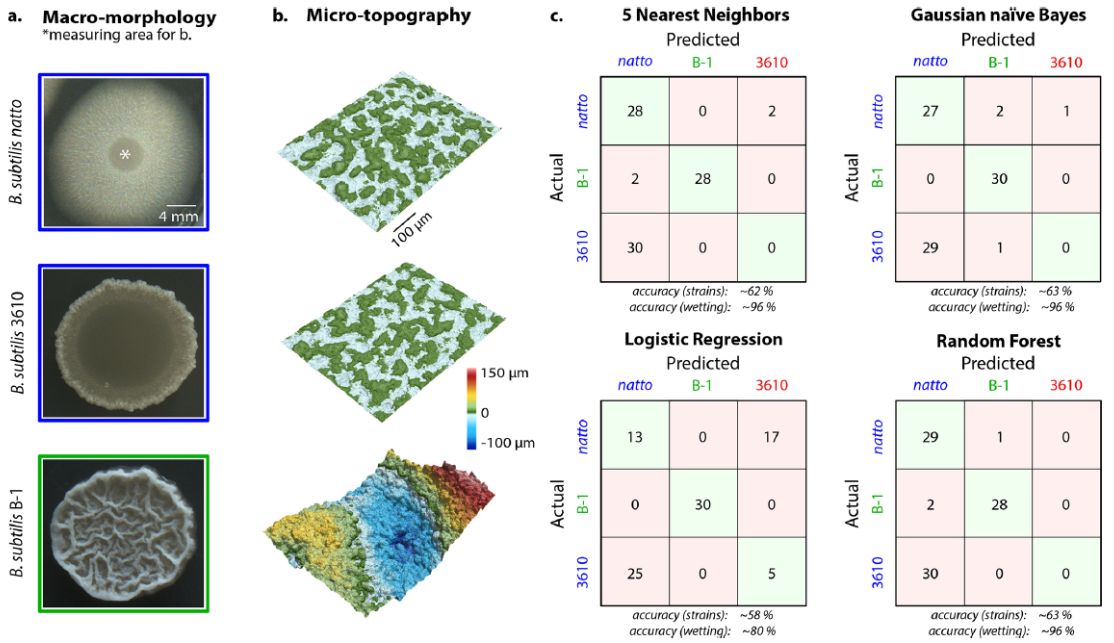

Figure 4. Surface structure and classification of biofilms grown on LB medium. Macroscopic colony images (a) and microscopic profilometric records (b) of biofilms generated by *B. subtilis natto*, *B. subtilis* NCIB 3610, and *B. subtilis* B-1 bacteria cultivated on LB agar. The scale bars in (a,b) apply to all three images within the respective subfigure. The confusion matrices (c) show the categorization results of such samples as achieved by the four algorithms when fed the set of microtopographical parameters: the actual classes (i.e., the names of the bacterial strains the biofilms were grown from) are compared to the predicted classes when a five nearest neighbor classifier, a Gaussian naïve Bayes model, multinomial logistic regression, and a Random Forest classifier are used. All algorithms were trained with data obtained for biofilms grown on MSgg medium. The label colors indicate the wetting behavior of the respective sample: blue indicates hydrophilic behavior, red indicates roselike hydrophobicity, and green denotes lotuslike hydrophobicity.

second observation is that all four algorithms mainly assign data obtained from 3610 biofilms to *natto* biofilms. At first glance, this seems to be a mistake as indicated by the calculated low accuracies, which are only in the range of 60%. However, when we ignore the detailed microbial species from which the biofilms are grown and instead focus on the previously mentioned wetting properties of the biofilm colonies (which are dictated by their surface topographies), this classification turns out to be highly meaningful: 3610 biofilms grown on LB medium exhibit the same wetting characteristics as *natto* biofilms grown on MSgg agar and both have hydrophilic surfaces. Thus, when we use the three variants of surface wetting properties as a class label, the KNN classifier, the Gaussian naïve Bayes algorithm, and the Random Forest classifier correctly assign almost all data and reach accuracies close to those obtained for the biofilms grown on MSgg agar (approximately 96% each). With this realization in mind, we now use those wetting-based labels for all data discussed in the remainder of this article. Importantly, even with those new labels used the comparatively low accuracy of the logistic regression algorithm remains. Probably, this issue arises from an overfitting of the training data by the regression function, which is a common issue of this method when applied to data with high dimensionality. Hence, this particular classifier is not used further in this study.

So far, we have identified three algorithms that are capable of classifying biofilms according to their surface wettability by using a set of metrological parameters determined from the microtopography of the biofilms. In a next step, we test if the same approach can be applied to a different class of biomaterials. For this purpose, we select three different plant samples (Figure 5a), which cover the same range of wetting properties as the biofilm samples analyzed above: *Rhododendron* leaves, that exhibit hydrophilic surfaces; *Rosa* "harlekin" petals that behave as roselike superhydrophobic; and *Caladium praetermissum* leaves, which have superhydrophobic surfaces similar to lotus leaves (see SI Section S9.1 for contact angles and tilt experiments). From those samples, we again capture profilometric images (Figure 5b, for more example images, please refer to Supporting Information, Section S13.2) and calculate the same set of surface parameters as before to quantify the microtopography (Figure 5c,d).

One major difference between this new data set and the one obtained for biofilms is that now the distributions of calculated parameter values overlap more strongly; in other words, in terms of microtopography the plant surfaces are more similar to each other than the three biofilm variants we discussed above. When we train the algorithms with the plant data and evaluate the classification accuracy with repeated cross-validation (again repeatedly using 80% of the data for training and the remaining 20% for testing), we observe the following: the Random Forest classifier performs best with a success rate of 92%; the KNN classifier delivers acceptable results (87% accuracy), and the Gaussian naïve Bayes algorithm returns the lowest yet still moderate accuracy (78%, see SI Section S9.2). These findings indicate how the ability of the three classifiers

https://doi.org/10.1021/acsbiomaterials.1c00869
ACS Biomater. Sci. Eng. 2021, 7, 4614−4625

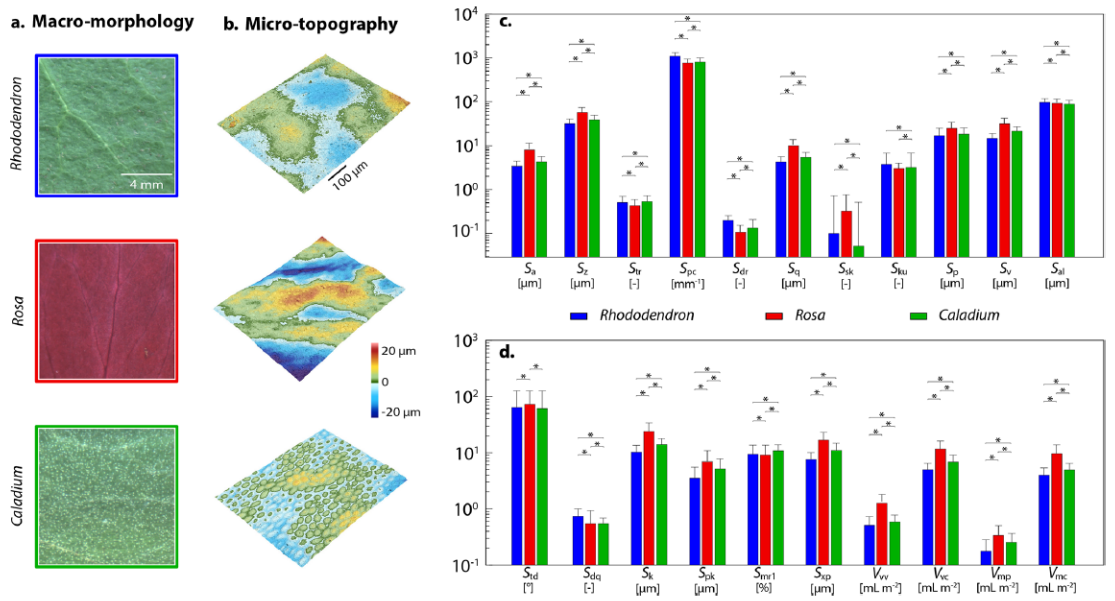

Figure 5. Surface topography of different plant samples. Macroscopic images (a), microscopic profilometric images (b), and metrological surface parameters (c,d) as determined from the latter are shown for *Rhododendron* leaves (n = 600), *Rosa* petals (n = 600), and *Caladium* leaves (n = 500). The scale bars in (a,b) apply to all three images within the respective subfigure. The error bars in (c,d) denote the standard deviation as obtained from $n \geq 500$ images each. Asterisks indicate statistical differences assessed with a Wilcoxon−Mann−Whitney test applying a p-value of 0.05.

to handle a data set with overlapping classes differs. When applying the KNN, for instance, samples located at the intersection of two or more classes are prone to be misclassified due to the presence of numerous "wrong neighbors". The Gaussian naïve Bayes classifier has even stronger problems in this particular case. Here, samples that exhibit feature values far away from the mean of their actual class are very likely to be classified wrongly: Owing to the overlapping probability distributions, those samples are more likely interpreted to belong to another (= "wrong") class. The Random Forest algorithm, in contrast, seems to handle such data sets quite well, and we attribute this outcome to the ability of this algorithm to narrowly subdivide the training samples when splitting the data set.

Ranking the Feature Importance Allows for Reducing the Dimensionality of the Data Sets. So far, training the algorithms with a subset of either biofilm or plant data allows for correctly sorting the rest of the data sets and using the wettability of the different samples as a classification criterion is a highly meaningful option. Naively, one might assume that training the algorithms with one set of data (e.g., using either biofilm or plant samples only) might also allow for classifying the other data set. However, in none of the two possible directions (biofilms → plants, plants → biofilms) is this possible as we obtain very low prediction accuracies that are only slightly higher than the probability of simple guessing (see SI Section S10). In retrospect, this outcome is not surprising considering the very different ranges of absolute values that we obtain for the metrological parameters calculated for biofilm and plant samples, respectively. In other words, during training the algorithms get adjusted to the feature scales of the respective material class (either biofilms or leaves) and thus are not generalized enough to be applied to other surfaces with features that cover a much broader (or much narrower) range of length-scales.

Thus, in the next step, we pool the data obtained from the two measurement series and attempt a training/classification approach with this mixed data set. When we now evaluate the classification result via cross-validation (80% training data and 20% test data), we find that the three algorithms handle the pooled data set differently but well (see SI Section S12). Once more, the Random Forest algorithm performs best; here, we obtain very high classification accuracies of 95%. The KNN classifier still reaches an acceptable accuracy of around 87% (which is similar to the result obtained with this classifier when using plant data only), but the Gaussian naïve Bayes classifier returns less accurate results than when applied to "biofilm-only" or "plant-only" data. This outcome is, however, not surprising considering that this algorithm assumes normally distributed parameter values, that is, a condition that is clearly violated when the two data sets are pooled.

In a last step, we ask which surface features of plant and biofilm samples are most suitable for a correct classification into objects with hydrophilic, roselike, and lotuslike properties. For this purpose, we focus on the Random Forest algorithm as this classifier for the data studied here has returned the best overall results. By tracing the subset of metrological parameters that this algorithm has used to make its predictions, we aim at identifying specific surface characteristics that influenced the decision-making progress of the classifier the most. This method, also known as feature elimination, is a common approach in machine learning and can help reduce the dimensionality of data sets. If this is possible, not only the runtime of the algorithms can be shortened but also the accuracy of the algorithms can be improved by eliminating redundant or less relevant parameters.

https://doi.org/10.1021/acsbiomaterials.1c00869
ACS Biomater. Sci. Eng. 2021, 7, 4614−4625

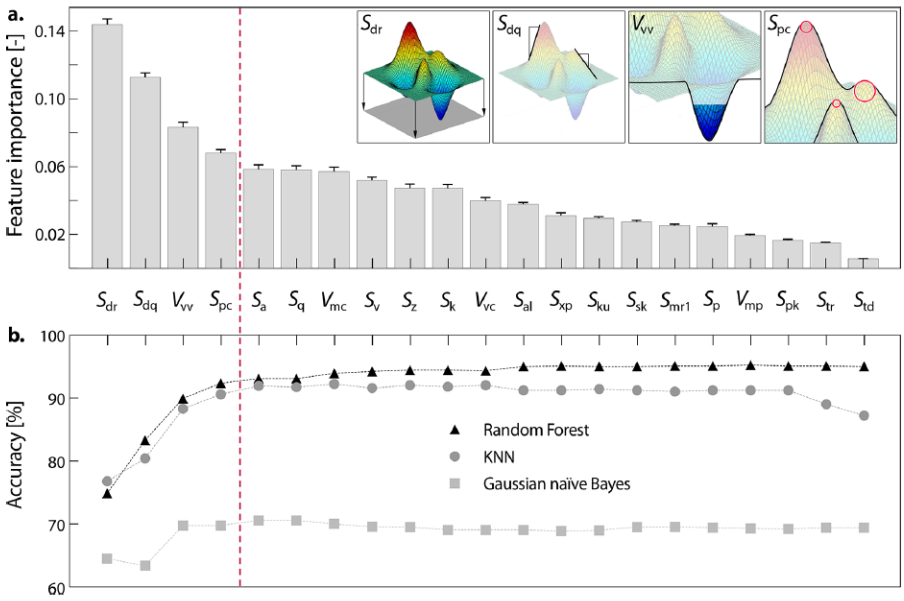

Figure 6. Reduction of data dimensionality based on feature elimination. Feature importance ranking as derived from the classification results obtained with the Random Forest classifier (a). The values shown denote the averaged Gini importance of each feature, that is, the total decrease of node impurity induced by a feature weighted by the number of samples the feature splits at the respective node. For each feature, the obtained values were averaged over n = 1000 trees. The error bars denote the standard error of the mean as obtained from n = 1000 tree estimators of one Random Forest model. On the basis of this importance ranking, features are stepwise eliminated starting with the least important feature until only the S_{dr} is left. The classification accuracies obtained during this feature elimination procedure are depicted in (b).

To do so, we calculate the Gini importance,[29] which describes the absolute decrease in node impurity induced by a feature weighted by the number of samples it splits. For each feature, these values are then averaged over all trees of the random forest (here: n = 1000) to obtain final importance scores. Then, we rank all parameters according to this score (see Figure 6a). Interestingly, some of the top ranked parameters from this sorted list have been used previously to distinguish various samples with regard to their surface properties. The developed interfacial ratio S_{dr}, peak curvature S_{pc}, and the root-mean-square gradient S_{dq}, for example, were shown to correlate well with the wettability of different synthetic surfaces.[30−32] Moreover, by making use of S_{dr} and the dale void volume V_{vv}, the wetting behavior of different biological surfaces could be discriminated,[33,34] and the peak curvature S_{pc} was discussed in context with the rose petal effect.[35] From a physical point of view, it is highly meaningful that the algorithm has identified this particular parameter subset to be relevant: The dale void volume together with the peak curvature, mean gradients, and the developed surface characterizes the size and shape of cavities in the surface structure of a given material; such surface cavities, in turn, were identified to crucially affect the wetting behavior of a material.[36] As the S_{dr} describes the increase of a surface area due to its texture, it quantifies the total area available for a surface−liquid interaction. The S_{pc}, in turn, hints toward the actual shape of some of those texture elements. A large surface area combined with smooth peak curvatures is typical for surfaces covered with "mushroomlike: structures, and such a particular surface topography can be described best by the Cassie−Baxter model, which is associated with lotuslike wettability.[37] These findings indicate that the physical models that were established for regularly shaped, synthetic surfaces can also be applied to the irregularly structured surfaces of the biomaterials studied here.

If some of those metrological parameters are more important than others, is it really necessary to provide the algorithms with 21 different numbers characterizing each topographical image? We test this question by repeating the classification procedure with the pooled data set but feeding the algorithms increasingly smaller parameter subsets. In detail, the Random Forest, the KNN, and the Gaussian naïve Bayes classifier are challenged to sort images again and again; yet, in each sorting step the least important feature left from the sorted list shown in Figure 6a is eliminated until only S_{dr} values are left (Figure 6b). Importantly, once fewer than the four top-scored parameters (i.e., S_{dr}, S_{dq}, V_{vv}, and S_{pc}) are considered, the accuracies achieved by the three algorithms are reduced (for specificity and sensitivity of the classification with the Random Forest classifier see Supporting Information, Section S14). In other words, the four parameters discussed above seem to be both necessary and sufficient to allow for a successful categorization of the different surfaces via machine-learning.

In summary, so far we showed that different model-based machine learning algorithms are capable of classifying the surfaces of two very different types of biological materials based on their microtopographical properties. This was even possible with relatively small, lab-scale training sets and as few as four different topographical parameters. Among the four algorithms compared in this study, the Random Forest classifier turned out to be the most robust one; this particular algorithm could reliably handle both broad and narrow data

https://doi.org/10.1021/acsbiomaterials.1c00869
ACS Biomater. Sci. Eng. 2021, 7, 4614−4625

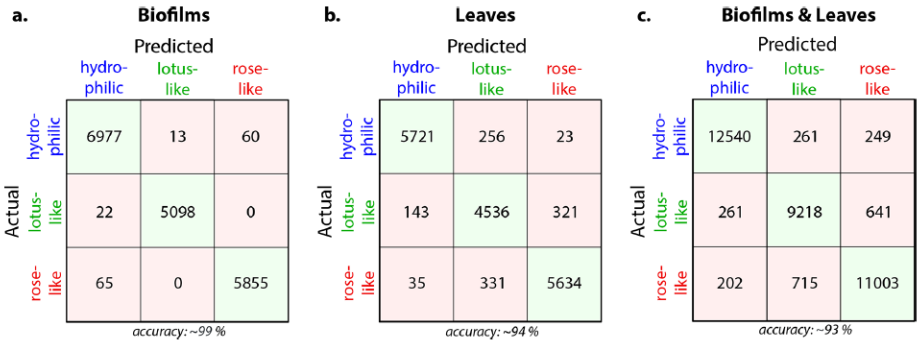

Figure 7. Categorization results obtained with a deep neural network. The confusion matrices compare the actual wetting behavior of data sets obtained from different biofilms (a), leaves (b), or pooled biofilm/leave samples (c) with the wetting behavior predicted by a DNN that was trained with 80% of the respective data set. The evaluation was performed by repeated (10 times) 5-fold cross validation, where the data set was shuffled before each iteration, that is, each sample served 10 times as a test sample but each time was analyzed by a differently trained algorithm. The main diagonal (green boxes) contains the numbers of correctly classified samples whereas all other boxes represent wrongly assigned samples. The accuracy values below the confusion matrices denote the total proportion of correctly classified samples.

sets of different sizes, densities, and distributions. The Gaussian naïve Bayes algorithm was efficient for normally distributed data sets but struggled when fed with more diverse data distributions. The multinomial logistic regression seemed to be prone to overfitting, which limited its suitability. Finally, the KNN classifier delivered satisfactory accuracies in most trials and was especially suitable when low-dimensional input data was used.

Finally, to complement the model-based algorithms applied so far, we ask if deep learning methods could possibly outperform the prediction accuracy of the machine learning approaches discussed above. Therefore, we establish a deep neural network (see Materials and Methods for details) which we train and test (via 10 times repeated stratified 5-fold cross-validation) with our three data sets, that is, those obtained with biofilms or plant samples and a pooled data set combining the two. Indeed, when classifying biofilms (after training the DNN with a subset of the biofilm data, Figure 7a) we obtain an exceptionally high accuracy of 99%. When analyzing the plant samples with the DNN (after training the DNN with plant data only, Figure 7b), we receive a very good classification accuracy of 94%. These results indicate that the DNN slightly outperforms the Random Forest classifier (which, among the model-based classifiers tested here, performed best). It is worth noting, that (similar to the model-based algorithms) the DNN cannot predict the wettability of plant samples when trained with biofilm data and vice versa (see Supporting Information section S13). For the pooled data set, however, an accuracy of 93% is reached (Figure 7c). This is satisfactory, yet slightly below the accuracy reached by the Random Forest classifier.

Just like all of the other algorithms applied in this study, the neural network is trained on classical metrological parameters calculated from the topographical images. Although those parameters have previously been shown to be good descriptors of the overall surface appearance of biofilms and other biological surfaces,[22,38] other surface properties that are not covered by those parameters will be overlooked by the algorithms. Novel deep learning approaches, such as convolutional neural networks or self-attention models, that can be used to directly analyze full topographical images, might be able to unveil such otherwise hidden features and could provide an even more detailed understanding of how the surface topography of a sample dictates its wetting behavior. Furthermore, the degree of generalization of the implemented algorithms could be tested by challenging them with a completely new class of biological materials. In this context, normalization approaches could be applied to allow for extrapolating beyond the computed data and to improve the classification accuracy of additional images acquired from "new" materials the algorithm has not yet been confronted with.

CONCLUSION

The characterization of complex surfaces is an ongoing challenge in many areas of materials science. We here used a machine learning approach to sort biological surfaces based on their microtopographical appearance and achieved a meaningful classification with regard to the wetting properties of the objects. Future investigations making use of similar algorithms are likely to unveil novel, to date undiscovered relations between the microtopographical features of a material and certain surface characteristics; we speculate that the friction response of a material as well as the biofouling properties of a surface could be interesting aspects to analyze. To achieve this, it might be necessary to obtain multifaceted data sets by including topographical data obtained with higher spatial resolution, measurement results from other experimental techniques or new classes of materials. When trying to predict the wettability of a sample based on its surface properties, it could be interesting to include additional parameters, such as physicochemical ones, into the data set to explore the interplay between surface topography and chemical composition. Also, analyzing such data with more advanced deep learning approaches, such as Bayesian Neural Networks or Convolutional Neural Networks, that directly evaluate full topographical images instead of a set of surface parameters calculated from them could be a very interesting next step. Overall, an automated structural analysis of complex surfaces as we introduce it here might also be useful in other areas of material science, for example, for damage assessment or predicting the interaction of a surface with other materials, such as flow resistance or adhesive properties.

https://doi.org/10.1021/acsbiomaterials.1c00869
ACS Biomater. Sci. Eng. 2021, 7, 4614−4625

MATERIALS AND METHODS

Chemicals. Unless stated otherwise, all chemicals were purchased from Carl Roth GmbH & Co. KG (Karlsruhe, Germany).

Biofilm Formation. *B. subtilis* NCIB 3610 (also referred to as "3610") and B-1 strains were kindly provided by Roberto Kolter and Masaaki Morikawa, respectively; the *B. subtilis natto* (27E3) strain was obtained from the Bacillus Genetic Stock Center (BGSC). To prepare planktonic cultures of each strain, a small piece from a frozen bacterial glycerol stock was inoculated in 10 mL of 2.5% (w/v) LB (Luria/Miller) medium at 37 °C overnight while shaking at a speed of 200 rpm (Certomat BS-1, Sartorius AG, Göttingen, Germany). To obtain biofilm colonies from these three strains, seven separate 5 μL droplets of a 16 h old bacterial overnight culture were placed onto 1.5% (w/v) agar plates enriched with either 2.5% (w/v) LB or MSgg[39] (minimal salt glycerol glutamate) medium (for details, please refer to the Supporting Information S1). All biofilm variants were grown for 24 h at 37 °C and ∼23% humidity. The three *Bacillus subtilis* strains (*natto*, 3610, and B-1) used here to cultivate biofilms are closely related; nevertheless, the generated biofilms differ in terms of their physical behavior.[40]

Preparation of Plant Leaves. Plant leaves of *Caladium praetermissum* (IPEN: XX-0-M-V/0926) were kindly provided by the Botanical Garden Munich-Nymphenburg (Staatliche Naturwissenschaftliche Sammlungen Bayerns, Munich, Germany). *Rosa* "harlekin" plants were purchased from Edeka (Edeka Ernst, Garching-Hochbrück, Germany). *Rhododendron* leaves were obtained from a local garden. From each plant leave/rose petal, pieces of approximately 3 cm × 2 cm size were freshly cut before conducting a measurement. To obtain a planar surface suitable for experiments, those pieces were attached to a glass slide on all four sides using fixation tape. Special care was taken to not damage those parts of the leaf/petal surfaces which were later analyzed.

Light Profilometry. To determine the topography of the different samples, profilometric images were captured using a laser scanning microscope (VK-X1000, Keyence, Neu-Isenburg, Germany) equipped with a 20× lens (CF Plan, NA = 0.46; Nikon, Chiyoda, Tokio, Japan). According to the manufacturer, this microscope achieves resolutions of 0.5 and 120 nm in the z-direction and in x-/y-direction, respectively. For single biofilm colonies, a 4 × 4 array of images was acquired from the central region of the biofilm. For plant samples, a 10 × 10 array of images was captured from the "upper" side of the leaves (for *Caladium* and *Rhododendron*) or the "outer" side of the petal (for *Rosa*). Each of those images was analyzed individually using the MultiFileAnalyzer software (v2.1.3.89, Keyence). After applying a tilt correction, 23 different metrological parameters (including height, spatial, hybrid, functional, and functional volume parameters) were calculated as described in the Supporting Information section S2 (all but one were determined according to ISO 25178-2). From those 23 parameters, a subset of 21 turned out to be robust enough so that they could be accurately calculated from the obtained images.

Machine Learning Algorithms. If not stated otherwise, all machine learning algorithms were implemented using python (Python Software Foundation; Python Language Reference, version 3.8.3; http://www.python.org)[41] with several extensions for data handling and visualization (Numpy[42] v1.19.4, Pandas[43,44] v1.2.2, Matplotlib[45] v3.2.2, Scipy[46] v1.6.0, and Seaborn[47] v0.11.1) as well as the machine learning toolbox scikit-learn[48] (v0.24.1). A schematic overview of how the four model-based algorithms used here to make decisions is depicted in Figure 2 and Figure S3.

k Nearest Neighbor Classifier (KNN). As an example of a nongeneralizing learning approach, a k nearest neighbor classifier was applied. Here, no internal model is developed; instead, the training data is memorized, and for each query point, its k nearest neighbors were determined using Manhattan distance (which was identified to be the most robust distance metric in a high dimensionality space as relevant here[49]). Each of those k nearest points was given a weight equal to the inverse of its distance to the point of interest. Considering those weights, the class of the query point was then determined in a popular votelike manner based on the neighbors' classes. For this algorithm, the optimal choice of the number of neighbors taken into account strongly depends on the data distribution. Overall, low k values render the classification more distinct, whereas higher k values lead to less noise. In this study, we selected k = 5 as it was shown to entail the highest accuracies on our initial data set (see SI Section S4). To find the nearest neighbors, a brute force search was chosen. This search algorithm is suitable for a data set with high dimensionality as used here and still justifiable in terms of runtime considering the overall size of the data set. Minmax feature scaling ($x_{\text{scaled}} = (x - \min_{\text{feature}})/(\max_{\text{feature}} - \min_{\text{feature}})$) was applied to each feature of both the training and test data; this helps to avoid parameters of larger magnitude that influence the prediction overly strongly.

Gaussian Naive Bayes Classifier. As one example of a probabilistic classifier, a Gaussian naïve Bayes algorithm was chosen. Such an algorithm can, although being comparably simple, outperform even highly sophisticated classification methods.[50] The GNB classifier applies Bayes' theorem with the naïve assumption of conditional independence between all features (x_1, ..., x_n) within a class y; mathematically, the resulting classifier can be formulated as (see also Supporting Information S4)[51,52]

$$\hat{y} = \arg\max_{y} P(y) \prod_{i=1}^{n} P(x_i|y) \tag{1}$$

With this approach, the posterior probability $P(y|x_i)$ is determined using a prior assumption on the output distribution $P(y)$ and a likelihood on the data given the labels $P(x_i|y)$. It is assumed that the distributions of the features is Gaussian (eq 2) where σ_y and μ_y are assessed with maximum likelihood[53] (eq 2). The predicted class of y is the one which maximizes the posterior probability

$$P(x_i|y) = \frac{1}{\sqrt{2\pi\sigma_y^2}} \exp\left(-\frac{(x_i - \mu_y)^2}{2\sigma_y^2}\right) \tag{2}$$

Multinomial Logistic Regression. As one example of a linear machine learning approach, multinomial logistic regression was applied using an "lbfgs" solver[54,55] and L2 regularization. Briefly, given the training data X, the probability $P(y_i = k|X)$ that the output of the ith query point would be class k (out of K total possible classes) was calculated using the following softmax function[56,57]

$$P(y_i = k|X) = \frac{e^{\beta_k x_i}}{\sum_{j=1}^{K} e^{\beta_j x_i}}$$

Therein, β_k denotes the coefficient weight vector obtained from the model fit and $\boldsymbol{x}_i$ is the feature vector of the query point i. To compensate for a (putative) imbalance present in the data set, class weights were applied that are inversely proportional to the class frequencies in the input data. Furthermore, standard scaling ($x_{\text{scaled}} = (x - \text{mean}_{\text{feature}})/\text{standard deviation}_{\text{feature}}$) was applied to prepare the data and to reduce the iteration depth.

Random Forest Classifier. The Random Forest classifier is derived from the family of ensemble classifiers, which combine the predictions of multiple independent base estimators.[58] For random forest methods, those base estimators are decision trees which are randomly created from bootstrap samples. To further ensure that the individual trees are not correlated, each tree can, at every node, only choose from a random set of features to split the data into subsets, which are then further evaluated by the tree until a final decision is reached. The ensemble decision is then made based on a popular votelike principle by averaging the probabilistic prediction of each tree with equal contributions.

Deep Neural Network. A deep neural network (DNN) consists of multiple layers, each of which can comprise a different number of neurons, which are units performing a linear sum of inputs. Such neurons can be activated with a typically nonlinear activation function and then transform the input variables by applying trainable weights and a bias. All neurons of the same layer receive the same input, yet they perform a different transformation. Each layer uses the previous

https://doi.org/10.1021/acsbiomaterials.1c00869
ACS Biomater. Sci. Eng. 2021, 7, 4614−4625

layer's output as input. For training, the model is first initialized with weights, and the input of the training data is processed. The output of the model is then compared to the true values of each data point and an error is calculated. By applying backpropagation, this error is then used to evaluate the effect of each weight to the final prediction error in the form of a gradient. Through this gradient, a correction for each weight is performed, and the inputs are processed through the model to generate a new prediction. This process is recursively repeated until the error has converged to an acceptable minimum.

The desired prediction shape was transformed into a one-hot encoded vector,[59] which is common practice in multiclass classification problems. The hyperparameters of the DNN used in this study were optimized by a grid search-based approach, and the following ones were found to perform optimally: The network contains 3 hidden layers comprising 20, 12, and 8 neurons each with each layer being activated by a ReLu,[60] ReLu, and tanh[61] activation function, respectively. The output layer was activated with the softmax function, and the loss function was chosen to be the categorical cross entropy.[62] For implementation, the TensorFlow library[63] (v2.5.0) was used.

Repeated Stratified k-Fold Cross-Validation. To estimate the performance of the implemented machine learning algorithms on a given set of data, repeated stratified k-fold cross-validation[64−66] was conducted. For this purpose, the data was split into k-folds (if not stated otherwise, $k = 5$), each of which was used as a test set once; for each selection of a test set, the rest of the data was collectively used to train the algorithm. To avoid noisy estimates arising from this data separation, the repeated version ($n_{repeats} = 10$) of the common cross-validation was chosen. Here, in each repetition, a different randomization was applied to the data set. Moreover, the stratification (see Supporting Information S6) ensures an approximately equal sample distribution within each target class compared to the whole training data set, that is, that each fold is a good representative of the whole. This approach helps compensate for the imbalance of the training data (i.e., the somewhat unequal numbers of training data obtained per biofilm strain).[67]

Statistical Analysis. To assess whether or not a sample group follows a normal distribution, a Shapiro Wilk test was performed by applying a p-value of 0.05. To probe significant differences of the non-normally distributed data, a Wilcoxon−Mann−Whitney-Test was performed.

■ ASSOCIATED CONTENT

Supporting Information

The Supporting Information is available free of charge at https://pubs.acs.org/doi/10.1021/acsbiomaterials.1c00869.

> The compositions of used media for bacterial growth; detailed descriptions of the metrological parameters calculated from the micro-topography; additional descriptions and examples of the model-based classifiers and their evaluation; confusion matrices, values for sensitivity and specificity, contact angles, and surface parameters that were not shown in the main paper; example profilometry images of the analyzed samples (PDF)

■ AUTHOR INFORMATION

Corresponding Author

Oliver Lieleg − *Department of Mechanical Engineering and Munich School of Bioengineering, Technical University of Munich, 85748 Garching b. München, Germany; Center for Functional Protein Assemblies (CPA), Technical University of Munich, 85748 Garching b. München, Germany;* orcid.org/0000-0002-6874-7456; Email: oliver.lieleg@tum.de

Authors

Carolin A. Rickert − *Department of Mechanical Engineering and Munich School of Bioengineering, Technical University of Munich, 85748 Garching b. München, Germany; Center for Functional Protein Assemblies (CPA), Technical University of Munich, 85748 Garching b. München, Germany;* orcid.org/0000-0001-5532-3980

Elif N. Hayta − *Department of Mechanical Engineering and Munich School of Bioengineering, Technical University of Munich, 85748 Garching b. München, Germany; Center for Functional Protein Assemblies (CPA), Technical University of Munich, 85748 Garching b. München, Germany*

Daniel M. Selle − *Department of Mechanical Engineering and Munich School of Bioengineering, Technical University of Munich, 85748 Garching b. München, Germany; Center for Functional Protein Assemblies (CPA), Technical University of Munich, 85748 Garching b. München, Germany*

Ioannis Kouroudis − *Department of Electrical and Computer Engineering, Technical University of Munich, 80333 München, Germany;* orcid.org/0000-0001-9759-6696

Milan Harth − *Department of Electrical and Computer Engineering, Technical University of Munich, 80333 München, Germany*

Alessio Gagliardi − *Department of Electrical and Computer Engineering, Technical University of Munich, 80333 München, Germany;* orcid.org/0000-0002-3322-2190

Complete contact information is available at: https://pubs.acs.org/10.1021/acsbiomaterials.1c00869

Author Contributions

The study was designed by C.A.R., E.N.H., and O.L.. Experiments were conducted by E.N.H. and D.M.S., and data were analyzed by D.M.S. and C.A.R. Machine learning analysis was conducted by C.A.R., I.K., M.H., and A.G.. The manuscript was written by C.A.R. and O.L. and critically revised by all authors.

Notes

The authors declare no competing financial interest.

■ ACKNOWLEDGMENTS

This project was conducted in the framework of TUM's innovation network "ARTEMIS". E.N.H. thankfully acknowledges a fellowship granted by the Turkish Ministry of Education. The authors acknowledge funding by the Deutsche Forschungsgemeinschaft (DFG, German Research Foundation)—SFB 863, Projekt B11—111166240.

■ REFERENCES

(1) Anguita, J. V.; Ahmad, M.; Haq, S.; Allam, J.; Silva, S. R. P. Ultra-broadband light trapping using nanotextured decoupled graphene multilayers. *Science Advances* **2016**, *2* (2), e1501238.

(2) Spinner, M.; Kovalev, A.; Gorb, S. N.; Westhoff, G. Snake velvet black: hierarchical micro-and nanostructure enhances dark colouration in Bitis rhinoceros. *Sci. Rep.* **2013**, *3* (1), 1−8.

(3) Davis, A. L.; Nijhout, H. F.; Johnsen, S. Diverse nanostructures underlie thin ultra-black scales in butterflies. *Nat. Commun.* **2020**, *11* (1), 1−7.

(4) Wong, T.-S.; Kang, S. H.; Tang, S. K.; Smythe, E. J.; Hatton, B. D.; Grinthal, A.; Aizenberg, J. Bioinspired self-repairing slippery surfaces with pressure-stable omniphobicity. *Nature* **2011**, *477* (7365), 443−447.

(5) Leslie, D. C.; Waterhouse, A.; Berthet, J. B.; Valentin, T. M.; Watters, A. L.; Jain, A.; Kim, P.; Hatton, B. D.; Nedder, A.; Donovan, K.; Super, E. H.; Howell, C.; Johnson, C. P.; Vu, T. L.; Bolgen, D. E.;

Rifai, S.; Hansen, A. R.; Aizenberg, M.; Super, M.; Aizenberg, J.; Ingber, D. E. A bioinspired omniphobic surface coating on medical devices prevents thrombosis and biofouling. *Nat. Biotechnol.* **2014**, *32* (11), 1134−1140.
(6) Vogel, N.; Belisle, R. A.; Hatton, B.; Wong, T.-S.; Aizenberg, J. Transparency and damage tolerance of patternable omniphobic lubricated surfaces based on inverse colloidal monolayers. *Nat. Commun.* **2013**, *4* (1), 2176.
(7) Kwaria, R. J.; Mondarte, E. A. Q.; Tahara, H.; Chang, R.; Hayashi, T. Data-driven prediction of protein adsorption on self-assembled monolayers toward material screening and design. *ACS Biomater. Sci. Eng.* **2020**, *6* (9), 4949−4956.
(8) Zhang, L.; Zhou, A. G.; Sun, B. R.; Chen, K. S.; Yu, H.-Z. Functional and versatile superhydrophobic coatings via stoichiometric silanization. *Nat. Commun.* **2021**, *12* (1), 1−7.
(9) Amini, S.; Kolle, S.; Petrone, L.; Ahanotu, O.; Sunny, S.; Sutanto, C. N.; Hoon, S.; Cohen, L.; Weaver, J. C.; Aizenberg, J.; Vogel, N.; Miserez, A. Preventing mussel adhesion using lubricant-infused materials. *Science* **2017**, *357* (6352), 668−673.
(10) Qiang, W. P.; He, X. D.; Zhang, K.; Cheng, Y. F.; Lu, Z. S.; Li, C. M.; Kang, E. T.; Xia, Q. Y.; Xu, L. Q. Mussel Adhesive Mimetic Silk Sericin Prepared by Enzymatic Oxidation for the Construction of Antibacterial Coatings. *ACS Biomater. Sci. Eng.* **2021**, *7*, 3379.
(11) Cannara, R. J.; Brukman, M. J.; Cimatu, K.; Sumant, A. V.; Baldelli, S.; Carpick, R. W. Nanoscale friction varied by isotopic shifting of surface vibrational frequencies. *Science* **2007**, *318* (5851), 780−783.
(12) Shen, M.; Zhu, S.; Wang, F. A general strategy for the ultrafast surface modification of metals. *Nat. Commun.* **2016**, *7* (1), 1−6.
(13) Baytekin, H.; Patashinski, A.; Branicki, M.; Baytekin, B.; Soh, S.; Grzybowski, B. A. The mosaic of surface charge in contact electrification. *Science* **2011**, *333* (6040), 308−312.
(14) Reidy, K.; Varnavides, G.; Thomsen, J. D.; Kumar, A.; Pham, T.; Blackburn, A. M.; Anikeeva, P.; Narang, P.; LeBeau, J. M.; Ross, F. M. Direct imaging and electronic structure modulation of moiré superlattices at the 2D/3D interface. *Nat. Commun.* **2021**, *12* (1), 1−9.
(15) Clauser, J. C.; Maas, J.; Arens, J.; Schmitz-Rode, T.; Steinseifer, U.; Berkels, B. Hemocompatibility Evaluation of Biomaterials—The Crucial Impact of Analyzed Area. *ACS Biomater. Sci. Eng.* **2021**, *7* (2), 553−561.
(16) Yu, C.; Wang, Q. J. Friction anisotropy with respect to topographic orientation. *Sci. Rep.* **2012**, *2* (1), 1−6.
(17) Yu, C.; Yu, H.; Liu, G.; Chen, W.; He, B.; Wang, Q. J. Understanding topographic dependence of friction with micro-and nano-grooved surfaces. *Tribol. Lett.* **2014**, *53* (1), 145−156.
(18) Zhang, P.; Wang, S.; Wang, S.; Jiang, L. Superwetting surfaces under different media: effects of surface topography on wettability. *Small* **2015**, *11* (16), 1939−1946.
(19) Roach, P.; Farrar, D.; Perry, C. C. Surface tailoring for controlled protein adsorption: effect of topography at the nanometer scale and chemistry. *J. Am. Chem. Soc.* **2006**, *128* (12), 3939−3945.
(20) Kobayashi, K.; Iwano, M. BslA (YuaB) forms a hydrophobic layer on the surface of Bacillus subtilis biofilms. *Mol. Microbiol.* **2012**, *85* (1), 51−66.
(21) Arnaouteli, S.; MacPhee, C. E.; Stanley-Wall, N. R. Just in case it rains: building a hydrophobic biofilm the Bacillus subtilis way. *Curr. Opin. Microbiol.* **2016**, *34*, 7−12.
(22) Werb, M.; García, C. F.; Bach, N. C.; Grumbein, S.; Sieber, S. A.; Opitz, M.; Lieleg, O. Surface topology affects wetting behavior of Bacillus subtilis biofilms. *npj Biofilms and Microbiomes* **2017**, *3* (1), 1−10.
(23) Gerdes, H.; Casado, P.; Dokal, A.; Hijazi, M.; Akhtar, N.; Osuntola, R.; Rajeeve, V.; Fitzgibbon, J.; Travers, J.; Britton, D.; Khorsandi, S.; Cutillas, P. R. Drug ranking using machine learning systematically predicts the efficacy of anti-cancer drugs. *Nat. Commun.* **2021**, *12* (1), 1−15.
(24) Bone, J. M.; Childs, C. M.; Menon, A.; Poczos, B.; Feinberg, A. W.; LeDuc, P. R.; Washburn, N. R. Hierarchical Machine Learning for High-Fidelity 3D Printed Biopolymers. *ACS Biomater. Sci. Eng.* **2020**, *6* (12), 7021−7031.
(25) Mansouri Tehrani, A.; Oliynyk, A. O.; Parry, M.; Rizvi, Z.; Couper, S.; Lin, F.; Miyagi, L.; Sparks, T. D.; Brgoch, J. Machine learning directed search for ultraincompressible, superhard materials. *J. Am. Chem. Soc.* **2018**, *140* (31), 9844−9853.
(26) Kesel, S.; von Bronk, B.; García, C. F.; Götz, A.; Lieleg, O.; Opitz, M. Matrix composition determines the dimensions of Bacillus subtilis NCIB 3610 biofilm colonies grown on LB agar. *RSC Adv.* **2017**, *7* (51), 31886−31898.
(27) Shim, M. H.; Kim, J.; Park, C. H. The effects of surface energy and roughness on the hydrophobicity of woven fabrics. *Text. Res. J.* **2014**, *84* (12), 1268−1278.
(28) Erbil, H. Y.; Demirel, A. L.; Avcı, Y.; Mert, O. Transformation of a simple plastic into a superhydrophobic surface. *Science* **2003**, *299* (5611), 1377−1380.
(29) Menze, B. H.; Kelm, B. M.; Masuch, R.; Himmelreich, U.; Bachert, P.; Petrich, W.; Hamprecht, F. A. A comparison of random forest and its Gini importance with standard chemometric methods for the feature selection and classification of spectral data. *BMC Bioinf.* **2009**, *10* (1), 213.
(30) Noro, A.; Kaneko, M.; Murata, I.; Yoshinari, M. Influence of surface topography and surface physicochemistry on wettability of zirconia (tetragonal zirconia polycrystal). *J. Biomed. Mater. Res., Part B* **2013**, *101B* (2), 355−363.
(31) Hosseinabadi, H. N.; Sajjady, S.; Amini, S. Creating micro textured surfaces for the improvement of surface wettability through ultrasonic vibration assisted turning. *International Journal of Advanced Manufacturing Technology* **2018**, *96* (5), 2825−2839.
(32) Melentiev, R.; Fang, F.; Narala, S. K. R. Influence of different pretreatments on Ti-6Al-4V surface integrity and scratch-resistance of epoxy coating: Analysis of topography, microstructure, chemistry and wettability. *Surf. Coat. Technol.* **2020**, *404*, 126436.
(33) García, C. F.; Stangl, F.; Götz, A.; Zhao, W.; Sieber, S. A.; Opitz, M.; Lieleg, O. Topographical alterations render bacterial biofilms susceptible to chemical and mechanical stress. *Biomater. Sci.* **2019**, *7* (1), 220−232.
(34) Hayta, E. N.; Lieleg, O. Biopolymer-enriched B. subtilis NCIB 3610 biofilms exhibit increased erosion resistance. *Biomater. Sci.* **2019**, *7* (11), 4675−4686.
(35) Bhushan, B.; Nosonovsky, M. The rose petal effect and the modes of superhydrophobicity. *Philos. Trans. R. Soc., A* **2010**, *368* (1929), 4713−4728.
(36) Sheng, Y.-J.; Jiang, S.; Tsao, H.-K. Effects of geometrical characteristics of surface roughness on droplet wetting. *J. Chem. Phys.* **2007**, *127* (23), 234704.
(37) Kang, S. M. Role of wide tip of mushroom-like micropillar arrays to make the Cassie state on superrepellent surfaces. *RSC Adv.* **2016**, *6* (78), 74670−74674.
(38) Deltombe, R.; Kubiak, K.; Bigerelle, M. How to select the most relevant 3D roughness parameters of a surface. *Scanning* **2014**, *36* (1), 150−160.
(39) Branda, S. S.; Chu, F.; Kearns, D. B.; Losick, R.; Kolter, R. A major protein component of the Bacillus subtilis biofilm matrix. *Mol. Microbiol.* **2006**, *59* (4), 1229−1238.
(40) Kesel, S.; Grumbein, S.; Gümperlein, I.; Tallawi, M.; Marel, A.-K.; Lieleg, O.; Opitz, M. Direct comparison of physical properties of Bacillus subtilis NCIB 3610 and B-1 biofilms. *Appl. Environ. Microbiol.* **2016**, *82* (8), 2424−2432.
(41) Van Rossum, G.; Drake, F. L. *Python 3 Reference Manual*; CreateSpace: Scotts Valley, CA, 2009.
(42) Harris, C. R.; Millman, K. J.; van der Walt, S. J.; Gommers, R.; Virtanen, P.; Cournapeau, D.; Wieser, E.; Taylor, J.; Berg, S.; Smith, N. J.; Kern, R.; Picus, M.; Hoyer, S.; van Kerkwijk, M. H.; Brett, M.; Haldane, A.; del Rio, J. F.; Wiebe, M.; Peterson, P.; Gerard-Marchant, P.; Sheppard, K.; Reddy, T.; Weckesser, W.; Abbasi, H.; Gohlke, C.; Oliphant, T. E. Array programming with NumPy. *Nature* **2020**, *585* (7825), 357−362.

https://doi.org/10.1021/acsbiomaterials.1c00869
ACS Biomater. Sci. Eng. 2021, 7, 4614−4625

(43) McKinney, W. In *Data structures for statistical computing in python*, Proceedings of the 9th Python in Science Conference, Austin, TX, 2010; pp 51−56.
(44) Reback, J.; McKinney, W.; Brockmendel; Bossche, J. V. d.; Augspurger, T.; Cloud, P.; gfyoung; Hawkins, S.; Sinhrks; Roeschke, M.; Klein, A.; Petersen, T.; Tratner, J.; She, C.; Ayd, W.; Naveh, S.; Garcia, M.; Schendel, J.; patrick; Hayden, A.; Saxton, D.; Jancauskas, V.; McMaster, A.; Gorelli, M.; Battiston, P.; Seabold, S.; Dong, K.; chris-b1; h-vetinari; Hoyer, S. *pandas-dev/pandas: Pandas 1.2.2*, v1.2.2; Zenodo, 2021.
(45) Hunter, J. D. Matplotlib: A 2D graphics environment. *Comput. Sci. Eng.* **2007**, *9* (03), 90−95.
(46) Virtanen, P.; Gommers, R.; Oliphant, T. E.; Haberland, M.; Reddy, T.; Cournapeau, D.; Burovski, E.; Peterson, P.; Weckesser, W.; Bright, J.; van der Walt, S. J.; Brett, M.; Wilson, J.; Millman, K. J.; Mayorov, N.; Nelson, A. R. J.; Jones, E.; Kern, R.; Larson, E.; Carey, C J; Polat, I.; Feng, Y.; Moore, E. W.; VanderPlas, J.; Laxalde, D.; Perktold, J.; Cimrman, R.; Henriksen, I.; Quintero, E. A.; Harris, C. R.; Archibald, A. M.; Ribeiro, A. H.; Pedregosa, F.; van Mulbregt, P. SciPy 1.0: fundamental algorithms for scientific computing in Python. *Nat. Methods* **2020**, *17* (3), 261−272.
(47) Waskom, M.; Botvinnik, O.; Gelbart, M.; Ostblom, J.; Hobson, P.; Lukauskas, S.; Gemperline, D. C.; Augspurger, T.; Halchenko, Y.; Warmenhoven, J., Seaborn: statistical data visualization. *Astrophysics Source Code Library* **2020**, ascl: 2012.015.
(48) Pedregosa, F.; Varoquaux, G.; Gramfort, A.; Michel, V.; Thirion, B.; Grisel, O.; Blondel, M.; Prettenhofer, P.; Weiss, R.; Dubourg, V. Scikit-learn: Machine learning in Python. *The. Journal of Machine Learning Research* **2011**, *12*, 2825−2830.
(49) Aggarwal, C. C.; Hinneburg, A.; Keim, D. A. In *On the surprising behavior of distance metrics in high dimensional space*, International Conference on Database Theory; , 2001; pp 420−434.
(50) VanderPlas, J. *Python data science handbook: Essential tools for working with data*; O'Reilly Media, Inc., 2016.
(51) Murphy, K. P. *Naive bayes classifiers*; University of British Columbia, 2006; Vol. *18*, p 60.
(52) Zhang, H. Exploring conditions for the optimality of naive Bayes. *International Journal of Pattern Recognition and Artificial Intelligence* **2005**, *19* (02), 183−198.
(53) Lou, W.; Wang, X.; Chen, F.; Chen, Y.; Jiang, B.; Zhang, H. Sequence based prediction of DNA-binding proteins based on hybrid feature selection using random forest and Gaussian naive Bayes. *PLoS One* **2014**, *9* (1), e86703.
(54) Byrd, R. H.; Lu, P.; Nocedal, J.; Zhu, C. A limited memory algorithm for bound constrained optimization. *SIAM Journal on Scientific Computing* **1995**, *16* (5), 1190−1208.
(55) Zhu, C.; Byrd, R. H.; Lu, P.; Nocedal, J. Algorithm 778: L-BFGS-B: Fortran subroutines for large-scale bound-constrained optimization. *ACM Transactions on Mathematical Software (TOMS)* **1997**, *23* (4), 550−560.
(56) Yu, H.-F.; Huang, F.-L.; Lin, C.-J. Dual coordinate descent methods for logistic regression and maximum entropy models. *Machine Learning* **2011**, *85* (1−2), 41−75.
(57) Bisong, E. Logistic Regression. In *Building Machine Learning and Deep Learning Models on Google Cloud Platform: A Comprehensive Guide for Beginners*; Apress: Berkeley, CA, 2019; pp 243−250.
(58) Breiman, L. Random forests. *Machine Learning* **2001**, *45* (1), 5−32.
(59) Seger, C. *An investigation of categorical variable encoding techniques in machine learning: binary versus one-hot and feature hashing*. Technical Report 2018:596; KTH, School of Electrical Engineering and Computer Science (EECS): Stockholm, Sweden 2018.
(60) Agarap, A. F. Deep learning using rectified linear units (relu). *arXiv preprint arXiv:1803.08375*, 2018.
(61) Sharma, S.; Sharma, S. Activation functions in neural networks. *Towards Data Science* **2017**, *6* (12), 310−316.
(62) Dunne, R. A.; Campbell, N. A. In *On the pairing of the softmax activation and cross-entropy penalty functions and the derivation of the softmax activation function*; Proc. 8th Aust. Conf. on the Neural Networks; Citeseer: Melbourne, 1997; p 185.
(63) Abadi, M.; Agarwal, A.; Barham, P.; Brevdo, E.; Chen, Z.; Citro, C.; Corrado, G. S.; Davis, A.; Dean, J.; Devin, M., Tensorflow: Large-scale machine learning on heterogeneous distributed systems. arXiv preprint arXiv:1603.04467 2016.
(64) Vanwinckelen, G.; Blockeel, H. In *On estimating model accuracy with repeated cross-validation*; Proceedings of the 21st Belgian-Dutch conference on machine learning; BeneLearn, 2012; pp 39−44.
(65) Berrar, D. Cross-validation. *Encyclopedia of Bioinformatics and Computational Biology* **2019**, *1*, 542−545.
(66) Purushotham, S.; Tripathy, B. In *Evaluation of classifier models using stratified tenfold cross validation techniques*, International Conference on Computing and Communication Systems; Springer, 2011; pp 680−690.
(67) Zeng, X.; Martinez, T. R. Distribution-balanced stratified cross-validation for accuracy estimation. *Journal of Experimental & Theoretical Artificial Intelligence* **2000**, *12* (1), 1−12.

https://doi.org/10.1021/acsbiomaterials.1c00869
ACS Biomater. Sci. Eng. 2021, 7, 4614−4625

Supporting Information for

A Machine Learning Approach to Analyze the Surface Properties of Biological Materials

Carolin A. Rickert[1,2], Elif N. Hayta[1,2], Daniel M. Selle[1,2], Ioannis Kouroudis[3], Milan Harth[3], Alessio Gagliardi[3], and Oliver Lieleg[1,2,*]

[1] Department of Mechanical Engineering and Munich School of Bioengineering, Technical University of Munich, Boltzmannstr. 15, 85748, Garching b. München, Germany

[2] Center for Functional Protein Assemblies (CPA), Technical University of Munich, Ernst-Otto-Fischer Straße 8, 85748, Garching b. München, Germany

[3] Department of Electrical and Computer Engineering, Technical University of Munich, Karlstrasse 45, 80333, München, Germany

S1 Bacterial growth media

If not stated otherwise, all chemicals were obtained from Carl Roth GmbH & Co. KG (Karlsruhe, Germany).

MSgg (Minimal Salt Glycerol Glutamate) medium (according to Branda *et al.*[1]):
5 mM potassium phosphate (K_2HPO_4 [Carl Roth] and KH_2PO_4 [AppliChem, Darmstadt, Germany]),
100 mM 3-(N-Morpholino)propanesulfonic acid (MOPS),
2 mM $MgCl_2 \cdot 6H_2O$,
700 µM $CaCl_2$,
50 µM $MnCl_2 \cdot 4H_2O$,
50 µM $FeCl_3 \cdot 6H_2O$ (Sigma Aldrich, St. Louis, Missouri, USA),
1 µM $ZnCl_2$,
2 µM thiamine hydrochloride (AppliChem),
0.5% (v/v) glycerol,
0.5% (w/v) glutamate (Sigma Aldrich),
50 µg/mL L-tryptophan (AppliChem),
50 µg/mL L-phenylalanine (AppliChem), and
50 µg/mL threonine (AppliChem).

LB (Luria/Miller) medium (purchased):
5 g/L yeast extract
10 g/L tryptone
10 g/L sodium chloride (NaCl)

S2 Metrological Parameters

S2.1 Height parameters

Arithmetical mean height: S_a

S_a denotes the average of the absolute values of the height at each point of the analyzed area.

$$S_a = \frac{1}{A}\iint_A |z(x,y)|\, dxdy \tag{1}$$

Root mean square height: S_q

The root mean square height denotes the standard deviation of the height profile at each point within the analyzed area.

$$S_q = \sqrt{\frac{1}{A}\iint_A z^2(x,y)dxdy} \tag{2}$$

Skewness: S_{sk}

The skewness is the cubic (normalized) average of the height. It indicates an asymmetry of the height distribution with regard to the reference plane: $S_{sk} < 0$ and $S_{sk} > 0$ indicate the predominance of pits or peak structures, respectively.

$$S_{sk} = \frac{1}{S_q^3}\left[\frac{1}{A}\iint_A z^3(x,y)dxdy\right] \tag{3}$$

Kurtosis: S_{ku}

The kurtosis is a measure for the sharpness of the height distribution, which is calculated as the average fourth power of the height normalized by the fourth power of S_q. An S_{ku} of 3 denotes a height distribution similar to a normal distribution, whereas $S_{ku} < 3$ or $S_{ku} > 3$ indicate an arched or spiked shape, respectively.

$$S_{ku} = \frac{1}{S_q^4}\left[\frac{1}{A}\iint_A z^4(x,y)dxdy\right] \tag{4}$$

Maximal individual values: S_p, S_v and S_z

These maximal individual values denote the maximum peak height S_p (*i.e.*, the height of the highest point in the definition area), the maximum pit height S_v (*i.e.*, the absolute height value of the lowest point within the definition area), and the maximum height S_z defined as the sum of both.

$$S_p = \max_A z(x,y) \tag{5}$$

$$S_v = \left|\min_A z(x,y)\right| \tag{6}$$

$$S_z = S_p + S_v \tag{7}$$

S2.2 Spatial parameters

The two following two spatial parameters are calculated based on the autocorrelation function, which is defined as:

$$f_{ACF}(t_x, t_x) = \frac{\iint_A z(x,y)z(x-t_x, y-t_y)dxdy}{\iint_A z(x,y)^2 dxdy} \quad (8)$$

Autocorrelation length: S_{al}

The autocorrelation length displays the horizontal distance of the autocorrelation function with the fastest decay to a pre-defined value s (here 0.2). High S_{al} values indicate that long-wavelength components are dominant, whereas small values indicate the dominance of small-wavelength features.

$$S_{al} = \min_{t_x, t_y \in R} \sqrt{t_x^2 + t_y^2} \quad where \quad R = \{(t_x, t_y): f_{ACF}(t_x, t_y) \leq s\} \quad (9)$$

Texture aspect ratio: S_{tr}

The texture aspect ratio indicates the uniformity of the surface texture by dividing S_{al} by the horizontal distance with the slowest decay to the predefined value s. S_{tr} can range from 0 to 1: $S_{tr} >$ 0.5 indicates an isotropic surface, whereas $S_{tr} < 0.3$ means that the surface texture has a certain orientation.

$$S_{tr} = \frac{\min_{t_x, t_y \in R} \sqrt{t_x^2 + t_y^2}}{\max_{t_x, t_y \in Q} \sqrt{t_x^2 + t_y^2}} \quad where \quad \begin{matrix} R = \{(t_x, t_y): f_{ACF}(t_x, t_y) \leq s\} \\ Q = \{(t_x, t_y): f_{ACF}(t_x, t_y) \geq s\} \end{matrix} \quad (10)$$

Texture direction: S_{td}

S_{td} indicates the value of the angle s, where the angular spectrum f_{APS} is maximized, *i.e.*, it gives a direction of the crease of the surface texture. With this parameter, no meaningful values can be obtained on isotropic surfaces (surfaces with $S_{tr} > 0.5$). The angular spectrum is defined as

$$f_{APS}(s) = \int_{R_2}^{R_1} r|F[r\,sin(s-\theta), r\,cos(s-\theta)]|^2 dr \quad (11)$$

with

$$F(p,q) = \iint_A z(x,y)e^{-(ipx+ipy)}dxdy \quad (12)$$

S2.3 Hybrid parameters

Root mean square gradient: S_{dq}

The S_{dq} value is calculated as the root mean square of the gradient at all points of the analyzed area. It is especially suitable to distinguish surfaces that have the same arithmetical height S_a. There, the S_{dq} value will become small for surfaces that are dominated by long-wavelength components, whereas S_{dq} will increase for surfaces that are dominated by small-wavelength features.

$$S_{dq} = \sqrt{\frac{1}{A}\iint_A \left[\left(\frac{\partial z(x,y)}{\partial x}\right)^2 + \left(\frac{\partial z(x,y)}{\partial y}\right)^2\right] dxdy} \tag{13}$$

Developed interfacial ratio: S_{dr}

The S_{dr} value quantifies the percentage of additional surface area contributed by the texture as compared to an ideal plane. It is zero if the surface is completely flat and perpendicular to the orientation of the height. The S_{dr} parameter is sensitive towards both, feature amplitude and wavelength.

$$S_{dr} = \frac{1}{A}\left[\iint_A \left(\sqrt{\left[1 + \left(\frac{\partial z(x,y)}{\partial x}\right)^2 + \left(\frac{\partial z(x,y)}{\partial y}\right)^2\right]} - 1\right) dxdy\right] \tag{14}$$

Arithmetic mean peak curvature: S_{pc}

S_{pc} quantifies the arithmetic mean of the principal curvatures of peaks on the surface. Due to our inability to perform Wolf pruning (*i.e.*, to merge the peaks of micro-hill areas with adjoining areas) with the software used here, this parameter does not conform with ISO 25178-2: 2012.

$$S_{pc} = -\frac{1}{2}\frac{1}{n}\sum_{k=1}^{n}\left(\frac{\partial^2 z(x,y)}{\partial x^2} + \frac{\partial^2 z(x,y)}{\partial y^2}\right) \tag{15}$$

S2.4 Functional volume parameters

Functional volume parameters can be calculated based on the Abbot Firestone curve, which displays the areal material ratio S_{mr} at each height h. From this curve, two basic metrics can be calculated: first, the void volume (Equation 16) which is defined as the volume of open space per unit area; second, the material volume (Equation 17), which describes the volume of actual substance per unit area. In those equations, S_{mc} refers to the inverse areal material ratio, which represents the height h which meets the areal material ratio. K is a constant introduced for converting the units to mL/mm^2.

$$V_{v(p)} = \frac{K}{100\%}\int_p^{100\%} [S_{mc(p)} - S_{mc(q)}]dq \tag{16}$$

$$V_{m(p)} = \frac{K}{100\%}\int_0^{p} [S_{mc(q)} - S_{mc(p)}]dq \tag{17}$$

From these definitions, four functional volume parameters were determined as depicted in Fig. S1.

Dale void volume (V_{vv}) and core void volume (V_{vc})

The dale void volume indicates a void volume in the range of $p = 80\ \%$ to $100\ \%$ of the areal material ratio. The core void volume is the difference in void volume between the areal material ratios of $p = 10\ \%$ and $q = 80\ \%$.

Peak material volume (V_{mp}) and core material volume (V_{mc})

The peak material volume is the material volume when the areal material ratio equals $p = 10\ \%$. The core material volume denotes the difference in material volume between $p = 10\ \%$ and $q = 80\ \%$ of the areal material ratio.

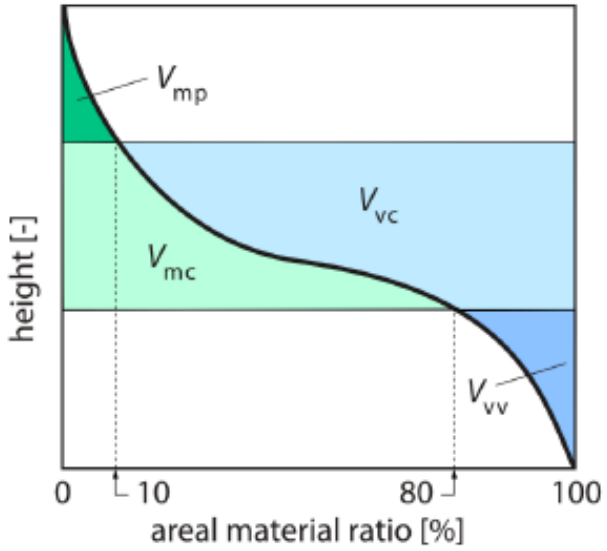

Figure S1: Exemplary Abbot Firestone curve explaining the meaning of different functional volume parameters. The areal material ratio S_{mr} is displayed for each height h. Based on this curve, four different functional volume parameters were determined here.

S2.5 Functional parameters

The following functional parameters were calculated using an Abbot Firestone curve as mentioned above. To do so, a regression line was determined as a secant on the curve for which first the slope and then the square sum of the deviation in the vertical axis direction are reduced to a minimum (see Figure S2). From that, the core surface is defined as the remaining surface, that is left, when those surface regions are removed, which do not contribute to the areal material ratio of the regression line.

Core height: S_k
The core height describes the difference between the maximum core height and the minimum core height as determined from the regression line.

Reduced peak height (S_{pk}) and reduced dale height (S_{vk})
S_{pk} denotes the average height of the reduced peak section, and S_{vk} the average depth of the reduced dale section. They are individually given by the height of the right-angled triangle whose area is equivalent to those grey peak/dale areas of the areal material ratio curve, that do not belong to the core section. However, due to the anisotropic and very wavy surfaces obtained for some biofilms (especially *B. subtilis* B-1), the S_{vk} turned out to not be robust enough for the characterization as it could not be determined for all samples.

Upper material ratio (S_{mr1}) and lower material ratio (S_{mr2})
S_{mr1} and S_{mr2} refer to the areal material ratio at the intersection of the material ratio curve and the core's upper-part height and lower-part height, respectively.

Peak extreme height: S_{xp}
The extreme peak height is defined as the difference in height between the areal material ratios of $p = 2.5$ % and $q = 50$ %.

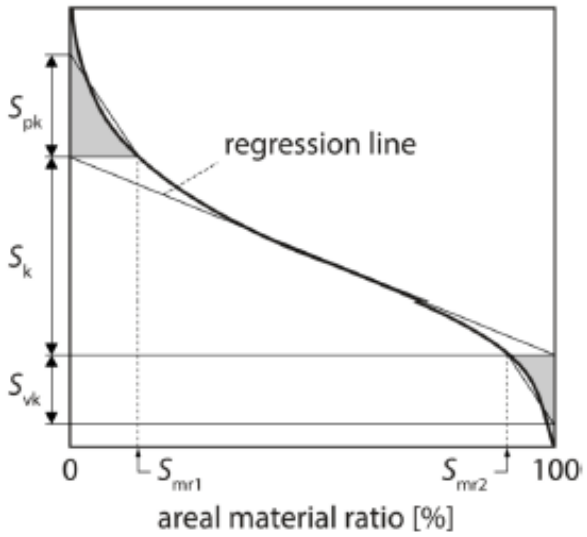

Figure S2: Exemplary Abbot Firestone curve explaining the meaning of different functional parameters. A regression line is drawn to reach a minimum square sum of the deviations in vertical direction. From that, the core surface can be defined, and different functional parameters can be calculated.

S3 Classification examples for model-based classifiers

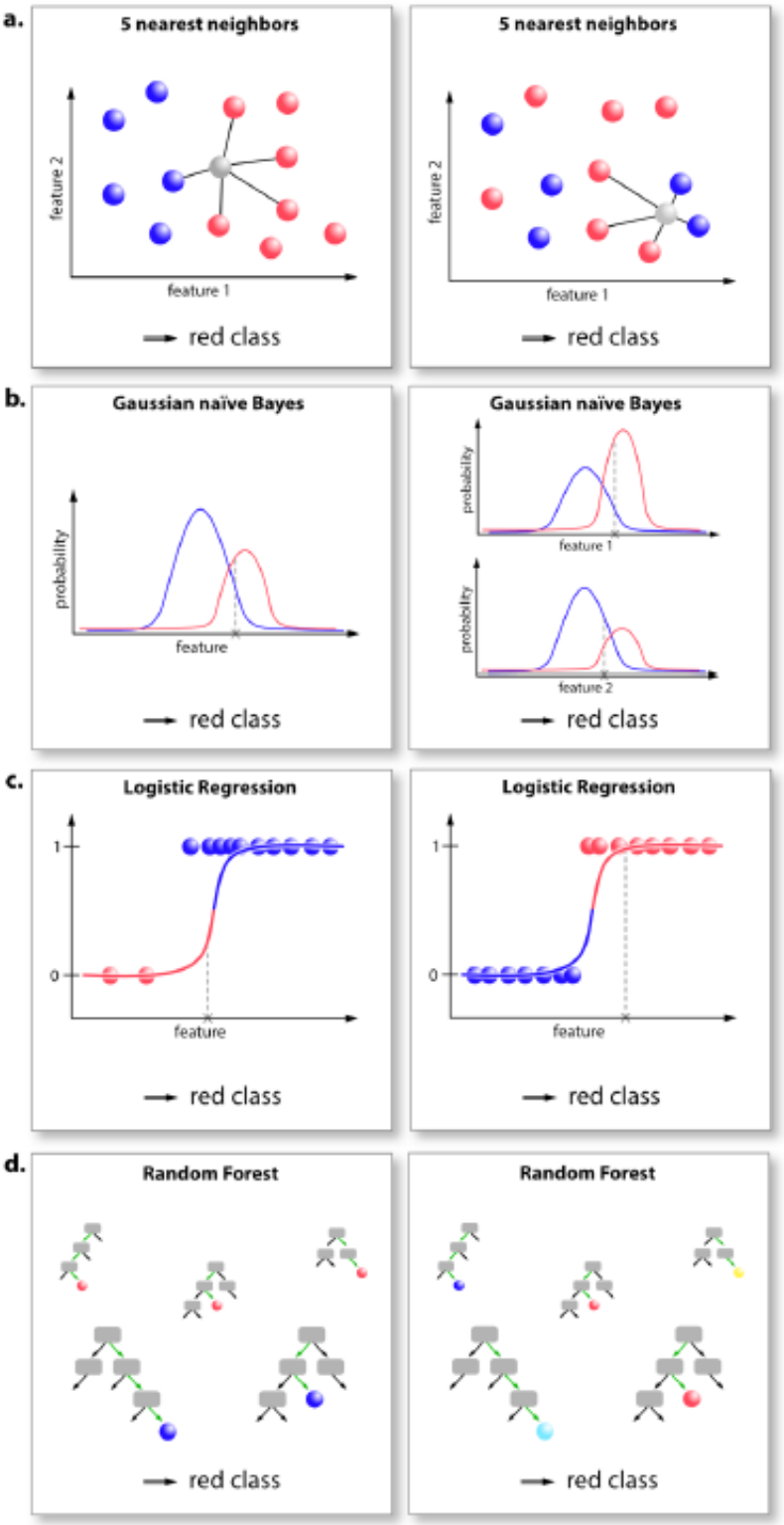

Figure S3: Exemplary classification problems visualizing the decision process of the four machine learning algorithms used in this study.

S4 Prediction accuracy of the *k* nearest neighbor classifier

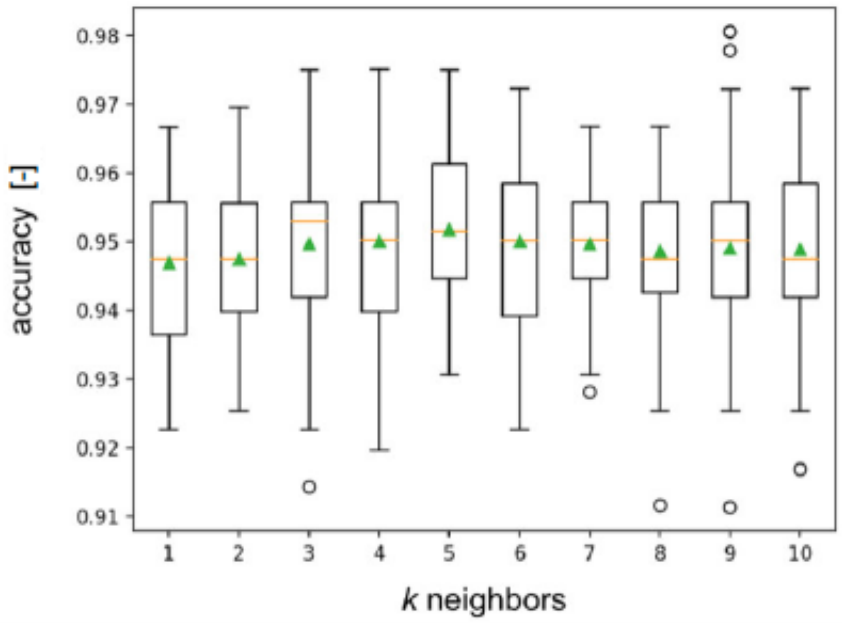

Figure S4: Whisker-boxplots showing the prediction accuracy of the *k* nearest neighbor classifier with increasing values of *k*. For these trials, the KNN classifier was applied to the initial data set (*Bacillus subtilis* NCIB 3610, *B. subtilis* B-1, and *B. subtilis natto* biofilms, each cultivated on MSgg agar, n = 1788). A repeated (10 times) stratified 5-fold cross validation was used to evaluate the accuracies. The green triangles indicate the mean obtained from the 50 (= 10 x 5) runs per trial.

S5 Naïve Bayes' theorem

The Bayes theorem defines the relation between the conditional probability of a class y and a dependent feature vector $(x_1, \ldots, x_n)$ as follows[2,3]:

$$P(y|x_1, \ldots, x_n) = \frac{P(y)P(x_1, \ldots, x_n \mid y)}{P(x_1, \ldots, x_n)}. \tag{18}$$

Applying the naïve assumption of conditional independence, which is

$$P(x_i \mid y, x_1, \ldots, x_{i-1}, x_{i+1}, \ldots, x_n) = P(x_i \mid y) \tag{19}$$

for all i, the following simplification results:

$$P(y|x_1, \ldots, x_n) = \frac{P(y)\prod_{i=1}^{n} P(x_i \mid y)}{P(x_1, \ldots, x_n)} \tag{20}$$

As $P(x_1, \ldots, x_n)$ is constant according to the input, a general classification rule as given by Equations 4 and 5, respectively, is obtained:

$$P(y \mid x_1, \ldots, x_n) \propto P(y) \prod_{i=1}^{n} P(x_i \mid y) \tag{21}$$

$$\Downarrow$$

$$\hat{y} = \arg\max_{y} P(y) \prod_{i=1}^{n} P(x_i \mid y) \tag{22}$$

S6 Stratification of Data Splits

The models used in this study were evaluated using repeated *k*-fold cross-validation. Since these evaluations tend to have issues with imbalanced data sets[4], we used a stratified version. This ensures that all created folds are good representatives of the whole data set, *i.e.*, that the proportions of each class found in the original data set is respected in all the folds. A visual explanation of the stratified sample split is depicted in Figure S5.

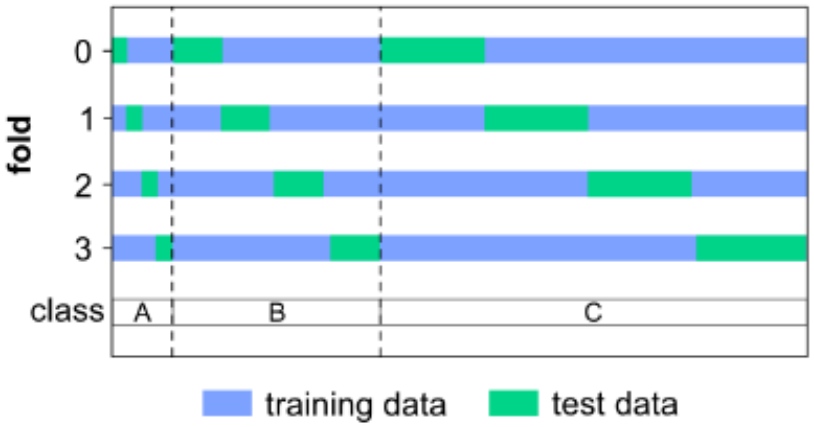

Figure S5: Stratification of a data set. To compensate for imbalances of the class distribution within a data set, the folds are created such that the class distribution in the respective training and test sets equals the class distribution of the whole data set.

S7 *B. subtilis* biofilms grown on MSgg agar

S7.1 Sensitivity and specificity of the different classifiers

The *B. subtilis* strains *natto*, NCIB 3610, and B-1 were grown on MSgg agar. Data evaluation was conducted *via* repeated (10 times) stratified 5-fold cross validation – *i.e.*, 80 % of the data were used to train the algorithm, while the other 20 % were used for testing (for details, please refer to the Methods section in the main paper). The sensitivity and specificity were then calculated according to the following equations:

$$sensitivity = \frac{true\ positive}{true\ positive + false\ negative} \tag{23}$$

$$specificity\ \frac{true\ negative}{true\ negative + false\ positive} \tag{24}$$

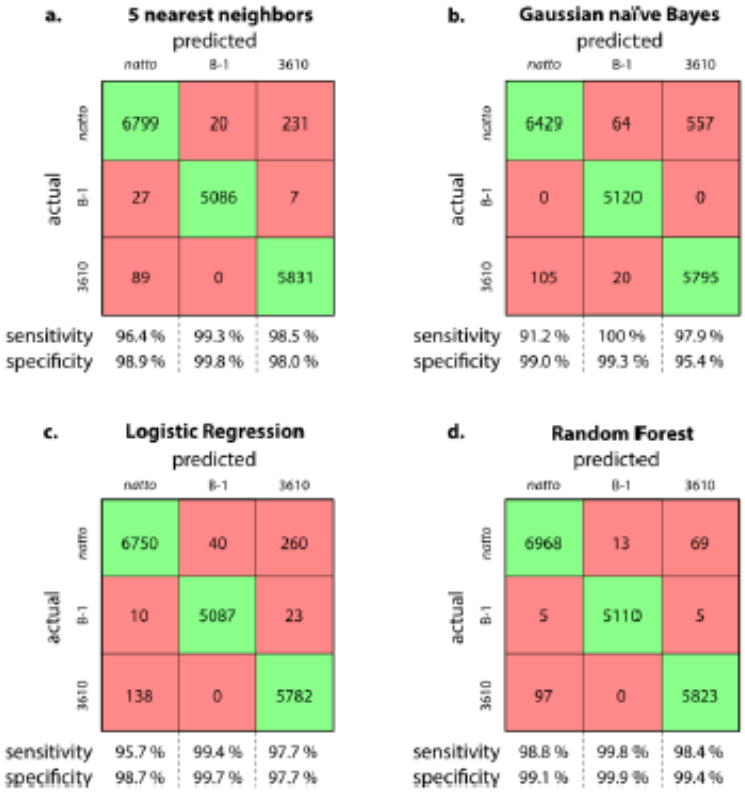

Figure S6: Categorization results obtained with four different machine learning algorithms fed with biofilm data obtained on MSgg agar. The confusion matrices (a-d) compare the actual classes (*i.e.*, the names of the bacterial strains the biofilms were grown from) with the predicted classes when a 5 nearest neighbor classifier (a), a Gaussian naïve Bayes model (b), multinomial logistic regression (c), and a Random Forest classifier (d) are applied to the data. Evaluation was performed by repeated (10 times) 5-fold cross validation including data shuffling before each iteration – *i.e.*, each sample served 10 times as a test sample but was each time analyzed by a differently trained algorithm. The main diagonal (green boxes) contains the numbers of correctly classified samples whereas all other boxes represent wrongly assigned samples.

S7 *B. subtilis* biofilms grown on MSgg agar

S7.1 Sensitivity and specificity of the different classifiers

The *B. subtilis* strains *natto*, NCIB 3610, and B-1 were grown on MSgg agar. Data evaluation was conducted *via* repeated (10 times) stratified 5-fold cross validation – *i.e.*, 80 % of the data were used to train the algorithm, while the other 20 % were used for testing (for details, please refer to the Methods section in the main paper). The sensitivity and specificity were then calculated according to the following equations:

$$sensitivity = \frac{true\ positive}{true\ positive + false\ negative} \tag{23}$$

$$specificity\ \frac{true\ negative}{true\ negative + false\ positive} \tag{24}$$

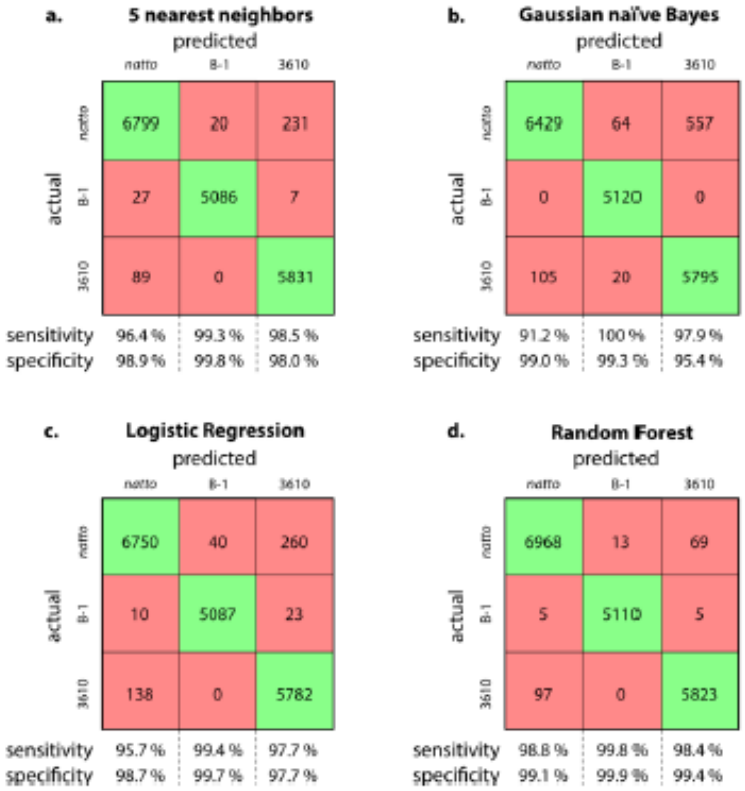

Figure S6: Categorization results obtained with four different machine learning algorithms fed with biofilm data obtained on MSgg agar. The confusion matrices (a-d) compare the actual classes (*i.e.*, the names of the bacterial strains the biofilms were grown from) with the predicted classes when a 5 nearest neighbor classifier (a), a Gaussian naïve Bayes model (b), multinomial logistic regression (c), and a Random Forest classifier (d) are applied to the data. Evaluation was performed by repeated (10 times) 5-fold cross validation including data shuffling before each iteration – *i.e.*, each sample served 10 times as a test sample but was each time analyzed by a differently trained algorithm. The main diagonal (green boxes) contains the numbers of correctly classified samples whereas all other boxes represent wrongly assigned samples.

S8 *B. subtilis* biofilms grown on LB agar

S8.1 Topographical surface parameters

The *B. subtilis* strains *natto*, NCIB 3610, and B-1 were grown on LB agar as described in the main paper. From the central part of the colonies, 16 profilometric images were obtained from which the topographical parameters shown in Figure S8 were determined.

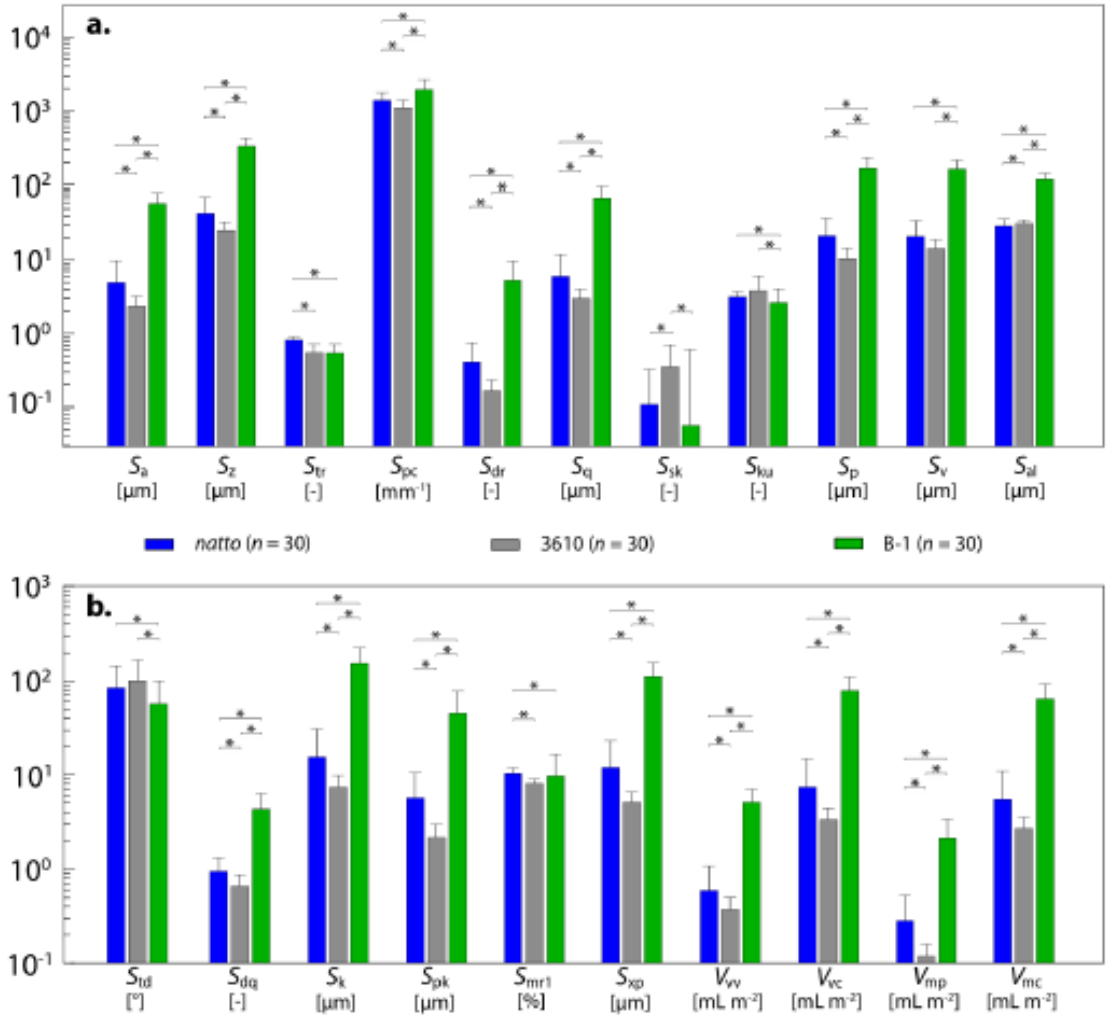

Figure S8: Micro-topographical parameters of biofilms generated by three *Bacillus subtilis* strains grown on LB agar. The topographical parameters were calculated from profilometric images as described in the Methods section of the main paper. Error bars denote the standard deviation obtained from $n = 30$ images. Asterisks indicate statistical differences as assessed with a Wilcoxon-Mann-Whitney test applying a p-value of 0.05.

S8.2 Contact angles and tilt experiments

Contact angle measurements and tilt experiments were performed for biofilms generated by the three different *B. subtilis* strains grown on LB agar as described for biofilms grown on MSgg agar in S7.2.

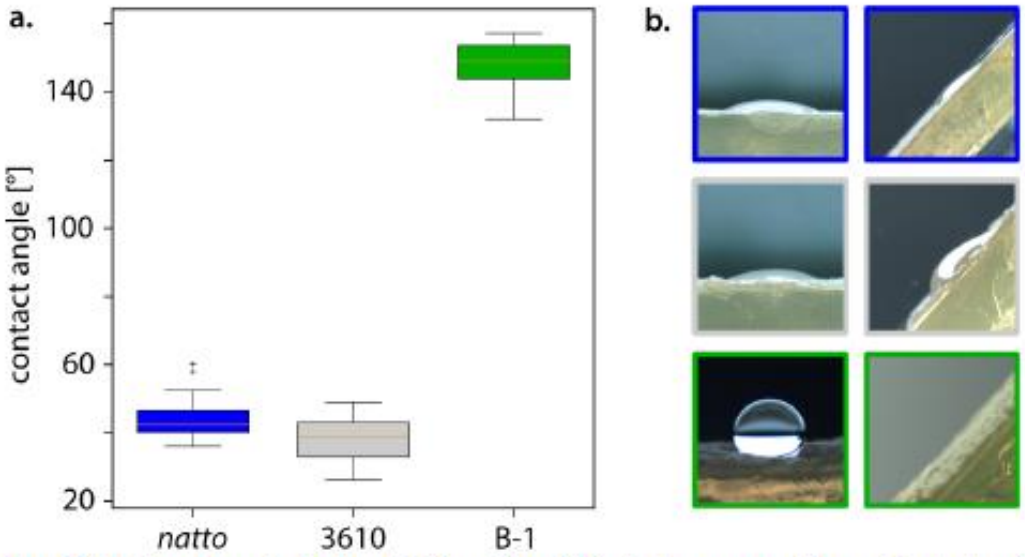

Figure S9: Wetting characterization of different *B. subtilis* strains grown on LB agar. Contact angles (a) and exemplary images of tilt experiments (b) are shown as obtained for biofilms generated from the three bacterial strains *B. subtilis* strains *natto* (blue, *n* = 20), NCIB 3610 (grey, *n* = 20), and B-1 (green, *n* = 20) when grown on LB agar. The contact angles were measured on the central regions of the colonies.

S9 Plant leaves/petals

S9.1 Contact angles and tilt experiments

Contact angles and tilt experiments were performed for different plant samples as described for biofilms grown on MSgg agar in S7.2.

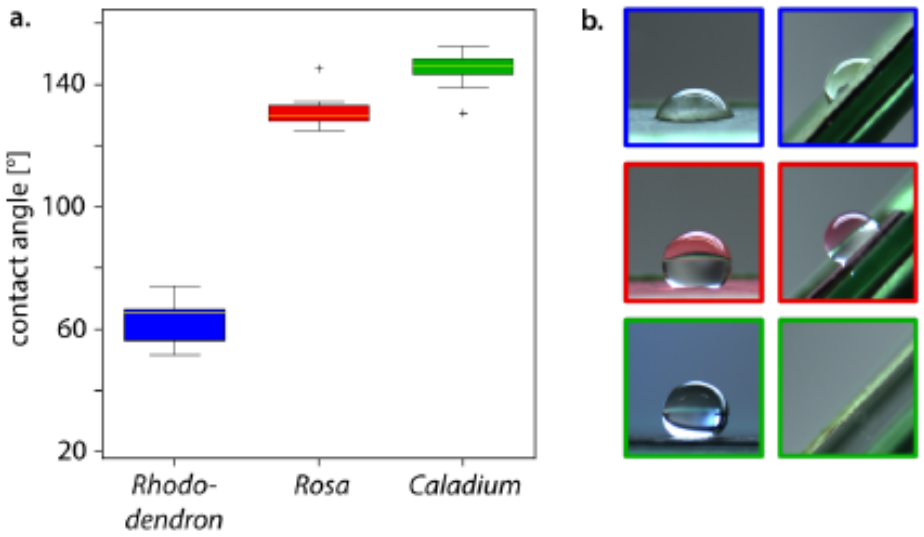

Figure S11: Wetting characterization of different plant samples. Contact angles (a) and exemplary images of tilt experiments (b) are show as obtained for *Rhododendron* leaves (blue, $n = 12$), rose petals (red, $n = 12$), and *Caladium* leaves (green, $n = 10$).

S9.2 Cross-validation of the classifiers

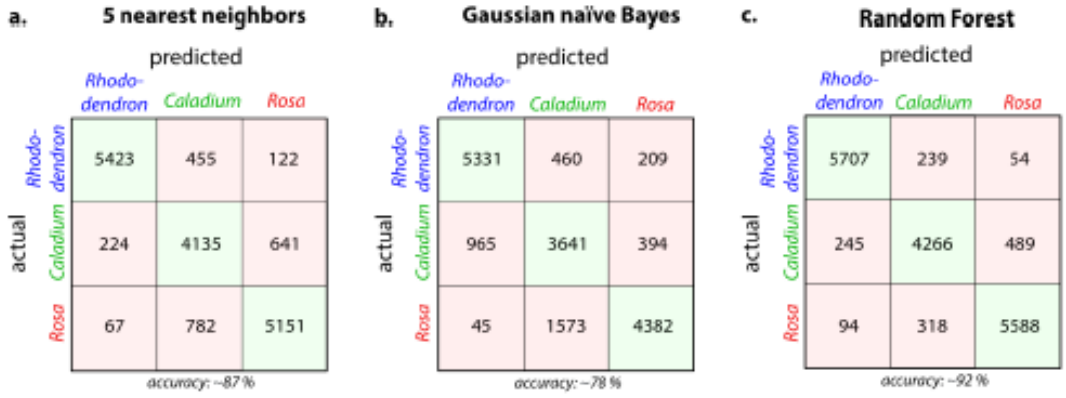

Figure S12: Categorization results obtained with three different machine learning algorithms fed with data obtained from plant samples. The confusion matrices compare the actual classes (*i.e.*, the names of the plants) with the predicted classes when a 5 nearest neighbor classifier (a), a Gaussian naïve Bayes model (b), and a Random Forest classifier (c) are applied to the data. The evaluation was performed by repeated (10 times) 5-fold cross validation with shuffling the data set before each iteration – *i.e.*, each sample served 10times as a test sample but was each time analyzed by a differently trained algorithm. The main diagonal (green boxes) contains the numbers of correctly classified samples whereas all other boxes represent wrongly assigned samples. The accuracies denote the ratio of correctly classified samples to all tested samples.

S10 Evaluation by cross-trained algorithms

S10.1 Trained on biofilms, tested with plant samples

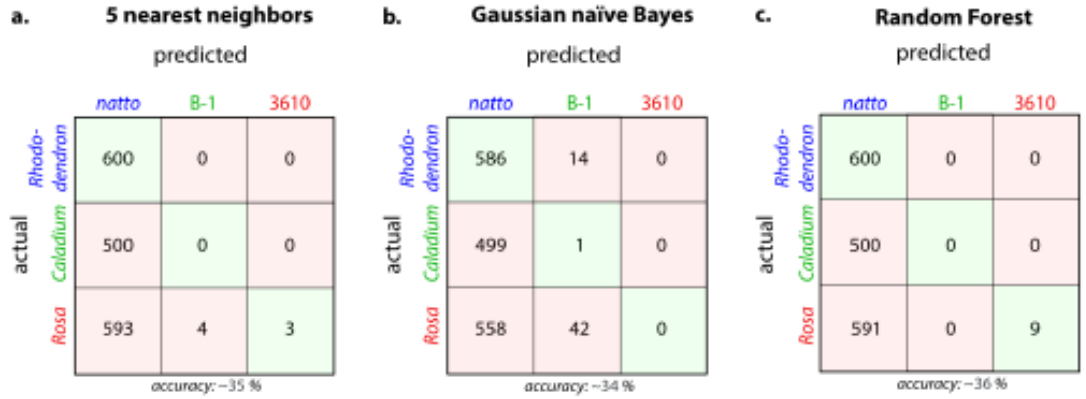

Figure S13: Categorization results of cross-trained algorithms. The confusion matrices compare the actual classes (*i.e.*, the plant names with the respective wetting behavior) with the predicted classes (*i.e.*, the names of the bacterial strains with the respective wetting behavior) when a 5 nearest neighbor classifier (a), a Gaussian naïve Bayes model (b), and a Random Forest classifier (c) are applied to the data. The algorithms were trained on biofilms grown on MSgg agar and tested with plant samples. The colors indicate the wetting behavior of the surfaces: blue denotes hydrophilic behavior, green displays lotus-like hydrophobicity, and red indicates rose-like hydrophobicity. The main diagonal (green boxes) contains the numbers of correctly classified samples whereas all other boxes represent wrongly assigned samples. The accuracies denote the ratio of correctly classified samples to all tested samples.

S10.2 Trained on plant samples, tested with biofilms

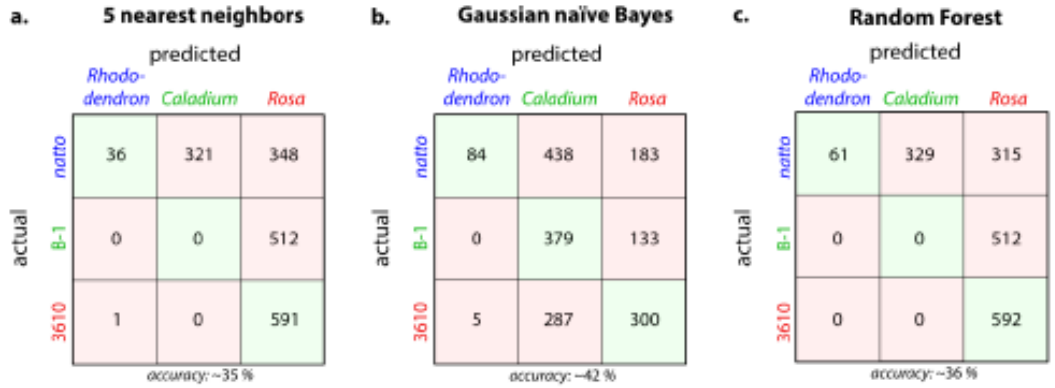

Figure S14: Categorization results of cross-trained algorithms. The confusion matrices compare the actual classes (*i.e.*, the names of the bacterial strains with the respective wetting behavior) with the predicted classes (*i.e.*, the names of the plant names with the respective wetting behavior) when a 5 nearest neighbor classifier (a), a Gaussian naïve Bayes model (b), and a Random Forest classifier (c) are applied to the data. The algorithms were trained on plant samples and tested with biofilms grown on MSgg agar. The colors indicate the wetting behavior of the surfaces: blue denotes hydrophilic behavior, green displays lotus-like hydrophobicity, and red indicates rose-like hydrophobicity. The main diagonal (green boxes) contains the numbers of correctly classified samples whereas all other boxes represent wrongly assigned samples. The accuracies denote the ratio of correctly classified samples to all tested samples.

S11 Evaluation of pooled data sets

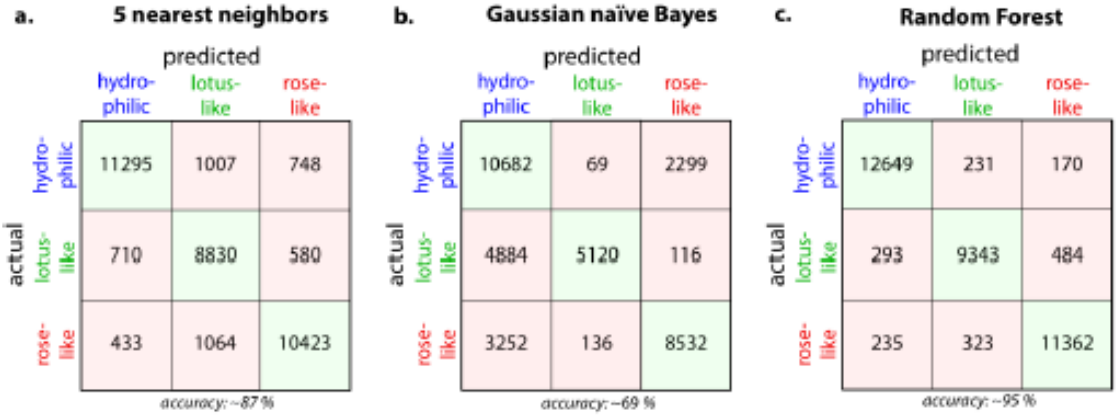

Figure S13: Categorization results of three different algorithms when fed a pooled biofilm/plant sample data set. The confusion matrices of three different classifiers used on the pooled data set are shown. The data set contains all data obtained for both, biofilms generated by three different bacterial strains grown on MSgg agar (*natto*: hydrophilic, 3610: hydrophobic rose-like, B-1: hydrophobic lotus-like) and plant samples (*Rhododendron*: hydrophilic, *Rosa*: hydrophobic rose-like, *Caladium*: hydrophobic lotus-like). All available metrological parameters were used. The evaluation was performed *via* repeated (10 times) 5-fold cross validation. The main diagonal (green boxes) contains the numbers of correctly classified samples whereas all other boxes represent wrongly assigned samples. The accuracies denote the ratio of correctly classified samples to all tested samples.

S12 Evaluation by a cross-trained Deep Neural Network

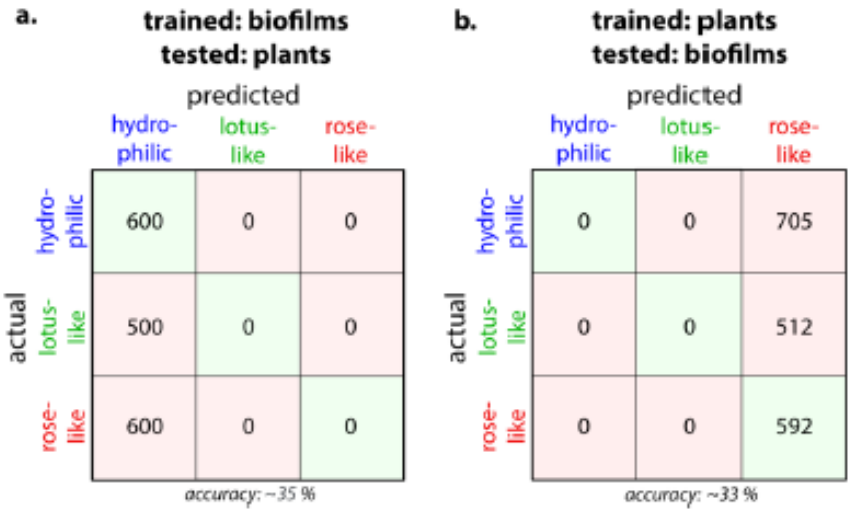

Figure S14: Categorization results of a Deep Neural Network trained and tested on different data sets. The confusion matrices of the deep neural network either trained with biofilm data and tested with plant samples (a) or *vice versa* (b) are displayed. The biofilm data set contains biofilms grown from three different bacterial strains on MSgg agar (*natto*: hydrophilic, 3610: hydrophobic rose-like, B-1: hydrophobic lotus-like). The plant set contains three different plant leaves/petals (*Rhododendron*: hydrophilic, *Rosa*: hydrophobic rose-like, *Caladium*: hydrophobic lotus-like). All available features were used. The main diagonal (green boxes) contains the numbers of correctly classified samples whereas all other boxes represent wrongly assigned samples. The accuracies denote the ratio of correctly classified samples to all tested samples.

S13 Example images

The following table displays exemplary surface images of samples analyzed in this study. However, it is important to keep in mind that not the images themselves, but topographical parameters calculated from the 3D images were fed to the algorithms. The classification results displayed below each image are those that were returned by the Random Forest classifier.

S13.1 Biofilm samples

Table S1: Exemplary 2D-laser scanning images of biofilm samples analyzed in this study. The classification results achieved by a Random Forest algorithm that was trained on (other) biofilm samples are depicted below each image. Please note that the ML analysis was not directly performed on those 2D images; instead, a set of metrological surface parameters was calculated from the three-dimensional topography of the samples and then fed into the algorithm (see main paper for details).

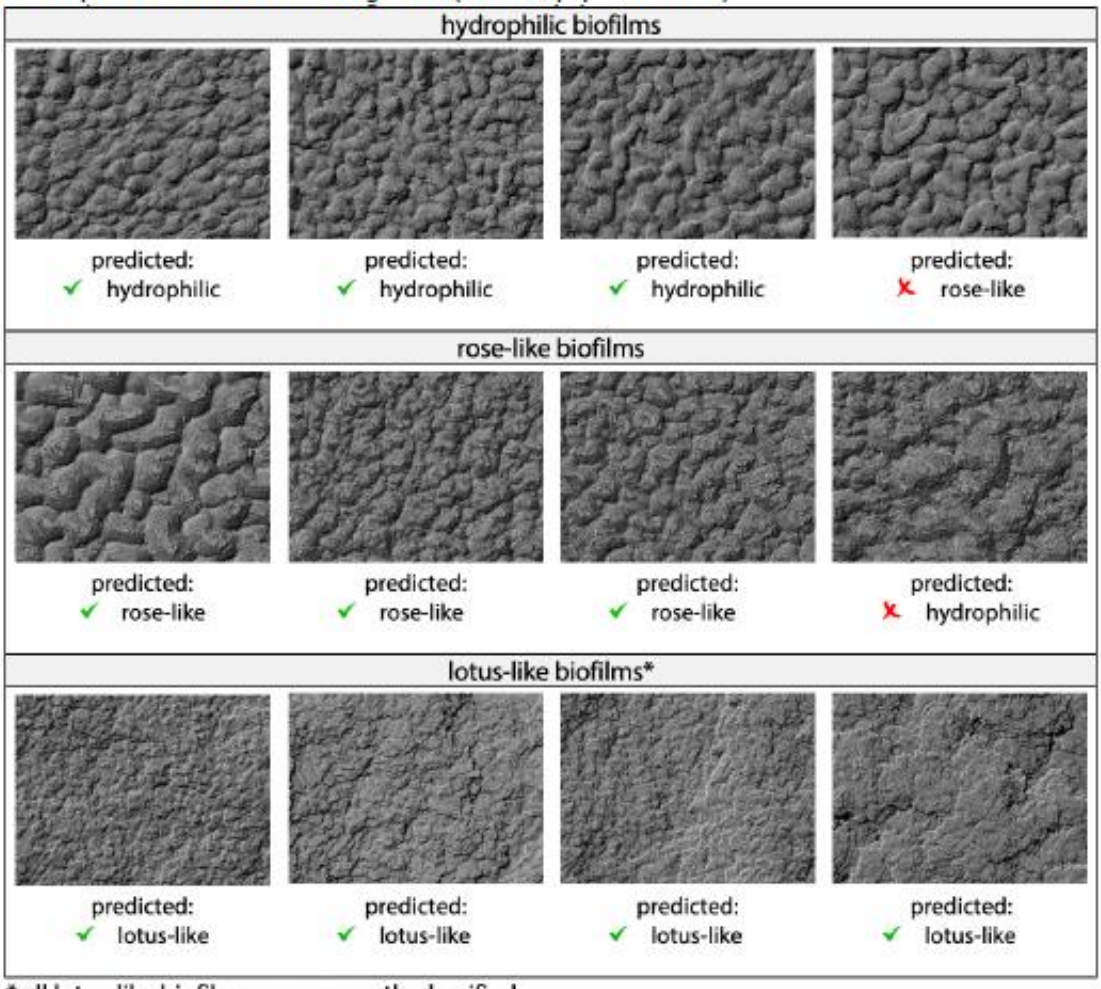

* all lotus-like biofilms were correctly classified

S13.2 Plant samples

Table S2: Exemplary 2D-laser scanning images of plant samples analyzed in this study. The classification results achieved by a Random Forest algorithm that was trained on (other) plant samples are depicted below each image. Please note that the ML analysis was not directly performed on those 2D images; instead, a set of metrological surface parameters was calculated from the three-dimensional topography of the samples and then fed into the algorithm (see main paper for details).

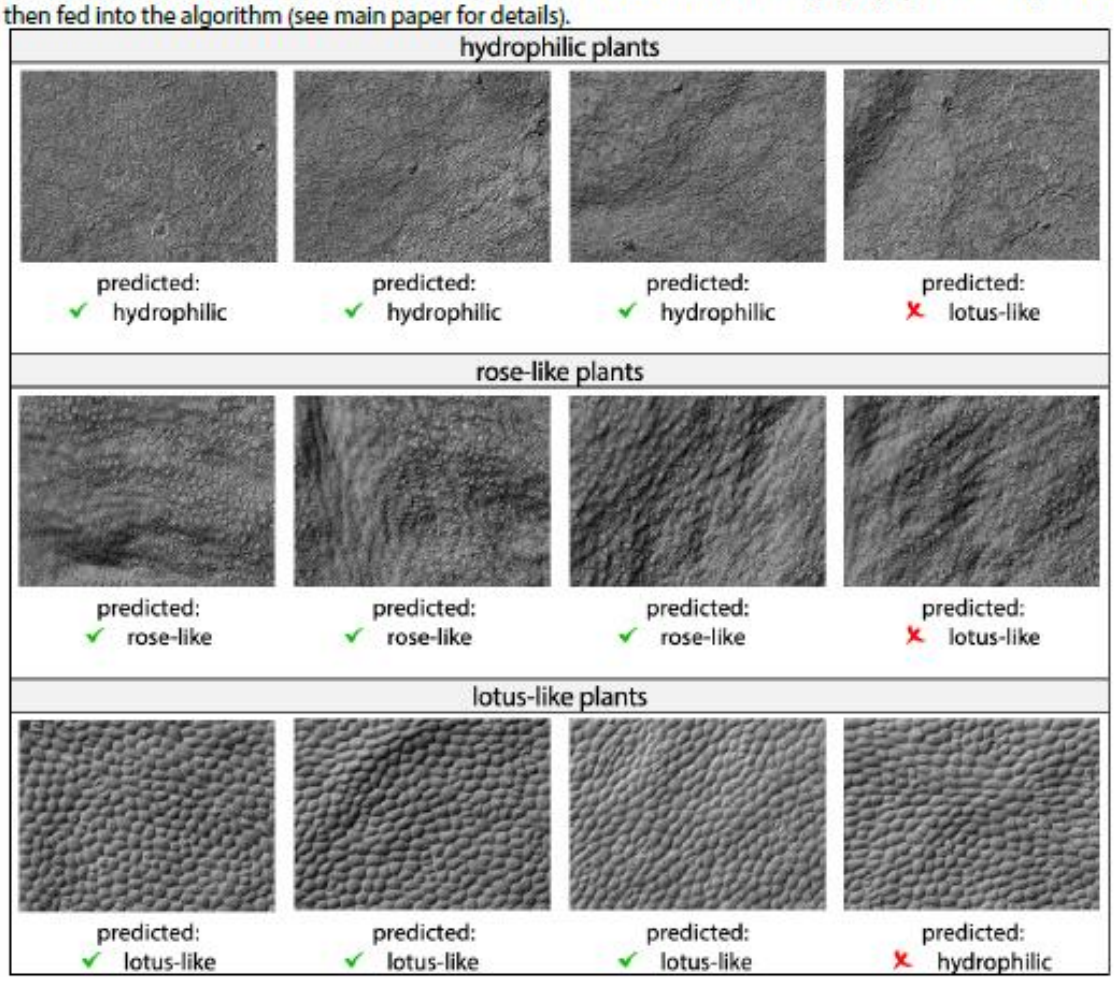

S14 Sensitivity and specificity with reduced input sets

In this section, the feature importance ranking is analyzed in more detail. Therefore, additional accuracy measures are calculated for the Random Forest classifier. Instead of the 21 available parameters, reduced input parameter sets are selected based on the importance analysis depicted in Figure 6a of the main paper: the initial input set contains the five highest-ranked parameters (*i.e.*, S_{dr}, S_{dq}, V_{vv}, S_{pc}, and S_a). Based on this, the sensitivity and the specificity are calculated for each class (*i.e.*, for hydrophobic, lotus-like, and rose-like samples). In addition to the overall accuracy shown in Figure 6b of the main paper, those two measures provide information if samples from certain classes are more difficult to classify than others. Both, sensitivity and specificity are then re-assessed while further reducing the number of input parameters, *i.e.*, by eliminating surface parameters in a stepwise manner (in full analogy to the accuracy calculation depicted in Figure 6b of the main paper): starting with the S_a parameter, also S_{pc}, V_{vv}, and S_{dq} are removed until only S_{dr} remains. Overall, we find that the sensitivity is lower than the specificity, and the former suffers more strongly than the latter when the parameter range is reduced. When comparing the three sample classes, we find that the decrease of sensitivity is strongest for rose-like samples. We attribute this to the intermediate surface roughness properties of this particular biofilm class[5], which probably results in a higher probability of misclassification than for the two other classes.

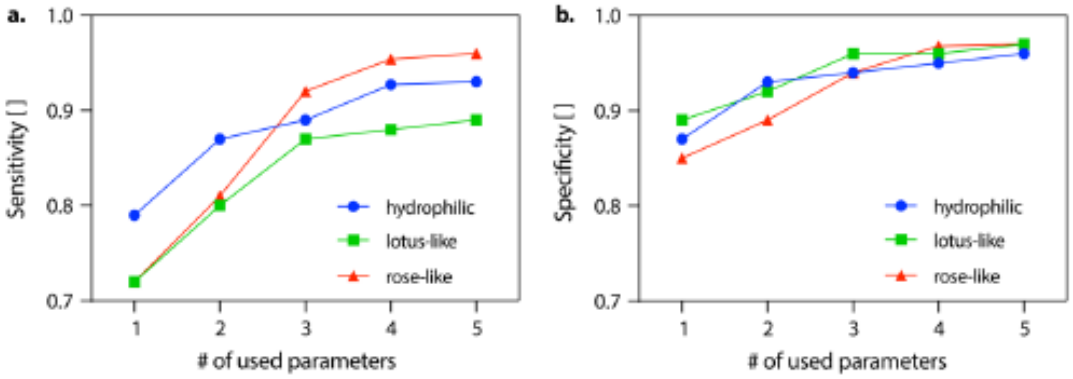

Figure S15: Sensitivity and specificity of the Random Forest classifier when fed with reduced input sets. The accuracy measures were calculated (as described in section S7) based on a repeated (10 times) 5-fold cross validation of the Random Forest classifier that was applied to the pooled data set (including both, biofilm samples and plant samples). The range of five surface parameters (S_{dr}, S_{dq}, V_{vv}, S_{pc}, and S_a) was reduced in a stepwise manner: starting with the S_a parameter, also S_{pc}, V_{vv} and S_{dq} were eliminated one after each other until only S_{dr} was left.

Literature

1. Branda, S. S.; Chu, F.; Kearns, D. B.; Losick, R.; Kolter, R., A major protein component of the Bacillus subtilis biofilm matrix. *Molecular Microbiology* **2006,** *59* (4), 1229-1238.
2. Murphy, K. P., Naive bayes classifiers. *University of British Columbia* **2006,** *18* (60).
3. Zhang, H., Exploring conditions for the optimality of naive Bayes. *International Journal of Pattern Recognition and Artificial Intelligence* **2005,** *19* (02), 183-198.
4. Raeder, T.; Forman, G.; Chawla, N. V., Learning from imbalanced data: Evaluation matters. In *Data mining: Foundations and intelligent paradigms*, Springer: 2012; pp 315-331.
5. García, C. F.; Stangl, F.; Götz, A.; Zhao, W.; Sieber, S. A.; Opitz, M.; Lieleg, O., Topographical alterations render bacterial biofilms susceptible to chemical and mechanical stress. *Biomaterials Science* **2019,** *7* (1), 220-232.

B. Lizenzen für die Publikationen

B.1 Bacterial Materials: Applications of Natural and Modified Biofilms

This article is licensed under a Creative Commons Attribution-NonCommercial 4.0 International Public Licence (CC BY-NC 4.0):

Creative Commons Attribution-NonCommercial 4.0 International Public License

By exercising the Licensed Rights (defined below), You accept and agree to be bound by the terms and conditions of this Creative Commons Attribution-NonCommercial 4.0 International Public License ("Public License"). To the extent this Public License may be interpreted as a contract, You are granted the Licensed Rights in consideration of Your acceptance of these terms and conditions, and the Licensor grants You such rights in consideration of benefits the Licensor receives from making the Licensed Material available under these terms and conditions.

Section 1 – Definitions.

a. **Adapted Material** means material subject to Copyright and Similar Rights that is derived from or based upon the Licensed Material and in which the Licensed Material is translated, altered, arranged, transformed, or otherwise modified in a manner requiring permission under the Copyright and Similar Rights held by the Licensor. For purposes of this Public License, where the Licensed Material is a musical work, performance, or sound recording, Adapted Material is always produced where the Licensed Material is synched in timed relation with a moving image.
b. **Adapter's License** means the license You apply to Your Copyright and Similar Rights in Your contributions to Adapted Material in accordance with the terms and conditions of this Public License.
c. **Copyright and Similar Rights** means copyright and/or similar rights closely related to copyright including, without limitation, performance, broadcast, sound recording, and Sui Generis Database Rights, without regard to how the rights are labeled or categorized. For purposes of this Public License, the rights specified in Section 2(b)(1)-(2) are not Copyright and Similar Rights.
d. **Effective Technological Measures** means those measures that, in the absence of proper authority, may not be circumvented under laws fulfilling obligations under Article 11 of the WIPO Copyright Treaty adopted on December 20, 1996, and/or similar international agreements.
e. **Exceptions and Limitations** means fair use, fair dealing, and/or any other exception or limitation to Copyright and Similar Rights that applies to Your use of the Licensed Material.
f. **Licensed Material** means the artistic or literary work, database, or other material to which the Licensor applied this Public License.
g. **Licensed Rights** means the rights granted to You subject to the terms and conditions of this Public License, which are limited to all Copyright and Similar Rights that apply to Your use of the Licensed Material and that the Licensor has authority to license.
h. **Licensor** means the individual(s) or entity(ies) granting rights under this Public License.
i. **NonCommercial** means not primarily intended for or directed towards commercial advantage or monetary compensation. For purposes of this Public License, the exchange of the Licensed Material for other material subject to Copyright and Similar Rights by digital file-sharing or similar means is NonCommercial provided there is no payment of monetary compensation in connection with the exchange.
j. **Share** means to provide material to the public by any means or process that requires permission under the Licensed Rights, such as reproduction, public display, public performance, distribution, dissemination, communication, or importation, and to make material available to the public including in ways that members of the public may access the material from a place and at a time individually chosen by them.
k. **Sui Generis Database Rights** means rights other than copyright resulting from Directive 96/9/EC of the European Parliament and of the Council of 11 March 1996 on the legal protection of databases, as amended and/or succeeded, as well as other essentially equivalent rights anywhere in the world.
l. **You** means the individual or entity exercising the Licensed Rights under this Public License. **Your** has a corresponding meaning.

Section 2 – Scope.

a. **License grant**.
    1. Subject to the terms and conditions of this Public License, the Licensor hereby grants You a worldwide, royalty-free, non-sublicensable, non-exclusive, irrevocable license to exercise the Licensed Rights in the Licensed Material to:
        A. reproduce and Share the Licensed Material, in whole or in part, for NonCommercial purposes only; and
        B. produce, reproduce, and Share Adapted Material for NonCommercial purposes only.
    2. Exceptions and Limitations. For the avoidance of doubt, where Exceptions and Limitations apply to Your use, this Public License does not apply, and You do not need to comply with its terms and conditions.
    3. Term. The term of this Public License is specified in Section 6(a).
    4. Media and formats; technical modifications allowed. The Licensor authorizes You to exercise the Licensed Rights in all media and formats whether now known or hereafter created, and to make technical modifications necessary to do so. The Licensor waives and/or agrees not to assert any right or authority to forbid You from making technical modifications necessary to exercise the Licensed Rights, including technical modifications necessary to circumvent Effective Technological Measures. For purposes of this Public License, simply making modifications authorized by this Section 2(a)(4) never produces Adapted Material.
    5. Downstream recipients.
        A. Offer from the Licensor – Licensed Material. Every recipient of the Licensed Material automatically receives an offer from the Licensor to exercise the Licensed Rights under the terms and conditions of this Public License.
        B. No downstream restrictions. You may not offer or impose any additional or different terms or conditions on, or apply any Effective Technological Measures to, the Licensed Material if doing so restricts exercise of the Licensed Rights by any recipient of the Licensed Material.
    6. No endorsement. Nothing in this Public License constitutes or may be construed as permission to assert or imply that You are, or that Your use of the Licensed Material is, connected with, or sponsored, endorsed, or granted official status by, the Licensor or others designated to receive attribution as provided in Section 3(a)(1)(A)(i).
b. **Other rights**.
    1. Moral rights, such as the right of integrity, are not licensed under this Public License, nor are publicity, privacy, and/or other similar personality rights; however, to the extent possible, the Licensor waives and/or agrees not to assert any such rights held by the Licensor to the limited extent necessary to allow You to exercise the Licensed Rights, but not otherwise.
    2. Patent and trademark rights are not licensed under this Public License.
    3. To the extent possible, the Licensor waives any right to collect royalties from You for the exercise of the Licensed Rights, whether directly or through a collecting society under any voluntary or waivable statutory or compulsory licensing scheme. In all other cases the Licensor expressly reserves any right to collect such royalties, including when the Licensed Material is used other than for NonCommercial purposes.

Section 3 – License Conditions.

Your exercise of the Licensed Rights is expressly made subject to the following conditions.

a. **Attribution**.
    1. If You Share the Licensed Material (including in modified form), You must:
        A. retain the following if it is supplied by the Licensor with the Licensed Material:
            i. identification of the creator(s) of the Licensed Material and any others designated to receive attribution, in any reasonable manner requested by the Licensor (including by pseudonym if designated);
            ii. a copyright notice;
            iii. a notice that refers to this Public License;
            iv. a notice that refers to the disclaimer of warranties;
            v. a URI or hyperlink to the Licensed Material to the extent reasonably practicable;
        B. indicate if You modified the Licensed Material and retain an indication of any previous modifications; and

C. indicate the Licensed Material is licensed under this Public License, and include the text of, or the URI or hyperlink to, this Public License.

2. You may satisfy the conditions in Section 3(a)(1) in any reasonable manner based on the medium, means, and context in which You Share the Licensed Material. For example, it may be reasonable to satisfy the conditions by providing a URI or hyperlink to a resource that includes the required information.
3. If requested by the Licensor, You must remove any of the information required by Section 3(a)(1)(A) to the extent reasonably practicable.
4. If You Share Adapted Material You produce, the Adapter's License You apply must not prevent recipients of the Adapted Material from complying with this Public License.

Section 4 – Sui Generis Database Rights.

Where the Licensed Rights include Sui Generis Database Rights that apply to Your use of the Licensed Material:

a. for the avoidance of doubt, Section 2(a)(1) grants You the right to extract, reuse, reproduce, and Share all or a substantial portion of the contents of the database for NonCommercial purposes only;
b. if You include all or a substantial portion of the database contents in a database in which You have Sui Generis Database Rights, then the database in which You have Sui Generis Database Rights (but not its individual contents) is Adapted Material; and
c. You must comply with the conditions in Section 3(a) if You Share all or a substantial portion of the contents of the database.

For the avoidance of doubt, this Section 4 supplements and does not replace Your obligations under this Public License where the Licensed Rights include other Copyright and Similar Rights.

Section 5 – Disclaimer of Warranties and Limitation of Liability.

a. Unless otherwise separately undertaken by the Licensor, to the extent possible, the Licensor offers the Licensed Material as-is and as-available, and makes no representations or warranties of any kind concerning the Licensed Material, whether express, implied, statutory, or other. This includes, without limitation, warranties of title, merchantability, fitness for a particular purpose, non-infringement, absence of latent or other defects, accuracy, or the presence or absence of errors, whether or not known or discoverable. Where disclaimers of warranties are not allowed in full or in part, this disclaimer may not apply to You.

b. To the extent possible, in no event will the Licensor be liable to You on any legal theory (including, without limitation, negligence) or otherwise for any direct, special, indirect, incidental, consequential, punitive, exemplary, or other losses, costs, expenses, or damages arising out of this Public License or use of the Licensed Material, even if the Licensor has been advised of the possibility of such losses, costs, expenses, or damages. Where a limitation of liability is not allowed in full or in part, this limitation may not apply to You.

c. The disclaimer of warranties and limitation of liability provided above shall be interpreted in a manner that, to the extent possible, most closely approximates an absolute disclaimer and waiver of all liability.

Section 6 – Term and Termination.

a. This Public License applies for the term of the Copyright and Similar Rights licensed here. However, if You fail to comply with this Public License, then Your rights under this Public License terminate automatically.
b. Where Your right to use the Licensed Material has terminated under Section 6(a), it reinstates:
    1. automatically as of the date the violation is cured, provided it is cured within 30 days of Your discovery of the violation; or
    2. upon express reinstatement by the Licensor.

    For the avoidance of doubt, this Section 6(b) does not affect any right the Licensor may have to seek remedies for Your violations of this Public License.

c. For the avoidance of doubt, the Licensor may also offer the Licensed Material under separate terms or conditions or stop distributing the Licensed Material at any time; however, doing so will not terminate this Public License.
d. Sections 1, 5, 6, 7, and 8 survive termination of this Public License.

Section 7 – Other Terms and Conditions.

a. The Licensor shall not be bound by any additional or different terms or conditions communicated by You unless expressly agreed.
b. Any arrangements, understandings, or agreements regarding the Licensed Material not stated herein are separate from and independent of the terms and conditions of this Public License.

Section 8 – Interpretation.

a. For the avoidance of doubt, this Public License does not, and shall not be interpreted to, reduce, limit, restrict, or impose conditions on any use of the Licensed Material that could lawfully be made without permission under this Public License.
b. To the extent possible, if any provision of this Public License is deemed unenforceable, it shall be automatically reformed to the minimum extent necessary to make it enforceable. If the provision cannot be reformed, it shall be severed from this Public License without affecting the enforceability of the remaining terms and conditions.
c. No term or condition of this Public License will be waived and no failure to comply consented to unless expressly agreed to by the Licensor.
d. Nothing in this Public License constitutes or may be interpreted as a limitation upon, or waiver of, any privileges and immunities that apply to the Licensor or You, including from the legal processes of any jurisdiction or authority.

B.2 Biopolymer-enriched *B. subtilis* NCIB 3610 biofilms exhibit increased erosion resistance

CCC Marketplace™

This is a License Agreement between Elif Nur Hayta ("User") and Copyright Clearance Center, Inc. ("CCC") on behalf of the Rightsholder identified in the order details below. The license consists of the order details, the CCC Terms and Conditions below, and any Rightsholder Terms and Conditions which are included below.

All payments must be made in full to CCC in accordance with the CCC Terms and Conditions below.

Order Date	13-Dec-2021	Type of Use	Republish in a thesis/dissertation
Order License ID	1167990-1		
ISSN	2047-4830	Publisher	Royal Society of Chemistry
		Portion	Chapter/article

LICENSED CONTENT

Publication Title	Biomaterials science	Rightsholder	Royal Society of Chemistry
Article Title	Biopolymer-enriched B. subtilis NCIB 3610 biofilms exhibit increased erosion resistance.	Publication Type	Journal
		Start Page	4675
		End Page	4686
Author/Editor	Kyōto Daigaku.Busshitsu-Saibō Tōgō Shisutemu Kyoten, Royal Society of Chemistry (Great Britain)	Issue	11
		Volume	7
Date	01/01/2013		
Language	English		
Country	United Kingdom of Great Britain and Northern Ireland		

REQUEST DETAILS

Portion Type	Chapter/article	Rights Requested	Main product and any product related to main product
Page range(s)	1-12		
Total number of pages	12	Distribution	Worldwide
Format (select all that apply)	Print, Electronic	Translation	Original language of publication
Who will republish the content?	Author of requested content	Copies for the disabled?	No
Duration of Use	Life of current edition	Minor editing privileges?	No
Lifetime Unit Quantity	Up to 1,000,000	Incidental promotional use?	Yes
		Currency	EUR

NEW WORK DETAILS

Title	Einfluss der Oberflächentopographie auf ausgewählte Materialeigenschaften von B. Subtilis Biofilmen	Institution name	Technical University of Munich
		Expected presentation date	2021-12-13
Instructor name	Elif Nur Hayta		

ADDITIONAL DETAILS

Order reference number	N/A

The requesting person / organization to appear on the license	Elif Nur Hayta

REUSE CONTENT DETAILS

Title, description or numeric reference of the portion(s)	Biopolymer-enriched B. subtilis NCIB 3610 biofilms exhibit increased erosion resistance.	Title of the article/chapter the portion is from	Biopolymer-enriched B. subtilis NCIB 3610 biofilms exhibit increased erosion resistance.
Editor of portion(s)	Hayta, Elif Nur; Lieleg, Oliver	Author of portion(s)	Hayta, Elif Nur; Lieleg, Oliver
Volume of serial or monograph	7	Issue, if republishing an article from a serial	11
Page or page range of portion	4675-4686	Publication date of portion	2019-01-01

SPECIAL RIGHTSHOLDER TERMS AND CONDITIONS

Permission is granted as long as the article is fully acknowledged and a link is given back to the article on our Platform. Please go to rsc.li/permissions for details. Please note that if the material specified above or any part of it appears with credit or acknowledgement to a third party then you must also secure permission from that third party before reproducing that material.

CCC Terms and Conditions

1. Description of Service; Defined Terms. This Republication License enables the User to obtain licenses for republication of one or more copyrighted works as described in detail on the relevant Order Confirmation (the "Work(s)"). Copyright Clearance Center, Inc. ("CCC") grants licenses through the Service on behalf of the rightsholder identified on the Order Confirmation (the "Rightsholder"). "Republication", as used herein, generally means the inclusion of a Work, in whole or in part, in a new work or works, also as described on the Order Confirmation. "User", as used herein, means the person or entity making such republication.

2. The terms set forth in the relevant Order Confirmation, and any terms set by the Rightsholder with respect to a particular Work, govern the terms of use of Works in connection with the Service. By using the Service, the person transacting for a republication license on behalf of the User represents and warrants that he/she/it (a) has been duly authorized by the User to accept, and hereby does accept, all such terms and conditions on behalf of User, and (b) shall inform User of all such terms and conditions. In the event such person is a "freelancer" or other third party independent of User and CCC, such party shall be deemed jointly a "User" for purposes of these terms and conditions. In any event, User shall be deemed to have accepted and agreed to all such terms and conditions if User republishes the Work in any fashion.

3. Scope of License; Limitations and Obligations.

    3.1. All Works and all rights therein, including copyright rights, remain the sole and exclusive property of the Rightsholder. The license created by the exchange of an Order Confirmation (and/or any invoice) and payment by User of the full amount set forth on that document includes only those rights expressly set forth in the Order Confirmation and in these terms and conditions, and conveys no other rights in the Work(s) to User. All rights not expressly granted are hereby reserved.

    3.2. General Payment Terms: You may pay by credit card or through an account with us payable at the end of the month. If you and we agree that you may establish a standing account with CCC, then the following terms apply: Remit Payment to: Copyright Clearance Center, 29118 Network Place, Chicago, IL 60673-1291. Payments Due: Invoices are payable upon their delivery to you (or upon our notice to you that they are available to you for downloading). After 30 days, outstanding amounts will be subject to a service charge of 1-1/2% per month or, if less, the maximum rate allowed by applicable law. Unless otherwise specifically set forth in the Order Confirmation or in a separate written agreement signed by CCC, invoices are due and payable on "net 30" terms. While User may exercise the rights licensed immediately upon issuance of the Order Confirmation, the license is automatically revoked and is null and void, as if it had never been issued, if complete payment for the license is not received on a timely basis either from User directly or through a payment agent, such as a credit card company.

3.3. Unless otherwise provided in the Order Confirmation, any grant of rights to User (i) is "one-time" (including the editions and product family specified in the license), (ii) is non-exclusive and non-transferable and (iii) is subject to any and all limitations and restrictions (such as, but not limited to, limitations on duration of use or circulation) included in the Order Confirmation or invoice and/or in these terms and conditions. Upon completion of the licensed use, User shall either secure a new permission for further use of the Work(s) or immediately cease any new use of the Work(s) and shall render inaccessible (such as by deleting or by removing or severing links or other locators) any further copies of the Work (except for copies printed on paper in accordance with this license and still in User's stock at the end of such period).

3.4. In the event that the material for which a republication license is sought includes third party materials (such as photographs, illustrations, graphs, inserts and similar materials) which are identified in such material as having been used by permission, User is responsible for identifying, and seeking separate licenses (under this Service or otherwise) for, any of such third party materials; without a separate license, such third party materials may not be used.

3.5. Use of proper copyright notice for a Work is required as a condition of any license granted under the Service. Unless otherwise provided in the Order Confirmation, a proper copyright notice will read substantially as follows: "Republished with permission of [Rightsholder's name], from [Work's title, author, volume, edition number and year of copyright]; permission conveyed through Copyright Clearance Center, Inc. " Such notice must be provided in a reasonably legible font size and must be placed either immediately adjacent to the Work as used (for example, as part of a by-line or footnote but not as a separate electronic link) or in the place where substantially all other credits or notices for the new work containing the republished Work are located. Failure to include the required notice results in loss to the Rightsholder and CCC, and the User shall be liable to pay liquidated damages for each such failure equal to twice the use fee specified in the Order Confirmation, in addition to the use fee itself and any other fees and charges specified.

3.6. User may only make alterations to the Work if and as expressly set forth in the Order Confirmation. No Work may be used in any way that is defamatory, violates the rights of third parties (including such third parties' rights of copyright, privacy, publicity, or other tangible or intangible property), or is otherwise illegal, sexually explicit or obscene. In addition, User may not conjoin a Work with any other material that may result in damage to the reputation of the Rightsholder. User agrees to inform CCC if it becomes aware of any infringement of any rights in a Work and to cooperate with any reasonable request of CCC or the Rightsholder in connection therewith.

4. Indemnity. User hereby indemnifies and agrees to defend the Rightsholder and CCC, and their respective employees and directors, against all claims, liability, damages, costs and expenses, including legal fees and expenses, arising out of any use of a Work beyond the scope of the rights granted herein, or any use of a Work which has been altered in any unauthorized way by User, including claims of defamation or infringement of rights of copyright, publicity, privacy or other tangible or intangible property.

5. Limitation of Liability. UNDER NO CIRCUMSTANCES WILL CCC OR THE RIGHTSHOLDER BE LIABLE FOR ANY DIRECT, INDIRECT, CONSEQUENTIAL OR INCIDENTAL DAMAGES (INCLUDING WITHOUT LIMITATION DAMAGES FOR LOSS OF BUSINESS PROFITS OR INFORMATION, OR FOR BUSINESS INTERRUPTION) ARISING OUT OF THE USE OR INABILITY TO USE A WORK, EVEN IF ONE OF THEM HAS BEEN ADVISED OF THE POSSIBILITY OF SUCH DAMAGES. In any event, the total liability of the Rightsholder and CCC (including their respective employees and directors) shall not exceed the total amount actually paid by User for this license. User assumes full liability for the actions and omissions of its principals, employees, agents, affiliates, successors and assigns.

6. Limited Warranties. THE WORK(S) AND RIGHT(S) ARE PROVIDED "AS IS". CCC HAS THE RIGHT TO GRANT TO USER THE RIGHTS GRANTED IN THE ORDER CONFIRMATION DOCUMENT. CCC AND THE RIGHTSHOLDER DISCLAIM ALL OTHER WARRANTIES RELATING TO THE WORK(S) AND RIGHT(S), EITHER EXPRESS OR IMPLIED, INCLUDING WITHOUT LIMITATION IMPLIED WARRANTIES OF MERCHANTABILITY OR FITNESS FOR A PARTICULAR PURPOSE. ADDITIONAL RIGHTS MAY BE REQUIRED TO USE ILLUSTRATIONS, GRAPHS, PHOTOGRAPHS, ABSTRACTS, INSERTS OR OTHER PORTIONS OF THE WORK (AS OPPOSED TO THE ENTIRE WORK) IN A MANNER CONTEMPLATED BY USER; USER UNDERSTANDS AND AGREES THAT NEITHER CCC NOR THE RIGHTSHOLDER MAY HAVE SUCH ADDITIONAL RIGHTS TO GRANT.

7. Effect of Breach. Any failure by User to pay any amount when due, or any use by User of a Work beyond the scope of the license set forth in the Order Confirmation and/or these terms and conditions, shall be a material breach of the license created by the Order Confirmation and these terms and conditions. Any breach not cured within 30 days

of written notice thereof shall result in immediate termination of such license without further notice. Any unauthorized (but licensable) use of a Work that is terminated immediately upon notice thereof may be liquidated by payment of the Rightsholder's ordinary license price therefor; any unauthorized (and unlicensable) use that is not terminated immediately for any reason (including, for example, because materials containing the Work cannot reasonably be recalled) will be subject to all remedies available at law or in equity, but in no event to a payment of less than three times the Rightsholder's ordinary license price for the most closely analogous licensable use plus Rightsholder's and/or CCC's costs and expenses incurred in collecting such payment.

8. Miscellaneous.

   8.1. User acknowledges that CCC may, from time to time, make changes or additions to the Service or to these terms and conditions, and CCC reserves the right to send notice to the User by electronic mail or otherwise for the purposes of notifying User of such changes or additions; provided that any such changes or additions shall not apply to permissions already secured and paid for.

   8.2. Use of User-related information collected through the Service is governed by CCC's privacy policy, available online here:https://marketplace.copyright.com/rs-ui-web/mp/privacy-policy

   8.3. The licensing transaction described in the Order Confirmation is personal to User. Therefore, User may not assign or transfer to any other person (whether a natural person or an organization of any kind) the license created by the Order Confirmation and these terms and conditions or any rights granted hereunder; provided, however, that User may assign such license in its entirety on written notice to CCC in the event of a transfer of all or substantially all of User's rights in the new material which includes the Work(s) licensed under this Service.

   8.4. No amendment or waiver of any terms is binding unless set forth in writing and signed by the parties. The Rightsholder and CCC hereby object to any terms contained in any writing prepared by the User or its principals, employees, agents or affiliates and purporting to govern or otherwise relate to the licensing transaction described in the Order Confirmation, which terms are in any way inconsistent with any terms set forth in the Order Confirmation and/or in these terms and conditions or CCC's standard operating procedures, whether such writing is prepared prior to, simultaneously with or subsequent to the Order Confirmation, and whether such writing appears on a copy of the Order Confirmation or in a separate instrument.

   8.5. The licensing transaction described in the Order Confirmation document shall be governed by and construed under the law of the State of New York, USA, without regard to the principles thereof of conflicts of law. Any case, controversy, suit, action, or proceeding arising out of, in connection with, or related to such licensing transaction shall be brought, at CCC's sole discretion, in any federal or state court located in the County of New York, State of New York, USA, or in any federal or state court whose geographical jurisdiction covers the location of the Rightsholder set forth in the Order Confirmation. The parties expressly submit to the personal jurisdiction and venue of each such federal or state court.If you have any comments or questions about the Service or Copyright Clearance Center, please contact us at 978-750-8400 or send an e-mail to support@copyright.com.

v 1.1

B.3 Topography quantifications allow for identifying the contribution of parental strains to physical properties of co-cultured biofilms

C. indicate the Licensed Material is licensed under this Public License, and include the text of, or the URI or hyperlink to, this Public License.

For the avoidance of doubt, You do not have permission under this Public License to Share Adapted Material.

2. You may satisfy the conditions in Section 3(a)(1) in any reasonable manner based on the medium, means, and context in which You Share the Licensed Material. For example, it may be reasonable to satisfy the conditions by providing a URI or hyperlink to a resource that includes the required information.
3. If requested by the Licensor, You must remove any of the information required by Section 3(a)(1)(A) to the extent reasonably practicable.

Section 4 – Sui Generis Database Rights.

Where the Licensed Rights include Sui Generis Database Rights that apply to Your use of the Licensed Material:

a. for the avoidance of doubt, Section 2(a)(1) grants You the right to extract, reuse, reproduce, and Share all or a substantial portion of the contents of the database for NonCommercial purposes only and provided You do not Share Adapted Material;
b. if You include all or a substantial portion of the database contents in a database in which You have Sui Generis Database Rights, then the database in which You have Sui Generis Database Rights (but not its individual contents) is Adapted Material; and
c. You must comply with the conditions in Section 3(a) if You Share all or a substantial portion of the contents of the database.

For the avoidance of doubt, this Section 4 supplements and does not replace Your obligations under this Public License where the Licensed Rights include other Copyright and Similar Rights.

Section 5 – Disclaimer of Warranties and Limitation of Liability.

a. Unless otherwise separately undertaken by the Licensor, to the extent possible, the Licensor offers the Licensed Material as-is and as-available, and makes no representations or warranties of any kind concerning the Licensed Material, whether express, implied, statutory, or other. This includes, without limitation, warranties of title, merchantability, fitness for a particular purpose, non-infringement, absence of latent or other defects, accuracy, or the presence or absence of errors, whether or not known or discoverable. Where disclaimers of warranties are not allowed in full or in part, this disclaimer may not apply to You.

b. To the extent possible, in no event will the Licensor be liable to You on any legal theory (including, without limitation, negligence) or otherwise for any direct, special, indirect, incidental, consequential, punitive, exemplary, or other losses, costs, expenses, or damages arising out of this Public License or use of the Licensed Material, even if the Licensor has been advised of the possibility of such losses, costs, expenses, or damages. Where a limitation of liability is not allowed in full or in part, this limitation may not apply to You.

c. The disclaimer of warranties and limitation of liability provided above shall be interpreted in a manner that, to the extent possible, most closely approximates an absolute disclaimer and waiver of all liability.

Section 6 – Term and Termination.

a. This Public License applies for the term of the Copyright and Similar Rights licensed here. However, if You fail to comply with this Public License, then Your rights under this Public License terminate automatically.
b. Where Your right to use the Licensed Material has terminated under Section 6(a), it reinstates:
    1. automatically as of the date the violation is cured, provided it is cured within 30 days of Your discovery of the violation; or
    2. upon express reinstatement by the Licensor.

    For the avoidance of doubt, this Section 6(b) does not affect any right the Licensor may have to seek remedies for Your violations of this Public License.

c. For the avoidance of doubt, the Licensor may also offer the Licensed Material under separate terms or conditions or stop distributing the Licensed Material at any time; however, doing so will not terminate this Public License.
d. Sections 1, 5, 6, 7, and 8 survive termination of this Public License.

Section 7 – Other Terms and Conditions.

a. The Licensor shall not be bound by any additional or different terms or conditions communicated by You unless expressly agreed.
b. Any arrangements, understandings, or agreements regarding the Licensed Material not stated herein are separate from and independent of the terms and conditions of this Public License.

Section 8 – Interpretation.

a. For the avoidance of doubt, this Public License does not, and shall not be interpreted to, reduce, limit, restrict, or impose conditions on any use of the Licensed Material that could lawfully be made without permission under this Public License.
b. To the extent possible, if any provision of this Public License is deemed unenforceable, it shall be automatically reformed to the minimum extent necessary to make it enforceable. If the provision cannot be reformed, it shall be severed from this Public License without affecting the enforceability of the remaining terms and conditions.
c. No term or condition of this Public License will be waived and no failure to comply consented to unless expressly agreed to by the Licensor.
d. Nothing in this Public License constitutes or may be interpreted as a limitation upon, or waiver of, any privileges and immunities that apply to the Licensor or You, including from the legal processes of any jurisdiction or authority.

B.4 Machine Learning Approach to Analyze the Surface Properties of Biological Materials

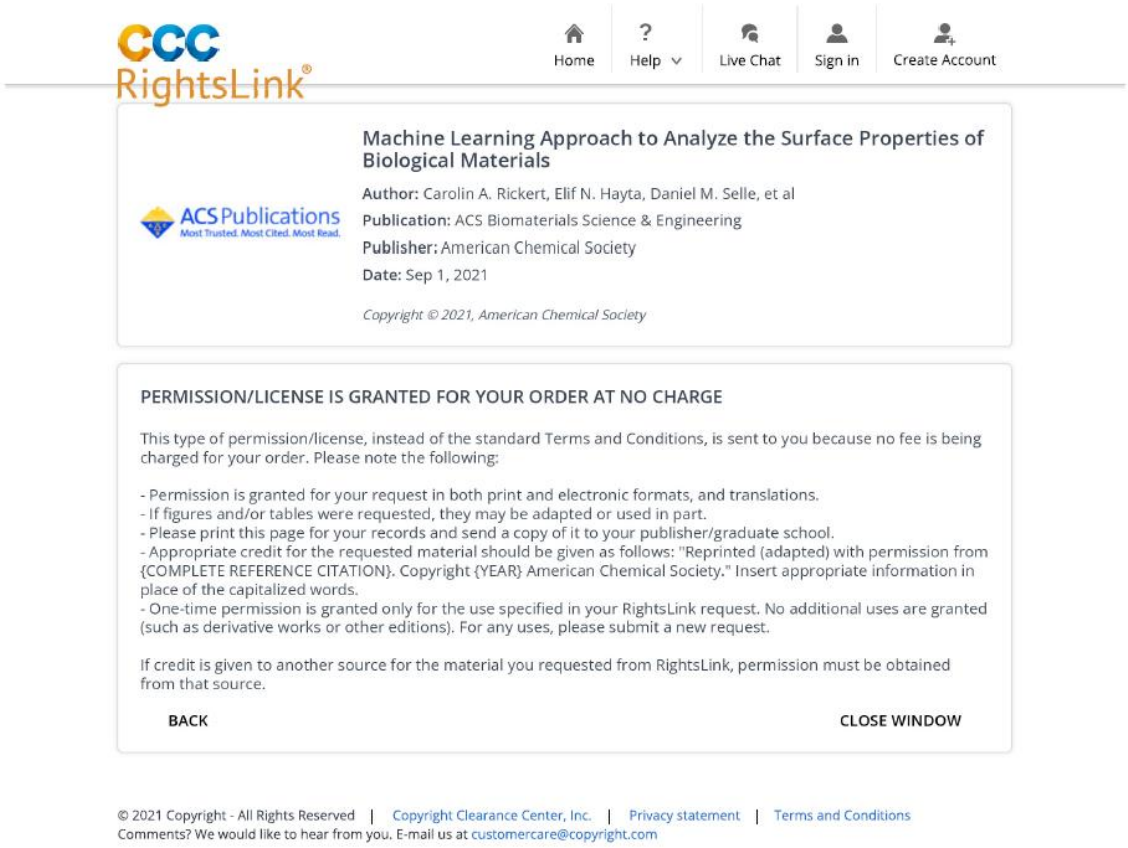

C. Vollständige Liste der Publikationen

1. Hayta, E.N; Lieleg, O. Biopolymer-enriched *B. subtilis* NCIB 3610 biofilms exhibit increased erosion resistance, *Biomaterials Science* 2019, 7, 4675 – 4686.

2. Hayta, E. N; Rickert, C. A; Lieleg, O. Topography quantifications allow for identifying the contribution of parental strains to physical properties of co-cultured biofilms, *Biofilm* 2021, 3, 100044.

3. Rickert, C. A; Hayta, E. N; Selle, D. M.; Kouroudis, I.; Harth, M.; Gagliardi, A; Lieleg, O. A Machine Learning Approach to Analyze the Surface Properties of Biological Materials, *ACS Biomaterials Science & Engineering* 2021, 7 (9), 4614-4625.

4. Hayta, E. N; Ertelt, M. J.; Kretschmer, M.; Lieleg, O. Bacterial Materials: Applications of Natural and Modified Biofilms, *Advanced Materials Interfaces* 2021, 8, 2101024.

5. Kretschmer, M.; Hayta, E. N.; Ertelt, M. J.; Würbser, M.A.; Boekhoven, J.; Lieleg, O. A rotating bioreactor for the production of biofilms at the solid-air interface (submitted).

Referenzen

[1] H.C. Flemming, J. Wingender, The biofilm matrix, Nat. Rev. Microbiol. 8 (2010) 623–633. https://doi.org/10.1038/nrmicro2415.

[2] V. Lazarova, J. Manem, Biofilm characterization and activity analysis in water and wastewater treatment, Water Res. 29 (1995) 2227–2245. https://doi.org/10.1016/0043-1354(95)00054-O.

[3] R. Singh, D. Paul, R.K. Jain, Biofilms: implications in bioremediation, Trends Microbiol. 14 (2006) 389–397. https://doi.org/10.1016/j.tim.2006.07.001.

[4] A. Keren-Paz, I. Kolodkin-Gal, A brick in the wall: Discovering a novel mineral component of the biofilm extracellular matrix, N. Biotechnol. 56 (2020) 9–15. https://doi.org/10.1016/j.nbt.2019.11.002.

[5] C.M. Heveran, S.L. Williams, J. Qiu, J. Artier, M.H. Hubler, S.M. Cook, J.C. Cameron, W. V. Srubar, Biomineralization and Successive Regeneration of Engineered Living Building Materials, Matter. 2 (2020) 481–494. https://doi.org/10.1016/j.matt.2019.11.016.

[6] J.P. Park, M. Do, S.H. Hong, J. Ryu, D. Kang, K. Rho, J.H. Ahn, H. Lee, BIOMOSAIC Film: Artificial Biofilms with Catalytic and Self-Sealing Properties, Adv. Mater. Interfaces. 6 (2019) 1–11. https://doi.org/10.1002/admi.201900379.

[7] H. Dong, W. Zhang, Y. Wang, D. Liu, P. Wang, Biofilm Polysaccharide Display Platform: A Natural, Renewable, and Biocompatible Material for Improved Lipase Performance, J. Agric. Food Chem. 68 (2020) 1373–1381. https://doi.org/10.1021/acs.jafc.9b07209.

[8] X. Wang, J. Pu, Y. Liu, F. Ba, M. Cui, K. Li, Y. Xie, Y. Nie, Q. Mi, T. Li, L. Liu, M. Zhu, C. Zhong, Immobilization of functional nano-objects in living engineered bacterial biofilms for catalytic applications, Natl. Sci. Rev. 6 (2019) 929–943. https://doi.org/10.1093/nsr/nwz104.

[9] M.A. Bakar, J. McKimm, S.Z. Haque, M.A.A. Majumder, M. Haque, Chronic tonsillitis and biofilms: A brief overview of treatment modalities, J. Inflamm. Res. 11 (2018) 329–337. https://doi.org/10.2147/JIR.S162486.

[10] B.W. Peterson, Y. He, Y. Ren, A. Zerdoum, M.R. Libera, P.K. Sharma, A.J. van Winkelhoff, D. Neut, P. Stoodley, H.C. van der Mei, H.J. Busscher, Viscoelasticity of biofilms and their recalcitrance to mechanical and chemical challenges, FEMS Microbiol. Rev. 39 (2015) 234–245. https://doi.org/10.1093/femsre/fuu008.

[11] S.M. Abdel-Aziz, A. Aeron, Bacterial Biofilm: Dispersal and Inhibition Strategies, Sch. J. Biotechnol. 1 (2014) 105. https://doi.org/10.18875/2375-6713.1.105.

[12] S. Galié, C. García-Gutiérrez, E.M. Miguélez, C.J. Villar, F. Lombó, Biofilms in

the food industry: Health aspects and control methods, Front. Microbiol. 9 (2018) 1–18. https://doi.org/10.3389/fmicb.2018.00898.

[13] J.B. Kaplan, Biofilm Dispersal: Mechanisms, Clinical Implications, and Potential Therapeutic Uses, J. Dent. Res. 89 (2010) 205–218. https://doi.org/10.1177/0022034509359403.

[14] L. Karygianni, Z. Ren, H. Koo, T. Thurnheer, Biofilm Matrixome: Extracellular Components in Structured Microbial Communities, Trends Microbiol. 28 (2020) 668–681. https://doi.org/10.1016/j.tim.2020.03.016.

[15] C. Falcón García, M. Kretschmer, C.N. Lozano-Andrade, M. Schönleitner, A. Dragoŝ, Á.T. Kovács, O. Lieleg, Metal ions weaken the hydrophobicity and antibiotic resistance of Bacillus subtilis NCIB 3610 biofilms, Npj Biofilms Microbiomes. 6 (2020) 1–11. https://doi.org/10.1038/s41522-019-0111-8.

[16] H.Y. Erbil, A.L. Demirel, Y. Avci, O. Mert, Transformation of a Simple Plastic into a Superhydrophobic Surface, Science (80-.). 299 (2003) 1377–1380. https://doi.org/10.1126/science.1078365.

[17] S. Kesel, S. Grumbein, M. Tallawi, A. Marel, O. Lieleg, M. Opitz, Direct Comparison of Physical Properties of Bacillus subtilis NCIB 3610 and B-1 Biofilms, Appl. Environ. Microbiol. 82 (2016) 2424–2432. https://doi.org/10.1128/AEM.03957-15.

[18] S. Kesel, B. Von Bronk, C. Falcón García, A. Götz, O. Lieleg, M. Opitz, Matrix composition determines the dimensions of: Bacillus subtilis NCIB 3610 biofilm colonies grown on LB agar, RSC Adv. 7 (2017) 31886–31898. https://doi.org/10.1039/c7ra05559e.

[19] Á.T. Kovács, J. van Gestel, O.P. Kuipers, The protective layer of biofilm: A repellent function for a new class of amphiphilic proteins, Mol. Microbiol. 85 (2012) 8–11. https://doi.org/10.1111/j.1365-2958.2012.08101.x.

[20] K.M. Bromley, R.J. Morris, L. Hobley, G. Brandani, R.M.C. Gillespie, M. McCluskey, U. Zachariae, D. Marenduzzo, N.R. Stanley-Wall, C.E. MacPhee, Interfacial self-assembly of a bacterial hydrophobin, Proc. Natl. Acad. Sci. U. S. A. 112 (2015) 5419–5424. https://doi.org/10.1073/pnas.1419016112.

[21] S. Arnaouteli, C.E. MacPhee, N.R. Stanley-Wall, Just in case it rains: building a hydrophobic biofilm the Bacillus subtilis way, Curr. Opin. Microbiol. 34 (2016) 7–12. https://doi.org/10.1016/j.mib.2016.07.012.

[22] L. Hobley, A. Ostrowski, F. V. Rao, K.M. Bromley, M. Porter, A.R. Prescott, C.E. MacPhee, D.M.F. Van Aalten, N.R. Stanley-Wall, BslA is a self-assembling bacterial hydrophobin that coats the Bacillus subtilis biofilm, Proc. Natl. Acad. Sci. U. S. A. 110 (2013) 13600–13605. https://doi.org/10.1073/pnas.1306390110.

[23] C. Falcón García, F. Stangl, A. Götz, W. Zhao, S.A. Sieber, M. Opitz, O. Lieleg, Topographical alterations render bacterial biofilms susceptible to chemical and mechanical stress, Biomater. Sci. 7 (2019) 220–232. https://doi.org/10.1039/c8bm00987b.

[24] M. Klotz, M. Kretschmer, A. Goetz, S. Ezendam, O. Lieleg, M. Opitz, Importance of the biofilm matrix for the erosion stability of Bacillus subtilis NCIB 3610 biofilms, RSC Adv. 9 (2019) 11521–11529. https://doi.org/10.1039/C9RA01955C.

[25] S. Grumbein, M. Opitz, O. Lieleg, Selected metal ions protect Bacillus subtilis biofilms from erosion, Metallomics. 6 (2014) 1441–1450. https://doi.org/10.1039/c4mt00049h.

[26] W.H. Bowen, R.A. Burne, H. Wu, H. Koo, Oral Biofilms: Pathogens, Matrix, and Polymicrobial Interactions in Microenvironments, Trends Microbiol. 26 (2018) 229–242. https://doi.org/10.1016/j.tim.2017.09.008.

[27] H.L. Røder, S.J. Sørensen, M. Burmølle, Studying Bacterial Multispecies Biofilms: Where to Start?, Trends Microbiol. 24 (2016) 503–513. https://doi.org/10.1016/j.tim.2016.02.019.

[28] F.A. Sadiq, L. Wenwei, M. Heyndrickx, S. Flint, C. Wei, Z. Jianxin, H. Zhang, Synergistic interactions prevail in multispecies biofilms formed by the human gut microbiota on mucin, FEMS Microbiol. Ecol. 97 (2021). https://doi.org/10.1093/femsec/fiab096.

[29] W. Liu, H.L. Røder, J.S. Madsen, T. Bjarnsholt, S.J. Sørensen, M. Burmølle, Interspecific bacterial interactions are reflected in multispecies biofilm spatial organization, Front. Microbiol. 7 (2016) 1–8. https://doi.org/10.3389/fmicb.2016.01366.

[30] M. Burmølle, D. Ren, T. Bjarnsholt, S.J. Sørensen, Interactions in multispecies biofilms: Do they actually matter?, Trends Microbiol. 22 (2014) 84–91. https://doi.org/10.1016/j.tim.2013.12.004.

[31] P.G. Jayathilake, S. Jana, S. Rushton, D. Swailes, B. Bridgens, T. Curtis, J. Chen, Extracellular polymeric substance production and aggregated bacteria colonization influence the competition of microbes in biofilms, Front. Microbiol. 8 (2017). https://doi.org/10.3389/fmicb.2017.01865.

[32] P.D. Marsh, A. Moter, D.A. Devine, Dental plaque biofilms: Communities, conflict and control, Periodontol. 2000. 55 (2011) 16–35. https://doi.org/10.1111/j.1600-0757.2009.00339.x.

[33] A.G. Harvey, E.W. Hill, A. Bayat, Designing implant surface topography for improved biocompatibility, Expert Rev. Med. Devices. 10 (2013) 257–267. https://doi.org/10.1586/erd.12.82.

[34] S. Wu, B. Zhang, Y. Liu, X. Suo, H. Li, Influence of surface topography on bacterial adhesion: A review, Biointerphases. 13 (2018) 060801. https://doi.org/10.1116/1.5054057.

[35] C. Falcón García, F. Stangl, A. Götz, W. Zhao, S.A. Sieber, M. Opitz, O. Lieleg, Topographical alterations render bacterial biofilms susceptible to chemical and mechanical stress, Biomater. Sci. 7 (2019) 220–232. https://doi.org/10.1039/c8bm00987b.

[36] K. Mouralova, T. Prokes, L. Benes, P. Sliwkova, Analysis of subsurface defects

occurrence in abrasion resistant Creusabro steel after WEDM including the study of morphology and surface topography, Mach. Sci. Technol. 24 (2020) 274–290. https://doi.org/10.1080/10910344.2019.1669166.

[37] C. Yu, H. Yu, G. Liu, W. Chen, B. He, Q.J. Wang, Understanding topographic dependence of friction with micro- and nano-grooved surfaces, Tribol. Lett. 53 (2014) 145–156. https://doi.org/10.1007/s11249-013-0252-5.

[38] G. Heydari, E. Thormann, M. Järn, E. Tyrode, P.M. Claesson, Hydrophobic surfaces: Topography effects on wetting by supercooled water and freezing delay, J. Phys. Chem. C. 117 (2013) 21752–21762. https://doi.org/10.1021/jp404396m.

[39] G. McHale, M.I. Newton, N.J. Shirtcliffe, Dynamic wetting and spreading and the role of topography, J. Phys. Condens. Matter. 21 (2009) 464122. https://doi.org/10.1088/0953-8984/21/46/464122.

[40] J.D. Eick, L.N. Johnson, J.R. Fromer, R.J. Good, A.W. Neumann, Surface Topography: Its Influence on Wetting and Adhesion in a Dental Adhesive System, J. Dent. Res. 51 (1972) 780–788. https://doi.org/10.1177/00220345720510031401.

[41] S. Wang, L. Jiang, Definition of superhydrophobic states, Adv. Mater. 19 (2007) 3423–3424. https://doi.org/10.1002/adma.200700934.

[42] M. Nosonovsky, B. Bhushan, Hierarchical roughness optimization for biomimetic superhydrophobic surfaces, Ultramicroscopy. 107 (2007) 969–979. https://doi.org/10.1016/j.ultramic.2007.04.011.

[43] B. Bhushan, M. Nosonovsky, The rose petal effect and the modes of superhydrophobicity, Philos. Trans. R. Soc. A Math. Phys. Eng. Sci. 368 (2010) 4713–4728. https://doi.org/10.1098/rsta.2010.0203.

[44] T. Darmanin, F. Guittard, Superhydrophobic and superoleophobic properties in nature, Mater. Today. 18 (2015) 273–285. https://doi.org/10.1016/j.mattod.2015.01.001.

[45] M. Werb, C. Falcón García, N.C. Bach, S. Grumbein, S.A. Sieber, M. Opitz, O. Lieleg, Surface topology affects wetting behavior of Bacillus subtilis biofilms, Npj Biofilms Microbiomes. 3 (2017) 1–10. https://doi.org/10.1038/s41522-017-0018-1.

[46] S.S. Branda, F. Chu, D.B. Kearns, R. Losick, R. Kolter, A major protein component of the Bacillus subtilis biofilm matrix, Mol. Microbiol. 59 (2006) 1229–1238. https://doi.org/10.1111/j.1365-2958.2005.05020.x.

[47] D. Romero, C. Aguilar, R. Losick, R. Kolter, Amyloid fibers provide structural integrity to Bacillus subtilis biofilms, Proc. Natl. Acad. Sci. U. S. A. 107 (2010) 2230–2234. https://doi.org/10.1073/pnas.0910560107.

[48] K. Kobayashi, M. Iwano, BslA(YuaB) forms a hydrophobic layer on the surface of Bacillus subtilis biofilms, Mol. Microbiol. 85 (2012) 51–66. https://doi.org/10.1111/j.1365-2958.2012.08094.x.

[49] D.B. Kearns, F. Chu, S.S. Branda, R. Kolter, R. Losick, A master regulator for biofilm formation by Bacillus subtilis, Mol. Microbiol. 55 (2005) 739–749. https://doi.org/10.1111/j.1365-2958.2004.04440.x.

[50] F. Stangl, Surface Topology and Wetting Behaviour of Biofilms, Technische Universität München, 2017.

[51] R. Gallegos-Monterrosa, E. Mhatre, Á.T. Kovács, Specific Bacillus subtilis 168 variants form biofilms on nutrient-rich medium, Microbiology. 162 (2016) 1922–1932. https://doi.org/10.1099/mic.0.000371.

[52] I.L. Shih, Y.T. Van, The production of poly-(γ-glutamic acid) from microorganisms and its various applications, Bioresour. Technol. 79 (2001) 207–225. https://doi.org/10.1016/S0960-8524(01)00074-8.

[53] T. Candela, A. Fouet, Poly-gamma-glutamate in bacteria, Mol. Microbiol. 60 (2006) 1091–1098. https://doi.org/10.1111/j.1365-2958.2006.05179.x.

[54] M. Morikawa, S. Kagihiro, M. Haruki, K. Takano, S. Branda, R. Kolter, S. Kanaya, Biofilm formation by a Bacillus subtilis strain that produces γ-polyglutamate, Microbiology. 152 (2006) 2801–2807. https://doi.org/10.1099/mic.0.29060-0.

[55] I. Donati, S. Paoletti, Material Properties of Alginates, in: 2009: pp. 1–53. https://doi.org/10.1007/978-3-540-92679-5_1.

[56] K.Y. Lee, D.J. Mooney, Alginate: Properties and biomedical applications, Prog. Polym. Sci. 37 (2012) 106–126. https://doi.org/10.1016/j.progpolymsci.2011.06.003.

[57] O. Orgad, Y. Oren, S.L. Walker, M. Herzberg, The role of alginate in Pseudomonas aeruginosa EPS adherence, viscoelastic properties and cell attachment, Biofouling. 27 (2011) 787–798. https://doi.org/10.1080/08927014.2011.603145.

[58] S.N. Pawar, K.J. Edgar, Alginate derivatization: A review of chemistry, properties and applications, Biomaterials. 33 (2012) 3279–3305. https://doi.org/10.1016/j.biomaterials.2012.01.007.

[59] M. Sønderholm, K.N. Kragh, K. Koren, T.H. Jakobsen, S.E. Darch, M. Alhede, P.Ø. Jensen, M. Whiteley, M. Kühl, T. Bjarnsholt, Pseudomonas aeruginosa aggregate formation in an alginate bead model system exhibits in vivo-like characteristics, Appl. Environ. Microbiol. 83 (2017). https://doi.org/10.1128/AEM.00113-17.

[60] A.A. D'souza, R. Shegokar, Polyethylene glycol (PEG): a versatile polymer for pharmaceutical applications, Expert Opin. Drug Deliv. 13 (2016) 1257–1275. https://doi.org/10.1080/17425247.2016.1182485.

[61] G. Pasut, F.M. Veronese, State of the art in PEGylation: The great versatility achieved after forty years of research, J. Control. Release. 161 (2012) 461–472. https://doi.org/10.1016/j.jconrel.2011.10.037.

[62] K. Knop, R. Hoogenboom, D. Fischer, U.S. Schubert, Poly(ethylene glycol) in drug delivery: Pros and cons as well as potential alternatives, Angew. Chemie - Int. Ed. 49 (2010) 6288–6308. https://doi.org/10.1002/anie.200902672.

[63] A. Thomas, S.S. Müller, H. Frey, Beyond poly(ethylene glycol): Linear polyglycerol as a multifunctional polyether for biomedical and pharmaceutical applications, Biomacromolecules. 15 (2014) 1935–1954. https://doi.org/10.1021/bm5002608.

[64] B.D. Hoyle, J.W. Costerton, Bacterial resistance to antibiotics: The role of biofilms, in: Prog. Drug Res. / Fortschritte Der Arzneimittelforsch. / Progrès Des Rech. Pharm., Birkhäuser Basel, Basel, 1991: pp. 91–105. https://doi.org/10.1007/978-3-0348-7139-6_2.

[65] D.B. Adimpong, K.I. Sørensen, L. Thorsen, B. Stuer-Lauridsen, W.S. Abdelgadir, D.S. Nielsen, P.M.F. Derkx, L. Jespersen, Antimicrobial Susceptibility of Bacillus Strains Isolated from Primary Starters for African Traditional Bread Production and Characterization of the Bacitracin Operon and Bacitracin Biosynthesis, Appl. Environ. Microbiol. 78 (2012) 7903–7914. https://doi.org/10.1128/aem.00730-12.

[66] T.C. Coonrod, J. Donald; Leadley, Peter J.; Eickhoff, Antibiotic susceptibility of Bacillus species, J. Infect. Dis. 123 (1971) 102–105.

[67] S.R. Connell, D.M. Tracz, K.H. Nierhaus, D.E. Taylor, Ribosomal Protection Proteins and Their Mechanism of Tetracycline Resistance, Antimicrob. Agents Chemother. 47 (2003) 3675–3681. https://doi.org/10.1128/AAC.47.12.3675-3681.2003.

[68] M.D. Schnappinger, W. Hillen, Tetracyclines: antibiotic action, uptake, and resistance mechanisms, Arch Microbiol. 165 (1996) 359–369.

[69] E. Lu, T. Trinh, T. Tsang, J. Yeung, Effect of growth in sublethal levels of kanamycin and streptomycin on capsular polysaccharide production and antibiotic resistance in Escherichia coli B23, J. Exp. Microbiol. Immunol. 12 (2008) 21–26.

[70] K.M.I. Bashir, M.-G. Cho, The Effect of Kanamycin and Tetracycline on Growth and Photosynthetic Activity of Two Chlorophyte Algae, Biomed Res. Int. 2016 (2016) 1–8. https://doi.org/10.1155/2016/5656304.

[71] J. Suzuki, T. Kunimoto, M. Hori, Effects of kanamycin on protein synthesis: inhibition of elongation of peptide chains, J. Antibiot. (Tokyo). 23 (1970) 99–101.

[72] Keyence, VK-X1000 Series User's Manual, 2019.

[73] J.B. Pawley, ed., Handbook of Biological Confocal Microscopy, Third Edit, Springer Science+Business Media, LLC, Madison, 2006.

[74] Keyence, VK-X1000 Series MultifileAnalyzer Reference Manual, 2019.

[75] Michigan Metrology, (2021). https://www.michmet.com/.

[76] E. Aescht, S. Büchl-Zimmermann, A. Burmester, S. Dänhardt-Pfeiffer, C. Desel,

C. Hamers, G. Jach, M. Kässens, J. Makovitzky, M. Mulisch, B. Nixdorf-Bergweiler, D. Pütz, B. Riedelsheimer, F. van den Boom, R. Wegerhoff, U. Welsch, Romeis Mikroskopische Technik, Spektrum Akademischer Verlag, Heidelberg, 2010. https://doi.org/10.1007/978-3-8274-2254-5.

[77] P.A. Tipler, Physik. 3. korrigierter Nachdruck der 1. Auflage, Spektrum Akademischer Verlag, 2000.

[78] T. Young, An essay on the cohesion of fluids, Philos. Trans. R. Soc. London. 95 (1805) 65–87. https://doi.org/10.1098/rstl.1805.0005.

[79] R.N. Wenzel, Resistance of solid surfaces to wetting by water, Ind. Eng. Chem. 28 (1936) 988–994. https://doi.org/10.1021/ie50320a024.

[80] A.B.D. Cassie, S. Baxter, Wettability of porous surfaces., Trans. Faraday Soc. 40 (1944) 546–551.

[81] T. Mezger, Das Rheologie-Handbuch: für Anwender von Rotations- und Oszillations-Rheometern, Vincentz, Hannover, 2000.

[82] O. Lieleg, M. Caldara, R. Baumgärtel, K. Ribbeck, Mechanical robustness of Pseudomonas aeruginosa biofilms, Soft Matter. 7 (2011) 3307–3314. https://doi.org/10.1039/c0sm01467b.

[83] S.G.V. Charlton, M.A. White, S. Jana, L.E. Eland, P.G. Jayathilake, J.G. Burgess, J. Chen, A. Wipat, T.P. Curtis, Regulating, measuring, and modeling the viscoelasticity of bacterial biofilms, J. Bacteriol. 201 (2019). https://doi.org/10.1128/JB.00101-19.

[84] M. Kretschmer, C.A. Schüßler, O. Lieleg, Biofilm Adhesion to Surfaces is Modulated by Biofilm Wettability and Stiffness, Adv. Mater. Interfaces. 8 (2021). https://doi.org/10.1002/admi.202001658.

[85] M. Klotz, M. Kretschmer, A. Goetz, S. Ezendam, O. Lieleg, M. Opitz, Importance of the biofilm matrix for the erosion stability of Bacillus subtilis NCIB 3610 biofilms, RSC Adv. 9 (2019) 11521–11529. https://doi.org/10.1039/C9RA01955C.

[86] A.D. Verderosa, M. Totsika, K.E. Fairfull-Smith, Bacterial Biofilm Eradication Agents: A Current Review, Front. Chem. 7 (2019) 824. https://doi.org/10.3389/fchem.2019.00824.

[87] H. Wolfmeier, D. Pletzer, S.C. Mansour, R.E.W. Hancock, New Perspectives in Biofilm Eradication, ACS Infect. Dis. 4 (2018) 93–106. https://doi.org/10.1021/acsinfecdis.7b00170.

[88] M.J. Angelaalincy, R. Navanietha Krishnaraj, G. Shakambari, B. Ashokkumar, S. Kathiresan, P. Varalakshmi, Biofilm Engineering Approaches for Improving the Performance of Microbial Fuel Cells and Bioelectrochemical Systems, Front. Energy Res. 6 (2018) 63. https://doi.org/10.3389/fenrg.2018.00063.

[89] Y. Hu, M. Mukherjee, B. Cao, Biofilm-Biology-Informed Biofilm Engineering for Environmental Biotechnology, ACS Symp. Ser. 1323 (2019) 59–82. https://doi.org/10.1021/bk-2019-1323.ch003.

[90] M. Mukherjee, N. Zaiden, A. Teng, Y. Hu, B. Cao, Shewanella biofilm development and engineering for environmental and bioenergy applications, Curr. Opin. Chem. Biol. 59 (2020) 84–92. https://doi.org/10.1016/j.cbpa.2020.05.004.

[91] M. Rosenbaum, M.A. Cotta, L.T. Angenent, Aerated Shewanella oneidensis in continuously fed bioelectrochemical systems for power and hydrogen production, Biotechnol. Bioeng. 105 (2010) 880–888. https://doi.org/10.1002/bit.22621.

[92] B.E. Logan, Exoelectrogenic bacteria that power microbial fuel cells, Nat. Rev. Microbiol. 7 (2009) 375–381. https://doi.org/10.1038/nrmicro2113.

[93] F.F. Yan, C. Wu, Y.Y. Cheng, Y.R. He, W.W. Li, H.Q. Yu, Carbon nanotubes promote Cr(VI) reduction by alginate-immobilized Shewanella oneidensis MR-1, Biochem. Eng. J. 77 (2013) 183–189. https://doi.org/10.1016/j.bej.2013.06.009.

[94] A.K. Epstein, B. Pokroy, A. Seminara, J. Aizenberg, Bacterial biofilm shows persistent resistance to liquid wetting and gas penetration, Proc. Natl. Acad. Sci. U. S. A. 108 (2011) 995–1000. https://doi.org/10.1073/pnas.1011033108.

[95] Keyence, Introduction to Roughness, (2021). https://www.keyence.com/ss/products/microscope/roughness/surface/svk-reduced-dale-height.jsp.

[96] A. Sarjit, S. Mei Tan, G. A. Dykes, Surface modification of materials to encourage beneficial biofilm formation, AIMS Bioeng. 2 (2015) 404–422. https://doi.org/10.3934/bioeng.2015.4.404.

[97] N. Raab, I. Bachelet, Resolving biofilm topography by native scanning electron microscopy, J. Biol. Methods. 4 (2017) e70. https://doi.org/10.14440/jbm.2017.173.

[98] E. Ning, G. Turnbull, J. Clarke, F. Picard, P. Riches, M. Vendrell, D. Graham, A.W. Wark, K. Faulds, W. Shu, 3D bioprinting of mature bacterial biofilms for antimicrobial resistance drug testing, Biofabrication. 11 (2019) 045018. https://doi.org/10.1088/1758-5090/ab37a0.

[99] S. Reese, B. Guggenheim, A novel TEM contrasting technique for extracellular polysaccharides in in vitro biofilms, Microsc. Res. Tech. 70 (2007) 816–822. https://doi.org/10.1002/jemt.20471.

[100] K. Weber, J. Delben, T.G. Bromage, S. Duarte, Comparison of SEM and VPSEM imaging techniques with respect to Streptococcus mutans biofilm topography, FEMS Microbiol. Lett. 350 (2014) 175–179. https://doi.org/10.1111/1574-6968.12334.

[101] A. Noro, M. Kaneko, I. Murata, M. Yoshinari, Influence of surface topography and surface physicochemistry on wettability of zirconia (tetragonal zirconia polycrystal), J. Biomed. Mater. Res. - Part B Appl. Biomater. 101 B (2013) 355–363. https://doi.org/10.1002/jbm.b.32846.

[102] H.N. Hosseinabadi, S.A. Sajjady, S. Amini, Creating micro textured surfaces for

the improvement of surface wettability through ultrasonic vibration assisted turning, Int. J. Adv. Manuf. Technol. 96 (2018) 2825–2839. https://doi.org/10.1007/s00170-018-1580-2.

[103] Y.-J. Sheng, S. Jiang, H.-K. Tsao, Effects of geometrical characteristics of surface roughness on droplet wetting, J. Chem. Phys. 127 (2007) 234704. https://doi.org/10.1063/1.2804425.

[104] S.M. Kang, Role of wide tip of mushroom-like micropillar arrays to make the Cassie state on superrepellent surfaces, RSC Adv. 6 (2016) 74670–74674. https://doi.org/10.1039/c6ra11224b.

Danksagung

I would like to thank all the people who contributed to the success of this thesis and supported me during my doctoral studies.

Especially, I thank my 'Doktorvater' Prof. Dr. Oliver Lieleg for the support he provided to me during my studies. I am grateful for everything that he taught me in patience. I owe my success in my PhD studies to his precious supervision. Furthermore, he deserves a great thank for being encouraging in any case. With everything that I learn from him, I will try my best to be an academician and a supervisor like him in future. I thank Prof. Lieleg for being such a nice role model for me in my academic path.

I thank my colleagues Martin Kretschmer, Theresa Lutz, Carolin Rickert, Matthias Marczynski, Maria Bauer and Bernardo Miller Naranjo for their support and cooperation during my studies. Also, I thank my student Daniel Selle for his collaboration and his friendship. I am thankful to Iris for being always so nice and supportive to me. I also thank our technical assistants Christina and Tobias for their help in my studies.

Moreover, I would like to thank Turkish Ministry of National Education for granting my PhD study. In particular, I thank Education Attaché of Consulate General of Turkish Republic Munich Prof. Dr. Mustafa Çakır for his endless support and understanding under all circumstances and Consul General Mehmet Günay for his special attention in my studies. I am grateful them for letting me to feel the support of Turkish Republic beside me throughout my PhD studies in Münich. Also, I would like to thank the Secretary of Office of Education Counselor Berlin, Hülya Kunig, for all support, advices and help that she provided whenever I need.

My special thanks goes to Korkut Terkan and John LaMaster from MBE for their warm friendship. Actually, I can not thank enough for it, you know what it means to me, guys. I will always remember the tea/turkish coffe breaks, turkish breakfasts and the Thanksgiving dinner and conversations that we have with a smile. Thank you for these nice memories!

I warmly thank my dearest friend Ebru Çayır-Cengiz and her dear husband Adem Cengiz for always being beside me from overseas. I thank them to be able to call them

without any hesitation at absurd hours of the day, sometimes for very absurd reasons. Whenever I gave way to despair during my studies, they encouraged me to carry on and they always supported me with their wisdom. Dear Cengiz Family, thank you for being in my life, it is more valuable with you.

I also thank my dear "former" neighbors Martin I and Martin II, Knudsen and Meinel, respectively. I am very glad that we met for a beer and started this friendship. I feel so lucky to have such neighbors. As being the only one who I meet in person during this Corona-pandemic, I owe a special thank to Martin I for helping me to keep my sanity. Thank you for introducing very beautiful places in Garching to me, for long walks and philosophical conversations we had.

As my greatest supporters during my PhD here, I sincerely thank my dearest friends Melis Akgün, (güzel insan) Halil Kaan Canan, Mehmet Bedelce and Özge Katırcı (aka "Lake Crew"). Any word cannot describe how I appreciate your being in my life for the last three year. Thank you for listening my repeating problems, never leaving me alone when I feel depressed, having fun together, organizing great birthday parties, baking the most delicious cakes for my birthday, walking along Ludwig Straße several times at the same night, and the more that I can not write down here. Staying beside "our" lake in Englischer Garten whole night to enjoy the full moon was crazy, but amazing with you. Thank you for this unique experience and more.

Also, I thank my dear friend Turgut Refik Çağlar for the best advice I have ever had and for helpful conversations over machine learning. Thank you for being there when I need to laugh and competing with me when we play "Unter Spannung". Although you beat me mostly, I enjoy it a lot. No-one plays Unter Spannung like you Turgut.

Moreover, I thank my friends Merve, Şurhan, Özgür and Müge. I would never imagine that I will play Okey here for hours, but we did. It was great fun with you. Thank you for having fun together, enjoying Mehmet's kitchen more than the residents of the dorm.

Last but not least, I would like to thank my family for their endless trust, support, encouragement and love. You are my biggest chance in this life.